Cronfa
Swansea University's Research Repository

Modelling of Bimodal Wave Overtopping of Coastal Defences

Stephen Tunde Orimoloye

Submitted to Swansea University
in fulfilment of the requirements for the
Degree of Doctor of Philosophy

2020

Copyright: The author, Stephen Tunde Orimoloye, 2020.

Declaration

This work has not previously been accepted in substance for any degree and is not being concurrently submitted in candidature for any degree.

Signed: stephen Orimoloye ..... (candidate)

Date: 06/07/2020 .....

Statement 1

This thesis is the result of my own investigations, except where otherwise stated. Where correction services have been used, the extent and nature of the correction is clearly marked in a footnote(s).
Other sources are acknowledged by footnotes giving explicit references. A bibliography is appended.

Signed: stephen Orimoloye ..... (candidate)

Date: 06/07/2020 .....

Statement 2

I hereby give consent for my thesis, if accepted, to be available for photocopying and for inter-library loans after expiry of a bar on access approved by the Swansea University.

Signed: stephen Orimoloye ..... (candidate)

Date: 06/07/2020 .....

Stephen Tunde Orimoloye
2020

I would like to dedicate this thesis to my loving parents

Acknowledgements

I will like to principally acknowledge and appreciate my supervisory Team, Professor Dominic E. Reeve and Professor Harshinie Karunarathna for their unending support during this research period. I thank them for their guidance and patience. I appreciate the assistance of Dr. Jose Horrillo-Caraballo during both my numerical and experimental works. I place much respect on my colleagues in the Energy and Environmental research group for their help and guidance during these research periods. I would also like to acknowledge the contribution of professor Thomas Lykke Andersen and Professor Peter Frigaad from the Aalborg University, Denmark for the generously-articulated workshop on the generation and analysis of waves in physical models conducted in their university during the course of my study. I sincerely appreciate Professor Javier Lara from the Institute of Hydraulics, Cantabria for providing the codes for the computational model. The PhD project was funded by the Petroleum Technology Development Fund (PTDF) with Award Ref Number: PTDF/ED/OSS/PHD/TOS/842/16.

Abstract

Wave overtopping from a few hours of violent storms can cause damage to infrastructure. Extensive knowledge is available on the prediction of wave overtopping of smooth, sloping and vertical impermeable seawalls. However, existing prediction methods provide less certain predictions when the sea state has a bimodal character, such as when there are strong components of both wind and swell. This thesis improves wave overtopping study of seawalls under storm-driven bimodal seas. Firstly, we developed an energy-conserved bimodal spectrum which contains the same energy as the unimodal spectrum derived from a sea state for easy comparison. The peak periods of the bimodal spectrum is occurring at four different spectra peak periods (11, 15, 20 and 25 secs, respectively), swell magnitude is defined with percentages (0, 25, 50, and 75 percentages). Both the unimodal and the bimodal spectra were used to perform wave overtopping experiments in a laboratory tank and numerical flume. Different bimodal spectra were created from the same sea state but the peak periods of the swell in the resulting bimodal spectrum were varied while retaining the same energy content. Bimodal wave sequences are derived from these spectra and used to investigate the overtopping of sloping seawalls. The reflection performances of the impermeable slopes were analysed in present study. The dimensionless overtopping rate for a range of seawalls was measured for bimodal storm conditions of a minimum of 1000 waves. Results for unimodal conditions agree closely with predictions using the EurOtop formulae. The current standard suggested in EurOtop (2018) underpredicts the observed wave overtopping rates for bimodal conditions even when using the recommended parameters for such cases. Under these conditions, it was found that there is a dependence between mean overtopping rate and swell occurrences. New sets of empirical influencing factors to describe these dependencies have been determined in terms of seawall designs at locations that are exposed to local storm waves and open Atlantic oceans.

Table of contents

List of figures

List of tables

List of Symbols

Roman Symbols

α	Slope angle
α_f	Irregularity factor of the wave
β_e	beta due to swell and wind
δ_{ij}	Kronecker coefficient
ε	Dissipation rate of the turbulent energy
γ_{ij}	spectrum peak enhancement factor for swell and wind waves
$\gamma_{n,ij}$	The damping coefficient
κ	Correlation coefficient based on first-order Markov's chain
λ	Groupiness parameter of the wave
μ	Mean of the distribution
μ_v	Molecular viscosity
μ_{ab}	Artificial viscosity
μ_{eff}	efficient dynamic viscosity
ω	Angular frequency of the wave
$\overline{\tau}_{ij}$	Mean viscous stress tensor
$\overline{E}$	Mean experimental dimensionless overtopping
$\overline{N}$	Mean numerical dimensionless overtopping
$\overline{u}_1$	Mean velocity

Π_{ab}	Artificial viscosity
ρ	Density of sea water
ρ_f	Fluid density
σ	Standard deviation
σ'	Coefficient of variation
σ_s	coefficient of surface tension
τ	Mean time differences between two successive crests and troughs
τ_{ij}	Total stress in the system
θ_r & θ_t	Additional model openness functions
ε	Broadness factor of the wave
ξ	The breaker parameter based on S
$\xi_{m-1,0}$	The breaker parameter based on $S_{m-1,0}$
ξ_{op}	The breaker parameter based on S_{op}
ξ_o	The breaker parameter based on S_o
$A\&B$	EurOtop's fitted coefficients for different structure slopes
A_s	Modified A-coefficient due to swell percentage
B_S	Modified B-coefficient due to swell percentage
BE	Bias error
CD	Central difference
CI	Confidence interval
D_{50}	Nominal Diameter of rock
$E(f)$	Total spectral energy in the spectrum
E_i	Experimental dimensionless overtopping
F	Frequency

f^n	Frequency in line with order of moment
F_d	Damping force
F_r	Repulsive Force
$f_{i,j}$	Peak frequencies of the swell and wind waves
$F_{n,ij}$	total normal force
FFT	Fast Fourier Transform
g	acceleration due to gravity
g_i	acceleration due to gravity due to the i^{th} component
$h(t)$	Flow thickness of overtopping wave
H_i	wave height
H_{m0S}	Spectral wave height due to swell sea
H_{m0W}	Spectral wave height due to wind sea
H_{m0}	Spectral wave height of the wave
H_s	Significant wave height of the entire wave
h_{toe}	Water depth at toe of the structure
i,j,k	dimensions of motion
$IFFT$	Inverse Fast Fourier Transform
k	The turbulent kinetic energy
K_r	Reflection coefficient
K_u	Kurtosis of the wave
$k_{n,ij}$	TThe stiffness parameter
L	Wave length of propagated wave
L_o	Deep water wave length
$L_{m-1,0}$	Spectral wave length in deep water

L_{om}	Mean wave length in deep water
L_{op}	Peak wave length in deep water
$m_1 \& m_2$	Slopes of the gradient of lines of empirically fitted coefficients
m_n	Spectral moments determined at different order n = -1, 0, 2, & 4
mod_{fac}	Model factor of calibration
Mod_{value}	Elevation recorded at model scale
N	number of individual waves
n	Order of moment defined as -1, 0, 2, & 4
N_i	Numerical dimensionless overtopping
NSE	Nash–Sutcliffe efficiency
p	Pressure field
p_i'	Pressure fluctuations
P^*	Pseudo dynamic pressure
PPE	Poisson pressure equation
q	Average overtopping discharge per meter width of a structure
$q(t)$	Instantaneous wave overtopping
q^*	Non-dimensional overtopping rate
$q^*_{measured}$	Measured overtopping rate
q^*_{pred}	Predicted overtopping rate
Q_p	peakedness parameter
R^*	Non-dimensional crest freeboard
R^2	Coefficient of determination
R_c	Crest freeboard
R_c/H_{m0}	Non-dimensional crest freeboard $\frac{R_c}{H_{m0Toe}}$

R_s	Quality parameter of the wave
$RMSE$	The root mean square errors
RSD	Relative standard deviation
S	Wave steepness H/L
$S(f)$	Total energy in the spectrum
S_0	Swell percentage
S_k	Skewness of the wave
S_{0m}	Wave steepness based on L_o and $T_m = \frac{H_m 0}{L_{0m}}$
S_{0p}	Wave steepness based on L_o and $T_p = \frac{H_m 0}{L_{0p}}$
S_{bim}	Bimodal spectrum
$S_{m-1,0}$	Wave steepness based on L_o and $T_{m-1,0} = \frac{H_m 0}{L_{m-1,0}}$
S_{ss}	Spectrum due to swell
S_{ss}	Spectrum due to wind
$sigma$	Standard deviation
T	Wave period
t	time steps in secs
T_i	period of wave
$T_{m-1,0deep}$	$T_{m-1,0}$ determined at deep water
$T_{m-1,0toe}$	$T_{m-1,0}$ determined at the structure's toe
$T_{m-1,0}$	Spectral wave period defined by $\frac{m_{-1}}{m_0}$
$T_{m0,1}$	Mean wave period defined by $\frac{m_0}{m_1}$
$T_{m0,2}$	Mean wave period defined by $\sqrt{\frac{m_0}{m_1}}$
T_m	Mean wave period
$T_{Sm-1,0}$	Spectral swell-wave peak period

$T_{Wm-1,0}$	Spectral wind-wave peak period
u_i'	Turbulent velocity
u_i	velocity in x-direction
u_j	velocity in z-direction
v	Narrowness parameter of the wave
$v(t)$	Depth averaged velocity
V_a	Volume of air
V_f	Volume of the fluid
v_i	Eddy viscosity
VOF	Volume of fluid function
x_i	x coordinate measured along x-axis in the domain
D	Discretised Domain
F	VOF Function
K	Kernel Function
P	Pressure
W	Modified Kernel Function

Chapter 1

Introduction

1.1 Coastal Flooding from Wave Overtopping

Coastal flooding may occur whenever there is extreme wave overtopping of coastal defences during storms. A large proportion of the world's coastlines are exposed to local storm waves and open oceans (Figure 1.1). Long period swell waves can be present, leading to bimodal wave conditions.

Extreme wave overtopping events often accompany storms. The occurrence of wave overtopping generally threatens human lives, causes damage to infrastructures and properties. With the ever-increasing threat of climate change, coastal areas are more vulnerable to storm-driven overtopping events. Attentions have drawn towards the accuracy of prediction of wave overtopping in coastal structure and seawall designs. There is no doubt that modelling has improved the coastal seawall design, predictions and have saved construction costs.

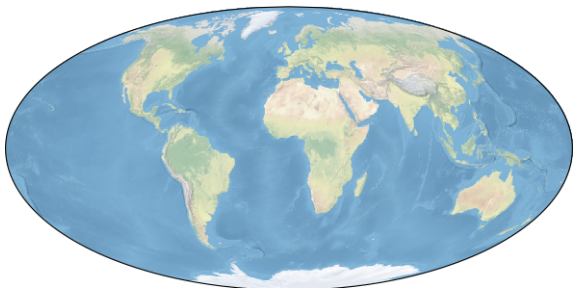

Figure 1.1 *A perspective of world's vulnerable coastlines under the influence of swell waves (Scitools, 2019)*

Sea defences are customarily being placed at shores to dissipate wave energy and prevent wave overtopping (see, van der Meer (2002), and van der Meer et al. (2016)). Most existing coastal defences have performed significantly reliably under usual wind-driven sea conditions in the absence of storms. Most recorded failures occur during

stormy sea conditions. Several processes occur during wave propagation. Obstacles in the path of waves create diffraction, including attenuation dispersion shoaling refraction refractions.

During storms, locally generated wind waves would naturally be combined with long-period ocean swells to produce bimodal waves. It has been noted that a bimodal sea state could be the worst-case sea conditions that sea defences may encounter. Currently, a great deal of research guidance is available on wind-driven wave overtopping caused by unimodal sea states; there is fewer available data focusing on bimodal seas. Thus, good knowledge of physics behind bimodal wave overtopping is vital to improve the design standards and reliability of coastal structures.

1.2 Waves Characterisation

The air-sea interaction concept has been a rapidly growing concept since the 1970s. Waves are generated in deep water under the influence of the wind. The generated waves are then propagated from the offshore to the shoreline while transferring energy along the way. As described in Goda (2010), swell waves are formed from wind-wave attenuation as propagates distances away from generating region.

The travelling waves consists of infinite number of wavelets (see, Goda et al. (1975) which are distributed across different frequencies and directions. Actions of storms would generally increases the sea surface fluctuations which have been described as sea randomness (e.g Ochi (2005)). Also Reeve et al. (2015) suggests that a random sea can be attributed to the transfer of energy from the wind to the sea. It therefore suggests that energy transfer and wave transformations would occur while creating more fluctuations as waves approach the shoreline.

Times series representation of random waves has been observed to be inefficient because wave-by-wave analysis of random waves appears impossible and unrealistic (Goda, 2010). The stochastic approach using the energy flux model is often preferred because the potential and the kinematics of random waves can be better represented by using the wave spectral density function (Ochi, 2005). Moreover, waves can be significantly represented in the energy spectrum phase. In this case, we can define a sea in only a form of spectral characteristics of the spectral shape and the corresponding moments computed from the wave energy spectrum. As highlighted by Ochi (2005), spectral shapes could vary concerning the severities of fetches, wind velocity, and duration of the wind blowing in the propagation area. The stochastic prediction of a linear and non-linear system is important to determine the information on the intrinsic

spectral analysis and the resonant condition of coastal seawalls with waves (Goda, 2010; Ochi, 2005).

At present, the most widely used techniques of describing wave spectrum depends largely on H_{m0} and $T_{m-1,0}$ or $T_{m0,2}$. However, there is more analysis of the spectrum and calculations that determine the type of sea-state. Spectrum representations of random seas are required for engineering applications and analysis. With spectrum analysis of waves, mixtures of swell and the wind can be easily identified from the energy peaks in the spectrum. Spectra representation of wind waves possess simple configuration and are easier to predict because they are characterised by one spectral peak (Unimodal spectrum) with one significant wave height and one peak period Battjes and Groenendijk (2000); Biesel F (1951); Burcharth (1978); Didier et al. (2014). A bimodal (Double-peaked) spectrum is usually formed during the transition from wind sea to swell because the wind speed would rise and start generating another wind sea after exceeding the separation frequency.

1.3 Modelling of Wave-Structures Interaction

The computational modelling techniques involve the use of computer models to investigate complex phenomena by incorporating various physics involved in the process. Conversely, a physical model replicates the actual flow parameters physically by applying scaled-up version of key parameters in the process. While a larger number of different model configurations can be easily initiated within a computational model, physical models are generally limited in terms of cost and time. However, accurate simulations in the numerical models can be computationally expensive.

Modelling techniques (computational and physical) have been applied extensively to investigate wave-structure interactions and wave overtopping of coastal structures under unimodal sea conditions, (e.g. Briganti et al., 2011; Franco et al., 1994; Goda et al., 1975; Owen, 1982; Tuan and Oumeraci, 2010). These studies provide guidance and data for wave overtopping estimates of coastal defences. (De Rouck et al., 2009a) provide a summary of numerous waves overtopping datasets compiled on different physical experiments covering various seawall geometries. More details of these studies can be found in (De Rouck et al., 2009a; Franco et al., 1994; Troch et al., 2004). These databases have been valuable and have been presented by (van der Meer et al., 2005, 2009) or more comprehensively in Pullen et al. (2007).

Recently, a series of wave overtopping tests have been performed at Ghent University (Belgium). These are presented in Gallach Sanchez et al. (2016) and Victor and

Troch (2012) whose focus is primarily on steep low-crested coastal seawalls in deep and shallow water conditions. Based on these, and other studies, some significant modifications to wave overtopping formulations have been made (van der Meer et al., 2018; van der Meer and Bruce, 2013). Concerning wave overtopping estimates for bimodal seas, EurOtop (2018) suggests using $T_{m-1,0}$ to account for bimodality as this weights the wave period towards higher values. While previous work on this topic is scarce, notable contributions include Hedges and Shareef (2003); Kashima et al. (2010); P. J. Hawkes and T. Coates and R. J. Jones (1998) who presented physical model tests, and Thompson et al. (2017) who presented a numerical assessment of overtopping performance of a simple coastal seawall under bimodal seas. The influence of wave directionality on wave overtopping oblique wind and swell waves was recently investigated by van der Werf and van Gent (2018). They found that the presence of swells with low steepness contributes more to wave overtopping in obliquely intersecting wind and swell seas.

1.4 Wave Overtopping Predictions

Prediction of wave overtopping is a crucial component of coastal structure and seawall design. The EurOtop tests (and most others) have been performed with unimodal conditions. Wave overtopping of sea defences occur when the local still water level *SWL* exceeds the crest freeboard *Rc* of the structure (Figure 1.3).

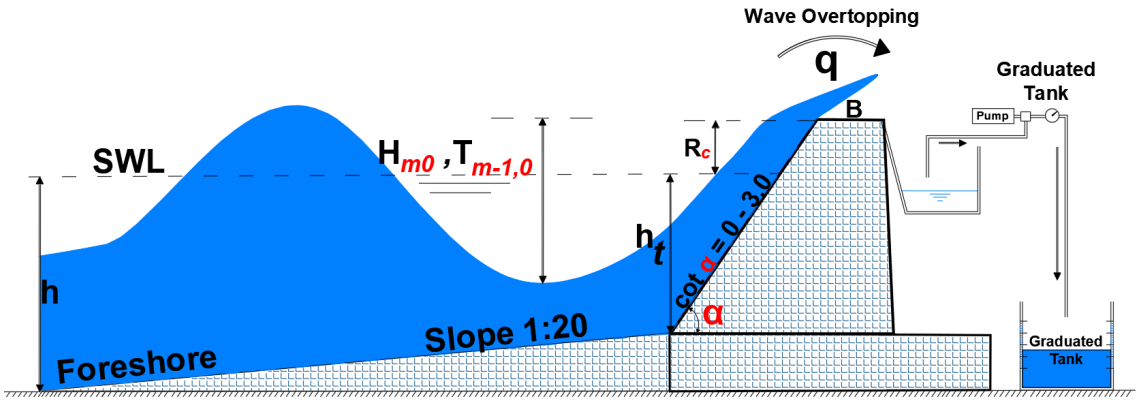

Figure 1.2 *A schematic representation of wave overtopping phenomenon*

Wave overtopping Q can be influenced by increasing random fluctuations of the sea surface. The Eurotop manual (van der Meer et al., 2018) acknowledges that the presence of swell can increase overtopping and recommends the use of $(T_{m-1,0})$ to account for

this. Also, the primary purpose of coastal defences is to provide efficient protection to the coast. It could be in the form of embankments, concrete, and composite structures.

Figure 1.3 *Selected photographs of Aberystwyth Promenade, Wales, before and during the overtopping events on Dec. 2014*

According to HR Wallingford report in the UK coastlines alone, coastal defences are protecting up to 23 per cent of the English coast, approximately 860 kilometres. Coastal defences provide efficient protection against erosion, inundation of the hinterland, and wave overtopping. Figure 1.3 demonstrates the relationship between a safe coast, wave overtopping as related with the 3-hour storm occurrence in Aberystwyth on December 2014. There is a significant failure of coastal defences during these 3 hours against wave

overtopping due to the extreme swell storms. The wave action causes lots of damages of coastal defences (Figure 1.4). The failure occurrence in England and Wales costs the UK government up to 1500 million pounds during this time (Thompson et al., 2016).

Sea states are irregular, being composed of a combination of harmonics with varying frequencies and directions, especially for shorelines exposed to very large fetches. These locations are influenced predominantly by wind and swell waves, and the energy characteristics are bimodal (Brodtkorb et al., 2000; Rychlik et al., 1997b). In these locations, direct application of overtopping formulations should include the presence of swell waves to prevent under-design. As observed by Goda (2010), random states are mostly created by the influence of the wind (from the local wind sources) and grow systematically until they decay.

Figure 1.4 *An example of damage by the 3-hour storm occurrence in Aberystwyth on Dec. 2014*

The decay processes are gradual and accompanied mainly by the transfer of energy from higher to lower frequencies (in the form of swell). Also described in P. J. Hawkes and T. Coates and R. J. Jones (1998) and Reeve et al. (2015), combinations of swell and wind waves would often result in more randomness of the sea. The few experiments of wave overtopping with bimodal conditions (e.g. Hedges and Shareef, 2003; P. J. Hawkes and T. Coates and R. J. Jones, 1998) suggest that overtopping can be enhanced relative to what would be expected from formulations based on unimodal wave conditions. Present design formulae are based predominantly on unimodal experiments because it is harder to include longer period waves. This is the main motivation of present work. In this research work, we present the first detailed modelling study of overtopping under bimodal conditions using carefully constructed spectra that relate the overtopping to the energy of the entire sea state.

1.5 Aims and Objectives

The overall aim of this research is the modelling of wave overtopping induced by bimodal waves. Creation of bimodal sea conditions containing swell has been constructed from the superposition of two JONSWAP spectra; one representing the wind sea and one the swell. With this construction, there will be a degree of overlap between the spectra and a sharp break between the swell and wind sea as a separation frequency is not present. It contrasts with the practice-based approach in which the swell and wind-sea components have no overlap (Bradbury et al., 2007). Here, we use the former method to create a set of bimodal sea states that have varying proportions of swell, while at the same time containing a fixed amount of energy. It refers to a set of sea states that have a fixed amount of energy but varying proportions of swell and wind sea as "energy conserved" bimodal waves. The advantage of this method is that it allows us to relate overtopping to the energy of the complete sea state. The extremes of these conditions are "pure wind sea" at one end and "pure swell" at the other; with both cases resulting in a unimodal spectrum. It was specifically targeted at whether changes in how the distribution of wave energy across swell and wind wave components quantifiably affects the properties of bimodal waves.

1.5.1 Specific Objectives

The following objectives will be considered in this thesis:

1. To develop a bimodal spectrum that will contain the same energy as the unimodal spectrum for easy adaptation of previously published formulations on wave overtopping.
2. Adapt the numerical model IH2VOF to simulate the formulated bimodal waves accurately.
3. Conduct experiments to increase data availability on predictions of wave overtopping under bimodal conditions.
4. Examine the significant changes caused by swell and different spectra parameters on the wave overtopping behaviour by the bimodal spectrum.
5. Modify existing formulations on the reflective behaviour of coastal seawalls to impinging wave bimodality
6. Examine a more practical numerical method of reducing wave overtopping by using storm walls or parapets.

1.6 Thesis Outline

This thesis comprises of ten chapters which will examine the aforementioned objectives. The main body of the work is covered in Chapters 2 to 9, and the conclusions of every chapter are presented in Chapter 10. A brief description of the contents of these chapters below:

Chapter 2 reviews commonly used wave overtopping numerical and experimental models. The aim is to apply both numerical and experimental approaches to model wave overtopping under the influence of bimodal waves. A typical bimodal wave is composed of the combined wind and swell waves. Understanding the previously applied modelling approach would enhance the selection of a suitable model that could accurately describe the physics of wave hydrodynamics of bimodal seas. Chapter 3 is devoted to the development of the model input. The chapter firstly introduce how a bimodal spectrum can be formulated by applying a well-established principle of double Jonswap spectra. A brief description of how bimodal energy can be combined from the wind and the swell waves was given. Description of conserved modes of the bimodal spectrum which bears the same energy as the unimodal sea states are presented. The presence of swell waves in the sea state is varied in terms of percentages and peak periods. The spectra were converted into random waves in the time domain. This

chapter finishes with a comparison of the distinguishing characteristics of the energy conserved-bimodal waves with those in unimodal waves.

Chapter 4 introduces the numerical model applied for the numerical simulation. A RANS-Based wave hydrodynamics model, validated for several overtopping studies under unimodal wave conditions was selected for this study. The aim is to examine how well the model performs under bimodal wave scenarios. The governing equations with the model, initial conditions, and boundary conditions are fully described. Chapter 4 also describes different methods of wave generation, absorption, and free surface tracking techniques in the RANS model. The chapter was concluded by propagating simple waves in the model and inspecting the performance of the wave under these conditions. Chapter 5 explores the capability of the RANS model to accurately propagate both pure unimodal waves and bimodal waves of the same energy component that was developed in Chapter 3. A smooth, impermeable seawall was installed in the model domain, and surface elevations were recorded using numerically-installed wave gauges. Influences of swell on the wave steepness, skewness, kurtosis, autocovariance function of numerically generated bimodal waves are presented. Finaly, the effect of swell waves on wave height distribution near the wavemaker and the structures was investigated.

In Chapter 6, an experimental programme was conducted to validate the numerical model developed in Chapter 4, and to increase the research guidance on wave overtopping of coastal defences under swell-driven bimodal seas. A great deal of research guidance is available on wind-driven unimodal sea states; fewer data with a focus on bimodal seas is available. Three smooth, impermeable, sloping seawalls were constructed, where different bimodal spectra are tested. This chapter describes the experiment and bimodal wave interactions with coastal seawalls. Measurements of wave overtopping of smooth, impermeable seawalls recorded under different unimodal and bimodal wave conditions are outlined and discussed. Moreover, an overview of the successful results obtained from more than 800 overtopping tests was presented. The experimental datasets obtained from chapter 6 was analysed in Chapter 7 using the presence of swell waves and spectra characteristics of the bimodal spectra involved. Special attention is placed on the analyses of the direct effect of the existence of swell in the sea state. Moreover, the effects of spectra shapes imposed by different spectra types were examined using the spectra characteristics of narrowness parameters, broadness parameters and peakedness parameters of each spectra types. The chapter was completed by presenting a new empirical influencing factor to describe the effects of swell percentages on wave overtopping discharges.

Chapter 8 presents the results of the reflection properties of smooth, impermeable structures. It was demonstrated that previously published formulations are only based

on unimodal sea conditions and cannot accurately describe reflection coefficients under bimodal waves. Simplified empirical equations that better represents the reflection coefficient of coastal seawalls under bimodal wave conditions than in previous literature are presented. Chapter 9 explores the validation of the numerical model IH2VOF in simulating wave overtopping processes. The extended capability of the numerical model to simulate wave overtopping behaviours of modified structures than simple ones were tested. Wave overtopping due to simple structures was validated, and then simulated for complex structures using different storm walls to reduce excess wave overtopping induced by bimodal waves.

Chapter 10 summarises all the results of the preceding chapters, and outlines possible research perspectives and applications. The chapter discussed the key contribution to research, and presented some directions into future work.

Chapter 2

Review of Wave Overtopping Modelling

This chapter will summarise the state of the art of experimental and numerical modelling of wave overtopping of coastal seawalls. First, an introduction of a comprehensive history of research into an experimental study of wave overtopping models of smooth, impermeable seawalls. In choosing an appropriate wave overtopping model suitable for bimodal seas, it is crucial to assess the performances of some novel wave overtopping models. Both numerical and experimental views are considered here. The numerical part is focus primarily on the physical theories involved, the computational wave generation pattern, model boundary conditions and proven limitations.

2.1 Experimental Modelling of Wave Overtopping

The experimental study of wave overtopping of impermeable coastal seawalls has a long history. A comprehensive histories of the research be found in Hedges and Reis (1998), and Burcharth and Hughes (2002). According to several previous studies (e.g. Burcharth and Andersen, 2007; Franco et al., 2009; van der Meer et al., 2018) and as earlier illustrated in Fig. (2.1), random waves can be expressed spectrally in terms of the spectral wave height H_{m0} and the spectral wave period $T_{m-1,0}$). The random waves would generally overtop a sloping impermeable structure whenever the wave run-up exceeds the crest freeboard R_c.

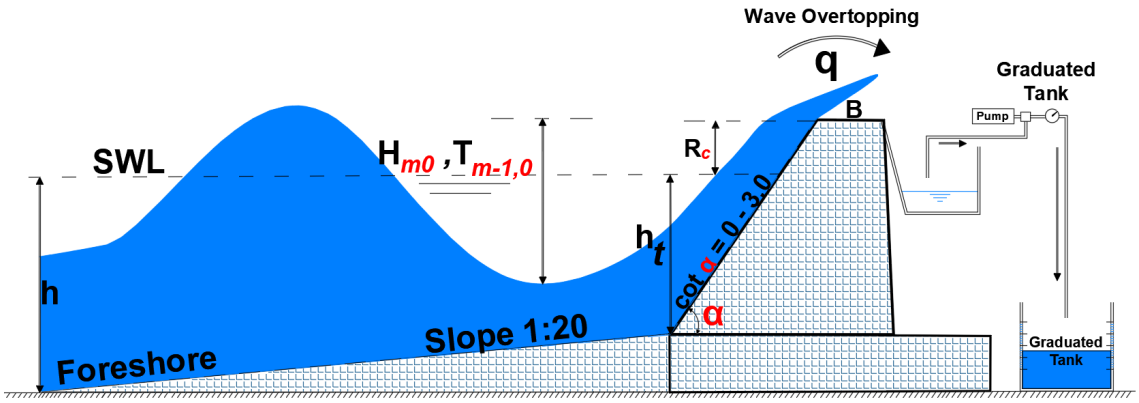

Figure 2.1 *A schematic representation of wave overtopping phenomenon*

As the waves are random the overtopping will vary from wave to wave. The mean overtopping rate, averaged over many waves, is denoted by Q_m. Firstly, Owen (1980) proposed a decreasing exponential relationship between the wave overtopping Q by a coastal seawall with respect to the crest freeboard R_c. Equation (2.1) shows the mathematical representation as:

$$Q_m = Q^* T_m g H_s \tag{2.1}$$

where $Q^* = A\ exp^{-\frac{BR^*}{r}}$, $R^* = \frac{R_c}{T_m\sqrt{g\ H_s}}$, and $Q_m = gH_sT_mA\ exp^{-\frac{BR_c}{rT_m\sqrt{gH_s}}}$

In this equation, H_s represents the significant wave height at the toe of the structure, T_m denotes the mean of the random wave period at the toe, A and B are empirically fitted coefficients, and r is a roughness factor. Since Owen's first formulation, several definitions have been given to coefficients A and B as additional experimental results became available. The relationship between wave overtopping and the crest freeboard has been refined by different authors. A summary of wave overtopping formulae have been presented by (Burcharth and Hughes, 2002; Hedges and Reis, 1998) and these are used as the basis of the extended tabulation in Table 2.1. One of the most significant definitions of wave overtopping formulae, was summarised by Pullen et al. (2007).

Table 2.1 Design formulations on dimensionless discharge, dimensionless freeboard and overtopping model (modified from Burcharth and Hughes, 2002; Hedges and Reis, 1998)

Reference	Dimensionless Discharge Q^*	Dimensionless Freeboard R^*	Overtopping Model	Applicability
Owen (1980)	$\frac{q}{gH_sT_m}$	$\frac{R_c}{T_m\sqrt{gH_s}}$	$Q^* = Aexp(-BR^*)$	Impermeable smooth, rough, straight and bermed slopes
Bradbury et al. (1988)	$\frac{q}{gH_sT_m}$	$\frac{R_c^2}{T_m\sqrt{gH_s^3}}$	$Q^* = A\left(R^*\right)^{-B}$	Rock armoured impermeable slopes with crown walls
Aminti and Franco (1988)	$\frac{q}{gH_sT_m}$	$\frac{R_c}{H_s}$	$Q^* = A(R^*)^{-B}$	Rock, cube, tetrapod, double layered armoured impermeable slopes with crown walls
Ahrens and Heimbaugh (1988)	$\frac{q}{\sqrt{gH_s^3}}$	$\frac{R_c}{H_sL_{0p}^{1/3}}$	$Q^* = Aexp(-BR^*)$	Different seawall designs
Pedersen and Burcharth (1993)	$\frac{qT_{0m}}{L_{0m}^2}$	$\frac{R_c}{H_s}$	$Q^* = AR^*$	Rock armoured impermeable slopes with crown walls
De Waal and van der Meer (1993)	$\frac{q}{\sqrt{gH_s^3}}$	$\frac{R_c - R_{2\%}}{H_s}$	$Q^* = Aexp(-BR^*)$	Impermeable smooth, rough, straight and bermed slopes
van der Meer (1993)	$\frac{q}{gH_sT_m}$	$\frac{R_c}{T_m\sqrt{gH_s}}$	$Q^* = Aexp(-BR^*)$	Impermeable smooth, rough, straight and bermed slopes
Franco et al. (1994)	$\frac{q}{\sqrt{gH_s^2}}$	$\frac{R_c}{gH_s}\cdot\frac{1}{\gamma}$	$Q^* = Aexp(-BR^*)$	Vertical wall breakwaters with/without perforated front wall
Smith et al. (1995); van der Meer (1993, 1995b)	$\frac{q}{\sqrt{gH_s^3}}\frac{tan\alpha}{\xi_{0p}}\ for\ \xi_{0p} < 2;$ $\frac{q}{\sqrt{gH_s^3}}\ for\ \xi_{0p} > 2$	$\frac{R_c}{H_s}\frac{tan\alpha}{\xi_{0p}}\cdot\frac{1}{\gamma}\xi_{0p} < 2;$ $\frac{R_c}{H_s}\cdot\frac{1}{\gamma}\ for\ \xi_{0p} > 2$	$Q^* = Aexp(-BR^*)$	Impermeable smooth, rough, straight and bermed slopes
Hedges and Reis (1998)	$\frac{q}{gR_{Umax}^3}$	$\frac{R_c}{R_u,max}$	$Q^* = A(1-R_c)^B$ $for\ 0 \le R_c \le 1;$ $Q = 0\ for\ R \ge 1$	Impermeable smooth, rough, straight and bermed slopes
Van Gent and Smith (1999)	$\frac{q}{\sqrt{gH_{m0}^3}}$	$\frac{R_c}{H_{m0}\xi_{m-1,0}}$	$Q^* = Aexp(-BR^*)$	Shallow and very shallow foreshore slopes
Pullen et al. (2007)	$\frac{q}{\sqrt{gH_{m0}^3}}$	$\frac{R_c}{H_{m0}}$	$Q^* = Aexp(-BR^*)$	Different seawalls designs including armoured rubble mounds and composite structures
Altomare et al. (2016)	$\frac{q}{\sqrt{gH_{m0}^3}}$	$\frac{R_c}{H_{m0}\cdot(0.33+0.022\cdot\xi_{m-1,0})}$	$Q^* = Aexp(-BR^*)$	Shallow and very shallow foreshore slopes
van der Meer et al. (2018)	$\frac{q}{\sqrt{gH_{m0}^3}}$	$\frac{R_c}{H_{m0}\xi_{m-1,0}\cdot\gamma_\tau}\ for\ breaking\ waves;$ $\frac{R_c}{H_{m0}}\ for\ non-breaking\ waves$	$Q^* = Aexp(-BR^*)$	Different seawalls and slope designs including armoured rubble mounds and composite structures
van der Werf and van Gent (2018)	$\frac{q}{\sqrt{gH_{m0}^3}}$	$\frac{R_c - 0.5H_{m0swell}}{H_{m0}\xi_{m-1,0}\cdot\gamma_\tau}\ for\ breaking\ waves;$ $\frac{R_c - 0.5H_{m0swell}}{H_{m0}}\ under\ non-breaking\ waves$	$Q^* = Aexp(-BR^*)$	Smooth impermeable sloping dike under oblique wind and swell waves

The more recent work of Victor and Troch (2012) and van der Meer and Bruce (2013) has enhanced the wave overtopping formulation of impermeable structures to low crest freeboards. Modifications based on varieties of smooth slopes are presented for breaking waves in Equation (2.2) and for non-breaking waves in Equation (2.3) (see van der Meer et al., 2018):

$$\frac{q}{\sqrt{gH_{m0}^3}} = \frac{0.023}{tan\alpha}\gamma_b.\xi_{m-1,0}.exp\left[-\left(2.7\frac{R_c}{\xi_{m-1,0}.H_{m0}.\gamma_b.\gamma_f.\gamma_\beta.\gamma_v}\right)^{1.3}\right] \tag{2.2}$$

Also, maximum estimates of wave overtopping values are generally represented by the non-breaking wave cases as:

$$\frac{q}{\sqrt{gH_{m0}^3}} = 0.09 * exp\left[-\left(1.5\frac{R_c}{\xi_{m-1,0}.H_{m0}.\gamma_f.\gamma_\beta.\gamma_v}\right)^{1.3}\right] \tag{2.3}$$

Refinements have generally been made to previous formulations to accommodate several other influence factors such as the presence of berms γ_b, permeability and roughness γ_f, for oblique wave attack, γ_β, influence factor by a vertical wall γ_v and for different geometries γ_* as shown in the equations. $\xi_{m-1,0}$ represents the surf similarity parameters of the wave. Equation (2.2) and (2.3) are the same general form as Equation (2.4) but take the form of a Weibull-shaped function as the power of the argument to the exponential is 1.3 instead of 1.0 as in overtopping Equations of sloping seawalls previously presented in Pullen et al. (2007). The study by Pullen et al. (2007) provides detailed guidelines for the estimation of dimensionless overtopping using different coefficients contained in Equation (2.2) and (2.3). The latest general form of these equations can then be summarised as in Equation (2.4) below:

$$\frac{q}{\sqrt{gH_{m0}^3}} = A.exp\left(-B\frac{R_c}{H_{m0}}\right)^C \tag{2.4}$$

Coefficients A and B for non-breaking waves across different slopes are defined deterministically by Equation (2.5) and Equation (2.6):

$$A = \begin{cases} 0.09 - 0.01(2 - cot\alpha)^{2.1} \; for \; cot\alpha \leq 2 \\ 0.09 \; for \; cot\alpha \geq 2 \end{cases} \tag{2.5}$$

Also, for coefficient B:

$$B = \begin{cases} 1.5 + 0.42(2 - cot\alpha)^{1.5} \; with \; a \; maximum \; of \; 2.35 \;\; cot\alpha \leq 2 \\ 1.5 \; for \; cot\alpha \geq 2 \end{cases} \tag{2.6}$$

2.2 Numerical Wave Overtopping Models

The numerical modelling of the wave overtopping is of interest to many applications of engineering such as coastal structures designs, ship decks stability and Floating Production Storage and Offloading FPSO units because they provide a more complex solution to the flow equations in a numerical domain than the empirical and semi-empirical methods (Zanuttigh et al. (2005), Zanuttigh et al. (2014), Battjes and Groenendijk (2000) and van der Meer et al. (2016)). Intensive research has been performed in the last four decades using different models to estimate wave overtopping. Some of these efforts are statistical in nature (Aziztayfun, 2009; Longuet-Higgins, 1952; Shi-Igai and Rong-Chung, 1977). These have been suitably applied to overtopping and flooding of berm breakwaters and longitudinal revetments (Coelho et al., 2016; Cox and Scott, 2001; van der Meer and Veldman, 1992). Some other modelling used different theories of physics in coupled Solutions of Non-Linear Shallow Water Equations NLSW and Navier-Stokes NS equations. Examples of these are the RBREAK, ODIFLOCS, AMAZON, the ANEMONE (Tuan and Oumeraci (2010) and van der Meer et al. (2016)). Other examples combined Eulerian field and depth averaging methods as proposed by Greenwood and Osborne (1990). The NLSW solver has been introduced in wave overtopping computations (Briganti et al., 2011).

Some other numerical models combined higher-order Boussinesq, Stoke and the non-linear dispersion theories. For example, Park and Cox (2016),Ohyama and Nadaoka (1994), Ohyama et al. (1995), and Tsung et al. (2012) to model wave-structure interaction and determine possibilities of wave overtopping. Mizanur and Hanif (1995) identified the method of St. Venant one-dimensional numerical model for wave-structure interaction and Hu et al. (2000) assessed the application of NLSW Equation in modelling wave overtopping AMAZON Model. Hubbard and Dodd (2002) and Brocchini et al. (2001) have applied an old and a newer 2-dimensional OTT-2D NLSW model towards computing wave run-up and overtopping on a sloppy seabed and an arbitrary beach respectively. Wavelet transform analysis has also been used to examine aerial landslide generated waves. Panizzo et al. (2002), and Lara et al. (2008) applied two-dimensional Volume-Averaged Reynolds Average Navier-Stokes (VARANS) equation to investigate

waves interaction with low-mound breakwaters in an experimental flume. Andersen and Burcharth (2009) conducted a three-dimensional Overtopping performance of rubble mound structures placed in the direction of incident oblique waves. Dong and Zhan (2009) proposed a wave run-up and evolution in shallow water using the Navier-Stokes equations and the Volume of Fluid (VOF) functions. Guanche et al. (2009) proposed a two-dimensional numerical approach to evaluating how wave loads affect the stability of a coastal structure. The COBRAS-UC model was adopted to simulate wave overtopping behaviour of rubble mound breakwaters.

Zheng et al. (2009) and Gao et al. (2012) established a numerical Smoothed Particle Hydrodynamics (SPH) model to depict the turbulence characteristics that occur at the time of wave breaking. Du et al. (2010) applied a depth-averaged COAST2D model to examine the effects of overtopping on the hydrodynamics and morphodynamics within the spatial shore-parallel breakwaters. Bakhtiary et al. (2010); Hsiao and Lin (2010); Peng and Zou (2011) used RANS to investigate wave overtopping caused by impinging and rough waves like the tsunami in front of a breakwater. Gao et al. (2012) developed a numerical model of the behaviour of regular waves slamming on an open pile structure. This model was based on and improved SPH model that incorporates CSPM and Riemann solution discretised into the Navier-Stokes equations. Garrido and Medina (2012) presented a new semi-empirical formula to depict the reflection patterns of waves on Jalan-type breakwaters using Neural Network model. Sun et al. (2012) improved the Boussinesq Equations and the Finite Element Method (FEM) to investigate wave run-up on a vertical surface cylinder. Tsung et al. (2012) combined some sets of laboratory datasets with the higher-order Boussinesq-type equation to model solitary wave run-up and to overtop on a plane sloppy experimental terrain.

In most of these approaches, applying coupled solutions of the RANS, VOF, non-linear shallow water equation and the higher-order Boussinesq algorithm to estimate wave overtopping appeared to be familiar to most of the modelling efforts McCabe et al. (2013), Casella et al. (2014), and Gui et al. (2015). Sometimes the turbulence field may be included or ignored to reduce the modelling complexities, but these usually affect the expected overtopping estimates (van der Meer et al., 2016). This report reviews the performance of four wave overtopping numerical models, namely NEWRANS model, IH2VOF, DSPH, and OpenFoam. Table 2.2 provides a detailed summary of this review.

2.3 New Reynolds-Averaged Navier-Stokes (NEWRANS)

The NEWRANS model is a mesh-based model that was proposed by Batchelor (1974). This model provides solutions to the Reynolds-averaged Navier-Stokes and the modified version of the turbulence equations. Initially, the model uses the boundary element method (BEM), which limits the design to the wave breaking point. However, the Boussinesq Depth average method and length turbulence have been incorporated into the model and have made it possible for the model to survive beyond the breaking points.

2.3.1 Theory and Assumptions in NEWRANS Model

NEWRANS model applies the RANS equation in a turbulence field. The fluid is assumed to be incompressible in a domain ω with motion in three dimensions i,j= 1, 2 respectively. These have been represented as a numerical solution of equations (2.7) to (2.16) Batchelor (1974) that are expressed as follows:

$$\frac{\partial u_i}{\partial x_i} = 0 \tag{2.7}$$

$$\frac{\partial u_i}{\partial t} + u_j \frac{\partial u_i}{\partial x_j} = -\frac{1}{\rho}\frac{\partial p}{\partial x_i} + g_i + \frac{1}{\rho}\frac{\partial \tau_{ij}}{\partial x_j} \tag{2.8}$$

The density change ρ_i that is being used to track the free surface can also be expressed as:

$$\frac{\partial \rho}{\partial t} + u_i \frac{\partial \rho}{\partial x_i} = 0 \tag{2.9}$$

and the turbulence model k - ε in all the three directions is given by:

$$\frac{\partial k}{\partial t} + u_j \frac{\partial k}{\partial x_j} = \frac{\partial}{\partial x_j}\left[(\frac{v_t}{\sigma_k} + v)\frac{\partial k}{\partial x_j}\right] + 2v_t \sigma_{ij}\frac{\partial u_i}{\partial x_j} - \varepsilon \tag{2.10}$$

$$\frac{\partial \varepsilon}{\partial t} + u_j \frac{\partial \varepsilon}{\partial x_j} = \frac{\partial}{\partial x_j}\left[(\frac{v_t}{\sigma_\varepsilon} + v)\frac{\partial \varepsilon}{\partial x_j}\right] + C_{1\varepsilon}\frac{\varepsilon}{k}2v_t\sigma_{ij}\frac{\partial u_i}{\partial x_j} - C_{2\varepsilon}\frac{\varepsilon^2}{k} \tag{2.11}$$

The total stress τ_{ij} in equation (2.2) can be linked to k - ε and σ_{ij} as:

$$\tau_{ij} = 2(v + C_d\frac{k^2}{\varepsilon}) - \frac{2}{3}k\delta_{ij} \tag{2.12}$$

These equations are solved using the two-step projection method proposed by Chorin (1968) and Chorin (1969):

$$\frac{\tilde{u_i}^{n+1} - u_i^n}{\Delta t} = u_j^n \frac{\partial u_j^n}{\partial x_j} + g_i + u_j^n \frac{\partial \tau u_{ij}^n}{\partial x_j} \tag{2.13}$$

The velocity is also projected to the divergence free plane as:

$$\frac{\tilde{u_i}^{n+1} - u_i^n}{\Delta t} = -\frac{1}{\rho^n} \frac{\partial p^{n+1}}{\partial x_i} \tag{2.14}$$

$$\frac{\partial u_i{}^{n+1} - u_i^n}{\partial x_i} = 0 \tag{2.15}$$

which can be combined with the Poison Pressure Equation PPE:

$$\frac{\partial}{\partial x_i} \left(\frac{1}{\rho^n} \frac{\partial p^{n+1}}{\partial x_i} \right) = \frac{1}{\Delta t} \frac{\tilde{u_i}^{n+1}}{\partial x_i} \tag{2.16}$$

Table 2.2 A review of numerical wave overtopping models

Disparity Criteria	NEWRAN Model	DualPhysics Model	IHFOAM Model	IH2VOF Model
1. Model structure & possible Dimension	Mesh based & 2-D	Meshless langragian approach with 2D & 3D functionalities	Meshed and poly meshed 2-D & 3D possibilities	Mesh-based with 2-D & 3D
2. Possible Wave Generation Methods	Wave paddle & internal point sources	Wave paddle & internal point sources	Wave paddle & internal point sources to generate both regular and irregular waves.	Piston wave type generator, Wave Paddle generation and internal point wave sources
3. Equation Solved	Reynolds-averaged Navier–Stokes and the turbulence ($\kappa - \varepsilon$) equations	Navier-Stokes equation in a langragian meshless mode. Fluid is treated as particles, artificial viscosity and turbulence	RANS equation containing the momentum and the continuity equations. Turbulence has recently been incorporated.	2DV Reynolds Averaged Navier–Stokes (RANS) equations and VARANS in porous media. Turbulence Kinetic κ and dissipation ε. VOF for tracking free surface movement
4. Model Inputs & Initial Conditions	Takes in a RIPPLE fortran based file containing a well structured input wave file, directional data, input parameters related with acceleration due to gravity, density, viscosity, initial velocity and wave generation and behaviour parameters	The model takes a .xml file that contains the input parameters, VOF, the wave maker information, piston movement info, and other configuration parameters. The VTK file and the object files are also accepted as input.	Initial velocity, VOF, and bouyancy pressures are applied to generate pressures at the wave generation phase.	Takes in a RIPPLE fortran based file containing a well structured input wave file, directional data, input parameters related with acceleration due to gravity g, density, viscosity, initial velocity and wave generation and behaviour parameters
5. Boundary Conditions	Open, moving and closed boundary conditions are possible. The Active Wave Absorption System, AWAS is adequately implemented in the model.	Absorption boundary condition, wave generation BC are specified at each faces which are owned by a unique cell. The gravity field is assumed to be negative direction of Z axis.	Dirichlet boundary conditions is applied. AWAS has just been recently been incorporated but no known publication on this yet.	Dirichlet boundary condition, moving boundary and the internal wave maker. The AWAS is applied to avert wave reflection at the boundary
6. Turbulence and AWAS Consideration	Turbulence, AWAS and bottom friction were adequately treated	No turbulence and AWAS in the model	Turbulence, AWAS and bottom friction were adequately treated	Turbulence, AWAS and bottom friction were adequately treated
7. Model Output	VOF Function, horizontal and vertical velocity field, pressure field , turbulent component, free surface elevation, free gauges, spectral outputs, wave run-up, mean overtopping discharge, instantaneous velocity and volume discharge, wave breaking results and gravity	Output files in types of Binary, csv, ascii are generated based on specified position, particle type, velocity limit, fixed or moving boundary, and variables like velocity, pressure, mass, volume, acceleration, and vorticity. Processes relying on these quantities can be simulated.	Volume averaged velocity and position, mass density, heat capacity, volume, surface, and emissivity of the thermocouple bead. pressure, mass, volume, acceleration, and vorticity can also be obtained for any time step.	VOF Function, horizontal and vertical velocity field, pressure field , turbulent component, free surface elevation, free gauges, spectral outputs, wave run-up, mean overtopping discharge, instantaneous velocity and volume discharge, wave breaking results and gravity
8. Maintaining the geometric and kinematic similarities for experimental flume Replication (Rank 1 to 5. 5 is most complex)	3	4	2	1
9. Model Limitation	It is computationally expensive. The absence of open sourced referenced materials makes it more difficult using the models for model implementation.	Absence of turbulence and wave absorption consideration	No proven updated publication has been made on the limitation of this version of Openfoam because it has just been recently released. The previous version of the model deviates from the 2D wave absorption theory. Turburlence was not considered also.	It provides an easier mode of replicating a wave overtopping experimental flume numerically. Most practitioners currently using Mike 21 BW to the toe of the structure and then use Eurotop to compute overtopping which might not work well in this case

2.3.2 Wave Generation in the NEWRANS Model

NEWRANS model is capable of generating waves using both internal point sources and by using wave paddles at one end. No dynamic boundary condition is applied to the free surface, but tangential stress, normal stress and inflow boundary condition are applied to one cell down from the surface. New values of quantities are obtained by the Finite difference method. The domain are generally discretised into a m by n domain. The centre of each cell is identified and defined with scalar quantities (p, k, e, and F). Under the assumption that the density ρ_f of the fluid remain unchanged but being averaged into the individual cell. Each cell is assumed to contain some volume of the fluid V_f and some V_a volume of air which would share up the density ρ_f on the basis that:

$$\rho = \frac{\rho_f V_f}{V_f + V_a} \tag{2.17}$$

The normalised average density for the centre of each cell can be described as the VOF function F expressed as:

$$F = \frac{\rho}{\rho_f} \tag{2.18}$$

Cell identification and classification becomes possible with the aid of the VOF function F. It is feasible to determine the exact density status of each cell to determine whether or not VOF F is full at F = 0 or F > 0. Final boundary conditions will then be applied to take care of the newly filled cells that were empty during the previous run.

2.3.3 The Limitation of the NEWRANS Model

NEWRANS model lacks useful open source materials. The model is also computationally expensive to run. At moment, the model cannot be cheaply implemented on GPU-based parallel computers. More coding on parallelization is required.

2.4 The IH2VOF Model

IH2VOF model provide a modified approach to the aforementioned NEWRANS model. The solutions to the 2DV RANS and the Volume-Averaged Reynolds Averaged Navier-Stokes (VARANS) equations in a porous media are provided using a meshed model set up. The model include a CORAL mesh generator which made it easily possible to generate a two-dimensional designed flume and structures. The instantaneous velocities and pressure field are decomposed to establish their mean and equivalent turbulent components. The VOF method has been applied to track the free surface movement

of particles used. Because this model has been selected for this research, elaborated details about the model is presented in Chapter 4.

The IH2VOF was chosen over the NEWRANS model because it runs on the Linux operating system. In this way, it leveraged on the linux operating speeds and functionalities. The compiled executables in the IH2VOF are reusable with different input files. In contrast with the window-based NEWRANS model, each simulation is accompanied with new sets of compilation making it difficult for batch simulation. Several simulations can be run simultaneously in the IH2VOF model while saving computaional cost in time. However, new sets of post-processing scripts are developed to analyse model results and produce visualisations in IH2VOF model.

2.5 DualSPHysics (DSPH) Wave Overtopping Model

DSPH is an upgrade of the Smoothed Particle Hydrodynamics Model Sphysics. It is based on a set of C++, CUDA and Java codes that solved free surface flow phenomena such as waves and breakwaters. The model operates in a fully Lagrangian approach with the fluid being discretised into a set of particles in a meshless mode. Computations of physical quantities of each particles (at nodes) are based on the aggregate interpolation of the nodal values of nearest neighbours. These are computed by using a kernel function (W) (Monaghan, 1992) and a well determined smooth length (h) generated from a weighted distance from the influence of nearest inter-particles on the targeted node. The aggregate contribution of the nearest neighbour can then be seen in an integral form as F expressed as:

$$F(r) = \int (F(\mathtt{r'}) \, . W(r - \mathtt{r'}) \, . \mathtt{h}) d\mathtt{r'}. \tag{2.19}$$

A modified version of the Kernel function K has been presented as $W(q)$ by Wendland (1995). Inter-neighbour contribution to particle values at each nodes were then set not to exceed $2h$ in this case as $0 \leqq q \leqq 2$. In a general form:

$$W(q) = \alpha_D \left(1 - \frac{q}{2}\right)^4 (2q+1) \tag{2.20}$$

Wendland (1995) then modified $q = r/h$ and α_D as $7/14\pi \; h^2$ for a two dimensional approximation.

In a discretised domain D for a point a, this would be aggregated from nearest neighbour b and Equation (2.21) (for a volume computation obtained from b using

m_b/ρ:

$$F(r_b) \approx \sum_b (F(r_b).W(r_a - r_b).h)\frac{m_b}{\rho_b} \tag{2.21}$$

2.5.1 DSPH Physical Theory and Assumptions

This was based on the solution to the Navier-Stokes equation. Water waves are treated like particles that are weakly compressible and the mass is kept constant in order to determine the density changes. The velocities of particle a at node a is computed by applying the kernel function to solve the law of conservation of momentum obtained from the nearest neighbours:

$$\frac{dv_a}{dt} = -\sum m_b \left(\frac{P_b}{\rho_b}^2 + \frac{P_a}{\rho_a}^2 + \Pi_a b\right) \nabla_a W_{ab} + g \tag{2.22}$$

The artificial viscosity Π_{ab} is also given by:

$$\Pi_{ab} = \{0^{\frac{-\alpha\overline{C_{ab}}\mu_{ab}}{\overline{\rho_{ab}}}} \tag{2.23}$$

V_{ab} . r_{ab} <0; V_{ab} . r_{ab} >0 with the values of μ_{ab} computed by using

$$\mu_{ab} = \frac{hv_{ab}.r_{ab}}{r_{ab}^2 + \eta^2} \tag{2.24}$$

while the

$$\overline{C_{ab}} = 0.5(C_a + C_b); \qquad \overline{\rho_{ab}} = \rho_a^2 + \rho_b^2 \tag{2.25}$$

Pressure changes are also usually computed from the Taint's equation presented by Batchelor (1974):

$$P_a = B\left[\left(\frac{\rho_a}{\rho_0}\right)^y\right] - 1 \tag{2.26}$$

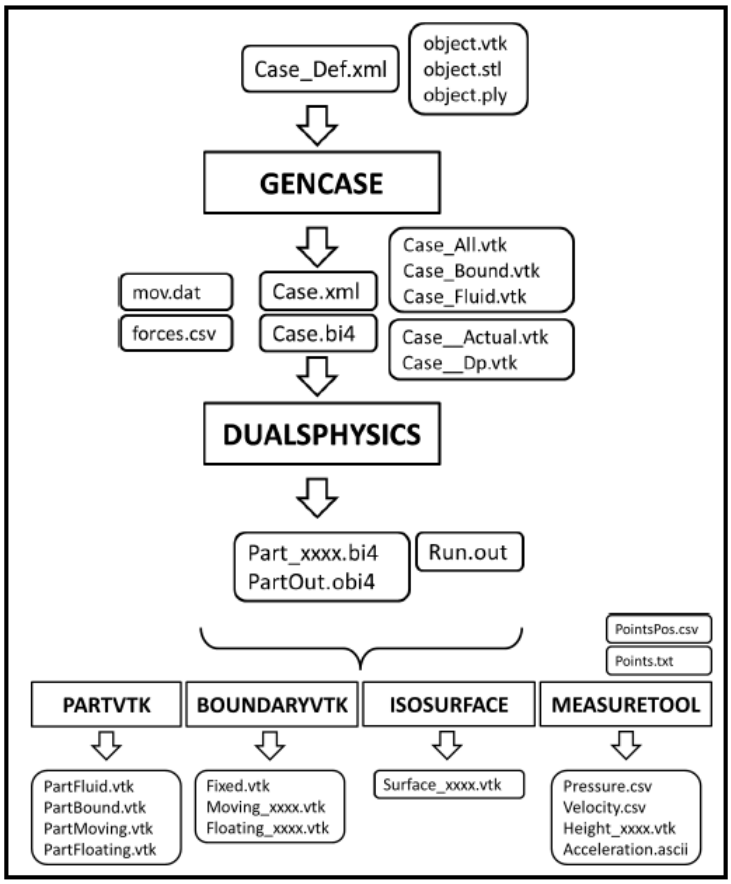

Figure 2.2 *General Workflow of DSPH (Canelas et al. (2016))*

2.5.2 Wave Generation and Particle Coupling in DSPH

The general workflow of DSPH is shown in Figure 2.2. The model is capable of generating a real wave flume for both long crested regular and random waves with both a point source and piston-type wavemaker. The first order wave equation proposed by Biesel F (1951) and second order wave equations by Madsen (1971) are possible in the model. Irregular waves based on the Jonswap spectrum have also been introduced (Liu and Frigaard, 2001).

The particles are coupled using the Discrete Element Method (DEM). The interaction between the particles are resolved numerically using the integration of SPH with DEM approach. These are decomposed into both damping force F_d and repulsive force F_r that are determined from the total normal force $F_{n,ij}$ respectively:

$$F_{n,ij} = F_n^r + F_n^d \quad = \quad k_{n,ij}\delta_{ij}{}^{\frac{3}{2}} e_{ij}{}^n - \gamma_{n,ij}\delta^{\frac{1}{2}}\delta_{ij}e_{ij}^n \tag{2.27}$$

The damping coefficient can be computed with

$$\gamma_{n,ij} = -\frac{loge_{ij}}{\sqrt{\pi^2 + loge_{ij}^2}}$$

and the stiffness parameter is determined as:

$$k_{n,ij} = \frac{4}{3}E^*\sqrt{R^*}$$

2.5.3 DSPH Integration and Boundary Conditions

The model makes use of a second order Verlet algorithm-based time stepping that adopts Courant Friedrich Lewy condition Verlet (1967) and Monaghan and Kos (1999). The fusion and diffusion terms are considered during computations in variable time steps and are expressed in the form:

$$V_a^{n+1} = V_a^n + 2\Delta t F_a^n; \quad r_a^{n+1} + \Delta t V_a^n + 0.5\Delta t^2 F_a^n; \quad \rho_a^n + 2\Delta t D_a^n \tag{2.28}$$

The dynamic boundary conditions for the DSPH model was introduced by Crespo et al. (2007). This considered that positions of the particles before waves are generated. The continuity and state equations were obeyed in the process. The particles moves according to the exerted force. This come in as a point floating object, or as gates of wave makers. The particles would then move outward from the position of displacement. The pressure of the system increases with time as the particles approach a boundary because of increased density as the separation distance between individual particles decreases than the smoothing length (h). After some DSPH model runs, the pressure builds up as described before. This created pressure usually poses a reflection effect along the boundary because there is no provision for active wave absorption (AWAS) in the system.

2.5.4 Limitations of DualSPHysics Model

The model composition described shows that the model is capable of modelling wave-structure interaction. The model still lacks in providing the wave absorption at the boundary after some sets of runs (Altomare et al., 2015). Reflection tends to occur which could impair the overtopping estimate that is expected to be captured. Small series of time run can be simulated which is not also good if a matured sea is to be modelled mostly for bimodal overtopping assessment. Turbulence created by the

particles after some model runs has not been considered. The disturbances could pose false observation of the expected overtopping result.

The model is also computationally expensive when compared to other mesh-based CFD methods, but this has been partially alleviated by introducing the GPU systems that can run on cluster machines.

2.6 OpenFOAM Model for Wave Overtopping

The Open-source Field Operation And Manipulation (OpenFOAM) has been described as one of the leading free and open source software for computational fluid dynamics (CFD). DSPH was introduced by Henry Weller (1989) based on C++ libraries and codes to solve turbulence and other fluid flow complex problems by applying the finite volume discretization method del Jesus et al. (2012). The model can run both on single system CPU and parallel cluster modes.

Some first sets of practical attempt to introduce OpenFOAM to simulate coastal engineering processes was made by (Higuera et al., 2013b). More studies on wave-structure interaction have been carried out using the same model (Higuera et al., 2013a, 2014, 2015; Maza et al., 2015). The latest form of the OpenFOAM for coastal modelling is the OpenFOAM v1612+/IHFoam that was released by IH Cantabria in 2016.

2.6.1 IHFoam Theory and Assumptions

Just like in DSPH, the model solves the RANS equation containing the momentum and the mass conservation equations. The continuity equation can be expressed as:

$$\nabla.u = 0 \tag{2.29}$$

$$\frac{\delta \rho u}{\delta t} + \nabla.(\rho uu) - \nabla.(\mu_{eff}\nabla u) = -\nabla p^* - g.X\nabla\rho + \nabla u.\nabla\mu_{eff} + \sigma_s\kappa\nabla\alpha \tag{2.30}$$

The pseudo dynamic pressure p^* and the vector velocity u are derivable from the two equations: σ represents the coefficient of surface tension, while μ_{eff} is the efficient dynamic viscosity which is obtained by adding the molecular dynamic viscosity to the turbulent kinetic viscosity. In IHFoam, The coefficient matrices are assembled for variables on the left hand side of the equality sign while independent equation terms are used to solve the variables on the right side of the equation to be solved by explicit

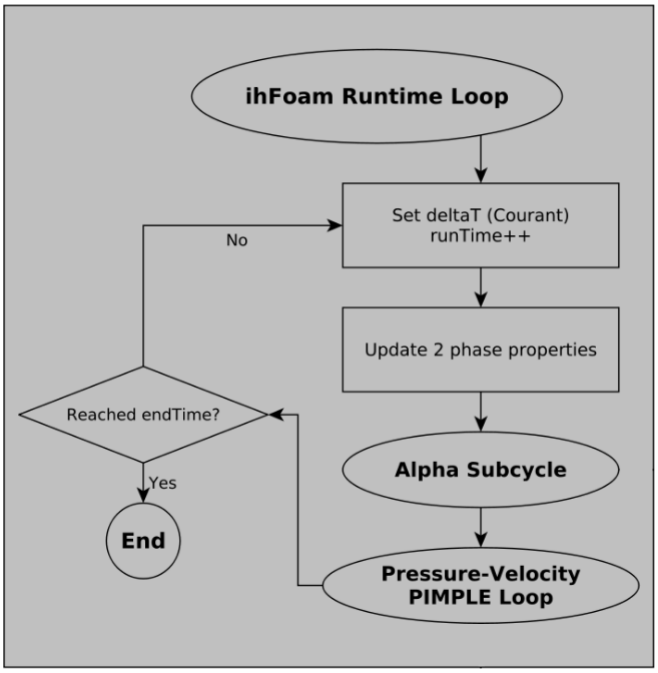

Figure 2.3 *A Simple PIMPLE Computation Loop (Adapted from Higuera et al. (2013b))*

calculations. The density of the cell is given by:

$$\rho = \alpha\rho_{water} + (1-\alpha)\rho_{air} \tag{2.31}$$

The advection effect for fluid movement tracking is given by

$$\frac{\delta\alpha}{\delta t} + \nabla.u\alpha + \nabla.u_c\alpha(1-\alpha) = 0 \tag{2.32}$$

These equations are bonded together by applying the Multidimensional Universal Limiter for Explicit Solution (MULES) proposed by Rusche (2002).

2.6.2 Integration of IHFoam and Boundary Conditions

IHFoam makes use of a new algorithm PIMPLE (Figure 2.3). A PIMPLE is a combination of the OpenFOAM-generated Semi-Implicit Method for pressure linked equations (SIMPLE) with Pressure Implicit Splitting Operators (PISO). PIMPLE was proposed by Kissling et al. (2010) and make provision for easy under relaxation and convergence condition for the variables that are being solved in the equations. The relationship between A PIMPLE and other model parameter runs is provided in Figure 2.3. The boundary conditions in IHFoam is done in modules for easy modification. These modules allow for possible automation of different wave theories in the model set up.

Boundary conditions are based on the faces because of its limited volume nature. It is feasible to access the centre of each face because different cells have been defined for them. Waves could be generated based on this and absorption can be controlled.

2.6.3 Wave Generation in IHFoam

Simple wave theories based on Stoke's I and II can be implemented in the usual OpenFOAM (freely available online). It has been observed that this model is too simple because it makes use of the VOF method to account for wet/dry cells but could not account for turbulence at an earlier stage of time runs and wave absorption at the boundary. Accurate wave generating and absorption boundary conditions were well represented in the model. Extensive coding will be required to accurately describe the boundary conditions that can generate most waves hydrodynamics. A modified approach was introduced by Higuera et al. (2013a). It has now been possible to replicate different wave theories and forms ranging from Stokes I and II, regular, solitary and irregular random waves. The piston wavemaker can also be replicated in this model. Dirichlet boundary conditions are specified based on the free surface and velocity functions only while pressures are solved based on special boundary conditions available in OpenFOAM. First order irregular waves are assumed to be obtained from the aggregate sum of N numbers of individual waves with each having their period T_i, wave height H_i and phases ω_i respectively:

$$\eta = \sum_{i=1}^{n} \frac{H_i}{2} cos(k_{xi}x + k_{yi}y - \omega_i t + \psi_i) \tag{2.33}$$

$$u = \sum_{i=1}^{n} \frac{H_i}{2} \omega_i cos^2(\Delta\beta_i) \frac{\cosh[k_i(h+z^*)]}{\sinh(k_i h)} \cos(\theta_i)\cos(\beta_i)$$

$$v = \sum_{i=1}^{n} \frac{H_i}{2} \omega_i cos^2(\Delta\beta_i) \frac{\cosh[k_i(h+z^*)]}{\sinh(k_i h)} \cos(\theta_i)\sin(\beta_i)$$

$$w = \sum_{i=1}^{n} \frac{H_i}{2} \omega_i cos^2(\Delta\beta_i) \frac{\cosh[k_i(h+z^*)]}{\sinh(k_i h)} \sin(\theta_i)$$

Active Wave absorption criteria proposed by Schäffer and Klopman (2000) has been implemented for both 2-D and quasi 3-D modes.

2.6.4 Proven Limitations of IHFoam

The previous version of the model deviates from the 2-D wave absorption theory. The older model also radiates waves at the boundary instead of absorbing them. The new 3-D absorption criteria would show a great performance for incident waves at the perpendicular directions (close to 0 or 90 degrees) because it might be difficult to anticipate the actual direction of the incident waves. Even though the quasi3-D takes care of this abnormality, it might very difficult using this for a two dimensional overtopping estimates that is needed for this research.

2.7 Neural Network Overtopping Models

The numerical and empirical models described above can efficiently predict overtopping rates based on specific structure geometries and wave conditions. Obviously, greater errors and uncertainties emerges at applying such models to other structure types or wave conditions that are different from the original model conditions. In this way, overtopping model formulations can reflect only most dominant parameters. On this premise, the prediction of overtopping was extended to the use of data-driven neural network (NN) models. Unlike the empirical models, the NN models can easily adapt existing training features to further interpolate and extrapolate to further predict overtopping for other structure geometries and test conditions. However, accuracies of predictions reduce with further departure from the training datasets. NN-based overtopping models are developed using training datasets from the CLASH database (De Rouck et al., 2009b). The single-phased NN was developed by the Delft Hydraulics (DNN) and is fully described in van Gent et al. (2007) and Coeveld et al. (2005). Verhaeghe et al. (2008) presented the double-phase overtopping prediction mode. The double-phase model consists of a classifier (to classify whether overtopping is significant or not), while a quantifier is provided to compute the overtopping. Once overtopping is significant in the double-phase mode, the two NN models are similar.

2.8 Review of Reflection Characteristics of Smooth Impermeable Slopes

Wave incidents on coastal seawalls will be partially reflected unless fully absorbed by the structure. The reflected wave component will interact with the incoming wave

creating interference. This can lead to wave amplification, wave breaking, and standing waves Andersen et al. (2014). In the case of vertical walls, standing waves can be pronounced (Zanuttigh and Martinelli, 2008). Standing waves lead to an amplification of wave-induced velocities which can lead to exacerbated scouring of sediments near the toe of the structure, and eventually to its failure and collapse. At locations exposed to local storm waves and open oceans, long period swell waves can be present leading to bimodal wave conditions. Existing literature provides little guidance on reflection characteristics in this situation, which P. J. Hawkes and T. Coates and R. J. Jones (1998) considers might constitute the worst-case in terms of wave conditions. Recent studies by Thompson et al. (2017) and Polidoro et al. (2018) provide evidence that bimodal wave conditions constitute worse storm conditions than pure wind wave conditions of similar total energy content. There remains a gap in our understanding of seawall performance under bimodal wave conditions. This thesis present the results of laboratory experiments of bimodal waves impinging on impermeable seawalls.

Previous studies including Miche (1951), Ursell et al. (1960), and Battjes (1974) propose the reflection coefficient of monochromatic waves on a plane beach. Miche's hypothesis was reformulated by Battjes (1974) in terms of waves breaker parameter index after an earlier study conducted by Iribarren and Nogales (1949). Zanuttigh and Martinelli (2008) pointed out that both studies from Ursell et al. (1960) and Battjes (1974) indicated overestimation of reflection coefficient criterion compared by Miche (1951) formulations. One of the main advantages of Zanuttigh and Martinelli's results is the fact that large reflection datasets covering several structures, have new formulations. The prediction formulae are applicable to both breaking and non-breaking waves. The formulation is also valid for breaker parameters between 1 and 4.1 and for wall slopes of cot α between 1.5 and 4.0. Studies by Battjes (1974) and Seelig and Ahrens (1981) are limited to breaker parameters less than 2.3 due to the limitations of their laboratory studies.

Some other notable studies were described in Numata (1976) and Losada and Gimenez-Curto (1981). Numata (1976) presented reflection and transmission performances of artificial blocks in a dimensionless form by comparing the ratio of breakwater width to the diameter of the armour. In Losada and Gimenez-Curto (1981), flow behaviours created by reflection and transmission were represented in an exponential form. Well-defined interaction curves obtained from wave heights and periods of regular waves were applied to obtain probabilistic standards which serve as input to predict flow patterns of equivalent irregular wave actions. The exponential probability model proposed by Losada and Gimenez-Curto (1981) were validated using experimental datasets. Other notable studies include, Postma (1989), Davidson et al. (1996), and

Allsop et al. (2005) in which reflection performances of different rock slopes and rock armours were presented. Postma (1989) investigated rock slopes under irregular wave attack which showed a greater dependence of the reflection coefficient K_r on the breaker index ξ. However, a weaker correlation was obtained in the relationship between K_r with spectral characteristics and depth at the structure-toe.

Relationships between K_r and ξ were later improved by van der Meer (1995a) by applying a multiple regression analysis combining influences of the characteristics of waves (in terms of heights and periods), and the structure (slope and permeability). Similarly, a modified version of the study by Seelig and Ahrens (1981) was presented by Allsop and Hettiarachchi (1989). Here values of wave steepness from 0.043 to 0.042 were investigated, which corresponds to ideal wind-sea states. Lower wave steepness which correspond to swell-driven sea conditions under bimodal wave conditions have not been considered. Newer coefficient values for predicting reflection performances of random waves were derived. A more recent study was presented by Neelamani and Sandhya (2003). Predictive equations were proposed based on a series of experimental tests derived from wave reflection measurements of several wave heights and wave periods. Different seawall types including plane, dentated and serrated and one water depth were used in all measurements obtained.

As observed in some previous studies including Thompson et al. (2017), Polidoro et al. (2018), and Orimoloye et al. (2019b) bimodality in sea waves generally increase the wavelength of the wave train. It would, in turn, reduced the wave steepness and could usually alter the breaker parameter indices. These occurrences have not yet been fully investigated for bimodal sea cases. In this thesis, the physical model tests were performed on three different seawalls to examine reflection performances under bimodal wave scenarios. Unimodal and bimodal cases were compared with previously formulated formulas. A new prediction formula which considers reflection coefficients under wave bimodality is proposed.

2.9 Input to Wave Overtopping Studies

In all the numerical and experimental modelling described above, accurate wave generation techniques are essential to wave overtopping predictions. In most cases, the JONSWAP spectrum is applied to produce irregularly randomised surface elevations of waves. A minimum of 1000 irregular waves are usually applied in most cases for wave overtopping studies (e.g. Burcharth and Andersen, 2007; Franco et al., 2009; van der Meer et al., 2018). As described in chapter 1 EurOtop (2018) suggests the use

of $T_{m-1,0}$ to account for bimodality in wave overtopping studies. It has been found that more weights can be assigned to wave period of higher values. There is limited prior research focusing on wave overtopping study that considers wave bimodality. Notable examples are Hedges and Shareef (2003); Kashima et al. (2010); P. J. Hawkes and T. Coates and R. J. Jones (1998) who presented physical model tests, and a numerical wave overtopping assessment by Thompson et al. (2017). The influence of wave directionality on wave overtopping oblique wind and swell waves was recently investigated by van der Werf and van Gent (2018). They found that the presence of swells with low steepness contributes more to wave overtopping in obliquely intersecting wind and swell seas. A great deal of research guidance is available on wind-driven unimodal sea states but on bimodal seas, less data can be found. It is imperative to consider the knowledge gap on bimodal wave overtopping of smooth impermeable seawalls.

2.10 Conclusion

This chapter presented a comprehensive review of wave overtopping models. A great deal of research guidance is available on wind-driven unimodal sea states, but on bimodal seas, less data can be found. Large portions of coasts across the globe are exposed to more complicated sea states under very large fetches that are bimodal in nature. The knowledge gap on bimodal wave overtopping of smooth, impermeable seawalls will be considered in subsequent chapters in order to improve the wave overtopping formulations representing the bimodal wave cases. For easy comparison of the bimodal sea states with the unimodal sea states already presented in previous literatures, a bimodal spectrum that will contain the same energy as the unimodal spectrum will be developed in the next chapter.

Chapter 3

Development of Energy-Conserved Bimodal Spectrum

This chapter presents the analytical development of a bimodal spectrum that contains the same energy as the unimodal wind-sea states. In bimodal seas, different percentages of swell can be present and the swell can appear at different frequencies while the energy content of the sea state remains unaltered. Commonly, bimodal sea conditions containing swell have been constructed from the superposition of two JONSWAP spectra; one representing the wind sea and one the swell. With this construction, there will be a degree of overlap between the spectra and a sharp break between the swell and wind sea as a separation frequency (usually between 0.09 and 0.1Hz) is not present. It contrasts with the practice-based approach in which the swell and wind-sea components have no overlap (Bradbury et al., 2007). Here, we use the former method to create a set of bimodal sea states that have varying proportions of swell, while at the same time containing a fixed amount of energy. We refer to a set of sea states that have a fixed amount of energy but varying proportions of swell and wind sea as "energy conserved" bimodal waves. To achieve this purpose, three different techniques were applied until the energy in the sea state became conserved. The formulated energy-conserved bimodal spectrum was created from unimodal sea states and converted into random waves time series using the Inverse Fast Fourier Transform (IFFT).

3.1 Development of a Bimodal Spectrum

In order to create an energy-conserved bimodal spectrum for this study, the four-parameter analytical approach proposed by Guedes Soares (1984) was adapted for this

purpose. Figure 3.1 contains the flow chart of the MATLAB algorithm for generating the bimodal spectrum. Firstly, a bimodal spectrum was created from the arithmetical combination of double modified JONSWAP spectrum, (due to Hasselmann et al. (1973). This is described in Equations (3.1) and (3.2) which detail the superposition of modified Jonswap spectra for swell and wind sea components.

$$\text{By superposition, the bimodal spectrum, } S_{bim} = S_{ss} + S_{ww} \tag{3.1}$$
$$S(f)_{ij} = S(f)_i + S(f)_j$$

$$S(f)_{ij} = \beta_e H_s^2 T_{ij}^{-4} f_{ij}^{-5} exp[-1.25(T_{ij}f_{ij})^{-4}]\gamma_{ij}^{exp\left[-\frac{(T_{ij}f_{ij}-1)^2}{2\sigma_{ij}^2}\right]} \tag{3.2}$$
$$\beta_e = \frac{0.0624}{0.230 + 0.0336\gamma - 0.185(1.094 - 0.01915 ln\gamma_{ij})}\left[1.094 - 0.01915 ln(\gamma_{ij})\right]$$

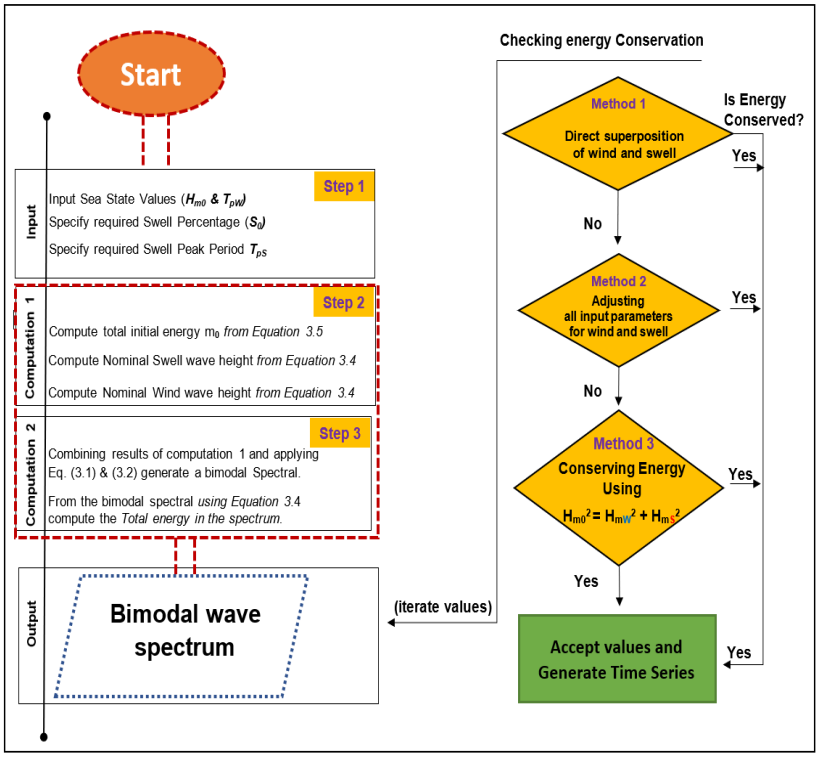

Figure 3.1 *Flow chart on the generation of an energy conserved bimodal spectrum*

In Equations (3.1) and (3.2) above, H_s represents the significant wave height, T_{ij} the peak period, and γ_{ij} is the peak enhancement factor of the spectrum with i, and j representing the equivalent swell and wind sea components. σ is sigma defining the frequency ranges of the spectra widths σ_a to the left and σ_b to the right of the peak frequencies f_{ij}.

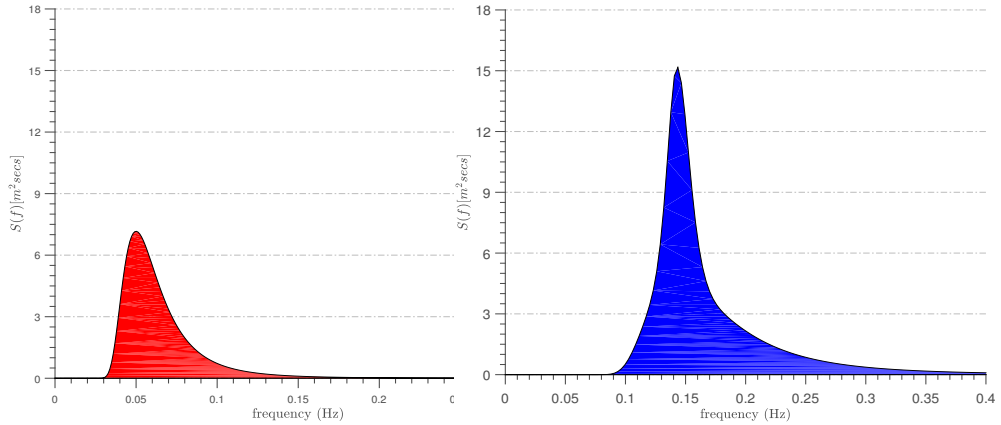

(a) Swell wave spectrum from Equation (3.2) for j

(b) Wind wave spectrum from Equation (3.2) for i

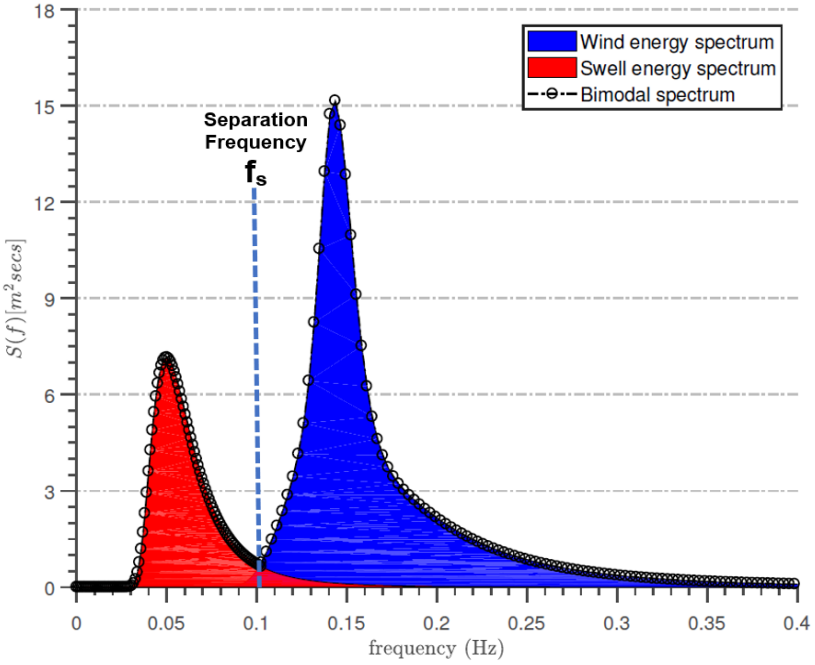

(c) Bimodal wave spectrum from wind and swell

Figure 3.2 *Building up of energy-conserved bimodal spectrum from separate swell and wind components*

The spectra widths σ can be expressed as:

$$\sigma = \begin{cases} \sigma_a : 0.07 \; for \; f \leq f_{ij} \\ \sigma_b : 0.09 \; for \; f \geq f_{ij} \end{cases} \tag{3.3}$$

To apply these sets of equations in this study, we first compute the equivalent wavelength for both swell and the wind and then combine the two wave systems as shown in Figure 3.2. Further details can be found in Goda (2010).

$$\begin{aligned} &\text{For wind sea, } H_{m0W} = 4 * \sqrt{1 - 0.25 m_0} \\ &\text{and for swell, } H_{m0S} = 4 * \sqrt{0.25 m_0} \end{aligned} \tag{3.4}$$

The H_{m0S} is the spectral wave height due to swell sea, H_{m0W} is the spectral wave height due to wind sea, and m_0 is the total energy in the overall bimodal spectrum.

It can be shown in Figure 3.2b that the wind wave spectrum and the swell can be separated by the separation frequency f_s. Goda (2010) suggested the frequency of occurrence to be approximately 90 percent of the spectral peak frequency of the resulting bimodal spectrum. This is equivalent to 0.124 H_z in Figure 3.2b.

3.1.1 Spectra Shape Parameter

Spectral shape changes according to the severities of the sea state. Ochi (2005) suggested that spectral shapes are dependent on the wind speed, the severity of wind velocity, the duration of wind blowing, and the fetch length. Values of spectral shapes (represented by γ) generally vary from 1 to 7. With each shape value representing the age of the sea. A fully developed sea-state is assumed to have a γ value of 1. Different studies have examined these fundamentals (for example see Goda, 2010; Hasselmann et al., 1973). However, it is challenging to determine whether or not sea-states are fully developed in practice because as a sea-state grows towards maturity, another sequence of swell waves is forming to disrupt the process. In this regard, a γ value of 3.3 was chosen for the wind sea according to the recommendations specified in Hasselmann et al. (1973) and Goda (2010). Similarly, a shape parameter value 2.5 was selected for the swell waves based on the recommendations in Bradbury et al. (2007). Figure 3.3 presents different assessment of γ values.

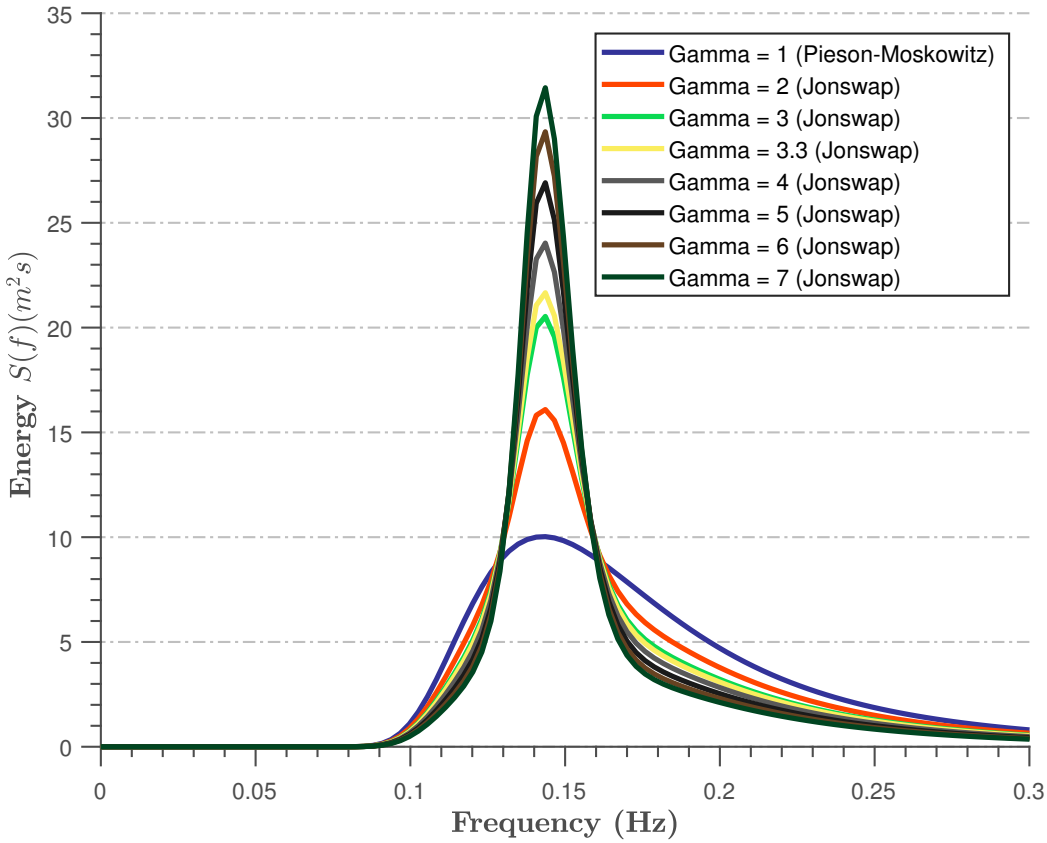

Figure 3.3 *Different peaks enhancements definitions for a sea state.*

3.2 Estimation of Total Energy in the Bimodal Spectrum

The total energy m_0 in the bimodal spectrum system was computed using Equation (3.4). As shown in step 1 of Figure 3.4, a direct combination of the energy of the superposition of swell waves on the local wind waves were estimated. The input parameters due to swell and wind waves were varied within some specified tolerance. The tolerance was specified in the beginning of the computation to define the degree of closeness of the computed parameters with the input parameters.

Inspecting the total energy as,

$$m_0 = \int f^n E(f) df \tag{3.5}$$

In Equation (3.4), n represents the n^{th} order of the spectral moment of the combined spectrum for total energy, n takes value of zero.

There will be a degree of overlap between the spectra and a sharp break between swell and wind sea as a separation frequency is not present. This contrasts with the practice-based approach, (see, Reeve et al., 2015), in which the swell and wind-sea components have no overlap, thus ensuring that the energy in the sea states is completely consistent with what it will be computed directly from the significant waveheight H_{m0}.

3.2.1 Choices of Bimodal Spectra

Different options can be applied to developing a bimodal sea state. The most conventional approach is based on a direct superposition of the swell wave on the wind-wave using Equation (3.1). An example of this is presented in Figure 3.4. Only the swell component of the bimodal spectrum is influenced. The growth of swell in the bimodal spectrum indicates an overall general increase in the total energy in the sea.

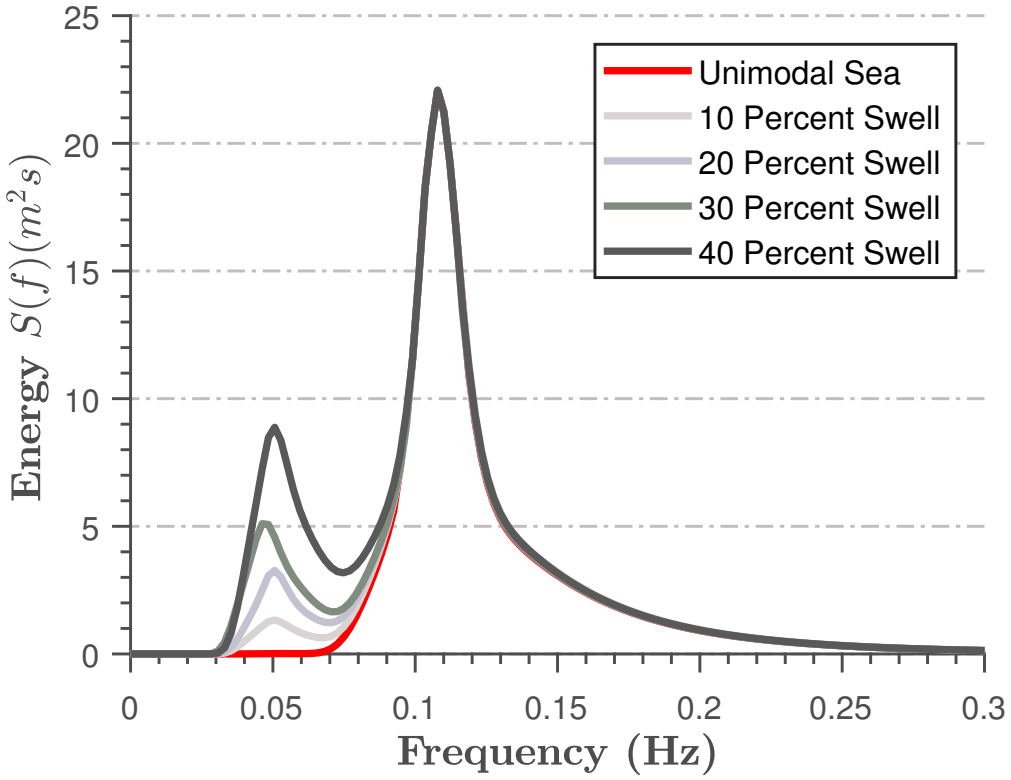

Figure 3.4 *An example of spectrum development using direct combination of different swell contents to the wind-sea states without any energy modification*

To avoid the geometric energy growth, the wave parameters were internally adjusted (gradual by increasing or decreasing the spectral wind wave height H_{mW}, the spectral wind wave period T_{pW}, the spectral swell wave height H_{mS}, and the spectral wind wave period T_{pS}) from the input bimodal wave components. It produced a more refined energy balance but not enough to conserve the sea state (Figure 3.5). Using this technique, the energy performance of the bimodal spectral was initially erratic but tended to balance to the percentages within the tolerance value. These were not enough to conserve the energy because the wave parameters in the bimodal sea do not consistently converge. The wave parameters are dynamically adjusted using the matlab iteration process described in the Figure 3.1. In this way, the intersection of the swell energy and the wind wave energy are required in order to conserve the total energy m_0 in the new bimodal spectrum.

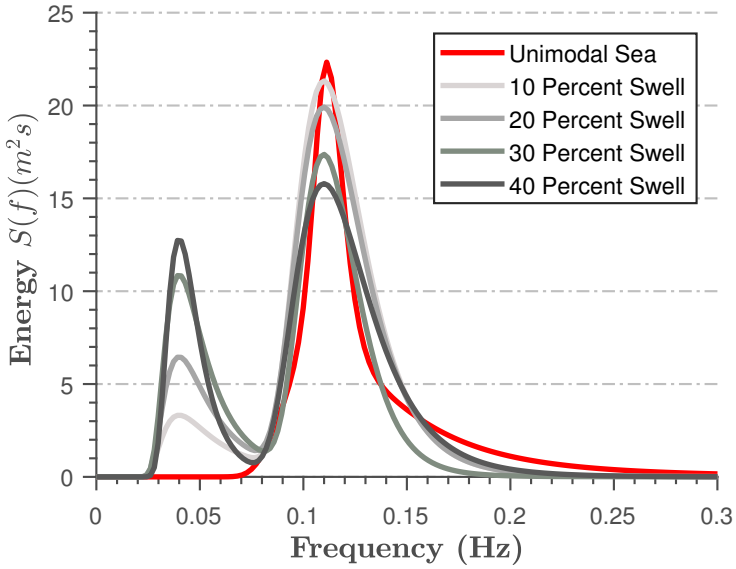

Figure 3.5 *An example of spectrum development by modifying parameter inputs while still combining different proportions of swell in the bimodal spectrum*

3.3 Ensuring Energy conservation in the Bimodal Spectrum

As proposed in the previous section, the influence of swell presence in a sea state condition can be best examined with bimodal sea states when the overall energy in the sea can be conserved by both components of the wind and the swell present in the sea. This was achieved in this case by solving Equations (3.1) – (3.4) iteratively as illustrated in Figure 3.1. The resulting bimodal spectrum yields the same total energy m_0 given by Equation (3.4). As shown in Figure 3.7, the newly computed significant wave height H_{m0} of the bimodal spectrum was ensured to be consistent with any swell percentage and swell frequency introduced.

To achieve this condition, the entire Equations (3.1) – (3.4) were solved iteratively until the energy m_0 obtained for the significant wave height H_{m0} in Equation (3.5) is fulfilled in step 3 of Figure 3.1. The resulting bimodal spectrum was converted into time series using the Inverse Fast Fourier Transform IFFT technique.

$$H_{m0} = \sqrt{H_{m0S}^2 + H_{m0W}^2} \tag{3.6}$$

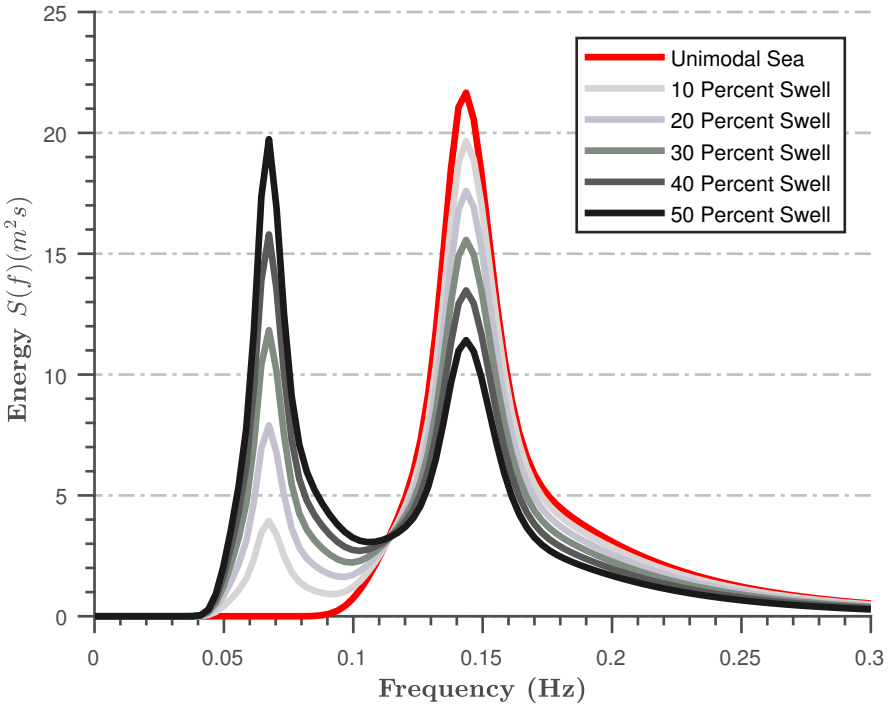

Figure 3.6 *An example of an energy-conserved bimodal spectrum*

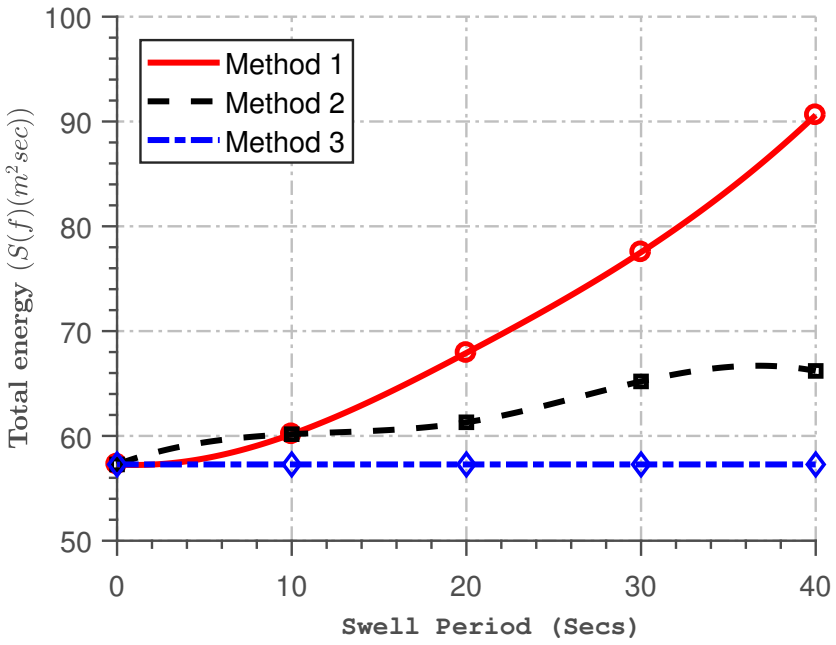

Figure 3.7 *Comparison of total energy obtained for different methods of combining swell and wind.*

3.4 Variations in Energy-Conserved Bimodal Spectrum

Figure 3.8 presents an example of a sea state with H_{m0} of 4 m and T_{pW} = 7 s. The swell component was fixed at a period varied from 11 s to 25 s while maintaining the same H_{m0}. Assuming an introduction of a 25 percent swell component into the sea, the remaining 75 % of the energy will be allocated to the wind-sea using the SSER approach proposed by Guedes Soares Guedes Soares (1984) as stated in Equation (3.3). The exception to the rule here is that the analytical relationship was solved iteratively until the total energy in the system was conserved.

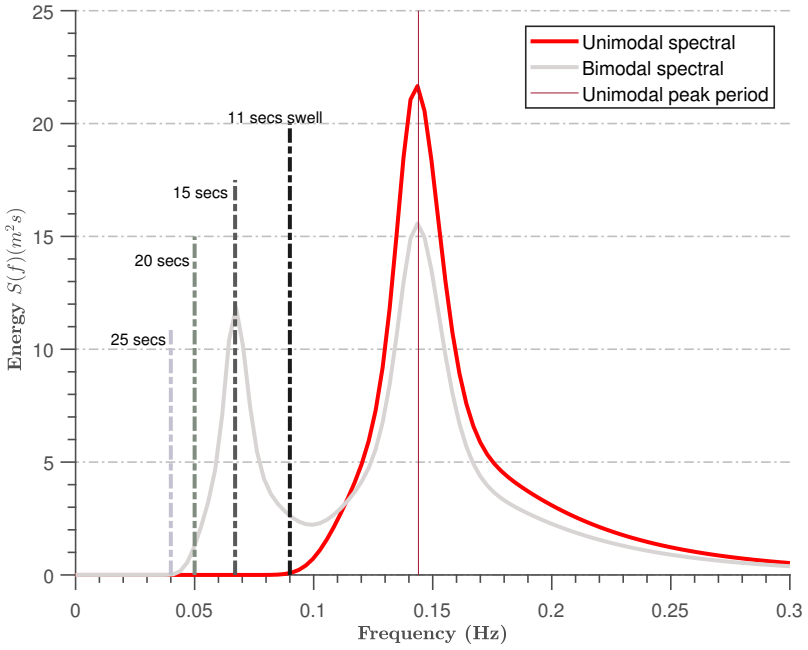

Figure 3.8 *An example of the development of energy-conserved showing different frequencies of swell*

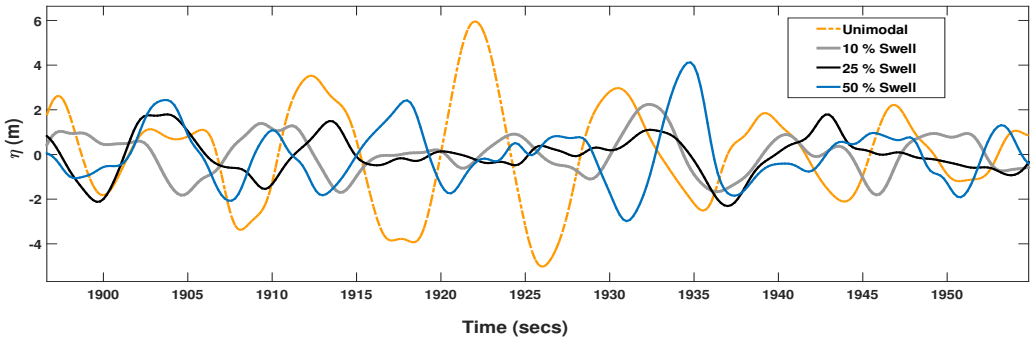

Figure 3.9 *An example of the development of energy-conserved bimodal spectrum showing surface elevation obtained by Inverse Fast Fourier Transform (IFFT).*

This method gives a different definition of swell compared to that based on separation of frequency because the overlap between the swell and the wind waves was preserved in this method. As earlier mentioned, different bimodal spectra were converted into time series using the Inverse Fast Fourier Transform IFFT technique. Figure 3.9 gives an example of the converted surface elevations for different swell content of a single bimodal spectrum containing the same energy. In this study, considering a sea state with H_{m0} of 4 metres and T_{pW} = 7 seconds, Table 3.1 gives a full representation of the number of wave conditions derived from this single state imposed by different swell components at differently occurring swell peak periods and percentages.

Table 3.1 Generation of 13 different wave conditions from the same-energy sea state with H_{m0} of 4 metres and T_{pW} = 7 secs.

ID	Test-No	T_{pW} (secs)	T_{pS} (secs)	Swell (%)	Mode (Unimodal = 1 Bimodal = 2)
1	T001-1	7	11	25	2
2	T001-2	7	15	25	2
3	T001-3	7	20	25	2
4	T001-4	7	25	25	2
5	T001-5	7	11	50	2
6	T001-6	7	15	50	2
7	T001-7	7	20	50	2
8	T001-8	7	25	50	2
9	T001-9	7	11	75	2
10	T001-10	7	15	75	2
11	T001-11	7	20	75	2
12	T001-12	7	25	75	2
13	T001-13	7	N/A	0	1

As clearly presented in this table, the presence of swell in a single sea state can be investigated using different bimodal spectra while the sea state still retains the same energy content. Generally in present study, more attention will be devoted to four main T_{pS} (11, 15, 20, & 25) and three swell percentages (25, 50, & 75) all matched up with the unimodal spectrum as presented in Table (3.1).

3.5 Conclusion

In this chapter, the formation of different bimodal spectra with constant energy was the unimodal sea states was proposed. These spectra are based on varying swell peak periods and percentages while preserving the overall energy content. In this way, the resulting spectra will be comparable to the original unimodal sea state rather than applying a sea state with continuously increasing energy due to swell. In contrast to the conventional methods, there will be a degree of overlap between the spectra and a sharp break between the swell and wind sea as a separation frequency is not present. It contrasts with the practice-based approach, in which the swell and wind-sea components have no overlap, thus ensuring that the energy in the sea states is entirely consistent with what it will be computed directly from the significant wave height H_{m0}. Specified bimodal spectra were converted into time series using inverse FFT. The energy-conserved bimodal spectrum will be applied as input into both the numerical and the experimental model to simulate the effect of swell waves in such simulations that will be carried out in the rest of the chapters. Moreover, how the present study conforms with previous formulations due to the presence of swell waves will be thoroughly investigated in this study.

Chapter 4

Numerical Implementation

This chapter examines the description of the IH2VOF computational model used in this study. This includes: the mathematical formulation of the model, boundary and initial conditions, methods of wave generation, the numerical domain, surface tracking techniques and the numerical resolution schemes. Basically, pre-computed bimodal wave conditions in the form of time-varying surface elevations, horizontal and vertical velocities were generated and simulated within the numerical model. As initial conditions, the model considers mean flow in the whole domain with still water level without waves under zero velocities and hydrostatic pressures. The model is also represented by the turbulence kinetic energy that produces a numerical perturbation. These conditions are specified in the input file of bimodal waves that are passed into the model boundary.

4.1 Governing Equations of IH2VOF

The IH2VOF model has been proposed by Lara et al. (2011) and Torres-Freyermuth et al. (2014). The numerical model is based on the Volume of Fluid (VOF) technique to create a modified version of the first generation RANS model introduced by Lin and Liu (1998). Fundamentally in turbulent flow, the instantaneous velocity field u_i and pressure field p can be expressed in terms of the mean velocity and pressure components ($\overline{u}_1$ and p), and complemented by the turbulent velocity u_i' and pressure fluctuations p'. All these can be expressed mathematically as Equations (4.1)a and (4.1)b. For instantaneous (mean) velocity,

$$u_i = \overline{u_i} + u_i' \tag{4.1a}$$

and for pressure components,

$$p = \overline{p} + p_i' \tag{4.1b}$$

Noting that from Equations 4.1(a and b), $i = 1,2$ for two dimensional flow. By assuming fluid incompressibility, the Navier-Stokes equations can be further decomposed into Equation 4.2:

$$\frac{\partial \overline{u_i}}{\partial x_i} = 0 \tag{4.2a}$$

$$\frac{\partial \overline{u_i}}{\partial t} + \overline{u_i}\frac{\partial \bar{u}_i}{\partial x_j} = -\frac{1}{\rho_f}\frac{\partial \overline{p}}{\partial x_i} + g_i + \frac{1}{\rho}\frac{\partial \overline{\tau_{ij}}}{\partial x_j} - \frac{\partial \overline{u_i' u_j'}}{\partial x_j} \tag{4.2b}$$

where ρ_f is the density of the fluid, g_i is the i^{th} component of gravitational acceleration, with μ describing the molecular viscosity and $\overline{\tau_{ij}}$ is mean viscous stress tensor. In can be represented mathematically as:

$$\overline{\tau_{ij}} = 2\mu\overline{\sigma_{ij}} \tag{4.3}$$

Equation 4.4 presents the mathematical aggregation of the rate of strain tensor described by the mean flow $\overline{\sigma_{ij}}$:

$$\overline{\sigma_{ij}} = \frac{1}{2}\left(\frac{\partial \overline{u_i}}{\partial x_i} + \frac{\partial \overline{u_j}}{\partial x_j}\right) \tag{4.4}$$

Also, the pattern of the Reynolds stress tensor R_{ij} of the momentum equation (already presented in Equation (4.2)b) can be defined in terms of the product of the density of the fluid ρ and combined turbulent velocities $\overline{u_i' u_j'}$.

$$R_{ij} = \rho\overline{u_i' u_j'} \tag{4.5}$$

IH2VOF performs calculation of complicated flows under breaking waves. The Reynolds stress term considered in Equation (4.5) is closed with a second order model described in Jaw and Chen (1998). The stress tensor is considered to be related to the strain rate of the mean flow through the algebraic non-linear $\kappa - \varepsilon$ model described in

Lin and Liu (1998):

$$\rho\overline{u_i'u_j'} = \frac{2}{3}\rho k\delta_y - C_d\rho\frac{\kappa^2}{\varepsilon}\left(\frac{\partial\overline{u_i}}{\partial x_i}+\frac{\partial\overline{u_j}}{\partial x_j}\right) - \rho\frac{\kappa^3}{\varepsilon^2}\left[C_1\left(\frac{\partial\overline{u_i}}{\partial x_l}\frac{\partial\overline{u_i}}{\partial x_i}+\frac{\partial\overline{u_j}}{\partial x_l}\frac{\partial\overline{u_j}}{\partial x_i}-\frac{2}{3}\frac{\partial\overline{u_l}}{\partial x_k}\frac{\partial\overline{u_k}}{\partial x_l}\delta_{ij}+\right)\right. \left.+C_2\left(\frac{\partial\overline{u_i}}{\partial x_k}\frac{\partial\overline{u_j}}{\partial x_k}-\frac{1}{3}\frac{\partial\overline{u_l}}{\partial x_k}\frac{\partial\overline{u_l}}{\partial x_l}\delta_{ij}\right)+C_3\left(\frac{\partial\overline{u_k}}{\partial x_i}\frac{\partial\overline{u_k}}{\partial x_k}-\frac{1}{3}\frac{\partial\overline{u_l}}{\partial x_k}\frac{\partial\overline{u_l}}{\partial x_k}\delta_{ij}\right)\right] \quad (4.6)$$

In Equation (4.6), C_d, C_1, C_2, and C_3 are empirical coefficients, while δ_{ij} is the Kronecker coefficient. The turbulent kinetic energy k can be expressed as:

$$k = \frac{1}{2}\overline{u_i'u_j'} \quad (4.7)$$

and the dissipation rate of the turbulent kinetic energy ε is given by:

$$\varepsilon = v\overline{\left(\partial u_i'/\partial x_j'\right)^2} \quad (4.8)$$

The molecular kinematic viscosity can be expressed in terms of the ratio of the molecular viscosity μ_v and the density ρ of the fluid is given by (μ_v/ρ).

Equating empirical coefficients $C1 = C2 = C3 = 0$ in Equation (4.6), results in the conventional linear (isotropic) eddy viscosity model for the Reynolds closure expressed in Equation (4.9):

$$\overline{u_i'u_j'} = -2v_i\overline{\sigma_{ij}} + \frac{2}{3}k\delta_{ij} \quad (4.9)$$

Similarly, the eddy viscosity v of the model can be mathematically represented as:

$$v_i = C_d\left(\frac{k^2}{\varepsilon}\right) \quad (4.10)$$

Champagne et al., (1970) determined the values of the coefficients C_2 and C_3 from results of experiments conducted on turbulent shear stress flow. Shih et al., (1996) assumed that $C_1 = 2C_3$. Rodi (1980) proposed the value of C_d. Altogether, the following values of coefficients have been proposed so far:

$$
\begin{aligned}
C_d &= 0.09 \\
C_1 &= 0.0054 \\
C_2 &= -0.0171 \\
C_3 &= 0.0027
\end{aligned}
\tag{4.11}
$$

However, it was observed in Lara et al. (2003) that these coefficients could lead to numerical inconsistencies when implemented in Equation (4.2)b. Therefore modified expressions were implemented in the IH2VOF as follows:

$$
\begin{aligned}
C_d &= \frac{2}{3}\left(\frac{1}{7.4+S_{max}}\right) \\
C_1 &= \left(\frac{1}{185.2+D_{max}^2}\right) \\
C_2 &= \left(\frac{1}{58.5+D_{max}^2}\right) \\
C_3 &= \left(\frac{1}{370.4+D_{max}^2}\right)
\end{aligned}
\tag{4.11}
$$

In these equations, S_{max} is given by:

$$
S_{max} = \frac{k}{\varepsilon} max\left[\left|\frac{\partial \overline{u_i}}{\partial x_i}\right|\right] \tag{4.12}
$$

and,

$$
D_{max} = \frac{k}{\varepsilon} max\left[\left|\frac{\partial \overline{u_i}}{\partial x_j}\right|\right] \tag{4.13}
$$

According to Rodi (1980), and also reiterated by Lin and Liu (1998), newer values are proposed for k and ε as shown in Equation (4.14) – (4.15):

$$\frac{\partial k}{\partial t}+\overline{u_j}\frac{\partial k}{\partial x_j}=\frac{\partial}{x_j}\left[\left(\frac{v_i}{\sigma_k}+v\right)\frac{\partial k}{\partial x_j}\right]-\overline{u_i'u_j'}\left(\frac{\partial \overline{u_i}}{\partial x_j}\right)-\varepsilon \tag{4.14}$$

$$\frac{\partial \varepsilon}{\partial t}+\overline{u_j}\frac{\partial \varepsilon}{\partial x_j}=\frac{\partial}{x_j}\left[\left(\frac{v_i}{\sigma_\varepsilon}+v\right)\frac{\partial \varepsilon}{\partial x_j}\right]+C_{l\varepsilon}\frac{\varepsilon}{k}v_i\left(\frac{\partial \overline{u_i}}{\partial x_j}+\frac{\partial \overline{u_j}}{\partial x_i}\right)\frac{\overline{\partial u_i}}{\partial x_j}-C_{2\varepsilon}\frac{\varepsilon^2}{k} \tag{4.15}$$

In Equations (4.14) & (4.15), σ_k, σ_ε and $C_{2\varepsilon}$ are empirical coefficients. The first and second terms represent the convection and advection terms respectively. Similarly, the third and fourth terms refer to the production and the dissipation of kinetic turbulent energy.

The IH2VOF model considers a better simulation of the porous nature of materials than most previously represented RANS models. It is because flows in porous media were described by using the volumes of the medium as described by the VARANS equation instead of the ordinary rigid boundary of obstacles (for example, Lin and Liu (1998)). The final form of the VARANS equation can be presented as Equation (4.16):

$$\begin{aligned}\frac{1+C_A}{n}\frac{\partial(\tilde{u}_i)}{\partial t}+\frac{\tilde{u_j}}{n^2}\frac{\partial \tilde{u}_i}{\partial x_j}=&-\frac{1}{\rho}\frac{\partial \tilde{p}}{\partial x_i}+\rho g_i+\frac{v}{n}\frac{\partial^2 \tilde{u}_i}{\partial x_j \partial x_j}\\&-\frac{1}{n^2}\frac{\partial \tilde{u}_i\tilde{u}_j}{\partial x_j}-\frac{\alpha v(1-n^2)}{n^3 D_{n50}^2}\tilde{u}_i-\frac{\beta v(1-n)}{n^3 D_50}\tilde{u}_i|\vec{\tilde{u}}|\end{aligned} \tag{4.16}$$

The porosity n, rock mean size D_{n50}, and the three coefficient of frictions (C_A, α and β parameters are used to establish the effects of porous media on the entire model behaviour.

The turbulence k - ε and the total stress τ_{ij} in all the directions in the model are given by:

$$\begin{aligned}
\frac{\partial k}{\partial t}+u_j\frac{\partial k}{\partial x_j} &= \frac{\partial}{\partial x_j}\left[(\frac{v_t}{\sigma_k}+v)\frac{\partial k}{\partial x_j}\right]+2v_t\sigma_{ij}\frac{\partial u_i}{\partial x_j}-\varepsilon \\
\frac{\partial \varepsilon}{\partial t}+u_j\frac{\partial \varepsilon}{\partial x_j} &= \frac{\partial}{\partial x_j}\left[(\frac{v_t}{\sigma_\varepsilon}+v)\frac{\partial \varepsilon}{\partial x_j}\right]+C_{1\varepsilon}\frac{\varepsilon}{k}2v_t\sigma_{ij}\frac{\partial u_i}{\partial x_j} \\
&\quad -C_{2\varepsilon}\frac{\varepsilon^2}{k} \\
\tau_{ij} &= 2(v+C_d\frac{k^2}{\varepsilon})-\frac{2}{3}k\delta_{ij}
\end{aligned} \tag{4.17}$$

The model has the capability of replicating the scalability and geometrical compatibility linking a numerical simulation and experimental studies. It can also replicate nearshore processes with minimal assumptions and complications. The initiation control of wave breaking in the design is accomplished by applying an advanced turbulence kinetic energy k and the equivalent dissipation ε as expressed in Equation (4.17).

4.2 Initial Conditions and Boundary Conditions

This model implements three different boundary conditions for wave generation and absorption. In IH2VOF, different boundary conditions are defined. Basically as in other 2 dimensional models, it consists of solid boundaries, free surface boundary, and the open boundary conditions. These will be considered in details here:

4.2.1 Initial Conditions

In the initial state, the model considers mean flow in the whole domain as still water level with no wave or current motion. This refers to a state of zero velocities and hydrostatic pressure. The model can also consider a pre-determined form for the free surface displacement or mean velocity field. In this mode, variations in the free surface and velocity conditions can be fully described. To prevent singularity errors due to turbulence during simulation in the model (defined in Equation (4.14)), the turbulence was initialised with a "seeding " value that produces a numerical perturbation as:

$$k=\frac{1}{2}u_i^2 \tag{4.18}$$

where $u_i = \delta c_i$, c_i the wave celerity in the wave generation zone, and δ is a numerical constant. The value of δ is defined by Lin and Liu, (1998) as equivalent to 0.0025.

For turbulent dissipation rate ε, IH2VOF initial value can be defined by this expression:

$$\varepsilon = C_d \frac{k^2}{v_i} \tag{4.19}$$

where $v_i = \xi v$ and ξ defined by Lin & Liu, (1998) as 0.1. The variations of δ and ξ have been determined to be insignificant on the final result of the computational model. Lin and Liu (1998) concluded that δ could induce slight delays in the initiation of wave breaking performances of flow conditions.

4.2.2 Solid Boundary Condition

Two types of conditions for mean flow are considered. These are:

- Free slip: $\overline{u_n} = 0$, $\frac{\partial \overline{u_\tau}}{\partial n} = 0$
- No slip: $\overline{u_n} = 0$, $\overline{u_\tau} = 0$

where n and τ are directions normal and parallel to the boundaries respectively. Also for turbulent flows, a log-law distribution for the mean tangential velocity is implemented in the model. This can be expressed as:

$$\frac{\partial \overline{u}}{y} = \frac{u_n}{\kappa y} \tag{4.20}$$

Where κ represents the von Karman constant ($\kappa = 0.41$), y is the distance from the solid domain, u is the friction velocity. By integration of Equation (4.20), we can obtain individual values of κ and ε as:

$$\kappa = \frac{u_n^2}{\sqrt{C_d}} \tag{4.21}$$

and,

$$\varepsilon = \frac{u_n^2}{\kappa y} \tag{4.22}$$

The values of u_n can also be determined from the values of mean flow as:

$$u_n^2 = v \frac{\partial \overline{u}}{\partial y} \Big|_{y=0} \tag{4.23}$$

4.2.3 Free Surface Boundaries

The IH2VOF computational model ignores the mean density fluctuations near the free surface. During laminar flow, the zero stress and zero pressure conditions are imposed at the free surface as:

$$\overline{p} = 0 \tag{4.24a}$$

$$\frac{\partial \overline{u_\tau}}{\partial n} = 0 \tag{4.24b}$$

for the turbulent field, zero-gradient boundary condition was applied to both k :

$$\frac{\partial k}{\partial n} = 0 \tag{4.25a}$$

and to ε:

$$\frac{\partial \varepsilon}{\partial n} = 0 \tag{4.25b}$$

where n is a unit normal to the free surface and its assumed that there is no turbulence exchange between water and air.

4.2.4 Open Boundaries

The open boundary condition implemented in IH2VOF can be expressed as:

$$\frac{\partial \phi}{\partial t} + c_0 \frac{\partial \phi}{\partial x} = 0 \tag{4.26}$$

where ϕ represents the variables to be evaluated during simulation such as $\overline{u}$, $\overline{v}$, k, and ε. The wave celerity of log waves at any position can be defined as:

$$c_0 = \sqrt{g(d+a)} \tag{4.27}$$

and for short waves:

$$c_0 = \sqrt{\frac{d\lambda}{2\pi} tanh\left(\frac{2\pi}{\lambda}(d+a)\right)} \tag{4.28}$$

where a is the wave amplitude, d is the water depth at the location, and λ the wave length.

4.3 Methods of Wave Generation

Three different wave generation methods are possible in the IH2VOF computational model. These are internal wave maker, static paddle using Dirichlet boundary condition, and the virtual force method employing dynamic paddle techniques. A more complete description has been described in Lara et al (2006).

4.3.1 Dirichlet Boundary Condition

The simplest wave generation method in IH2VOF is the Dirichlet boundary condition. This is implemented in most wave generation models because this method provides analytical expressions for free surface and velocity distribution throughout the water column. Here waves are generated on the one side of the domain and it is actively absorbed at the same side of the numerical flume. The VOF and the horizontal and vertical velocity components are two variables needed at each time step. The velocities are generated initially and are then interpolated in a linear fashion into the entire model system. The Dirichlet method is suitable to replicate the behaviour of any laboratory wave paddle at a cell size resolution such as the piston-type wave generators. When replicating a piston-type wave maker, evanescent modes are shown in the wave generation area as will be expected in a physical flume.

4.3.2 Internal Wave Maker

IH2VOF computational model is capable of generating waves at any specific region using the mass function defined within this region. The mass source method is developed to avoid re-reflection of waves in the boundary where they are generated. The introduction of a mass source function at any point in the fluid domain creates a physical effect. Alternatively, fluid is introduced or sucked into this region to generate waves in terms of crests and troughs. Full details of this wave generation are described in Lin and Liu (1998). The target wavelength is always larger than the width of the mass source function, and the waves are described to have started right above the centre of the region. The relationship between the source function $s(x, z, t)$ and the expected free surface displacement $\eta(t)$ can be expressed as:

$$\int_0^t \int_\Omega s(x,z,t) d\Omega dt = 2 \sum \int_0^t c_i \eta_i(t) dt \tag{4.29}$$

In above equation, c is the target wave phase velocity and the factor of two shows that waves are propagating in both directions of the domain. Only one component $n = 1$ is described for regular (monochromatic) waves. In randomly irregular waves with n components, Equation (4.29) consists of sum of n linear waves, with each of them having a wave height, wave period and phase.

4.3.3 Dynamic Boundary Condition

The dynamic boundary conditions can replicate piston type wave generators. A simulated solid object within the mesh is usually used to push the fluid in motion. An openness coefficients would then be used to absorb the movement of the solid object to the wave paddle position $X(t)$ and velocity $U(t)$ at each time step. The virtual body force is applied to bodies of partial cells ($0 < \theta < 1$). This method differs from the Dirichlet method because only the horizontal velocity component and free surface locations are specified within the mesh according to the wave maker movement. The mesh should be large enough to accommodate the movement of the wave maker.

4.4 Wave Absorption Methods

The wave absorption method implemented in the IH2VOF is efficient to cater for reflection of any physical structure present in the model and also to ensure that the simulation could run for longer duration. Both active and passive absorptions are implemented in the model. The active absorption is efficient for the Dirichlet and moving boundary conditions. On the other hand, the passive absorption helps to efficiently absorb reflected waves propagating backwards towards the wave generating end.

4.4.1 Active Wave Absorption

The details of the active absorption implemented in IH2VOF can be found in Schäffer and Klopman (2000). This method involves a clear identification of incident waves approaching the domain and generation of equivalent reverse waves to cancel out the incoming waves. In this way, it possible to implement both the moving boundary and the Dirichlet conditions simultaneously. Cancellation of incident waves by the generated reverse reflected waves in IH2VOF was first implemented in Torres-Freyermuth et al. (2010). The difference between the targeted theoretical free surface η_t and the one

measured in the model η_m is computed. Then the wave maker velocity is modified to reproduce the target wave in agreement with the waves to be absorbed. The correction to the target wave velocity U_r can be expressed mathematically as:

$$U_r = \sqrt{\frac{g}{h}\eta} \tag{4.30}$$

where $\eta_r = \eta_t - \eta_m$. In the case of the moving paddle method, it is necessary to adjust the position of the wave maker by integrating the corrected velocity $U_c = U_t + U_r$

$$X(t) = X(t-dt) + \int_{tdt}^{t} (U_t + U_r)dt \tag{4.31}$$

One of the simplest active absorption cases occurs with using the open boundary condition. In this case the target setting of the IH2VOF will be set to zero to absorb waves that approached the boundary.

4.4.2 Passive (Sponge Layer) Wave Absorption

The passive absorption implemented in IH2VOF model follows after Israeli and Orszag (1981). It made it possible to absorb waves that are generated above the source region when using the source generation method. In this case, a dissipation method is applied which can be described mathematically as:

$$\gamma_d(x) = 1 - \alpha_d \beta_d^3 - (1 - \alpha_d)\beta_d^6 \tag{4.32}$$

where $\alpha_d = 0.4$ and

$$\beta_d(x) = \frac{x_0 - x}{\lambda} \tag{4.33a}$$

Also, x_0 is the coordinate of the origin of the source region seaward boundary and λ is the wavelength at the same point. The introduction of sponge layer for wave absorption increases the length of computational domain. This makes the point source method unsuitable for long storm simulation as desired for this study.

4.5 Free Surface Tracking

In the IH2VOF model, free surfaces are tracked by using the Volume of Fluid (VOF) method first suggested by Hirt and Nichols (1981). In this technique, the exact location of the free surface cannot be accurately traced by the model. Free surface is identified by tracking the change in density of each cell. Different cell types are identified within the model and values of VOF are assigned to them: interior (I), surface (S) or empty (E). It is illustrated in Figure 4.1:

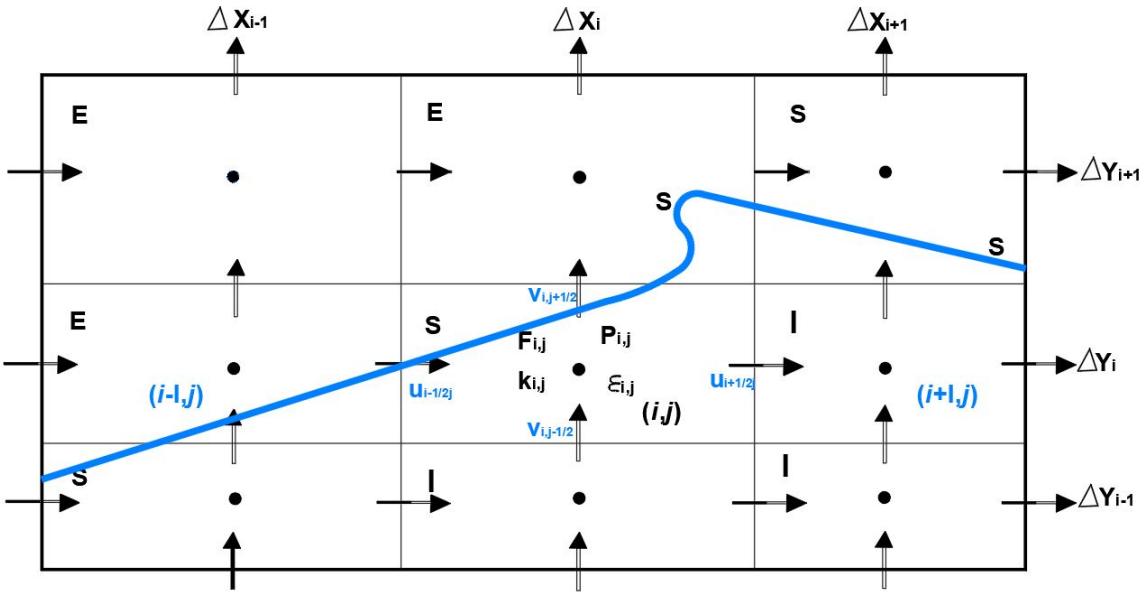

Figure 4.1 *The computational domain and the free surface tracking in the model*

The density ratio can be stated as,

$$F = \frac{\rho}{\rho_f} \tag{4.34}$$

where,

$$\rho = \frac{\rho_f V_f}{V_f + V_a} \tag{4.35}$$

ρ_f, represents the fluid density, V_f, the volume of the fluid in the cell and V_a being the volume of air within the cell. F = 1 represents the interior cell, F > 0 for surface

cells, and F = 0 for empty cells. As a result of this modification, the mass conservation equation can be transformed into the transport equation in the form of:

$$\rho(x,y,t) = F(x,y,t)\rho_f \tag{4.36}$$

or can be expressed as:

$$\frac{\partial F}{\partial t} + \frac{\partial}{\partial x}(\overline{v}F) = 0 \tag{4.37}$$

Hirt and Nichols (1981) presented an algorithm to eliminate error in the convection of F by evaluating F gradients in two directions to identify the free surface location. VOF algorithm was modified by Lin and Liu (1998). For full details of VOF implementation, readers should consult Hirt and Nichols (1981) and Lin and Liu (1998).

4.6 Numerical Resolution of RANS Equation

Within the numerical domain of the IH2VOF, RANS equations are solved by applying the Chorin (1968, 1969) finite difference two-step projection approach (Maza et al., 2017). Firstly, the following intermediate velocity was introduced into the momentum equation as:

$$\frac{\tilde{u}_i^{n+1} - u_i^n}{\Delta_t} = -u_j^n \frac{\partial u_j^n}{\partial x_j} + g_i + \frac{\partial \tau_{ij}^n}{\partial x_j} \tag{4.38}$$

This equation is a forward time difference equation where $\tilde{u}_i^n$ denotes the intermediate velocity, Δ_t is the time step that correspond to $(n+1)^{th}$ time level. Equation (4.38) does not include the pressure gradient term and the intermediate velocity does not satisfy the continuity equation.

Using Equation (4.39), the intermediate velocity can be well represented on a divergence-free plane to obtain the final velocity:

$$\frac{u_i^{n+1} - \tilde{u}^n}{\Delta_t} = -\frac{1}{\rho^n}\frac{\partial p^{n+1}}{\partial x_j} \tag{4.39}$$

$$\frac{\partial u_i^{n+1}}{\partial x_i} = 0, \tag{4.40}$$

Moreover, the pressure gradient at the next time step ($(n+1)^{th}$) can be estimated in the form of the Poisson Pressure Equation (PPE):

$$\frac{\partial}{\partial x_i}\left(\frac{1}{\rho^n}\frac{\partial p^{n+1}}{\partial x_i}\right) = \frac{1}{\Delta t}\frac{\partial \tilde{u}_i^{n+1}}{\partial x_i} \tag{4.41}$$

By combining Equations (4.39)–(4.41), we can derive a complete momentum conservation equation as:

$$\frac{\tilde{u}_i^{n+1} - u_i^n}{\Delta_t} + u_j^n\frac{\partial u_j^n}{\partial x_j} = \frac{1}{\rho^n}\frac{\partial p^{n+1}}{\partial x_i} + g_i + \frac{\partial \tau_{ij}^n}{\partial x_j} \tag{4.42}$$

With the application of the two projection method, velocity components and pressure fields can be spatially derived in finite difference forms. To obtain the convection terms, both the central difference (CD) and the upwind method (UM) are applied. The advantage of the combined methods is to complement the individual drawbacks of implementing each method separately. In this way, the numerical instability and tendencies for wave damping are reduced. Weighing factors are used in the numerical spatial scheme to regulate the influence of each of the two methods (Maza et al., 2017).

For example, for pressure gradients terms, and the stress gradient terms only the central difference method was applied. Detailed implementation of the numerical model can be found in Lin & Liu (1998).

4.7 The Computational Domain

The numerical domain is usually discretised into rectangular cells as shown in Figure 4.1. Sub-meshes can be defined within the domain to represent areas of special interest. Within every cell in the domain, all scalar quantities are defined (including the VOF function (F), pressure (P), turbulent kinetic energy (k), and the rate of dissipation (ε). Vector quantities including, the mean velocity components $\bar{v}$, and the additional openness function (θ_r & θ_t) are also defined.

To test capability of the model at propagating waves, a simple numerical two-dimensional wave flume was set up. As shown in Figures 4.2 & 4.3, the domains each 25 metres long and 1 metres high. The computational domain discretised into 0.004 m along the x-axes (34,394 nodes in green) and 0.01 m along y-axes mesh-sizes (81 meshes in yellow colour) were used to run the simulation with a time step of 0.004 s to maintain a stable simulation over a storm duration. As shown in Figure 4.2, wave gauges spaced out in the numerical flume (W1, W2, W3, and W4) were used to obtain the time series of the surface elevation.

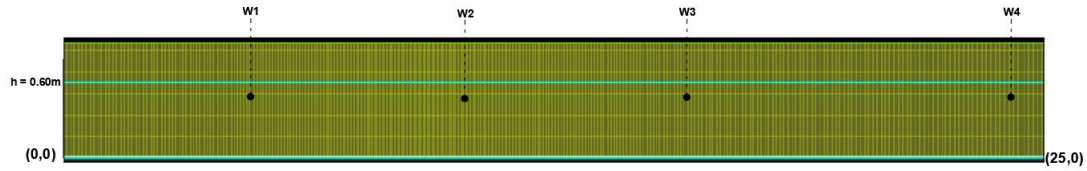

Figure 4.2 *An example of simple IH2VOF model domain without any structure*

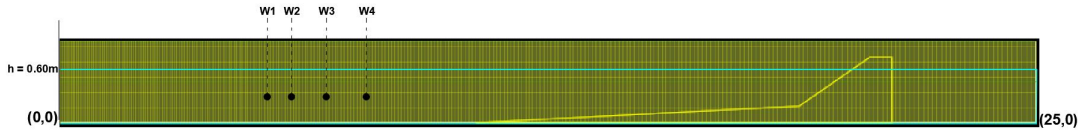

Figure 4.3 *An example of simple IH2VOF model domain with a sloping simple seawall*

Also, the capability of the model at reproducing a simple sloping seawall was tested. A simple sloping seawall with cot $\alpha = 1.5$ was positioned in the numerical domain. This configuration will be further described in Chapter 6.

4.7.1 Mesh Convergence Settings

For optimal numerical simulation, it is essential to apply suitable mesh resolutions (Δx:Δy) that can balance the simulation time, and still able to accurately model the nu-

merically determined wave parameters. For this purpose, six different mesh resolutions are applied to determine the numerical domain that will optimally reproduce the input wave conditions. An H_{m0} of 0.125 meters was used as a base for this purpose. As a rule of thumb, $\Delta x < \Delta y$ has been recommended to avoid premature wave breaking and damping (Maza et al., 2017). Also, mesh sizes along the vertical axis must accommodate at least one-tenth of the wave height to be propagated. Along the x-axis, the domain must be stretched to evolve a minimum of 4 wavelengths before intersecting any obstacles.

Figure 4.4 shows an example of the H_{m0} obtained for tests conducted using six different mesh sizes. There is more accurate convergence of H_{m0} between mesh sizes of 7.5 mm to 12.5 mm in every tested cases against the benchmark. The convergence rates are slower for larger number of mesh sizes. Consequently, vertical mesh sizes less than one tenth of the H_{m0} are often selected along the vertical axis as previously suggested in (Maza et al., 2017).

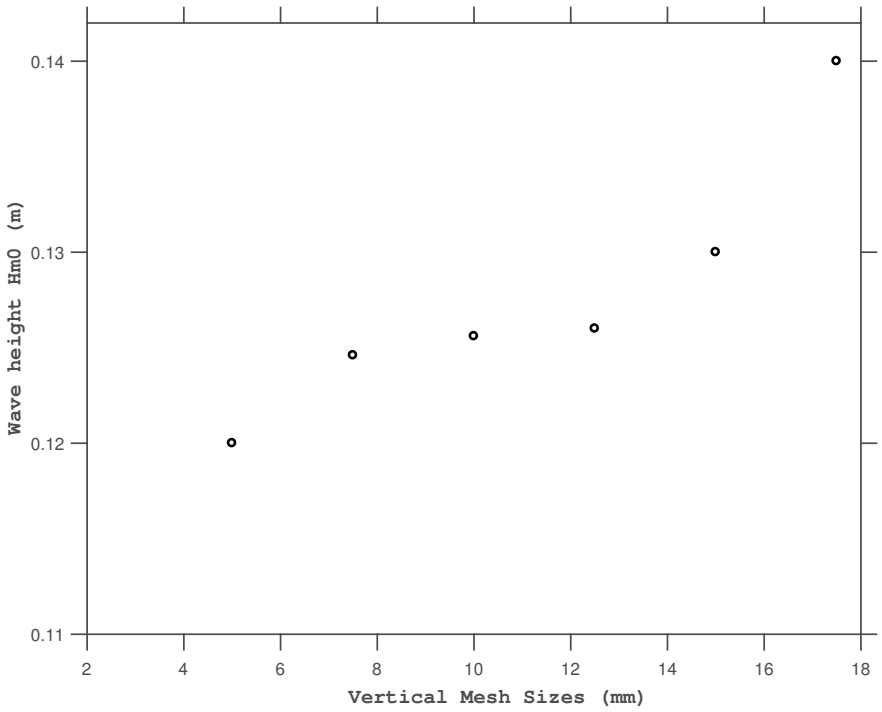

Figure 4.4 *An example of the RMSE of the mesh resolution settings for optimal mesh sizing applied*

For the regular wave cases, only the empty computational domain was applied. Figure 4.5 presents a representation propagation of a wave with significant waveheight $H_s = 0.08\ metres$ and peak period $T_p = 1.27\ secs$ in a water depth $h = 0.6\ metres$. As clearly shown, the model is capable of reproducing this wave. The performances were good as the wave arrives each of the wave gauges and the energy build up appear.

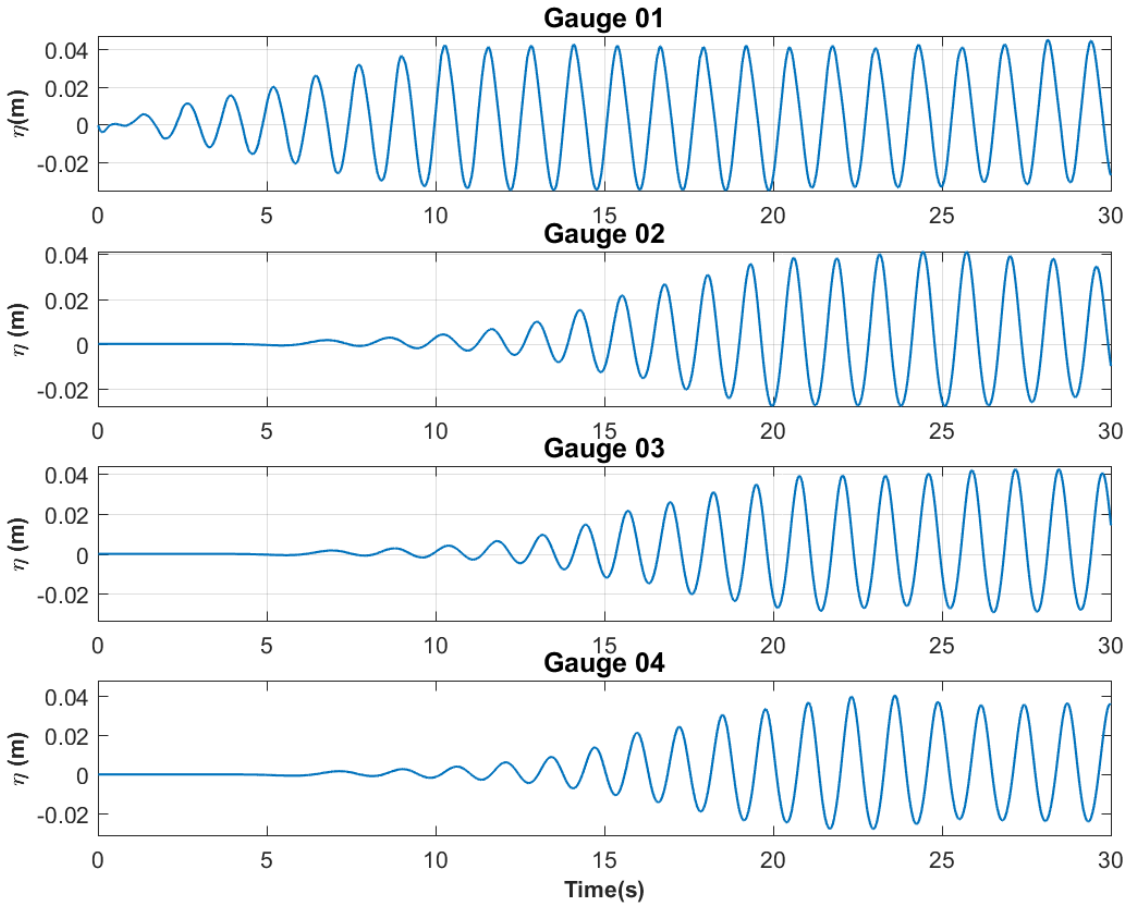

Figure 4.5 *An example of regular wave propagation in the computational model for* $H_s = 0.08\ metres$ *and* $T_p = 1.27\ secs$ *in a water depth* $h = 0.6\ metres$ *recorded with wave gauges placed at W1, W2, W3 and W4.*

For all the cases considered, 7 wave gauges are used. The numbers and positions of the gauges are listed in Table 4.1. In every cases in this study, waves are generated from the position of $Y = 0$ (Figure 4.3), and are propagated progressively towards the positive X-axis as presented. From the wave elevations across the wave gauges in Figure 4.5, earlier arrival of waves can be seen from earlier wave gauges Gauge 01) than later ones (Gauges 02 to 04). During this simulation, active absorption of waves is defined at the other side of the domain to avoid excessive inherent reflections.

Table 4.1 Location of wave gauges

Gauge Number (X)	Location (m)
1	10
2	10.3
3	11.1
4	11.6
5	18.1
6	23.6

4.7.2 Generation of Solitary Waves

An example of surface elevations representing the capability of the computational model to accurately generate solitary waves is presented in Figure 4.6. The model propagates the inputed waveheight and wave periods through selected wave gauges. A 10 seconds solitary wave was simulated within 85.71 seconds on an Intel Core $i7-6700$ CPU processor with 3.40 GH_z x 8 cores and 15.5 GiB RAM.

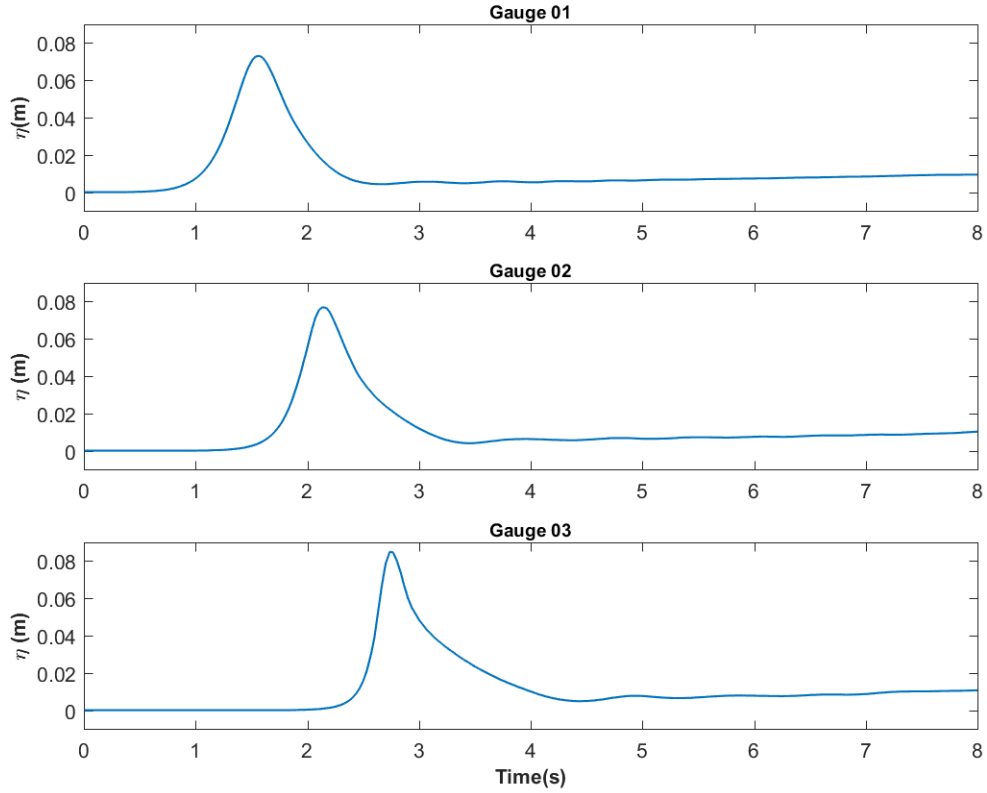

Figure 4.6 *Solitary wave propagation in the numerical flume for* $H_s = 0.1$ *metres and* $T_s = 2.01$ *secs in a water depth* $h = 0.25$ *metres recorded at wave gauges placed at W1, W2 and W3.*

4.7.3 Generation of Irregular waves

An example of an accurately generated irregular wave by the model is presented in Figure 4.7. Individual irregular wave components are well defined.

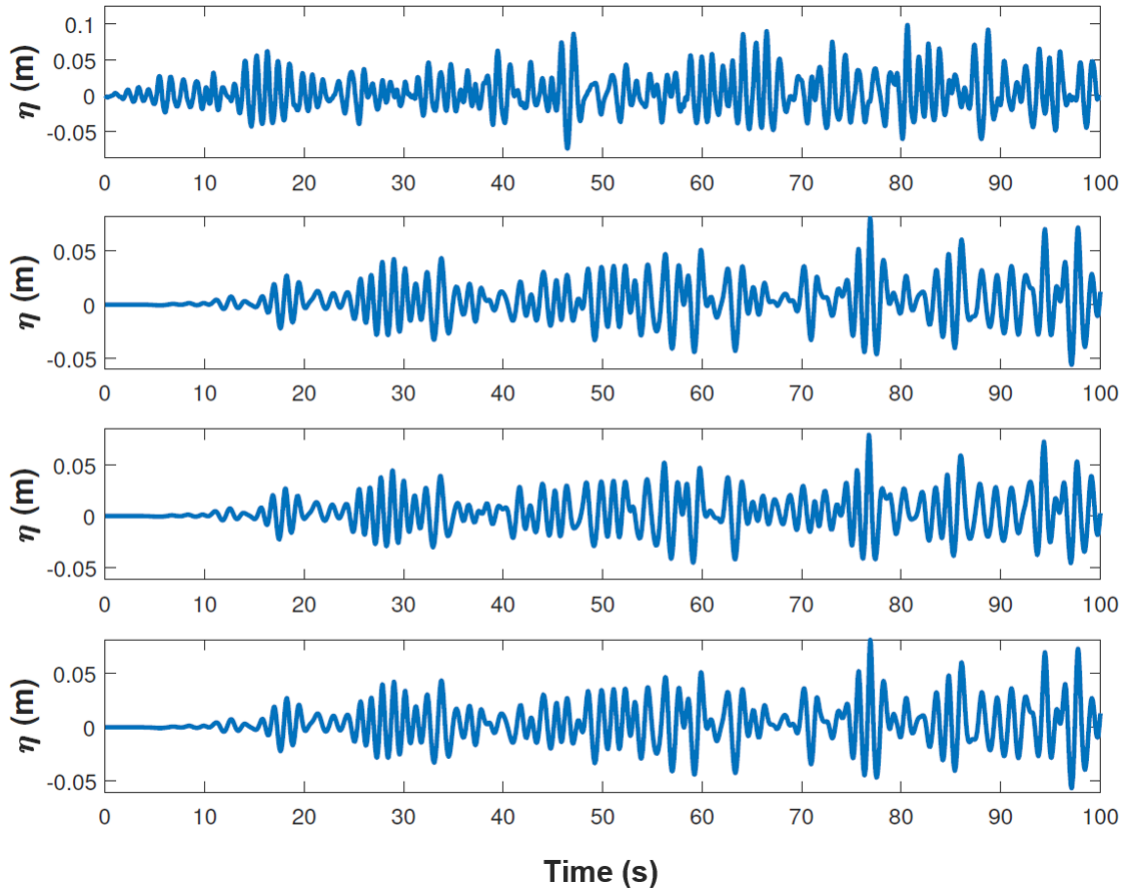

Figure 4.7 *Propagation of irregular wave using the dynamic paddles in the numerical flume for* $H_s = 0.08$ *metres and* $T_p = 1.27$ *secs in a water depth* $h = 0.6$ *metres recorded at wave gauges placed at W1, W2, W3 and W4.*

4.8 Evaluating Model Performance

Performance of an hydrodynamic model is essential to determine the reliability of the model at propagating and absorbing waves. To achieve this aim, the mass conservation of the model is evaluated in terms of the energy balance equation (Equation (4.43)) in both active and inactive absorption mode. Firstly by operating a closed boundary domain and also by applying the open ones against wave absorption requirements. To assess the performance of this model, the porous switch was set to zero. A wave height

of 0.1 metres was propagated through an inflow and outflow water depth each of 0.6 metres.

$$\frac{\partial \rho}{\partial t} + \bigtriangledown.(\rho u) = \odot \tag{4.43}$$

By total integration of Equation (4.43) across the entire domain, and then applying the divergence theorem we have:

$$\int_{\omega} \frac{\partial \rho}{\partial t} + \bigtriangledown.(\rho u) dV = \int_{\omega} \frac{\partial \rho}{\partial t} dV + \int_{\partial \Omega} (\rho u).ndS \tag{4.44}$$

The turbulence and roughness functionalities were initiated. The active absorption were set active at both ends of the computational flume to avoid poor judgement due to reflection effects. From Figure 4.8, both the energy buld up with time and dissipation are presented in the Figure.

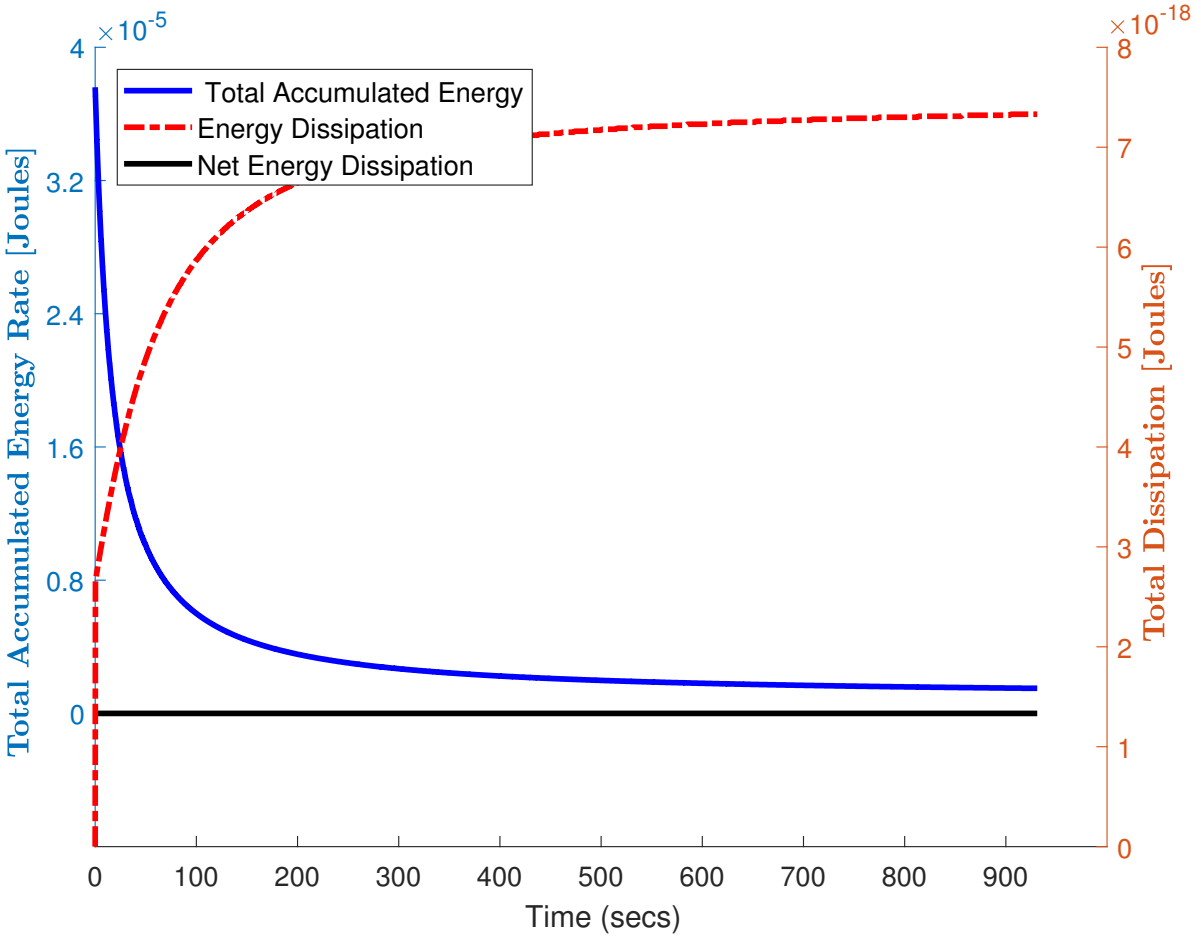

Figure 4.8 *An example of the energy rate in IH2VOF with respect to time.*

It can be seen in Figure 4.8 that the total accumulated energy rate vanishes as soon as the steady state is reached. There is a progressive increase in the energy dissipation until it reaches a steady state. The black line is the energy balance absolute error. There is a good agreement in the net energy balance which should be zero in this case.

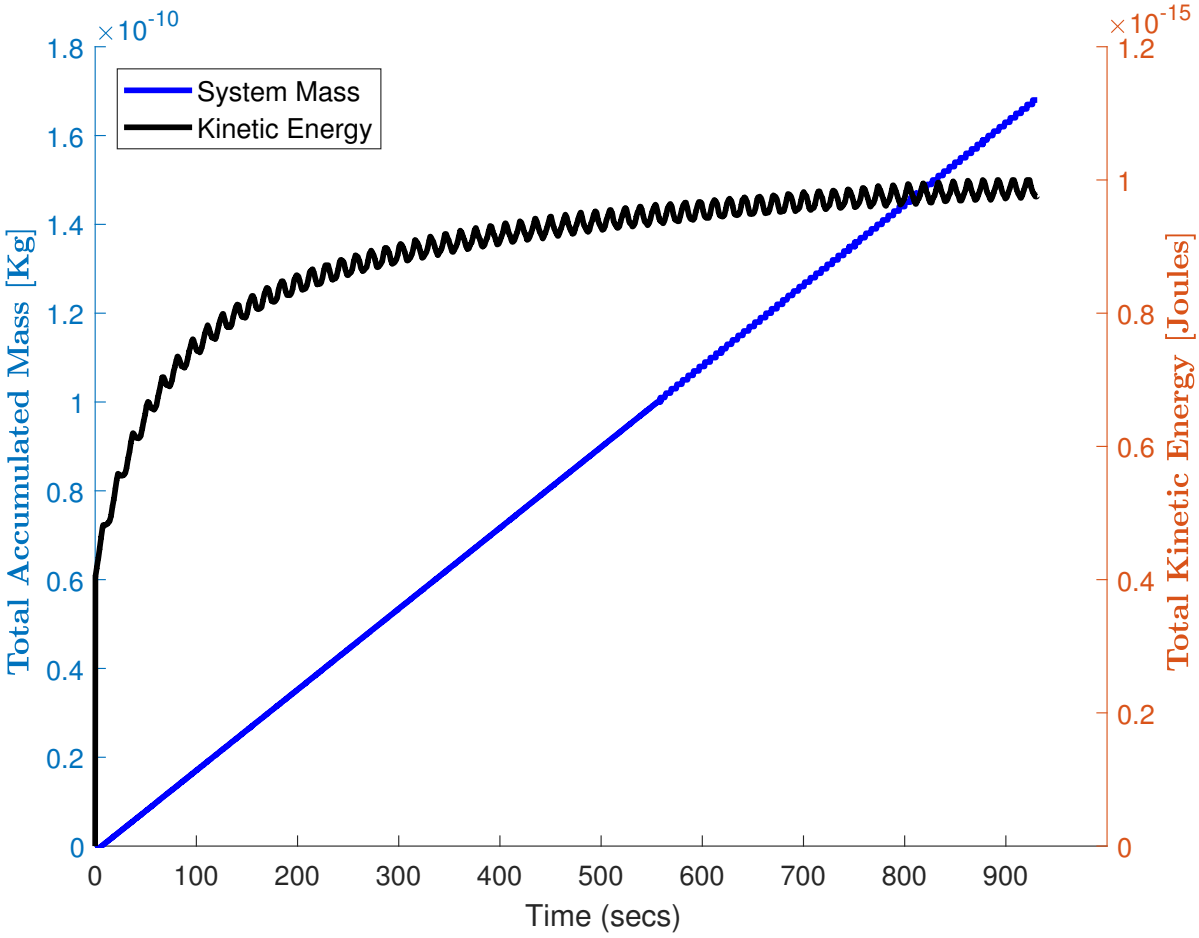

Figure 4.9 *Variations of total mass (Kg) and kinetic energy (Joules) with time*

The mass growth in the computational model is presented in Figure 4.9. There is a progressive growth in the mass component of the system with time. In the closed domain, there is mass accumulation with time. This evidence is confirmed with the variations of the kinetic energy KE in the system. The (K E) also grows systematically until the model reaches a stable state. It can be evidenced that the model performed accurately in conserving both mass and energy.

4.9 Conclusion

The numerical implementation of the IH2VOF computational model has been examined in this chapter. The functionalities of the model at generating different wave types, including regular, irregular waves, and solitary waves. The generation of bimodal waves will be discussed in Chapter 5. Both active and inactive absorption boundary conditions can be implemented. Waves can be both pre-determined at the boundaries using appropriately designed still water levels, or generated using dynamic piston-like paddle motions as in physical flumes. Because the model is very stable after a long period of the simulation period, it makes the model suitable for simulating a long period of bimodal storm conditions. Moreover, several wave gauges can be introduced into the domain to capture several occurrences of instantaneous velocities and water levels; it is possible to determine wave overtopping on top of the crests. More details of the computational performances of the model are presented in Chapters 5 and 9.

Chapter 5

Numerical study of Swell Effects in Bimodal Seas

An understanding of the wave height distribution of a sea state is essential in forecasting extreme wave height and lifetime fatigue predictions of marine structures. As earlier described in Chapter 3, swell can be present at different proportions and at different frequencies, while the energy content of the sea state remains unaltered. This chapter applies the numerical model (already described in Chapter 4) to investigate how the wave height distribution is affected by different swell percentages and long swell periods in an energy-conserved bimodal sea both near a wave maker and in shallow water. More specifically, wave elevations, steepness, auto-covariances, skewness, kurtosis obtained from the time variance analysis of bimodal waves are shown and discussed. Effects of swell waves on wave height distribution near the wavemaker and the structures are presented. This chapter is important because the interactions of these parameters with wave overtopping estimates will be discussed in later chapters.

5.1 Introduction

The IH2VOF computational model is applied to assess the distribution of wave heights in energy-conserved bimodal sea states described in chapter 3. There have been studies on wave height distribution in deep water and shallow water. Longuet-Higgins (1952) proposed the Rayleigh distribution of wave heights and several modifications have been made to low-wave-height-exceedance distributions (Boccotti, 2000; Forristall, 1978; Guedes Soares, 1984; Naess, 1985; Tayfun, 1981; Vinje, 1989). Specifically, a depth-modified version of the Rayleigh distribution was proposed in Battjes and

Groenendijk (2000) which is applied only to unimodal waves. Similarly, Rodriguez et al. (2002) studied the wave height probability distributions using extracted Gaussian bimodal waves from numerical simulations.

Petrova and Guedes Soares (2011) applied a linear quasi-deterministic theory to compare energies from the wind and swell seas using a simplified Sea Swell Energy Ratio (SSER) on the assumption of wave nonlinearity. Nørgaard and Andersen (2016) developed a slope dependent version of the Rayleigh distribution based on an Ursell number criterion. Nørgaard and Andersen (2016) only consider swell wave height distribution of highly non-linear swell waves due to shoaling on gentle slopes ranging from 1 in 30 to 1 in 100 slopes without considering the energy built-up in the overall bimodal spectrum. None of these studies have applied bimodal sea states that have varying proportions of swell, while at the same time containing a fixed amount of energy to investigate wave height distribution in shallow water close to a structure, which is what occurs very often in practice.

None of these studies has examined steep sloping structures in shallow water conditions that are close to a structure, a situation that is often found in practice. We focus on this critical case where the wavefield contains incoming and reflected waves which may also have been modified by breaking. The energy-conserved bimodal spectrum that was created from unimodal sea states are converted into random waves time series using the Inverse Fast Fourier Transform (IFFT).

The resulting time series was used to drive a Reynolds-Averaged Navier Stokes (RANS) computational model. Wave height values were then extracted from the model results (both away from and near to the structure) using down-crossing analysis to inspect the non-linearity imposed by wave-wave interactions and through transformations as they propagate into shallow waters near the structure.

5.2 Wave Height Extraction Using Numerical Model

A long flume is required to extract values of wave height for the assessment of the non-linearity characteristics of bimodal seas. The wave propagation model used for the present study is the validated IH2VOF model that has been fully described in Chapter 4. IH2VOF model has been validated against several hydrodynamic scenarios including plane beaches and rubble mound breakwaters (Lara et al., 2011; Ruju et al., 2014).

Surface elevations (time series) obtained from the inverse FFT were used to create sets of mesh-dependent pre-designed horizontal and vertical velocities that were used to determine the model boundary conditions. These computations were based on the

linear wave theory. The computational domain discretised into 0.005 m on x-axes (33,514 meshes) and 0.01 metres along y-axes mesh-sizes (51 meshes) were used to run the simulation with a time step of 0.004 s to maintain a stable simulation over a storm duration. As shown in Figure 5.1, wave gauges placed near both the wave-maker (W1, W2 and W3) and near the structures (W10, W11, and W12) were used to obtain the time series of the surface elevation. First three wave gauges are placed at 2 to 3 metres from the wave maker while the last three are positioned near the structure at 20 to 22 metres away from the wave maker.

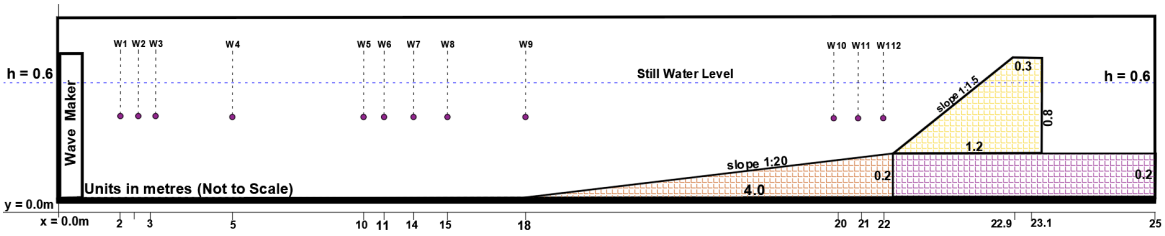

Figure 5.1 *Layout of a 2-D numerical model (not to scale) for a waveheight extraction using the wave gauges near the wavemaker and the structure.*

The wave conditions tested in this study are presented in Table 5.1. The same grid sizes were applied in each case. Varying percentages of swell waves were introduced into the wind sea states and at different swell periods. An equivalence of storm duration of 3 hours was propagated as represented by 1000 waves in the numerical model. The bimodal spectrum formed in this process were then converted into surface elevations which are used to drive the IH2VOF model as previously described in Chapter 4.

Table 5.1 Tested bimodal wave conditions

H_{m0} (m)	T_{pW} (secs)	T_{pS} (secs)	Swell Percentages	Gamma
1.0	7.0	15, 20, 25	25	Wind = 3.3; Swell = 2.5
1.5	8.0	15, 20, 25	50	Wind = 3.3; Swell = 2.5
2.0	9.0	15, 20, 25	75	Wind = 3.3; Swell = 2.5

5.2.1 Determination of Kurtosis and Skewness of the Bimodal Spectrum

The relationship between the kurtosis K_u and the skewness S_k of the energy conserved bimodal seas was examined using the method proposed by Marthinsen and Winterstein

(1992). A second-order approximation of the resulting bimodal spectrum S_{bim} is determined using Equation (5.1). Moreover, different orders of spectrum moments are computed from order 1 to 4 designated as m_0, m_1, m_2, and m_4 using the approaches detailed in Cavannie et al. (1976).

The kurtosis, K_u, can be computed using m_3 and m_4, and is defined as,

$$K_u = \frac{m_4}{m_3^2} \tag{5.1}$$

1st, 2nd, 3rd and 4th moments can be computed as:

$$m_n = \int_0^\infty f^n S(f) df \tag{5.2}$$

Skewness is defined according to

$$S_k = 6 \int \int f_{sum}(f_{ij}) + f_{diff}(f_{ij}) \frac{S(f_i) df_i * S(f_j) df_j}{m_0^{(3/2)}} \tag{5.3}$$

where $f_{sum}(f_{ij})$ and $f_{diff}(f_{ij})$ represent the sum and the difference of frequency effects observed from individual spectra combined.

5.2.2 Analysis of Free Surface From the Energy-Conserved Bimodal Spectrum

Examples of free surface derived from bimodal spectra are presented in Figure 5.2. The bimodal sea time series contained different swell percentages and the swell peak periods that were gradually varied as detailed in Table 5.1. As shown in Figures 5.2a, and b, there is no significant graphical noticeable differences between the surface elevation of waves time series generated by different swell percentages that was simulated for 1000 waves. This could happen because the overall energy contained in the sea states are preserved even though different random waves that was applied when obtaining the time series as presented. Energy conservation was evident in Figure 5.2b by further inspection of the minimum and maximum values of the surface elevations. The values are fluctuating around a specific mean of minimum and maximum values of -0.1 m and 0.1 m respectively for the sea state (4 m, 7 s) investigated at a scale of 1:20. These results agree with the standard weakly stationarity assumptions of a sea state with zero mean described by Rychlik et al. (1997a) because the overall wave spectra properties are preserved.

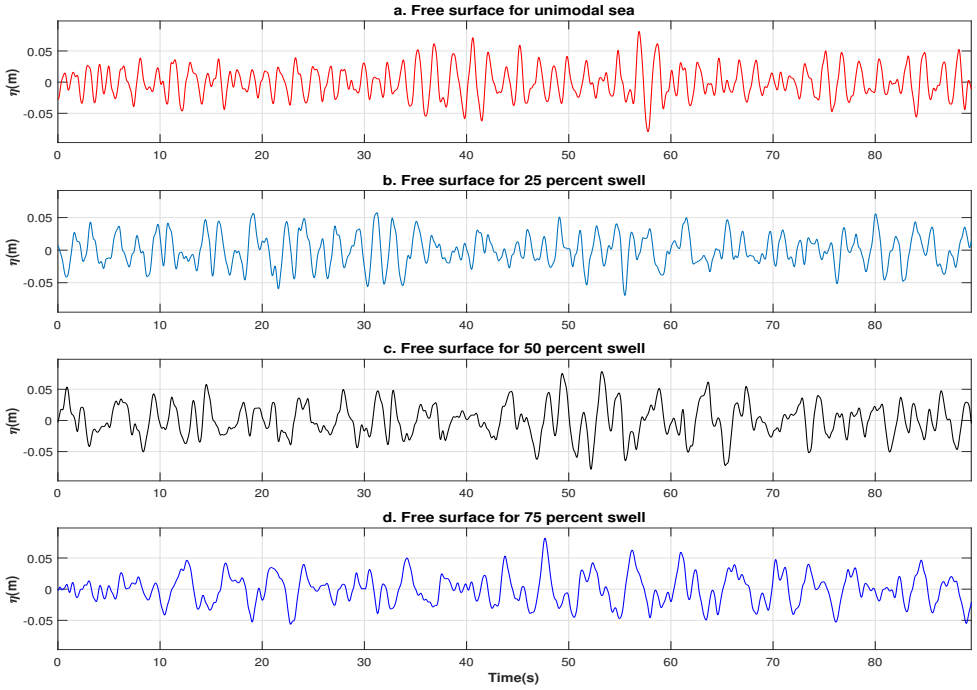

(a)

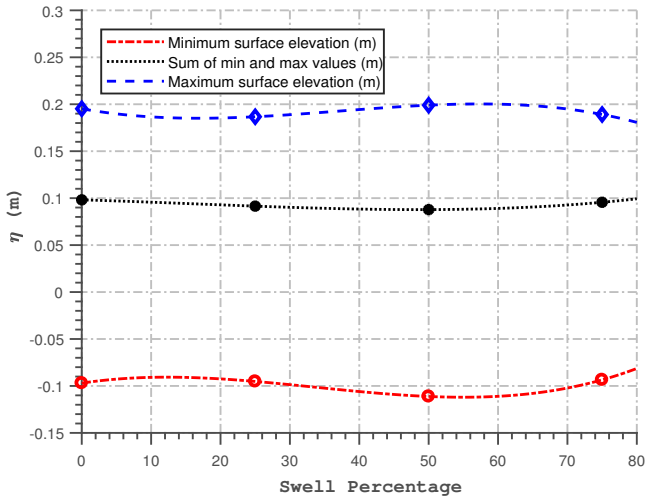

(b)

Figure 5.2 *Comparison of the different free surface elevations for different swell percentages at swell peak period of 25 s. (a) Free surface elevation obtained for different swell percentages as shown; (b) Analysis of the surface elevation shown in (a).*

5.3 Influence of Swell on Time Variance Analysis of Bimodal Waves

Time variance analysis of waves provides an essential background towards variablity of time series. Regular and irregular characteristics of surface elevations can be identified for further analysis. Moreover, better understanding of the physical processes that is responsible for the variations can be provided. In this study, the influence of swell on the autocovariances of waves have been analysed from the extracted time series. Figures 5.3 and 5.4 presented the relationship between the auto-covariance function, (ACF), with increasing overall swell percentages and swell periods of the individual wave characteristics extracted from the computational model. The cross-correlation function in Figure 5.4 reveals that by increasing the swell percentages of a sea state, the individual waves are still largely independent of each other. There is a slight decrease in the independence as the swell percentages increase from 25 to 75 percent swell sea conditions. It can be described in terms of the variance of different swell percentages in as shown by the time lag between these waves. This effect is similar to what is observed as the swell peak period increased from 11 s to 25 secs in Figure 5.5.

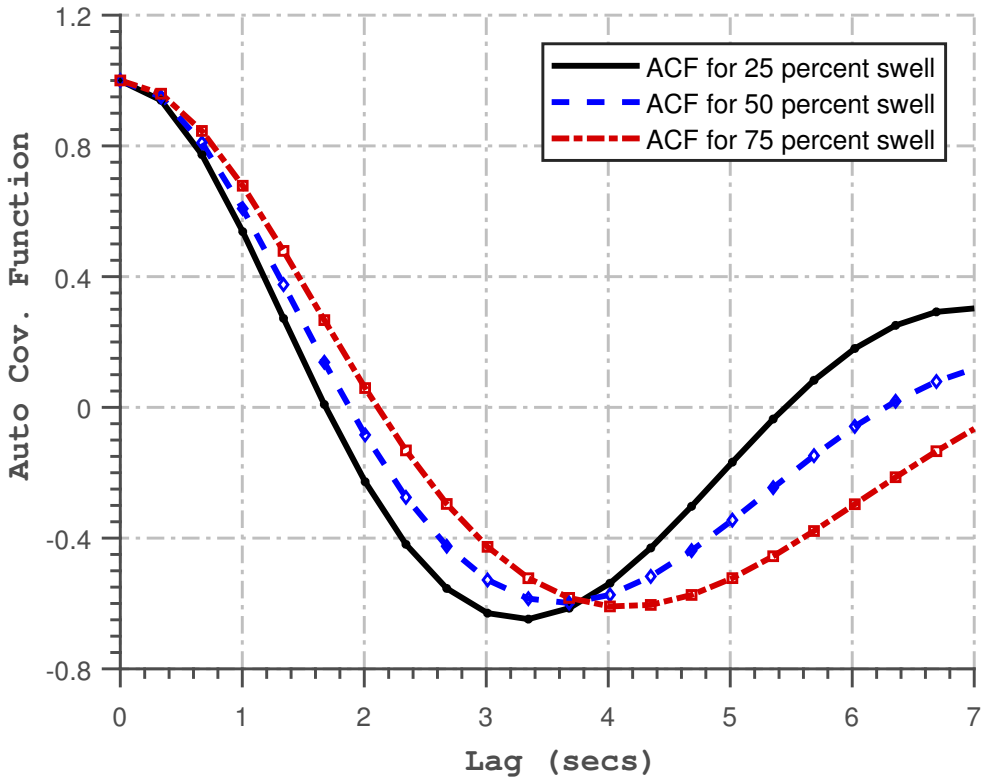

Figure 5.3 *Time variance analysis of the effects swell periods and percentages in a bimodal sea with $H_{m0} = 4metres$ and $T_{pW} = 7secs$ showing the relationship between the auto-covariance function ACF with increasing overall swell percentages in a bimodal sea*

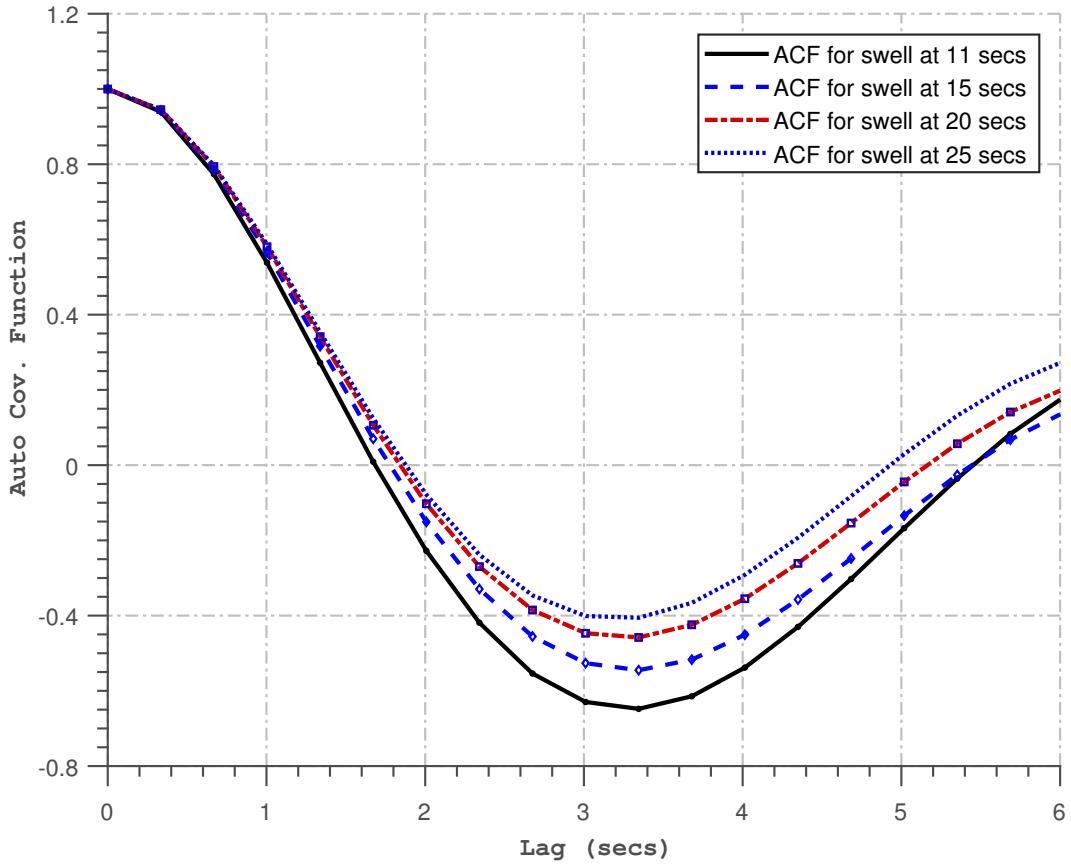

Figure 5.4 *Time variance analysis of the effects swell periods and percentages in a bimodal sea with $H_{m0} = 4metres$ and $T_{pW} = 7secs$ showing the relationship between the ACF with increasing swell periods in a bimodal sea*

5.4 Influence of Swell on Wave Skewness and Kurtosis

Wave skewness and kurtosis derived by applying Equations (5.1) – (5.6) presented the performance of skewness parameter with varying proportions of swell periods. The results are presented in Figures (5.5 & 5.6). As clearly shown in Figure 5.6, there is an inverse relationship between the wave kurtosis and the skewness. Skewness reduces with increasing swell peak periods. Skewness behaviour was tending towards a constant value as swell peak periods increases in the same sea state. Skewness behaviour was highest for the unimodal sea than for equivalent bimodal sea conditions; reduction of skewness was observed with increasing swell percentages.

As shown in Figure 5.5, under the conserved energy bimodal sea states, there is a dynamic reduction in the relationship between the kurtosis K_u and skewness S_k as the swell percentage and the peak period increases. This is an increasing smooth and

continuous exponential relationship that can be expressed as:

$$K_u = 2.99 \exp^{0.11 S_k} \tag{5.4}$$

A sea state with 25 percent swell at a peak period of 11 s has the largest skewness-kurtosis relationship as compared with the lowest affinity relationship portrayed by the 75 percent swell at a much lower frequency of 25 s. The coefficient of kurtosis deviate significantly from linear predictions. The results obtained here near the structure are similar to those Forristall (1978) observed on a shoaling beach.

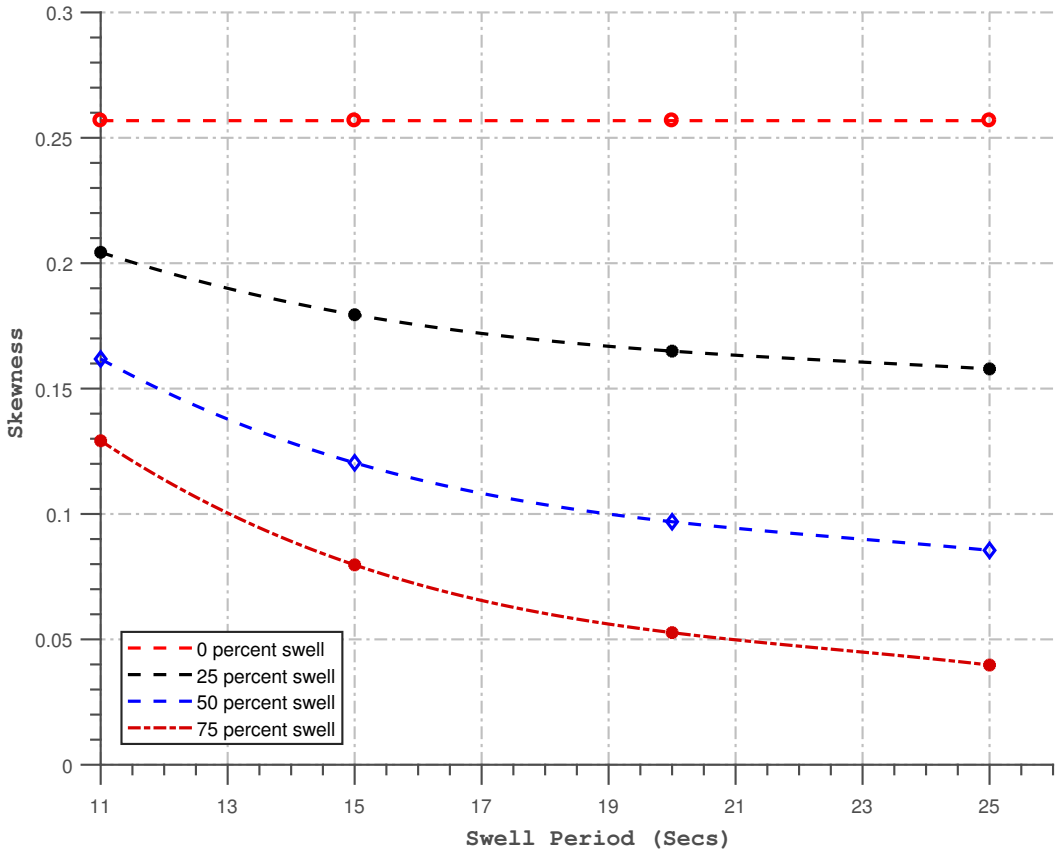

Figure 5.5 *Time variance analysis of the effects swell periods and percentages in a bimodal sea with $H_{m0} = 4m$ and $T_{pW} = 7s$ showing the variation of skewness with swell periods and percentages*

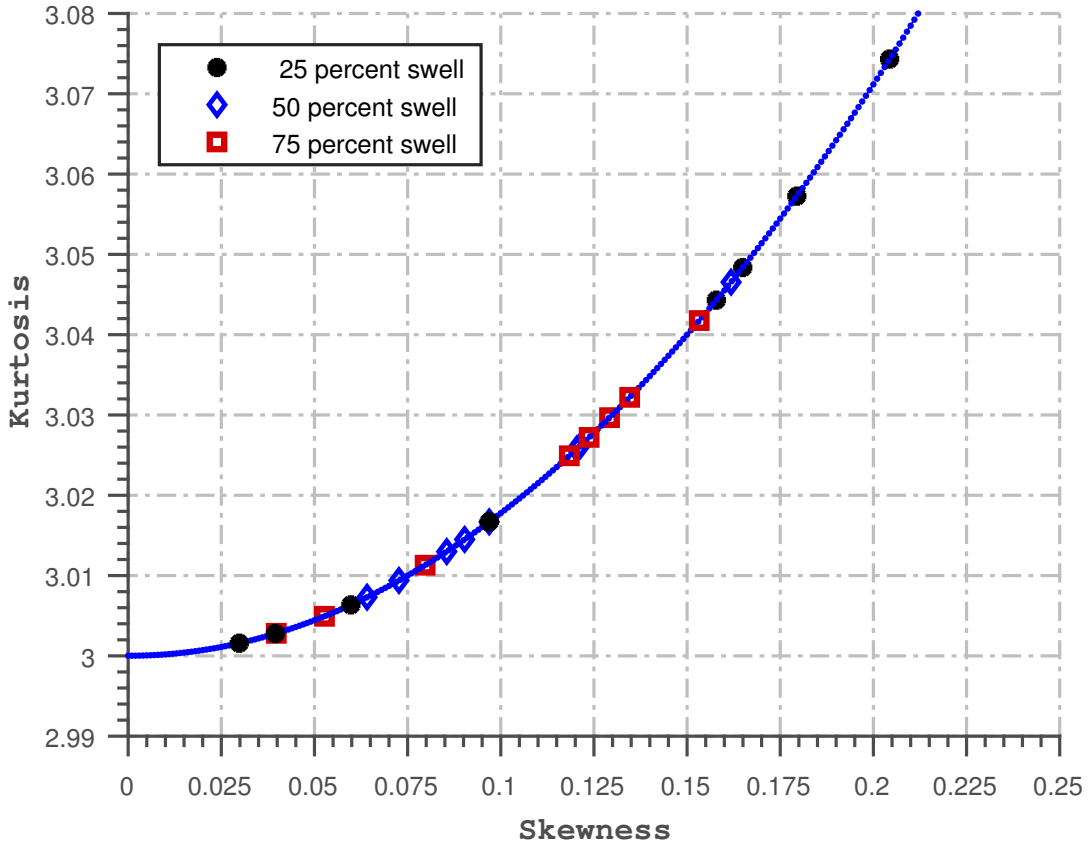

Figure 5.6 *Time variance analysis of the effects of swell percentage in a bimodal sea with* $H_{m0} = 4 metres$ *and* $T_{pW} = 7 secs$ *showing the variations of kurtosis against skewness for different swell.*

5.5 Influence of Swell on Wave Height Distribution

5.5.1 Influence of Swell Period

The probability distribution curves in Figures 5.7 and 5.8 show how wave height distribution is influenced by different frequencies of swell in the bimodal energy spectrum as observed both near (at 2 metres) from the wave maker and at farther distances away (at 20 metres) near the structure.

If the waves followed a Rayleigh distribution, all the points would fall on the full straight line shown in each figure. Wave height distribution is greatly affected by the peak period of the swell. Non-linearity patterns are indicated by deviation from the Rayleigh linear scale, and strongly related to the swell peak period. This is because the Rayleigh distribution better represents narrow-band sea states such as observed by Toffoli et al. (2006). These deviations increase with the closeness of

the two peak frequencies (for swell and wind) on the energy spectrum. Increasing the swell peak period in the energy spectrum expands the width occupied by the bimodal spectrum. This occurrence would in turn increase the overall spectra period obtainable from the resulting spectrum when transformed. In general, higher wave values deviates significantly from Rayleigh predictions. Boccotti (2000) suggests that the waves become more unstable because of the non-linearities from long crested conditions. Further observations are that the non-linearities of wave height became more pronounced near the structure because of wave-wave interactions and through shoaling as they propagate into shallow waters.

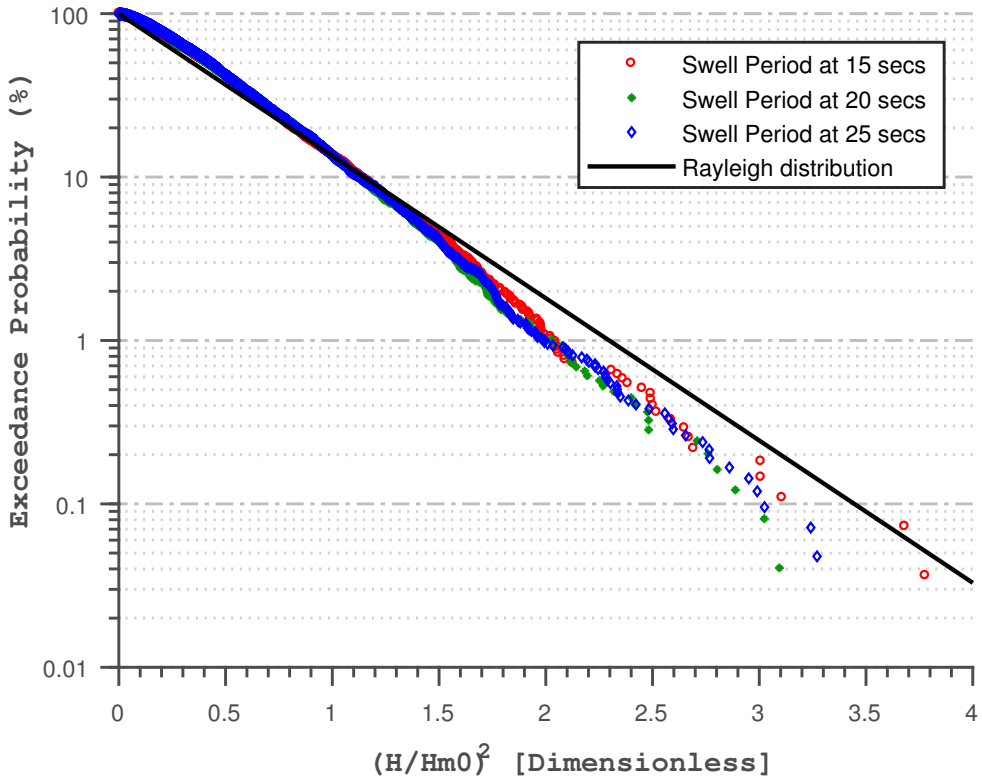

Figure 5.7 *Effects of swell periods on wave height distribution near and away from the structure. Wave height distribution for different swell periods observed away from the structure*

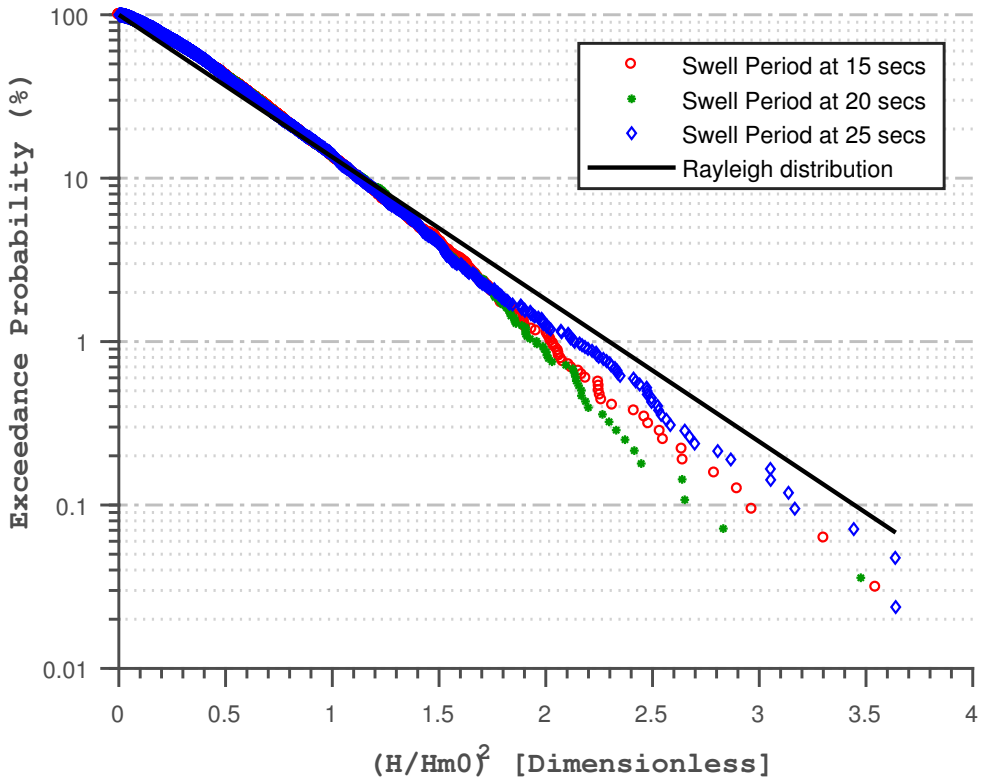

Figure 5.8 *Distribution of wave height for different swell periods observed near the structure.*

5.5.2 Influence of swell percentages

Following the previous section, Figure 5.9 depicts the wave height statistics within the domain for different swell percentages introduced into an energy-conserved sea state. The non-linearity patterns were extended to a unimodal sea. In all the sea cases considered (unimodal and bimodal), the non-linearity pattern was highest near the seawall than near the wave maker. This is expected because of the shoaling process and reflection created by the wave interaction with the sea-wall. As shown in Figure 5.10, non-linearity behaviour is higher in the unimodal seas state than for the bimodal seas (in this case). This trend of non-linearities reduces with increasing swell percentages. However, some deviations from this trend are observed in 50 percent swell. This may be due to the uneven distribution of energy formed by the double Jonswap spectra and may require further study.

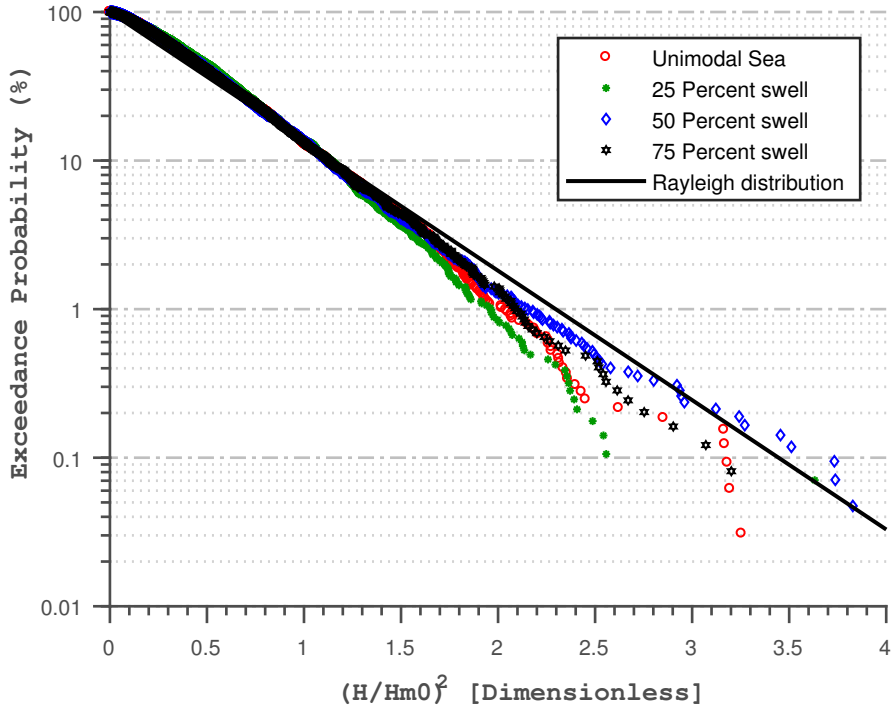

Figure 5.9 *Effects of wave bi-modality caused by wave height distribution for different swell percentages observed near the structure*

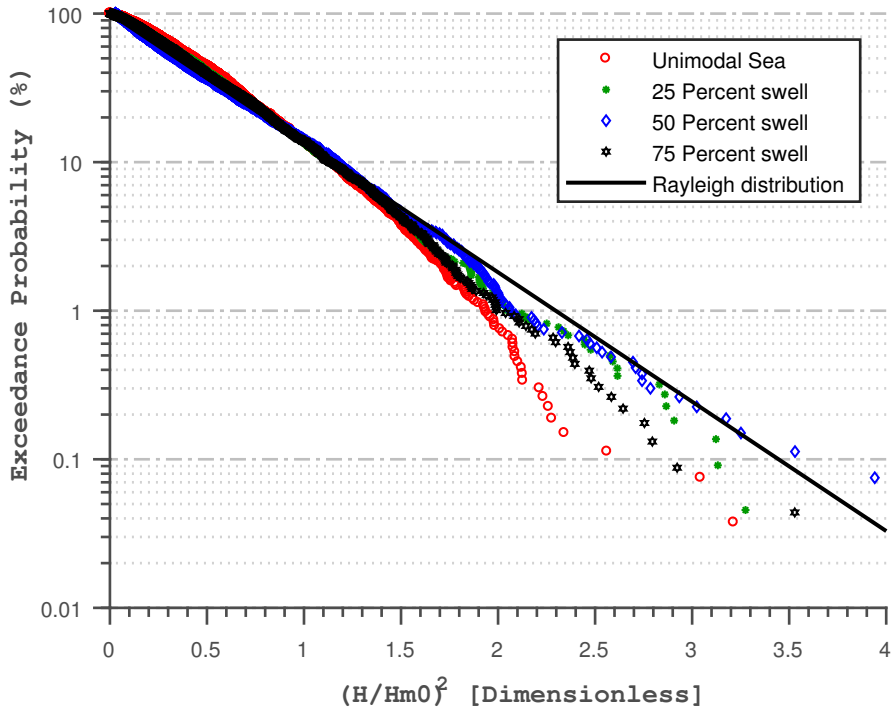

Figure 5.10 *Effects of wave bi-modality caused by the distribution of wave heights for different swell percentages observed near the wave-maker.*

5.5.3 Patterns of Wave Height Distribution

Figures 5.11(a–c) and 5.12(a–d) shows Weibull and the Rayleigh plots depicting the wave height distribution performance of different swell percentages in the unimodal and the bimodal sea states. In all the cases considered (both near and away the structure), wave height is better predicted by the Weibull distribution than the Rayleigh plots.

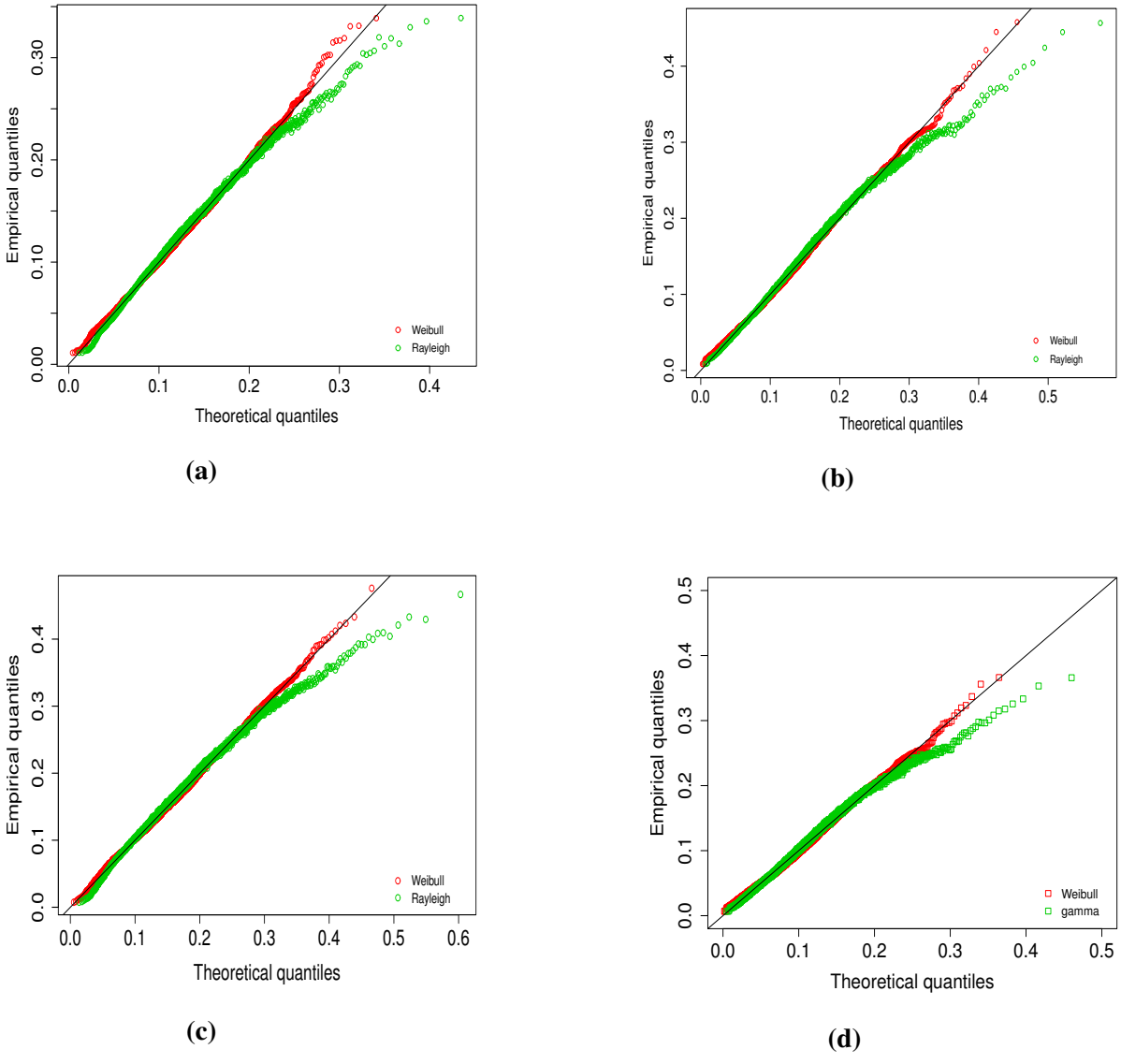

Figure 5.11 *Comparisons of performance of wave height distribution using Weibull and Rayleigh plots for different swell percentages away from the structure slope for (a) 25 percent swell, (b) 50 percent swell, (c) 75 percent swell and (d) the unimodal sea*

However, both distributions show great agreement at representing lower to middle part of wave height values. Some deviations from normal were evident for Rayleigh distributions in the lower quantiles.

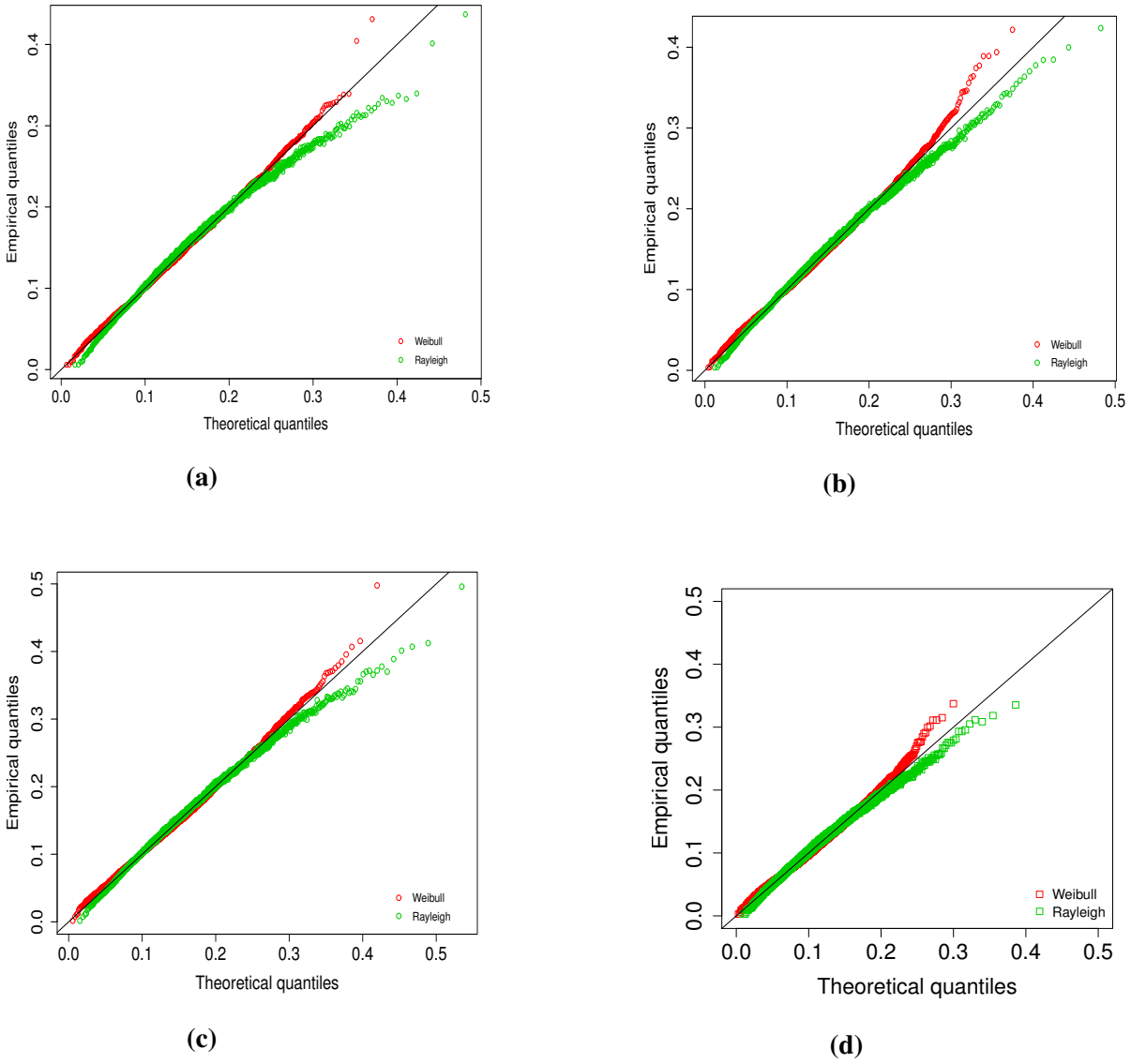

Figure 5.12 *Comparisons of performance of wave height distribution using Weibull and Rayleigh plots for different swell percentages near the structure for (a) 25 percent swell, (b) 50 percent swell, (c) 75 percent swell, and (d) the unimodal sea.*

The degree of fitness achieved by the weibull plots decreases slightly as the wave approaches the structure as shown in Figure 5.12(a–d) because more non-linearity patterns are possible by waves transformation caused by the wave-structure interactions. Also as expected, Rayleigh distribution underpredict higher waveheight values while the

Weibull plots are over-predicting in a way. As observed in all cases, non-linear trends are greatest in the 25 percent swell in Figure 5.12(a) and gradually reduce as the swell percentages increase towards the 75 percent swell in Figure 5.12(b–c). However as shown in Figure 5.12(d), the unimodal sea states is characterised by an earlier departure from the fit line. This is another evidence of more non-linearities in the unimodal sea states. The observed behaviour is similar to the Petrova and Guedes Soares (2014), wherein the non-linearities in the wave height distribution decreases with increasing swell percentages in the bimodal sea conditions. The energy within both initial unimodal and bimodal cases inputted into the model are identical in present study.

5.6 Conclusion

This chapter has addressed the influence of swell in a bimodal sea state with constant energy content while varying swell peak periods and percentages. Specified bimodal spectra were converted into time series using inverse FFT. The time series was used to drive the VOF-model in a numerical domain. The downcrossing analyses of numerical wave-gauge results sampled from near the wavemaker and the structure were used to assess the physical non-linearity of the bimodal sea state. There is an increasingly smooth and continuous exponential relationship between the skewness and kurtosis as the swell percentage and the peak period grows in an energy conserved bimodal sea. The extracted wave height distribution were represented by the Weibull and Rayleigh distribution to inspect the non-linearity imposed by wave-wave interactions and through dispersions as they propagate into shallow waters near the structure. The Weibull distributions produced the best fitness for wave patterns of high swell percentages considered. As the swell frequency and percentages increases in a bimodal sea, the relationship between the skewness and the kurtosis are tending towards a unimodal sea. The distribution of the waveheight on the Rayleigh model shows that the non-linearity slightly increases with the distance away from the wave maker. This could be caused by the development of other physical processes like reflection, wave breaking, and other shoaling processes arising from wave-structure interactions. In agreement with previous studies, the unimodal sea states showed the greatest non-linear behaviour however, non-linearity patterns vary as the swell grows. The Rayleigh distribution could not properly represent bimodal seas with wider spectral width and also overpredicts waveheight at low exceedances in these conditions.

Chapter 6

Experimental Test Programme

Much research guidance is available on wind-driven unimodal sea states, but fewer data can be found on bimodal seas. To bridge this research gap, the following experimental programme was conducted. Results of the 823 datasets obtained in present study will be applied to validate numerical results. This chapter is devoted to capturing new experimental datasets using incident bimodal sea. Models of three different seawalls were designed and experimented at the Swansea University Coastal Laboratory flume. The bimodal overtopping of different unimodal sea states were tested on the incorporation of swell waves at 25, 50 and 75 percentages arriving from different peak periods of 11, 15, 20, and 25 secs and propagating with 1000 random waves. Three levels of the crest freeboard R_c were tested using three different water levels of 0.60, 0.65 and 0.70 meters. Response of three different seawalls to the incoming waves were then assessed by introducing varying slopes of 1:1.5, 1:3 and vertical seawalls. In order to compare data to previous overtopping estimates, the equivalent unimodal spectra of the sea conditions were also used in each test. The quantity of water waves that over-topped the crest of the proposed breakwater were captured into a wave overtopping tank using a chute.

6.1 The Wave Flume at Swansea University

The Coastal Laboratory wave tank at Swansea University consists of an Armfield wave tank which is 30 metres in length, 0.8 metres in width and 1.2 metres in depth. Waves are generated with a HR Wallingford computer-controlled piston paddle, which has the capability to reproduce user-defined spectra of different types, includes a second-order wave correction due Schaeffer (1996), and is also equipped with an active

wave absorption system to minimise the wave reflection emerging during the wave propagation (Figure 6.1).

As a result of the configurations, the flume is particularly suitable for wave overtopping formulation and assessment studies. To represent a more realistic bathymetry for the experiment, the seabed was modified to a slope of 1:20 and the seawall was positioned to accommodate a large number of wavelengths to allow proper development of the random wave train (Figure D.1). This also gave room for a deeper water at the wavemaker than at the structure-toe. The model is constructed with stainless steel with adjustable edges to facilitate easy reformation into other geometries. A constant crest width of 0.40 metres was tested in all the experiments.

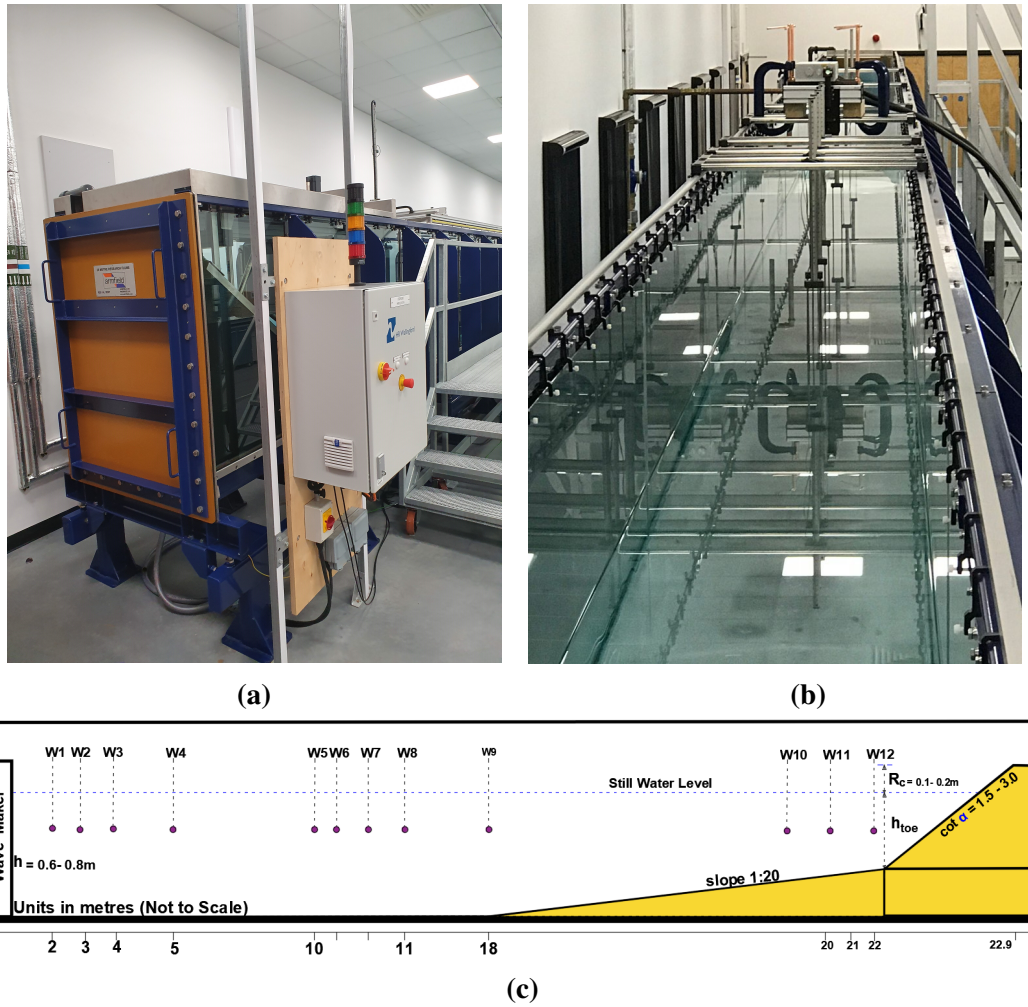

Figure 6.1 *Photographs showing (a) the wave paddle system, (b) array of wave gauges, and (c) an annotated sketch of the structure set-up for the wave overtopping experiment in the Swansea University Coastal Laboratory*

6.1.1 Wave Measurement Systems

The entire wave generating system is integrated into HR Daq suite Software. It comprises a range of integrated programs for use with hydraulic models. It can acquire and analyse a range of instrumentation. Accurate spectral analysis is possible within the software to generate wave spectra outputs and associated parameters. Wave probes (shown in Figures 6.3 and 6.4) are driven using the HR Daq software. Whenever the wave probes are immersed in water, flowing current between two stainless wires are converted into an output voltage to determine the surface elevation. The surface elevation is directly proportional to the output voltage. Because of variations in water conductivity due to changes in laboratory temperature conditions, periodic calibration is required for reliable results.

HR Daq systems are equipped with the calibration routines to determine accurate relationships between observed voltages and the water level. For these set of experiments, calibrations of wave probes were performed mostly twice a day or whenever there was a noticeable drop in temperatures within the laboratory.

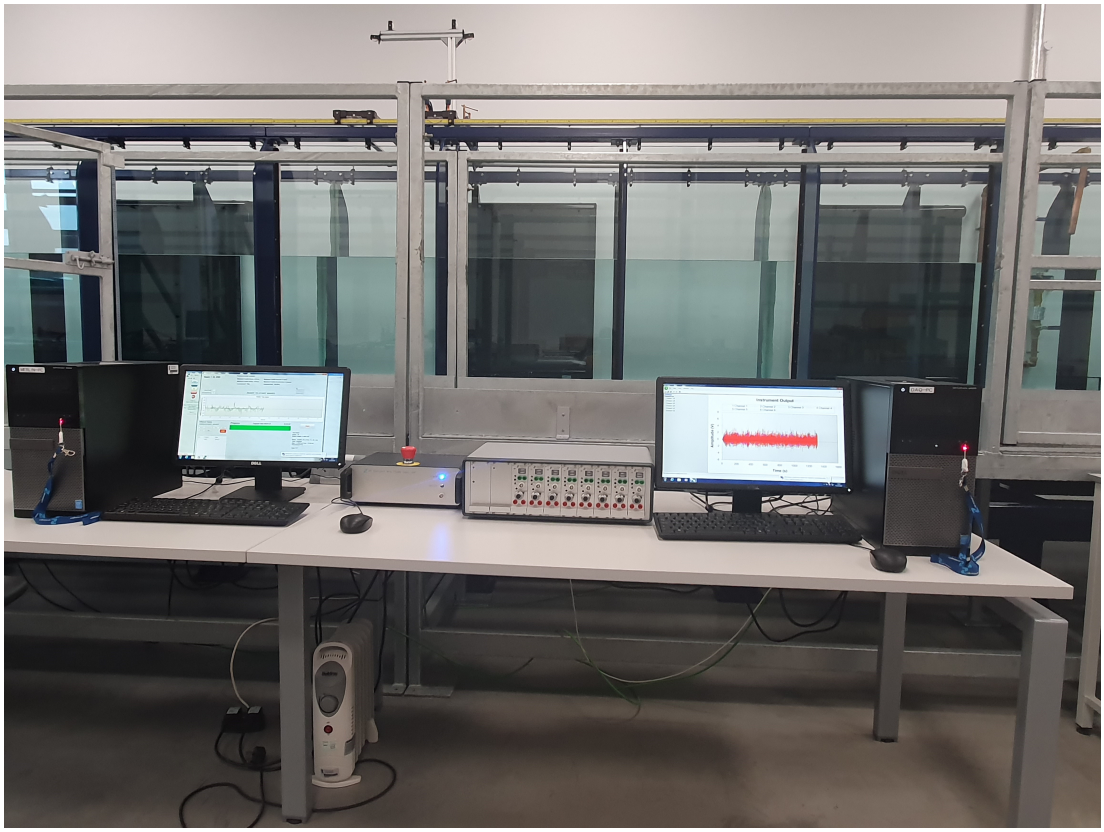

Figure 6.2 *A photograph of the HR Daq system integration of various wave generation and capturing systems*

Figure 6.3 *Connection pattern of the HR Wallingford wave probe system*

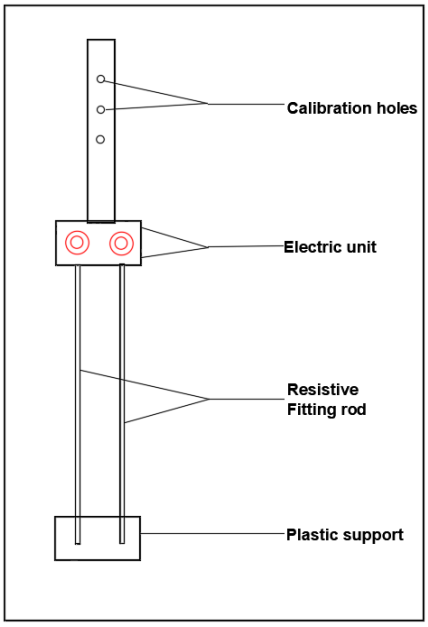

Figure 6.4 *A sketch of HR Wallingford wave probe system for measuring surface elevation*

Apart from real time acquisition of wave data by the Daq system, a module is also provided for reflection analysis. In this module, a minimum of four well positioned wave gauges are required.

6.2 Experimental Procedure

The bimodal spectra, (discussed in chapter 3), were input into the wave generator in a user-defined format to generate bimodal waves in random mode. As recommended in previous studies, a minimum of 1000 waves were tested for each wave condition. Overtopping volumes were collected using a chute fitted directly on top of the structures placed at the rear end of the crest (Figure 6.5). The chute emptied the water into the overtopping collection tank using a simplified pumping method that has been previously adopted (see, for example, Kortenhaus et al., 2005; Troch et al., 2004). The overtopping volume was obtained by measuring the water level in the calibrated tank before and after each test. A direct volumetric measurement in a calibrated tank was applied to minimise uncertainties due to multiple conversions.

In order to obtain the dimensionless wave overtopping, H_{m0toe} is required. It is determined by applying the bulk reflection coefficient obtained from the reflection analysis. The reflection analysis of acquired signals was performed using the reflection module incorporated with the HR-Daq data acquisition and processing software. This package removes reflected waves from the total signals using the method Zelt and Skjelbreia (1992) with four wave gauges. The method is an extension of the three-wave gauges least-squares solution of reflection analysis, which was first introduced by Mansard and Funke (1980). In this experiment, the reflection analysis of wave signals was analysed using four wave gauges that were placed at the flat, and deeper end of the flume. These wave gauges are WG5, WG6, WG7, and WG8 (Figure 6.5a).

Separation distances between the gauges were computed using offshore based linear wavelength $L_{m-1,0}$ of the incident waves. This can be expressed as $X_1 = 0$, $X_{12} = L/10$, $X_{13} = L/4$, $X_{14} = L/3$ as shown in Figure 6.5a. During these tests, the wave gauges were fixed at distances 10, 10.33, 10.83 and 11.1 metres from the wave maker respectively. These distances satisfy the normalised denominator criteria of the HR-Daq reflection analysis module (Figure 6.6a). The wave signals were analysed using Fast Fourier Transform (FFT) producing amplitude components in the frequency domain. Some portions of wave elevation at earlier and later parts of each simulation were ignored to allow for consistency of wave elevations. Bandpass filtering was applied to isolate the frequency band of $0.33f_p \leq f_p \leq 3f_p$ (f_p is the peak frequency of the spectrum). Three levels of the crest freeboard were tested at 0.1, 0.15 and 0.20 metres respectively for seawalls with slopes of 1:1.5, 1:3 and vertical seawalls.

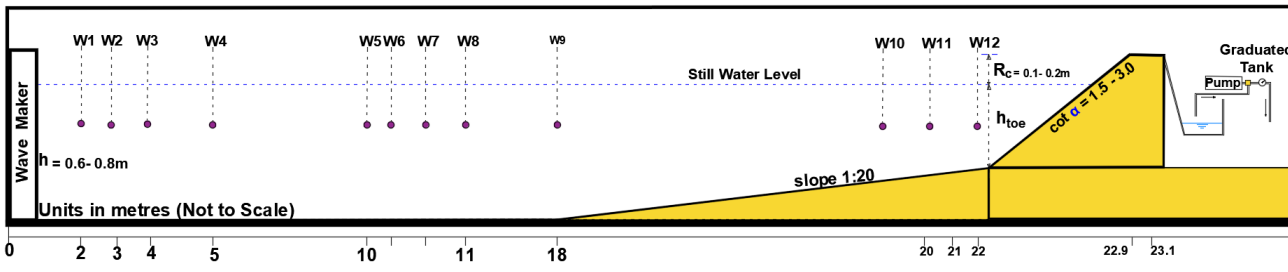

(a)

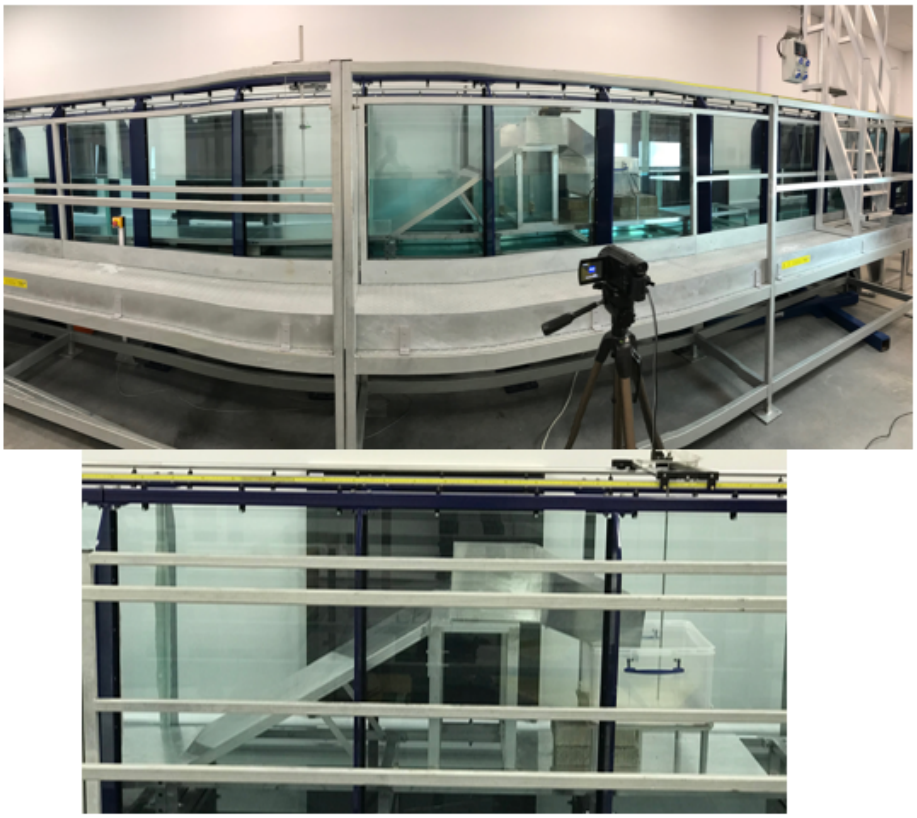

(b)

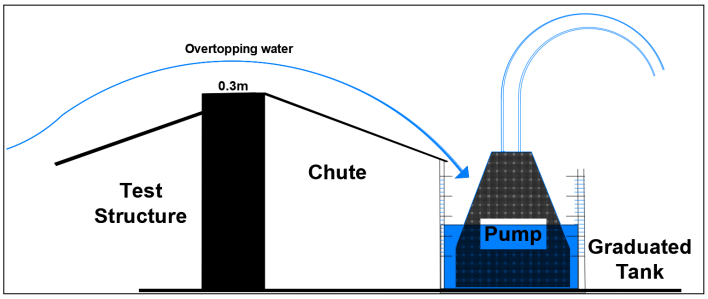

(c)

Figure 6.5 *(a) Sketch of the model set-up, and (b) Photographs showing the panoramic view of the flume depicting a section the seaward slope, and (c) the schematic sketch of the overtopping tank.*

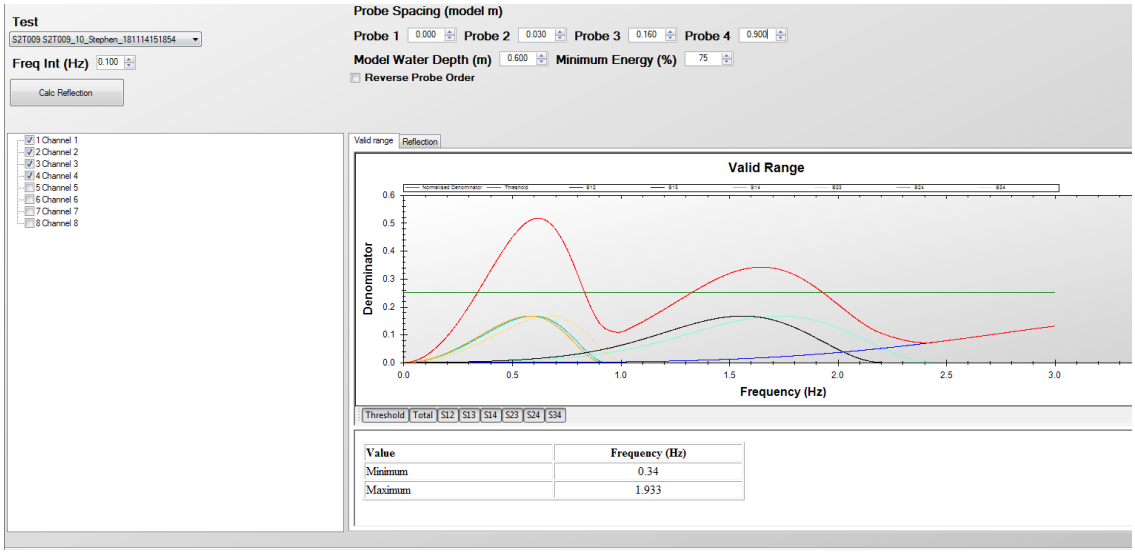

(a)

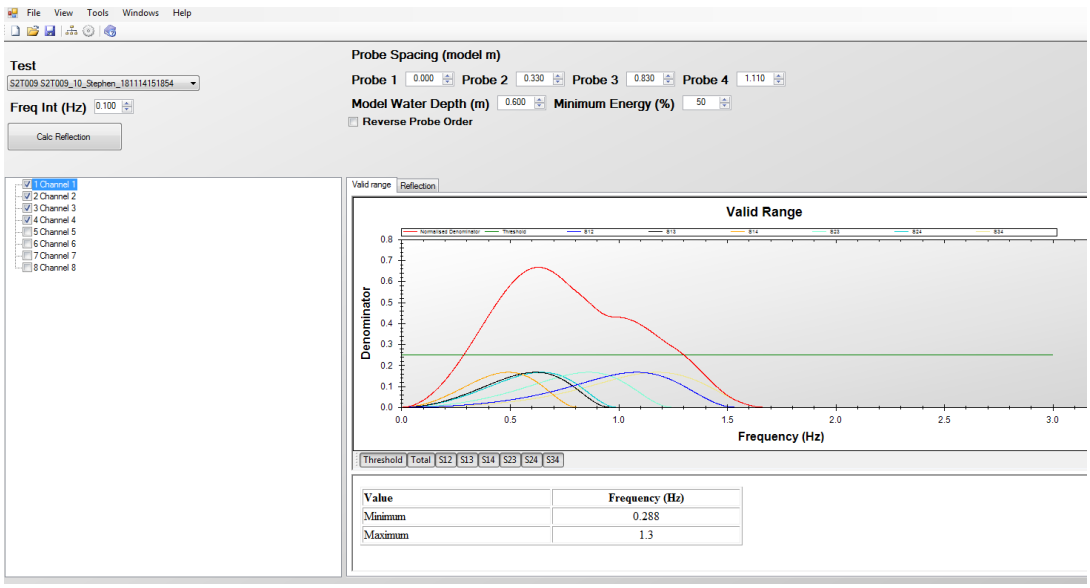

(b)

Figure 6.6 *A snapshot of the HR-Daq system showing the normalised denominator for reflection analysis using different wave gauge positions with (a) poor wave gauge position, and (b)suitably calibrated wave gauge position based on the frequency band frequency band of* $0.33f_p \leq f_p \leq 3f_p$

6.2.1 Tested Wave Conditions

Full details of the methodology, and how the spectra were defined while conserving total wave energy were discussed in Chapter 3 of this thesis. They are also available in Orimoloye et al. (2019b).

Table 6.1 Generation of 13 different wave conditions from the same-energy sea state with H_{m0} of 4 metres and T_{pW} = 7 secs.

ID	Test-No	T_{pW} (secs)	T_{pS} (secs)	Swell (%)	Mode (Unimodal = 1 Bimodal = 2)
1	T001-1	7	11	25	2
2	T001-2	7	15	25	2
3	T001-3	7	20	25	2
4	T001-4	7	25	25	2
5	T001-5	7	11	50	2
6	T001-6	7	15	50	2
7	T001-7	7	20	50	2
8	T001-8	7	25	50	2
9	T001-9	7	11	75	2
10	T001-10	7	15	75	2
11	T001-11	7	20	75	2
12	T001-12	7	25	75	2
13	T001-13	7	N/A	0	1

Different bimodal spectra with the same energy were then developed by introducing different swell components of different percentages at different frequencies, as shown in Figures 3.6 & 3.8. Table 6.1 contains the ranges of parameters tested in this study. Different spectral components H_{m0} and ($T_{Wm-1,0}$, and $T_{Sm-1,0}$) each for wind, and, swell seas were selected within the ranges shown in the Table. The spectral wave height H_{m0} obtained from the bimodal spectrum were varied from 0.05 to 0.18 metres. In this case, the spectral peak period of the wind-wave $T_{Wm-1,0}$ (varying from 1.106 to 1.581 secs) were combined with different corresponding spectral peak period $T_{Sm-1,0}$ of the swell wave. Only three swell percentages (25, 50 and 75) were investigated to accommodate more swell condition. Also, four different swell peak periods of 1.739, 2.372, 3.162 and 3.953 secs at a model scale of 1:40, which are equivalent to 11, 15, 20 and 25 seconds at the prototype scale were considered. These were tested across three

crest freeboards as stated in Table 6.1. The crest width of the structure are fixed at 0.3 metres (Figure 6.5c). Therefore, there are 13 different spectra, (including the unimodal case). As seen from Table 6.1, a broad range of $S_{m-1,0}$ (from 0.01-–0.07) were achieved from current experiments. It gives room for investigating a large number of bimodal wave cases.

Table 6.2 Ranges of Parameters tested.

Parameter (unit)	Range
Spectral wave height H_{m0} (m)	0.05, 0.075, 0.10, 0.125
Crest freeboard R_c (m)	0.1, 0.15, 0.2
Water depth at wave maker h (m)	0.60, 0.65, 0.70
Water depth at structure toe h_{toe} (m)	0.49, 0.54, 0.59
Spectral wind-wave peak period $T_{Wm-1,0}$ (s)	1.106, 1.265, 1.423, 1.581
Spectral swell-wave peak period $T_{Sm-1,0}$ (s)	1.739, 2.371, 3.1622, 3.952
Swell percentage S_w	0, 25, 50, 75
Surf similarity Parameter $\xi_{m-1,0}$	2.4 - 5.5
Non-dimensional freeboard R_c/H_{m0}	0.8 - 4
Wave steepness $S_{m-1,0}$	0.8 - 4.0
cot α	0, 1.5, 3.0
Slope angle	90, 33.70 and 18.43
Total successful tests	823

Implementing different percentages and periods of swell in the sea states yields different spectra and time series with the same energy content. Details of varying wind wave spectra that were combined with their equivalent swell periods and percentages are presented Table 6.2. Datasets in Table 6.2 are based on a Froude's scaling of 1:40 for all test cases. These tests are chosen based on the bimodal characteristics of UK coastline.

Table 6.3 Combinations of wave conditions tested in the present study.

Test No	H_{m0} **(m)**	T_{pW} **(secs)**	T_{pS} **(secs)**	$h(m)$	$cot\alpha$
T001	0.125	1.107	1.739, 2.3712, 3.162, 3.953	0.7	0, 1.5, 3.0
T002	0.125	1.264	1.739, 2.3712, 3.162, 3.953	0.7	0, 1.5, 3.0
T003	0.125	1.423	1.739, 2.3712, 3.162, 3.953	0.7	0, 1.5, 3.0
T004	0.125	1.581	1.739, 2.3712, 3.162, 3.953	0.7	0, 1.5, 3.0
T005	0.1	1.107	1.739, 2.3712, 3.162, 3.953	0.65	0, 1.5, 3.0
T006	0.125	1.264	1.739, 2.3712, 3.162, 3.953	0.65	0, 1.5, 3.0
T007	0.1	1.423	1.739, 2.3712, 3.162, 3.953	0.65	0, 1.5, 3.0
T008	0.125	1.581	1.739, 2.3712, 3.162, 3.953	0.65	0, 1.5, 3.0
T009	0.1	1.107	1.739, 2.3712, 3.162, 3.953	0.6	0, 1.5, 3.0
T010	0.1	1.264	1.739, 2.3712, 3.162, 3.953	0.6	0, 1.5, 3.0
T011	0.125	1.423	1.739, 2.3712, 3.162, 3.953	0.6	0, 1.5, 3.0
T012	0.125	1.581	1.739, 2.3712, 3.162, 3.953	0.6	0, 1.5, 3.0
T013	0.075	1.107	1.739, 2.3712, 3.162, 3.953	0.65	0, 1.5, 3.0
T014	0.075	1.264	1.739, 2.3712, 3.162, 3.953	0.65	0, 1.5, 3.0
T015	0.075	1.423	1.739, 2.3712, 3.162, 3.953	0.65	0, 1.5, 3.0
T016	0.075	1.581	1.739, 2.3712, 3.162, 3.953	0.65	0, 1.5, 3.0
T017	0.1	1.107	1.739, 2.3712, 3.162, 3.953	0.7	0, 1.5, 3.0
T018	0.1	1.264	1.739, 2.3712, 3.162, 3.953	0.7	0, 1.5, 3.0
T019	0.1	1.423	1.739, 2.3712, 3.162, 3.953	0.7	0, 1.5, 3.0
T020	0.1	1.581	1.739, 2.3712, 3.162, 3.953	0.7	0, 1.5, 3.0
T021	0.075	1.107	1.739, 2.3712, 3.162, 3.953	0.6	0, 1.5, 3.0
T022	0.075	1.264	1.739, 2.3712, 3.162, 3.953	0.6	0, 1.5, 3.0
T023	0.075	1.423	1.739, 2.3712, 3.162, 3.953	0.6	0, 1.5, 3.0
T024	0.075	1.581	1.739, 2.3712, 3.162, 3.953	0.6	0, 1.5, 3.0

6.3 Overview of Experimental Tests

To ensure that appropriate formulations are applied in analysing observed results, it is important to examine the data range of the captured datasets perceptually. Figure 6.7 presents a general representation of the relative wave height H_{m0}/h and the non-dimensional freeboard R_c/H_{m0} of the successful tests across the three slopes $cot\alpha = 0.0$, $cot\alpha = 1.5$, and $cot\alpha = 3.0$. H_{m0} was determined from the spectral conversion of the wave surface elevation at the toe of the structure. Figure 6.7, it can be seen at a glance

that the majority of the observations fall within the deep-water range $H_{m0}/h \leq 0.2$ (as suggested in the EurOtop (2018) manual). It is this ratio that describes the shallow water effects expected in the results afterwards. It also affirms that wave breaking effects would not be considered in later analyses of these test cases.

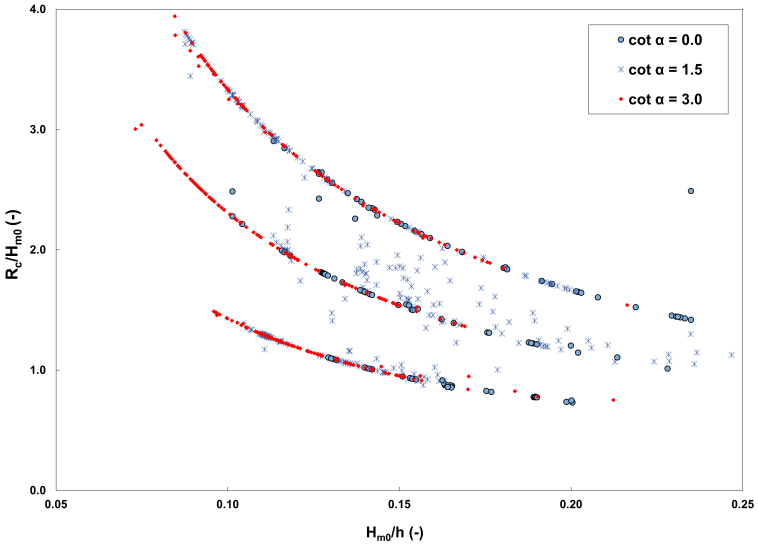

Figure 6.7 *An overview of comparison of the relative wave height H_{m0}/h with the non-dimensional freeboard R_c/H_{m0} of successful tests across the three slopes $cot\alpha = 0.0$, $cot\alpha = 1.5$, and $cot\alpha = 3.0$*

6.3.1 Spectra Validation

It is crucial to examine how well the wave maker can reproduce the input bimodal spectrum. The theoretical spectra were validated in this section by comparing the results of the target wave conditions with the recorded output by wave gauges. Figure 6.8 shows example of comparisons between the target (red line) and the reproduced (black lines with markers) incident bimodal spectra under laboratory conditions. The result is presented for all the gauges before the structure toe after reflection analysis has been carried out. As shown in Figure 6.8, a good overall agreement is obtained for different swell content. The frequencies of the modal values are well captured, but the spectral values are under-predicted, an outcome of the limitations imposed by scaling. It is challenging to generate long period bimodal waves in the laboratory. Consequently, the wave periods have to scaled down significantly for the wave paddle motion.

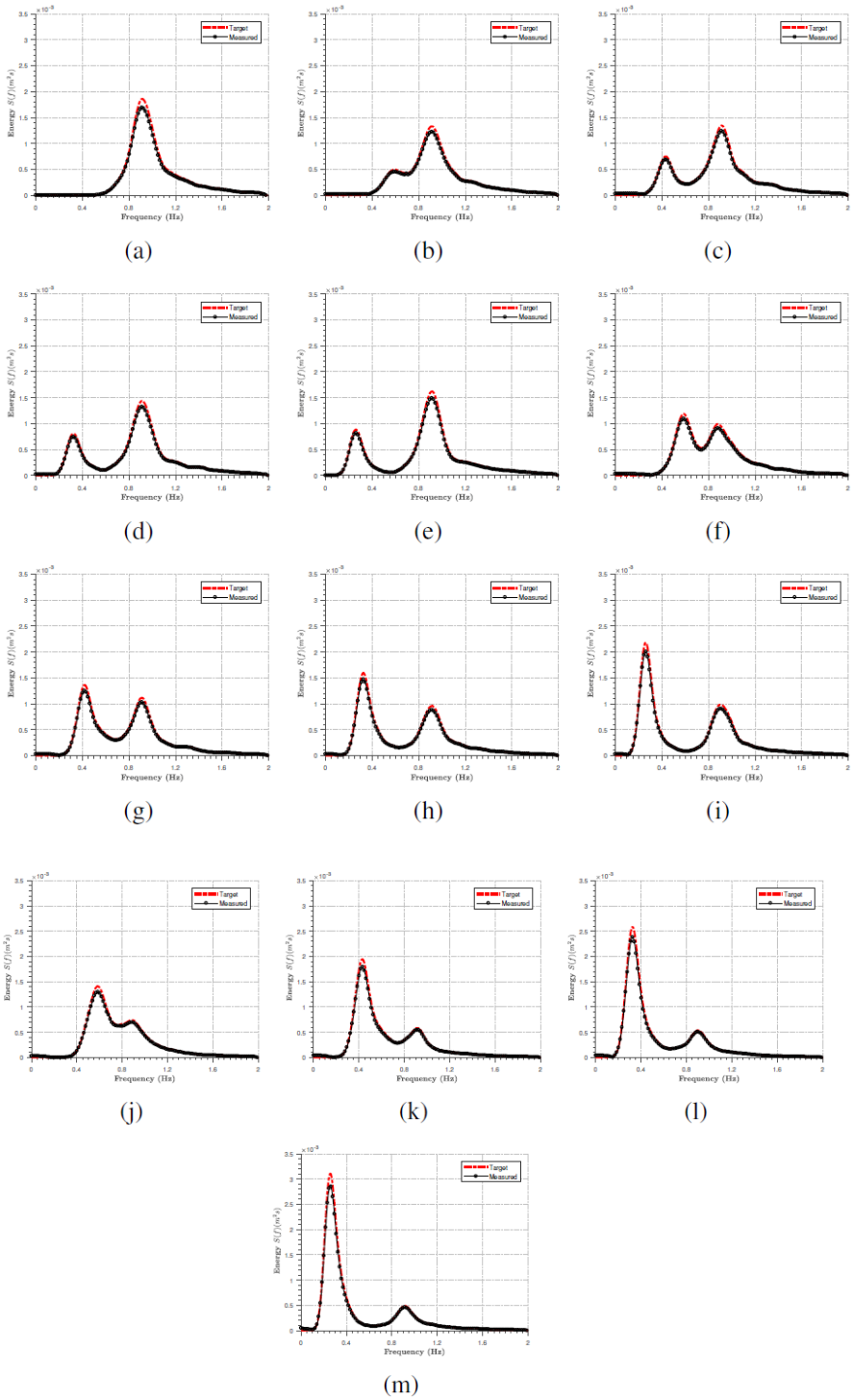

Figure 6.8 *Comparison between the target bimodal spectrum (in dashed lines) and measured (with markers) for (a) unimodal wind-sea with 0 percent swell, (b – e) 25 percent swell, (f – i) 50 percent swell, (j – m) 75 percent swell obtained for a sea state with wave height of 4 metres and wind wave period of 7 secs with equal energy but different swell percentages and swell peak periods*

6.3.2 Repeatability of Experiments

Repeatability of measurements is essential in experimental studies to ensure the acceptability of results. In this way, uncertainties of measurements can be reduced and in turn, enhance the reliability of outputs. Kortenhaus et al. (2005) suggested the use of the coefficient of variation (CV) to assess the variability of wave overtopping parameters. The following parameter σ' are proposed as the CV with the assumption that the individually observed datasets are each normally distributed around a mean μ, and standard deviation σ:

$$\sigma' = \frac{\sigma}{\mu} \tag{6.1}$$

Equation (6.1) has also been regarded as the Relative Standard Deviation (RSD) of each repeated tests in terms of the nominal test. Because a minimum of 1000 random waves are generated in this experiment, it is essential to inspect the repeatability of the tests. It can be achieved by examining the wave parameters and the overall wave overtopping captured during the test. Based on FFT, from the inputted wave spectra, an infinite number of random wave elevations can be produced from these sets. Whenever waves are generated with the HR Daq software, a random seeding number is generated and assigned to the collection of observation. The number keeps track of all different wave sequences generated.

Table 6.4 Repeated observations captured at different wave gauge positions for a wave case with H_{m0} = 0.125 metres

Location (m)	**Set 1 (m)**	**Set 2 (m)**	**Set 3 (m)**
0	0.128	0.127	0.128
3.075	0.128	0.127	0.128
6.15	0.128	0.128	0.128
9.225	0.128	0.127	0.128
12.3	0.128	0.128	0.127
15.375	0.128	0.127	0.127
18.45	0.128	0.128	0.129
21.525	0.14	0.139	0.135
24.6	0	0	0

For a repeatable wave sequence, the seeding number must be applied while specifying waves. Inputting another seeding number will create a new set of wave sequences even if the spectral characteristics of the waves are the same. The same random numbers are maintained while conducting all these experiments.

During this study, using each of the slopes, three random repeated tests were carried out to ascertain the repeatability of random waves within the system across three slopes. Tables 6.3 and 6.4 shows example of the repeated wave height captured at different wave gauges across the flume. Recorded wave height values are precise and accurate.

Table 6.5 An example of the coefficient of variations obtained for overtopping and H_{m0} for the repeated observations captured for different sets of observations

Parameter Measured	**Set 1** σ' **(%)**	**Set 2** σ' **(%)**	**Set 3** σ' **(%)**
$q(l/s/m)$	22.3	24.1	20.6
H_{m0}	3.28	3.22	2.14

Repeatability of wave height evolution across different wave gauges in the domain are represented. This is presented in Figure 6.9. H_{m0} of 0.125 metres were very well described across the wave gauges in the deep-water zones. Moreover as shown in the Figure, patterns of wave shoaling across the and the wave breaking are repeatedly well represented by the three sets of observation.

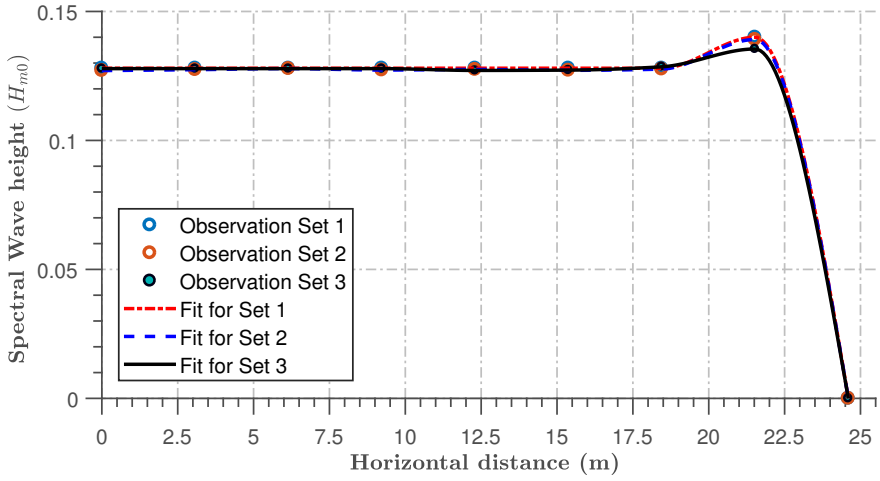

Figure 6.9 *Performance of repeated wave heights captured at different wave gauge positions during the experiment for* $H_{m0} = 0.125$ *metres with* $\cot\alpha = 3.0$*, and 75 % swell*

Table 6.6 Summary of the slope angle cot α, observation average μ, standard deviation σ and CV σ' for the same sets of observations with $H_{m0} = 0.125$ *metres* and 75% swell

Slope Angle	**Parameter Measured**	μ	σ	σ' (%)
$cot\alpha = 3.0$	$q(l/s/m)$	0.000832	0.000041	4.93
	H_{m0}	0.121	0.0066	1.82
	$\frac{q}{\sqrt{gH_{m0}^3}}$	0.00631	0.0613	9.71
$cot\alpha = 1.5$	$q(l/s/m)$	0.000562	0.000033	5.87
	H_{m0}	0.116	0.001	0.86
	$\frac{q}{\sqrt{gH_{m0}^3}}$	0.0045	0.0143	3.15
$cot\alpha = 0.0$	$q(l/s/m)$	0.000172	0.000019	11.05
	H_{m0}	0.112	0.0005	0.45
	$\frac{q}{\sqrt{gH_{m0}^3}}$	0.00147	0.0096	6.55

Full summaries of repeatability tests conducted in this study are shown in Table 6.6. Three sets of data were repeatedly observed across the three slopes for $H_{m0} = 0.125$ *metres* and 75% swell. It can be observed that the there is a minimal variation observed between different sets of the CV σ' obtained across slopes. As shown in Table 6.6, it is expected that the CV σ' values measured for the overtopping should be higher than for observed H_{m0}. It is because there are more uncertainties associated with the overtopping estimation than the H_{m0} derived from the wave elevations recorded by wave gauges. Lesser values of variations are observed in the present study than ones recorded by Kortenhaus et al. (2005).

6.3.3 Wave Breaking and Overtopping Events

In this section, examples of snapshots of waves interacting with coastal structures, obtained from this overtopping experiment are presented (Figures 6.10, 6.11, & 6.12). These figures demonstrate different wave breaking patterns. In Figure 6.12(b), wave breaking accompanied a wave overtopping event. Conversely, photographs in Figures 6.10a and 6.10b, show the the seawall dissipating the wave energy, and so there is not sufficient energy for wave overtopping to occur. The wave propagating pattern shown in the figure is hypothetical of a unimodal sea states with less energy. As the wave energy builds up over time, the flow becomes more turbulent This in turn yields progressively higher wave surges, overtopping the seawall (Figure 6.12).

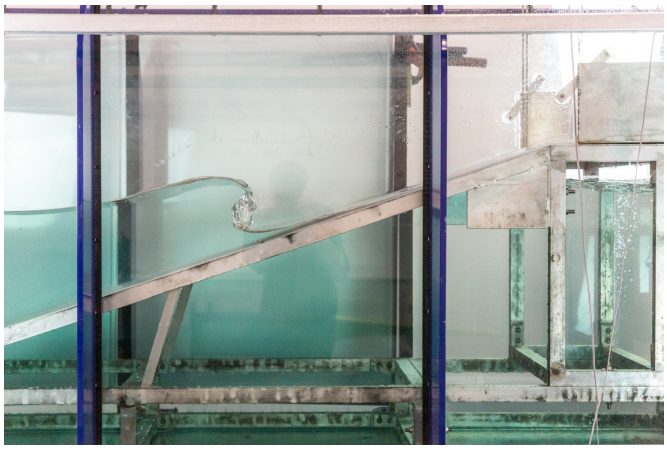

(a)

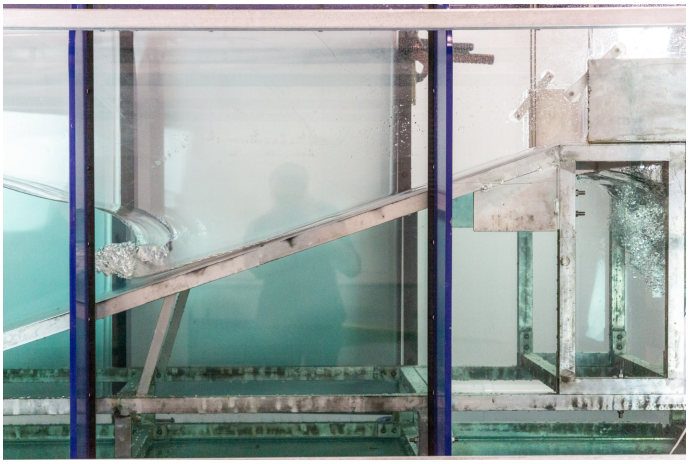

(b)

Figure 6.10 *Snapshots from the experimental test showing: some wave breaking events at the seawall without wave overtopping by a wave with H_{m0} = 0.1 metres at a water depth 0.5 metres approaching a slope with* $\cot\alpha = 3.0$

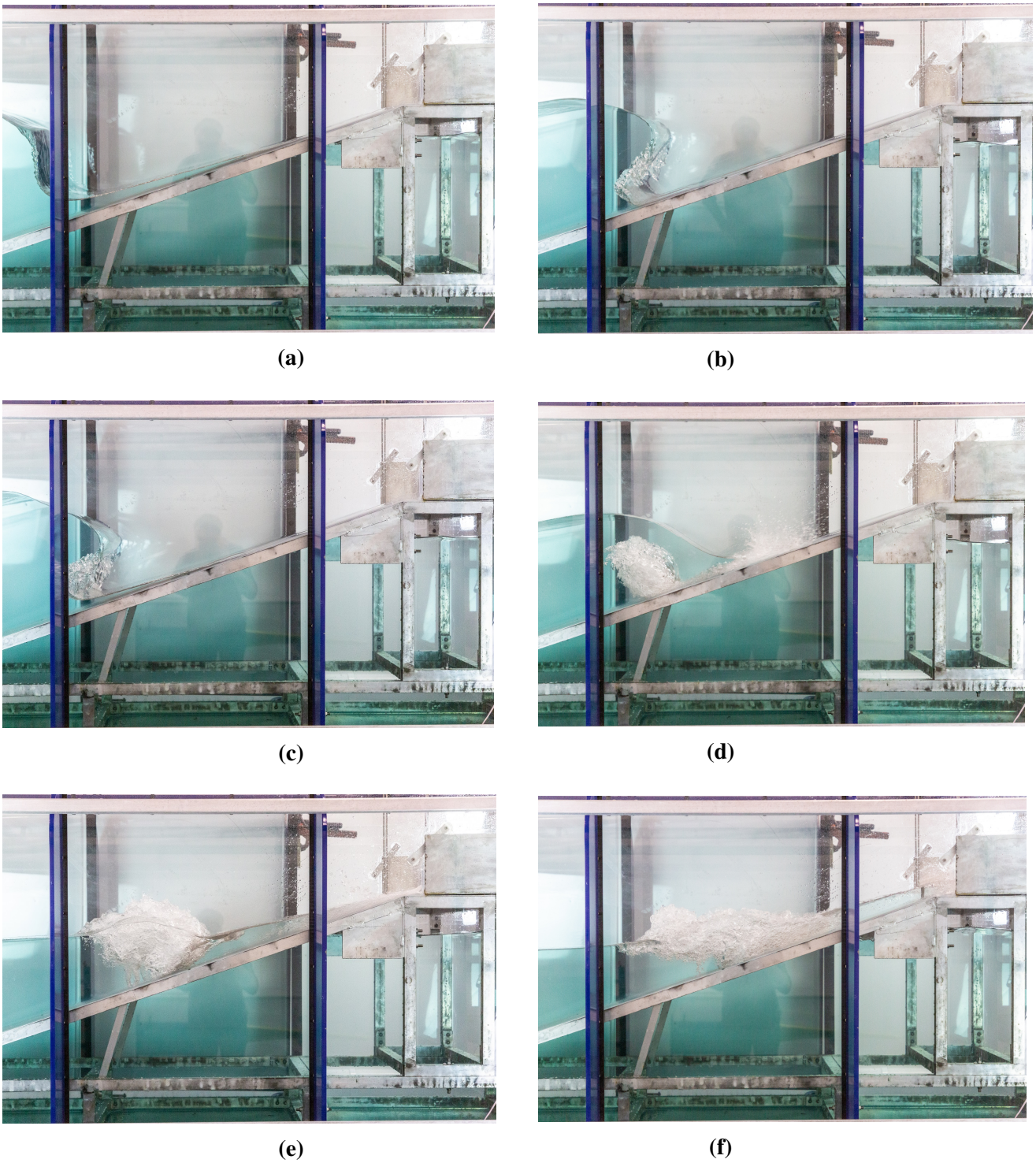

(a) **(b)** **(c)** **(d)** **(e)** **(f)**

Figure 6.11 *Snapshots from the experimental test showing some wave breaking events at the seawall with fewer wave overtopping events by a wave with H_{m0} = 0.1 metres at a water depth 0.58 metres approaching a slope with* $\cot\alpha = 3.0$

As soon as more progressive waves are involved in this process, due to increasing swell, the wave overtops the crest of the structure straightforwardly, without breaking

(Figure 6.12). This occurs because the forward thrust of the wave enhances more overtopping. At the time these experiments were conducted wave overtopping, caused by breaking waves, was not considered. As such formulations for non-breaking waves have been applied to each case retrospectively.

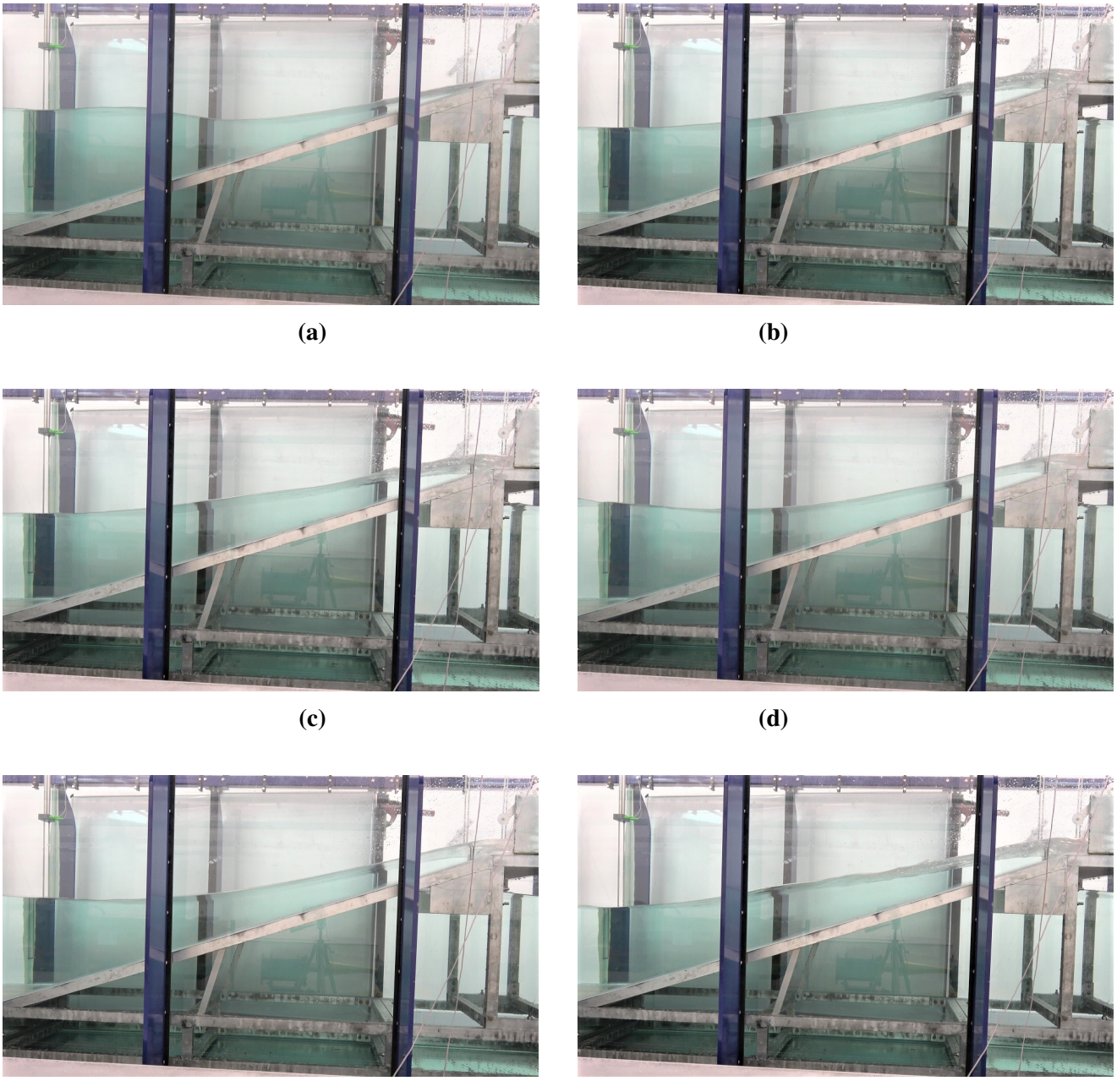

(a) **(b)**

(c) **(d)**

(e) **(f)**

Figure 6.12 *Snapshots from the experimental test showing: wave overtopping from non-breaking waves by a wave with H_{m0} = 0.1 metres at a water depth 0.6 metres approaching a slope with* $cot\alpha = 3.0$

6.4 Non-dimensional Wave Overtopping

Figure 6.13 shows the combined results of all conducted tests. As such, it depicts wave overtopping, caused by non-breaking waves, on three sloped seawalls. These estimates are derived using the EurOtop (2018) overtopping formula (Equation (2.4)). Coefficients A and B applied in Equation (2.4), also change with individual slopes using Equations (2.5) and (2.6) for the non-breaking wave cases.

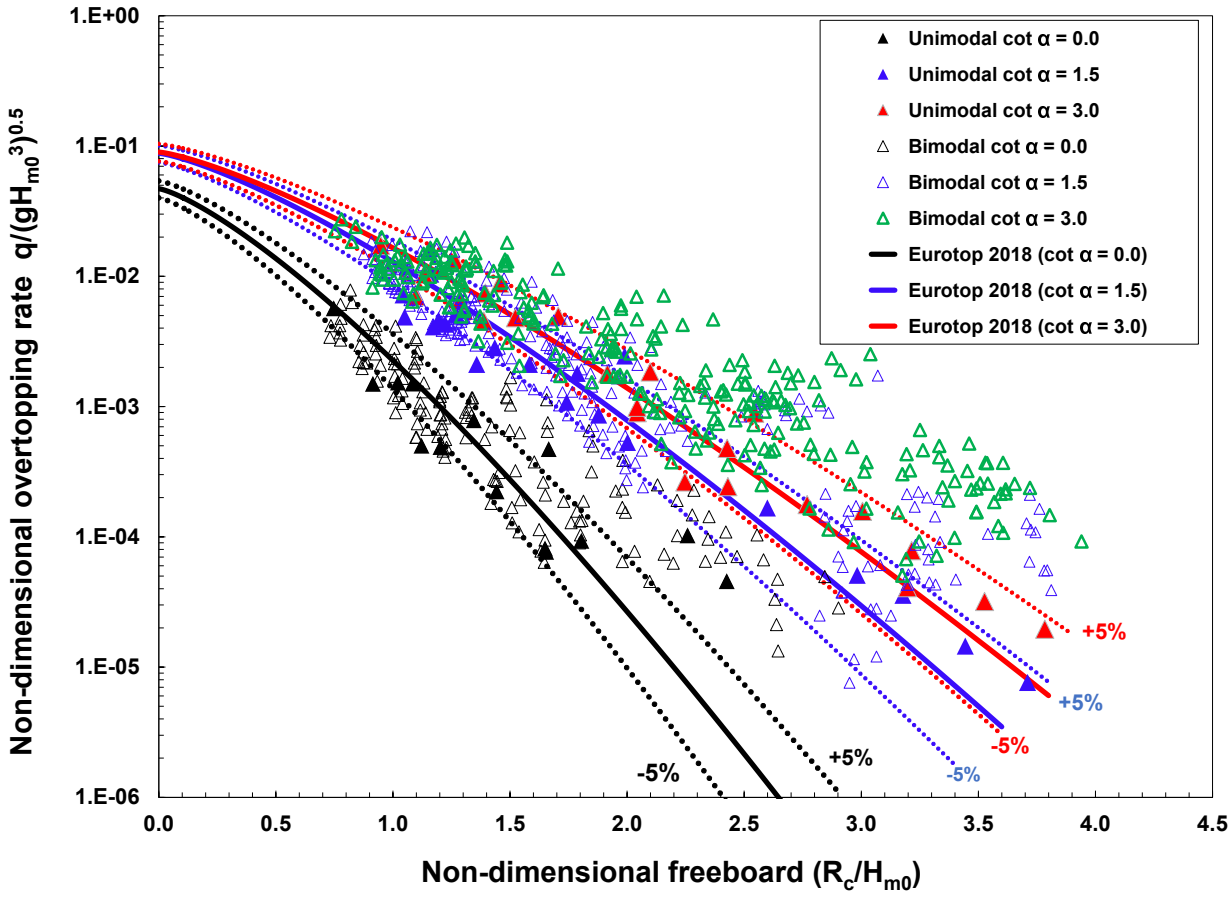

Figure 6.13 *Non-dimensional average overtopping rate* $\frac{q}{\sqrt{H_{m0}^3}}$ *against relative crest freeboard* $\frac{R_c}{H_{m0}}$ *for all tests captured for both unimodal and bimodal sea states across slopes with cot* $\alpha = 0.0$*, cot* $\alpha = 1.5$ *and cot* $\alpha = 3.0$

6.4.1 Bimodal Wave Overtopping of Sloping Seawalls

For clarity, a replotted version of Figure 6.13 for sloping seawalls has been reproduced as Figures 6.14 and 6.15. The predicted overtopping and corresponding 90 % confidence limits of EurOTop (2018), for both unimodal and bimodal cases, are presented in each

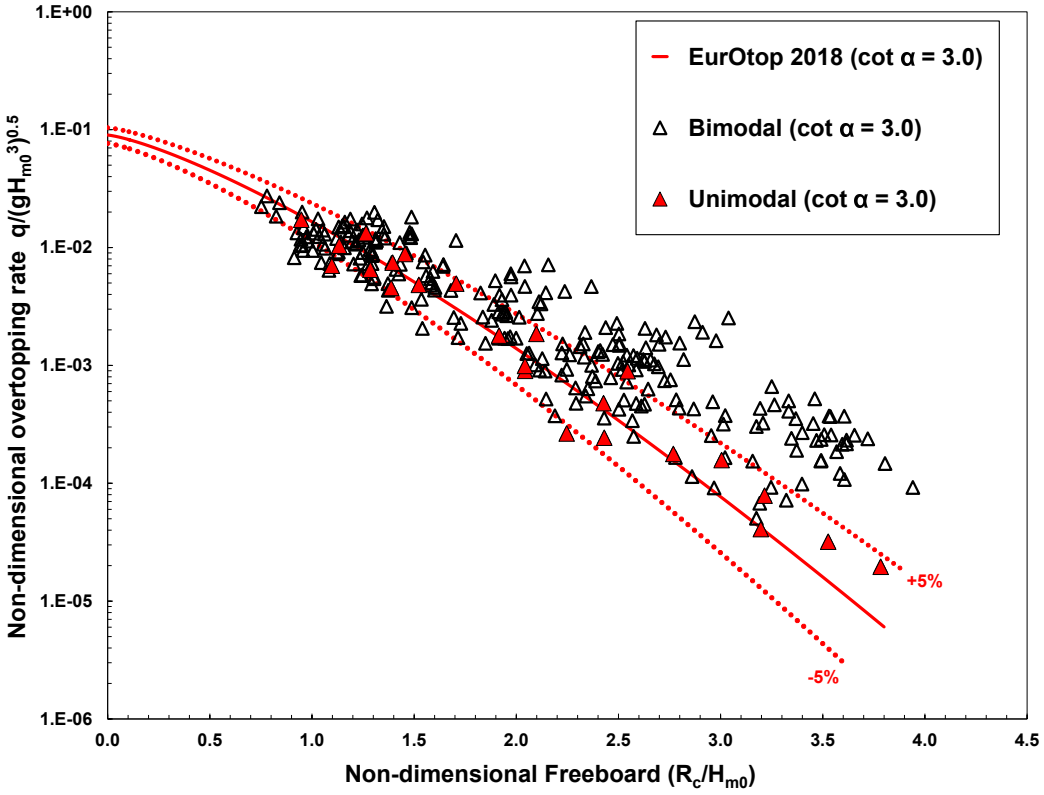

Figure 6.14 *Results of non-dimensional overtopping rate* $\frac{q}{\sqrt{H_{m0}^3}}$ *against non-dimensional crest freeboard* $\frac{R_c}{H_{m0}}$ *plotted within the corresponding prediction band of EurOTop (2018) obtained for a sloping seawall with cot* $\alpha = 3.0$.

plot. Figure 6.14 represents a gentle seawall slope (cot $\alpha = 3.0$), and Figure 6.15, a steeper seawall slope (cot $\alpha = 1.5$). Different coefficients A, and B corresponding to individual slopes were obtained from Equations (2.5) and (2.6) for non-breaking overtopping cases. These were also applied to predict the confidence limits. As is visible from these results, the majority of non-dimensional wave overtopping results observed for unimodal cases fitted very well within the prediction and uncertainty intervals from the EurOtop (2018) non-breaking overtopping prediction formula that corresponds to individual slopes.

Using the conventional 90 percent prediction band in the figures, a large number of bimodal cases lie outside these intervals, especially for larger dimensionless freeboard (Figures 6.14 and 6.15), and are largely underpredicted by the EurOtop (2018) formula.

In Figures 6.14 and 6.15, the overtopping for bimodal waves spreads beyond the confidence intervals and is more pronounced for values of $Rc/Hm0 > 2.0$. There seems to be more scatter at lower $Rc/Hm0$ for bimodal sea cases than in the unimodal results.

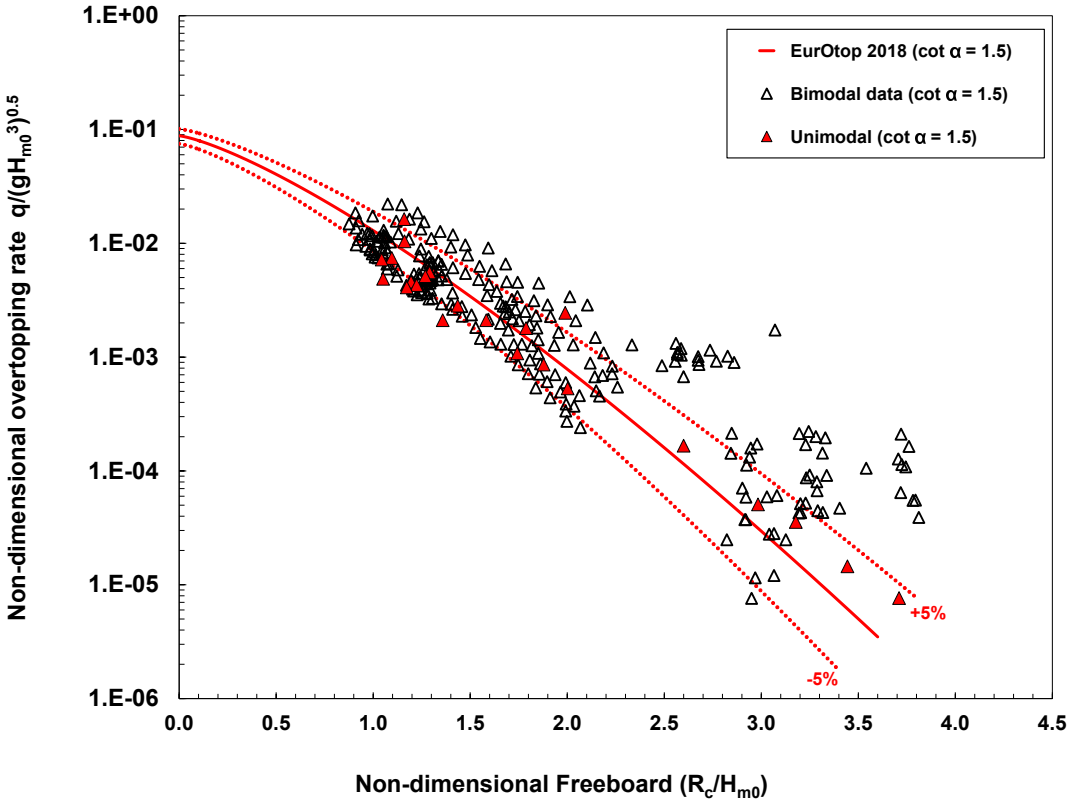

Figure 6.15 *Results of non-dimensional overtopping rate* $\frac{q}{\sqrt{H_{m0}^3}}$ *against non-dimensional crest freeboard* $\frac{R_c}{H_{m0}}$ *plotted within the corresponding prediction band of EurOTop (2018) obtained for a sloping seawall with cot* $\alpha = 1.5$

Victor and Troch (2012) suggested that for unimodal seas, the scatter values could be due to the influence of wave periods of the tested wave conditions. However, for bimodal seas, the scatter effects due to wave periods are more significant. The effect seems to be more significant in terms of overtopping for larger crest freeboards for steeper wall slope (see Figure 6.16 in the next section) than for milder wall slopes with cot $\alpha = 3.0$ (Figure 6.14).

6.4.2 Wave Overtopping of Vertical Seawalls

Results for the vertical seawall are presented in Figure 6.16 for both unimodal and bimodal sea conditions. In all the tests considered in this study, the wave overtopping discriminator for a vertical seawall $h*$ recommended in EurOtop (2018) was applied. With this assessment, all our experiments may be categorised as simple vertical walls, with influencing foreshore, under non-impulsive conditions (i.e., $h^2/H_{m0}.L_{m-1,0} > 0.23$). A similar expression to Equations (2.5) and (2.6) was applied for both unimodal and

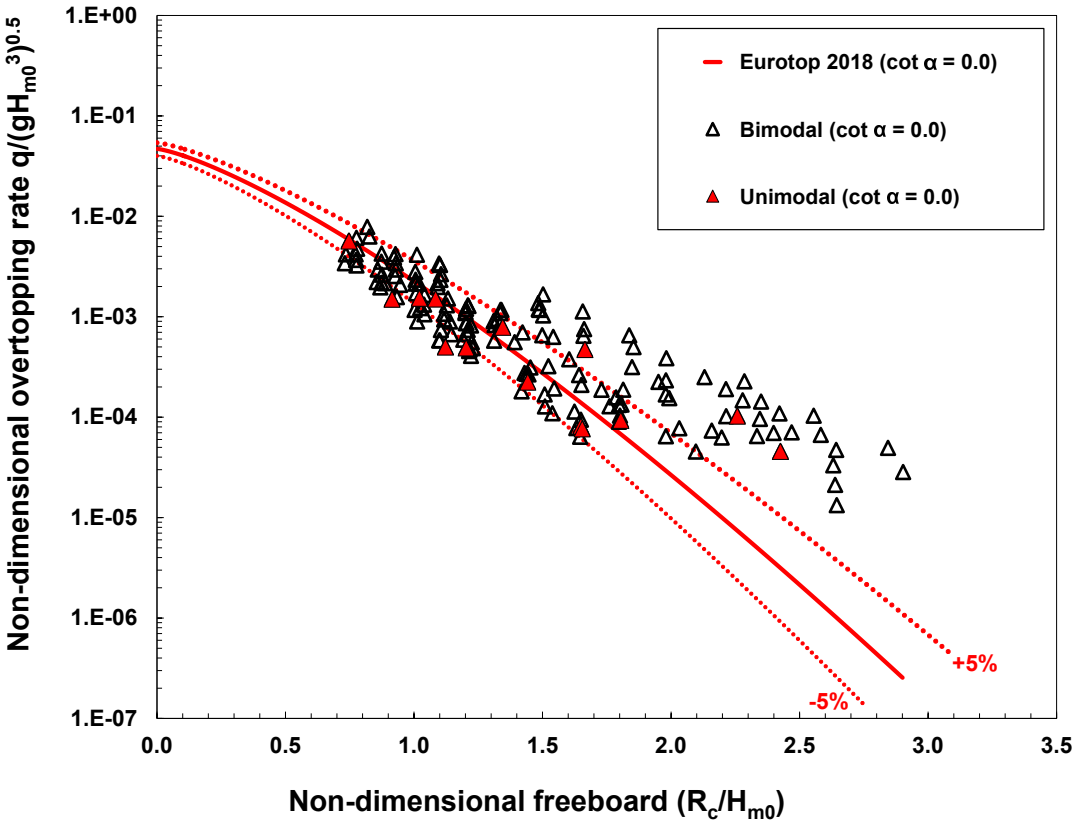

Figure 6.16 *Results of non-dimensional overtopping rate* $\frac{q}{\sqrt{H_{m0}^3}}$ *against non-dimensional crest freeboard* $\frac{R_c}{H_{m0}}$ *plotted within the corresponding prediction band of EurOTop (2018) obtained for a vertical seawall with cot* $\alpha = 0.0$

bimodal conditions. As described in Figures 6.14 and 6.15, the 5 percent lower and upper confidence limits have been plotted, unimodal sea results are shown as red shaded triangles while bimodal seas are represented by black triangles. As can be seen from Figure 6.16, sets of predicted unimodal results are mostly within the 90 % confidence limits of the EurOtop (2018) model. As with the sloping walls most of the results for bimodal seas are outside the confidence limits. Although it is evident from Figure 6.16 that overtopping under both unimodal and bimodal waves were very well reduced by the vertical seawalls, they are less effective at dissipating wave energy than smooth, sloping seawalls (Neelamani and Sandhya, 2003; Van Gent, 1994) presented by Figure 6.14. In this case, more standing waves are created, which reflects waves in a seaward direction with less chance of overtopping the crest.

6.5 Assessment of Prediction Accuracy

It is informative to quantify the accuracy of the predictions provided by the EurOtop formulations, as presented in Figures 6.13 – 6.16. In this section, the root mean square errors RMSE and the bias of the errors BE are both applied to assess the accuracy provided by the EurOtop (2018) as presented in Equations (2.4) – (2.6). The RMSE can be generally represented as:

$$RMSE = \sqrt{\frac{1}{N_t} * \sum_{n=1}^{N_t} \left[q^*_{pred} - q^*_{measured} \right]^2} \tag{6.2}$$

where n is test identifier, N_t is the total number of tests under consideration, q^*_{pred} is the predicted dimensionless overtopping, and $q^*_{measured}$ is the measured dimensionless overtopping value. The bias of the measurement can be defined in terms of the average of the overall dispersion of individual values of q^*_{pred} and the $q^*_{measured}$:

$$BIASError = \frac{1}{N_t} * \sum_{n=1}^{N_t} \left[q^*_{pred} - q^*_{measured} \right] \tag{6.3}$$

With the bias estimates of the results, it is easier to describe both overprediction patterns (when bias is positive) and under-predictions (negative bias values).

By combining predicted values from Equations (2.4) – (2.6) with Equations (6.2) – (6.3) using observed experimental datasets across the three slopes, the accuracy assessment by RMSE and Bias are shown in Table 6.7. It is evident in this table that the unimodal datasets are very well predicted in terms of the RMSE and Bias values using the EurOtop (2018) formulations. As earlier presented in previous figures for bimodal datasets, the RMSE and bias values are not very well predicted.

Table 6.7 Values computed for *RMSE* (Equation (6.2)) and bias (Equations 6.3) by assessing the EurOtop Equation (2.4) for different ranges of relative crest freeboard $R_c = H_{m0}$ and slope angles

Formulation	**Equations (2.4) – (2.6)**	
Tested Cases	**RMSE (-)**	**Bias (-)**
All tests (cot α = 3.0)	0.00365	–7.46 x 10^{-6}
Unimodal	0.00284	8.83 x 10^{-4}
Bimodal	0.00463	– 7.41 x 10^{-5}
All tests (cot α = 1.5)	0.00336	– 1.69 x 10^{-3}
Unimodal	0.00191	1.36 x 10^{-4}
Bimodal	0.00304	– 5.18 x 10^{-4}
All tests (cot α = 0.0)	0.00972	–3.84 x 10^{-4}
Unimodal	0.00103	5.80 x 10^{-4}
Bimodal	0.00967	–3.65 x 10^{-4}

The least bias values as indicated by the vertical seawall (cot $\alpha = 0.0$) in present study. It may be due to the accuracy of Equations (2.4)–(2.6) at predicting the overtopping of simple vertical walls, with influencing foreshore, under non-impulsive conditions (i.e., $h^2/H_{m0}.L_{m-1,0} > 0.23$).

6.6 Influence of Shallow Water Conditions on Non-Breaking Wave Overtopping

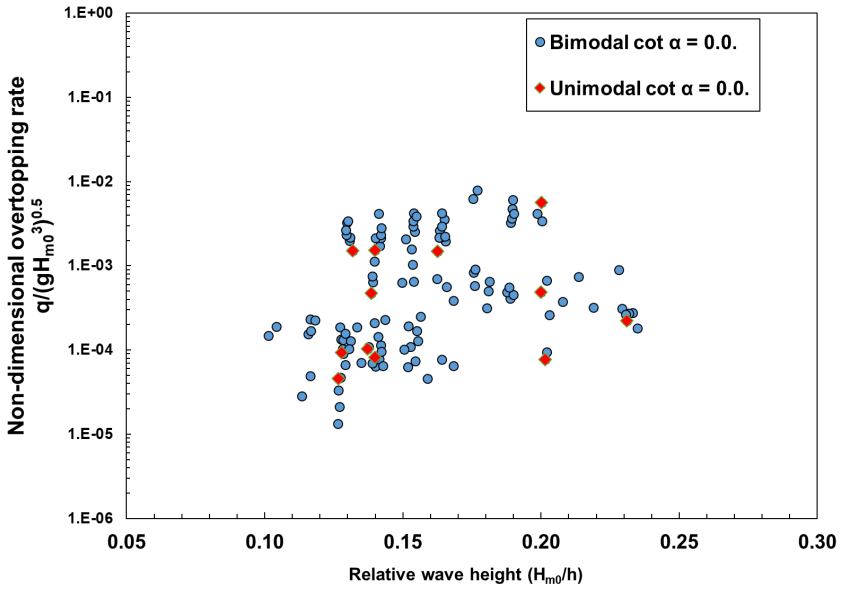

Figure 6.17 *The relationship between the non-dimensional overtopping rate* $\frac{q}{\sqrt{H_{m0}^3}}$ *against the relative wave height* H_{m0}/h *for the dataset of cot* $\alpha = 0.0$

The influence of the relative wave height on the dimensionless wave overtopping across the two slopes for both unimodal and bimodal cases are each presented in Figure 6.17 (for cot $\alpha = 0.0$), Figure 6.18 (for cot $\alpha = 1.5$), and Figure 6.19 (for cot $\alpha = 3.0$). The figures reveal that the majority of the observations fall within what may be categorized as deep-water conditions ($H_{m0}/h \leq 0.2$) as anticipated for non-breaking waves that are studied in this thesis. The shallow water effects can be described in terms of this ratio. This ratio is also useful in describing the water depth condition within different test groups Orimoloye et al. (2019a). As previously observed in Figures 6.14 and 6.15 that results for the steeper slope, (cot $\alpha = 1.5$), show more scatter than for the milder slope, (cot $\alpha = 3.0$), when the dimensionless freeboard is greater than 2.0 as shown in the figures. In deep-water conditions, no clear trend is observed in these results except for a small increase in the non-dimensional wave overtopping within the range $0.08 \leq H_{m0}/h \leq 0.12$ for the steepest slope (cot $\alpha = 1.5$). Figure 6.18 shows that shallow water effects are less significant for the milder slope (cot $\alpha = 3.0$). Nevertheless, there seems to be an increase in the lower values of the dimensionless wave overtopping with increasing relative wave height conditions (Orimoloye et al. (2019a)).

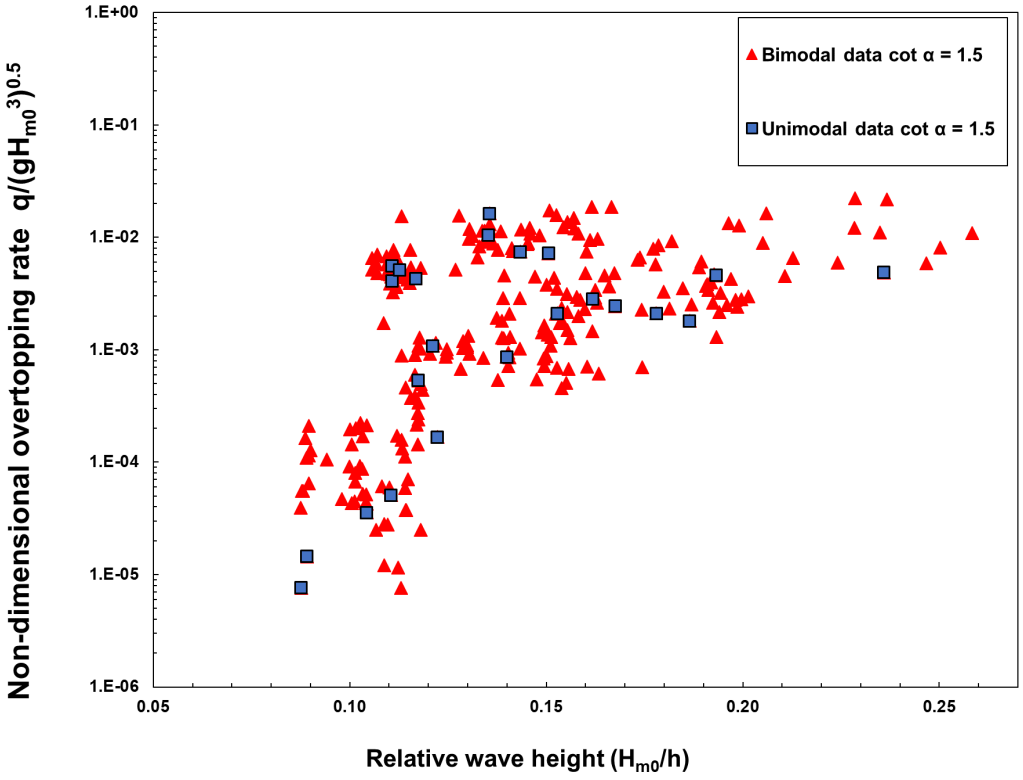

Figure 6.18 *The relationship between the non-dimensional overtopping rate* $\frac{q}{\sqrt{H_{m0}^3}}$ *against the relative wave height* H_{m0}/h *for the dataset of cot* $\alpha = 1.5$

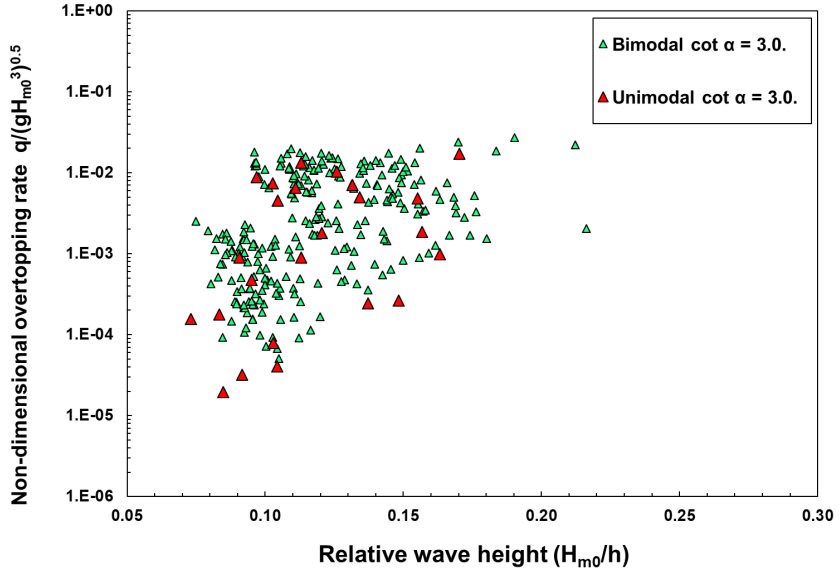

Figure 6.19 *The relationship between the non-dimensional overtopping rate* $\frac{q}{\sqrt{H_{m0}^3}}$ *against the relative wave height* H_{m0}/h *for the dataset of cot* $\alpha = 3.0$

6.7 Conclusion

823 successful wave overtopping tests have been conducted to study the wave overtopping performance of sloping impermeable seawalls under the influence of bimodal sea conditions. Series of bimodal spectra that contain the same energy as the equivalent wind sea have been applied in all the tests. Different percentages of swell components were derived for each sea-state and were evaluated at different peak periods of each of the swell sea. Both unimodal and equivalent bimodal waves were tested. A minimum of 1000 waves were used for each wave condition to obtain the average wave overtopping in each case. For the fixed wave conditions, more wave overtopping was observed with increasing slope mildness, as established in previous studies. The unimodal tests agree closely with predictions using the EurOtop formulae. EurOtop formulae underpredict the observed wave overtopping rates for bimodal conditions, (even when using the $T_{m-1,0}$ period for such cases). Improvement of the EurOtop formulae reflecting effects of presence swell will be presented in Chapter 7.

Chapter 7

Effects of Swell and Spectra Parameters on Wave Overtopping

In this chapter, the experimental datasets obtained from chapter 6 are analysed using the presence of swell waves and spectra characteristics of the bimodal spectra involved. Special attention is placed on the analyses of effects of swell percentages and swell peak periods on overtopping features of coastal seawalls under bimodal sea conditions. Moreover, the effects of spectra shapes imposed by different spectra types were examined using the spectral characteristics of narrowness parameters, broadness parameters and peakedness parameters of each spectra types. Both unimodal and corresponding bimodal waves that have been simulated in Chapter 6 under different slopes and crest freeboards are applied. Until now, wave overtopping equations in the EurOtop (2018) have not specifically include the direct effect of swell percentages under each wave conditions. Because the proportions of swell in the bimodal sea have been varied in each test, it is possible to present the specific influence of swell percentages on overtopping rates. From analysis of the experimental results, a new empirical influencing factor to describe the effects of swell percentages on wave overtopping discharges are presented.

7.1 Spectral Characterisation

To investigate effects of spectral parameters on wave overtopping estimates, surface elevation η recorded by wave gauges from experiments are further inspected and analysed. According to Ochi (2005), each surface elevations can be described as an equivalence of individually statistically independent random variables X_i, which have

the same probability distribution of the form:

$$\eta = X_1 + X_2 + X_3 + ...X_n. \tag{7.1}$$

Also, the general description of the wave spectrum $S(f)$ can be estimated. If according to Goda (2010) we assume $S(f)$ as a major input towards estimating the spectral moments m_n of n^{th} order:

$$mn = \int_0^\infty f^n E(f) \mathrm{d}f. \tag{7.2}$$

In turn, if values of n are defined as -1, 0, 2, and 4 respectively as presented in Reeve et al. (2015), the spectral significant wave height H_{m0} and different spectra periods ($T_{m-1,0}$ & $T_{m0,2}$) can be determined from m_n as:

$$H_{m0} = 4.004\sqrt{m_0} \tag{7.3}$$

where m_0 is the zeroth moment of the spectrum and

$$T_{m-1,0} = \frac{m_{-1}}{m_0} \tag{7.4}$$

The following spectral parameters were also estimated from surface elevations recorded during each test:

1. Peakedness factor

   According to Goda et al. (1975), the grouping of successive wave height can be expressed in terms of its peakedness parameter Q_p with frequency f:

   $$Q_p = \frac{2}{m_0^2} \int_0^\infty E(f) \mathrm{d}f. \tag{7.5}$$

   Bradbury et al. (2007) suggested that values of Q_p increase with the narrowness of the spectrum. Fully developed wind-seas were observed to have values Q_p within the range of 2 while swell seas may possess Q_p of higher values in some cases. Battjes and Groenendijk (2000) verified the correlation κ that was earlier formulated by Kimura (1980). It is the κ coefficient that was based on the first-order Markov's chain. Values of κ can be determined as follows:

   $$\kappa = \frac{1}{m_0} \left| \int_0^\infty E(f) e^{i2\pi f \tau} \mathrm{d}f \right|. \tag{7.6}$$

κ also increases as the spectral bandwidth decreases, and τ denotes the mean time difference between two successive wave crests or troughs. For a well-represented wave spectrum, the peakedness of the wave spectrum would show a high correlation with the wave groupiness parameter λ. The groupiness of individual wave group with angular frequency ω can be determined using an expression suggested by Rychlik et al. (1997a):

$$\lambda = \frac{abs(\int_0^\infty S(f) * exp^{2\pi f \tau} df)}{m_0} \quad and\ \tau\ is\ equivalent\ to\ T_{m02} = \sqrt{\frac{m_0}{m_2}} \tag{7.7}$$

2. Narrowness parameter

   Longuet-Higgins (1983) proposed the Gaussian process of the narrow-banded spectrum. The narrowness parameter v of a sea-state can be defined in terms of the measurement of the distribution of the frequency component in the sea-state. It can be expressed mathematically as:

$$v = \sqrt{\left(\frac{m_2 m_0}{m_1^2} - 1\right)} \tag{7.8}$$

3. Spectral width parameter

   The spectral width parameter or the broadness factor ε of a wave spectrum is essential to describe the frequency band where the wave energy mostly concentrates. As presented by Rychlik et al. (1997a), this could be narrow-banded with $\varepsilon \approx 0$ or broad-banded with $\varepsilon \gg 0$:

$$\varepsilon = \sqrt{\left(1 - \frac{m_2^2}{m_0^2 m_4}\right)} \tag{7.9}$$

4. Quality and irregularity parameters

   In this study, the quality parameter R_s is expressed in terms of the total wave spectrum $S(f)$ while the irregularity factor α_f is extracted using some moment ratio. It is mathematically defined by Rychlik et al. (1997a) as follows:

$$Rs = \frac{S(0.092) + S(0.12) + S(0.15)}{3 * max(S(f))} \qquad also, \alpha_f = \frac{m_2}{\sqrt{m_0 * m_4}} \tag{7.10}$$

7.1.1 Wave transformation

Figure 7.1 describes the wave evolution pattern for both unimodal and bimodal spectral with the same H_{m0} of 0.125 meters propagating across the 1:20 slope interacting with a slope of 1:1.5. After removing the effect of reflection (full details are presented in Chapter 6), wave shoaling and breaking are fully described in the figure. A distance of 0 metres represents the wavemaker position while the waves propagate towards the toe of the structure. The water depth is kept at 0.6 metres at offshore while reduces by the sloping structure to 0.39 metres at the toe. Similar to Lorenzo et al. (2001), the swell percentages greatly influences shoaling and breaking over a short distance. As shown, the expected wave height of 0.125 metres was accurately captured by the wave gauges in both unimodal and bimodal sea conditions. However, effects of shoaling are more significant in the bimodal sea (to a maximum of 0.16 metres for bimodal waves) than in the unimodal sea (which shoals to a maximum of 0.14 metres) just before breaking. As previously described by van der Meer et al. (2016), it is the lower steepness that is responsible for the higher shoaling occurrences in the bimodal seas than observed in unimodal cases.

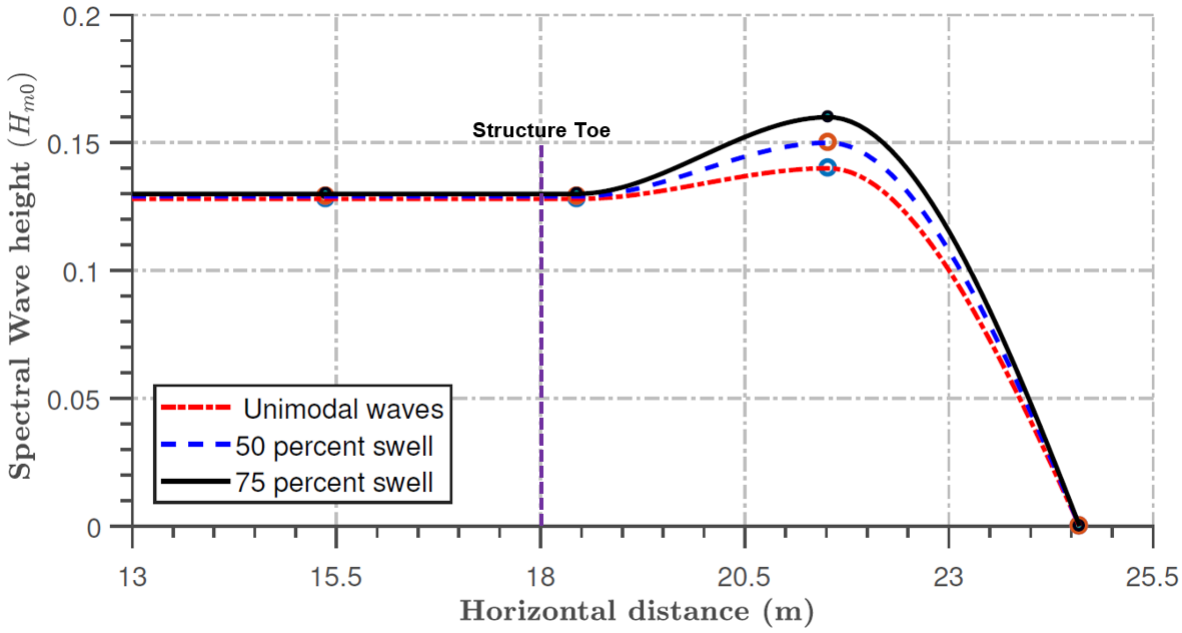

Figure 7.1 *Wave height deformation observed on a foreshore slope of 1:20 at a constant water depth of 0.6 metres for unimodal and bimodal waves*

7.2 Spectral effects on wave overtopping

Spectral characteristics of a sea-state is an essential requirement in describing the severity of the sea. In this section, we describe the complexities of the sea-state in terms of the swell content (percentage) of the sea-state. Firstly, in Figure 7.2, we presented how well the experimental result correlates with different spectra characteristics earlier described.

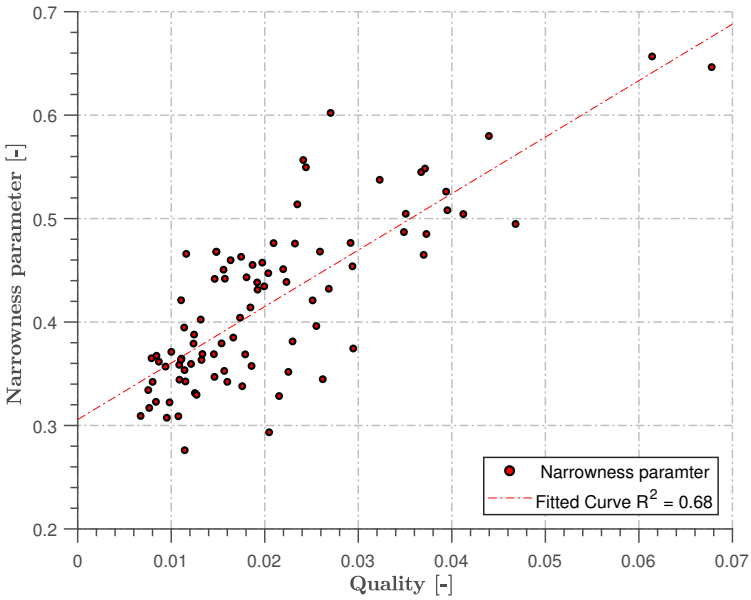

(a)

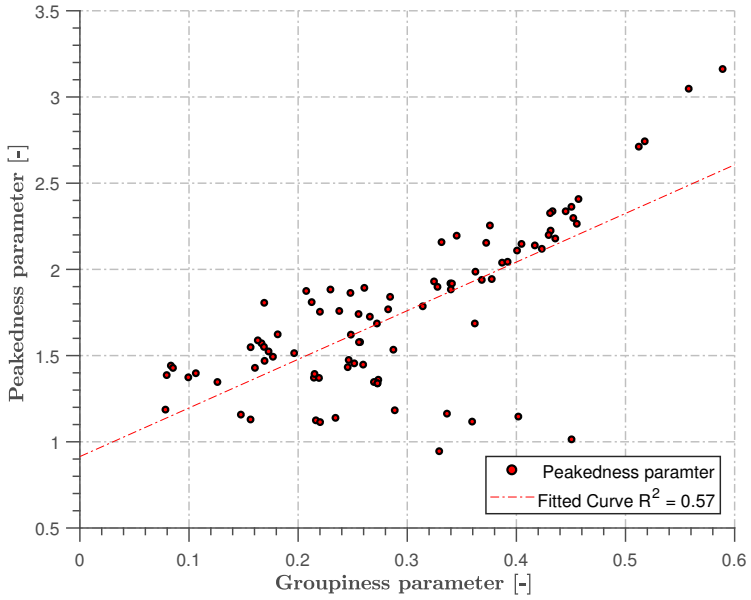

(b)

Figure 7.2 *Performances of shape parameters computed for: (a) narrowness, and (b) peakedness for different bimodal tests obtained from selected datasets*

Altogether, as shown in Figure 7.2, the narrowness and the peakedness parameters of the wave show a positive correlation with wave quality and groupiness parameters respectively. The wave peakedness is well associated with the groupiness parameter of the wave. There are variations in the wave spectral characteristics as shown by the spectra values on the vertical axis.

The peak period at which a swell wave occurs has the potential to alter the characteristics of the resulting bimodal wave. In Figure 7.3, a cross-section of the potential influence of different computed spectral characteristics of swell waves occurring at 11, 20, and 25 secs peak periods, as presented.

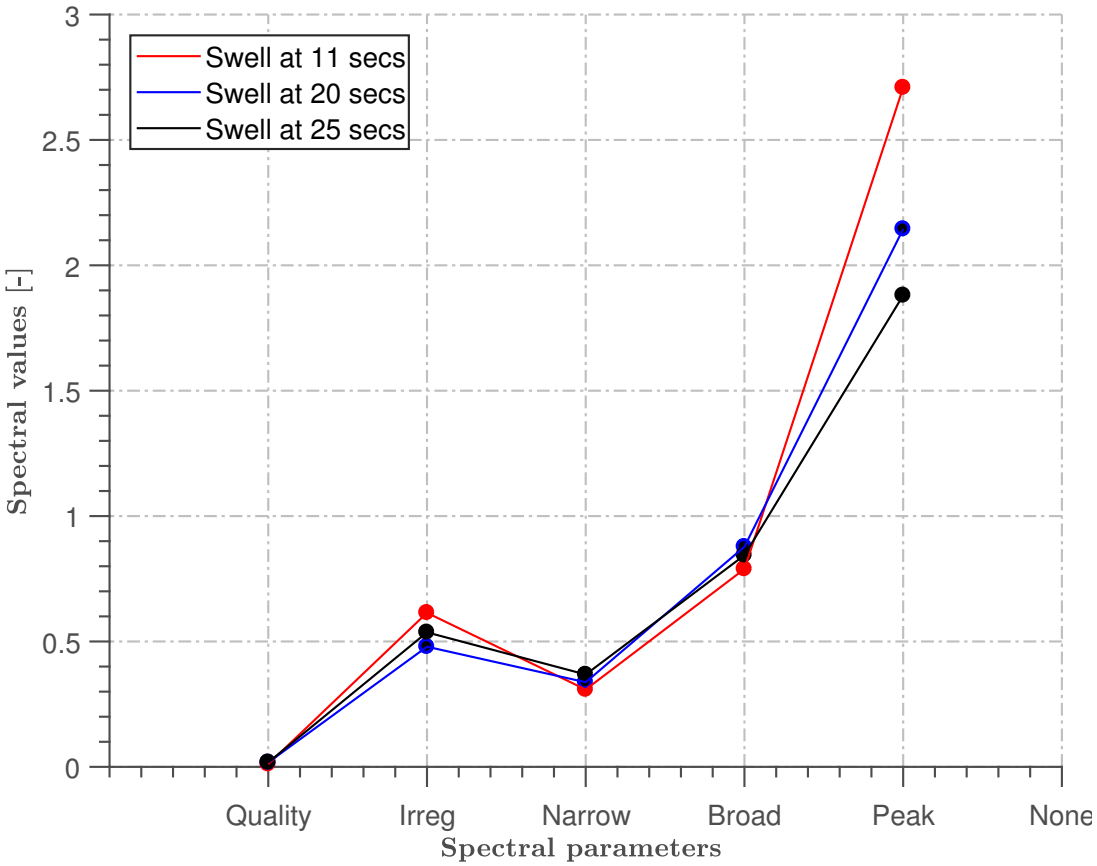

Figure 7.3 *Variations of spectral parameters with swell peak periods in a bimodal sea with H_{m0} = 0.125 metres at a water depth of 0.60 metres.*

Non-Linear behaviour exists in the spectral values portrayed by various spectra aspects. There are no significant observable differences in the broadness and narrowness parameters across swell peak periods. However, more significant variations are observed in spectral irregularities and narrowness parameters that are present in the low period swell (11 secs) than higher ones (20 & 25 secs). It could be due to continuous occurrences of bimodal waves due to a smaller value of wave periods compared to higher

ones. Also, disparities in spectral behaviour is an indication that wave characteristics would be different as the swell in the sea state changes. These observations are similar to the work of Bradbury et al. (2007) where it was suggested that a minimal difference occurs in both narrowness and broadness parameters of different spectral types.

On the other hand, relationships between the rate of wave overtopping and different spectral parameters are presented in Figures 7.4 – 7.6. Overtopping estimates are plotted on the primary axis while other spectral characteristics are plotted on the secondary axis. From the three figures, overtopping rates are increasing with swell percentages while the spectral values reduce for all the three parameters. However, in Figures 7.4 and 7.5, the trends are tending towards asymptotic values as swell percentages increase from 0 to 75 whereas, waves peakedness parameter approaches zero for higher swell percentages (Figure 7.6). These observations, however, suggested that seas that are characterised by low-peaked wave spectrum tend to impose more severe flooding of extensive coastlines than higher-peaked seas. Similarly, less flooding tendencies are expected for broad-banded seas. Overtopping is highly sensitive to the succession of wave groups and wave patterns in the random wave sequence than overtopping caused by individual peaks. The evidence of extreme wave events have been previously observed most especially in Hunt (2003) and Weston et al. (2005).

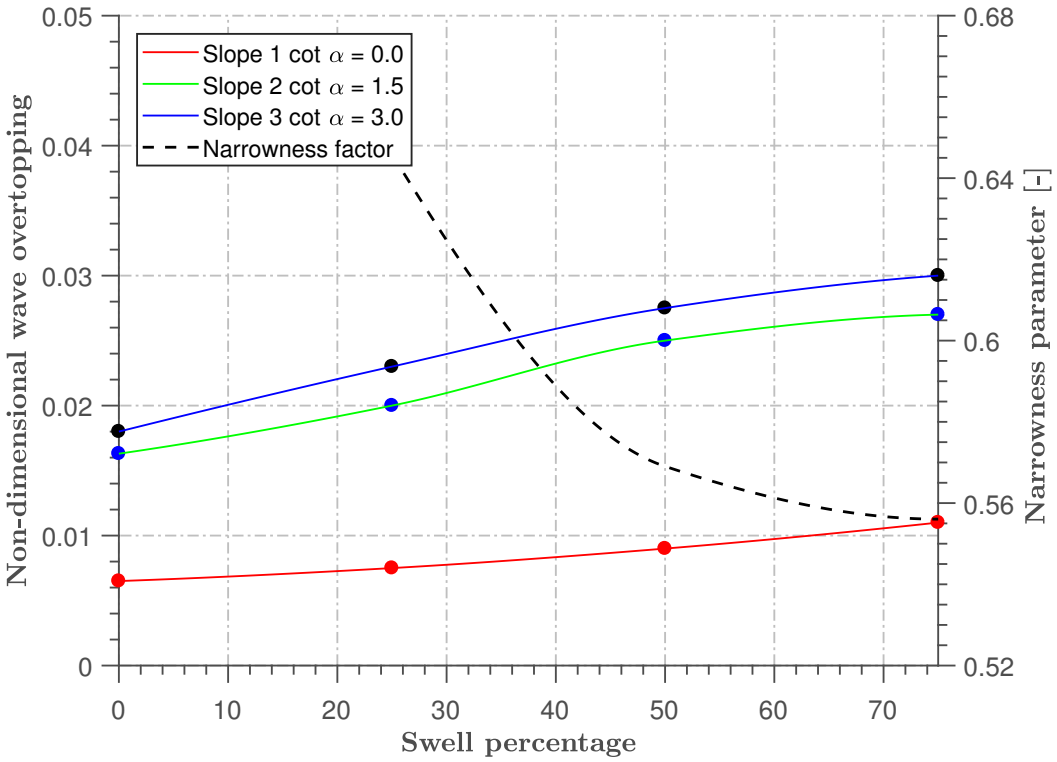

Figure 7.4 *Influences of narrowness parameters on the wave overtopping of sloping seawall under different swell percentages*

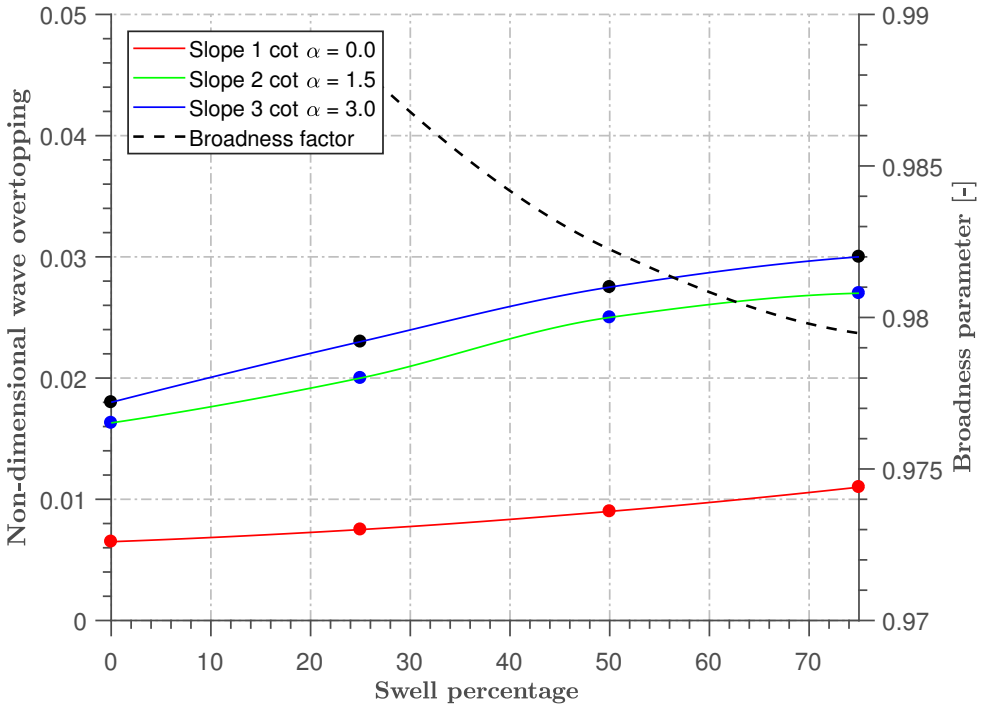

Figure 7.5 *Influences of broadness parameters on the wave overtopping of sloping seawall under different swell percentages*

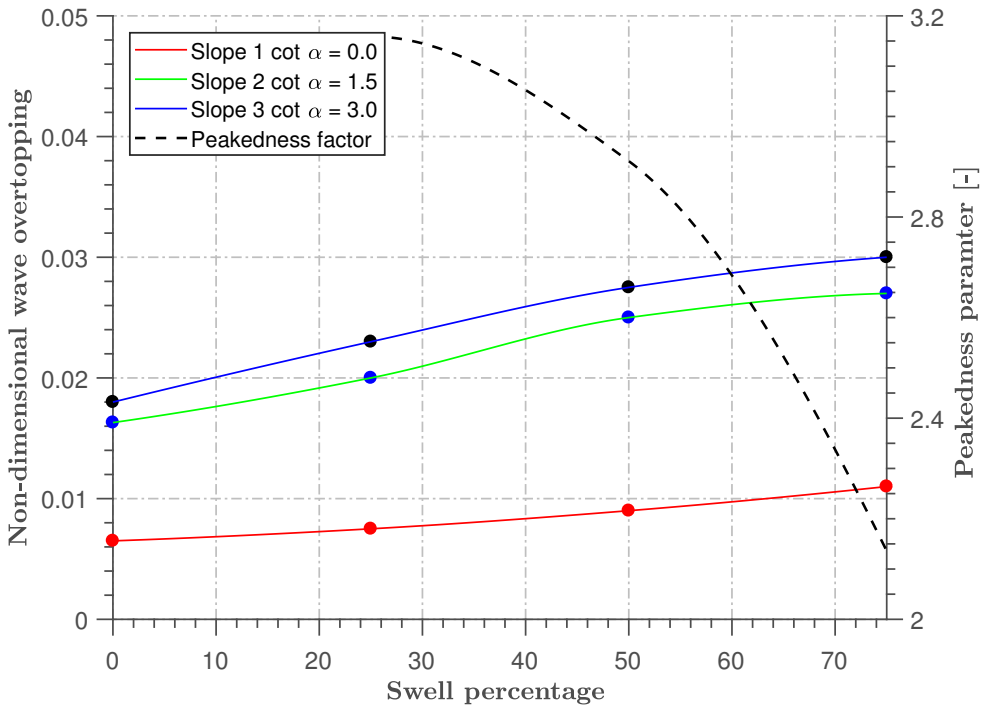

Figure 7.6 *Influences of peakedness parameters on the wave overtopping of sloping seawall under different swell percentages*

7.2.1 Variations of Wave Steepness with Swell Percentages

The wave steepness $S_{m-1,0}$ is an important physical parameter in describing the severity of a sea state. Most especially defining the physical indication of wave breaking for a design of coastal structures. In order to accurately describe both unimodal and bimodal sea states in this study, a wide range of $S_{m-1,0}$ between 0.01 and 0.07 has been tested as calculated from the ratio of wavelength H_{m0} and wavelength $L_{m-1,0}$.

Figures 7.7 – 7.8 show an example of the relationship between wave steepness and different swell components that were applied during this study. As suggested in the EurOtop manual (EurOtop 2018), wave steepness reduced with increasing swell percentage and R^* respectively.

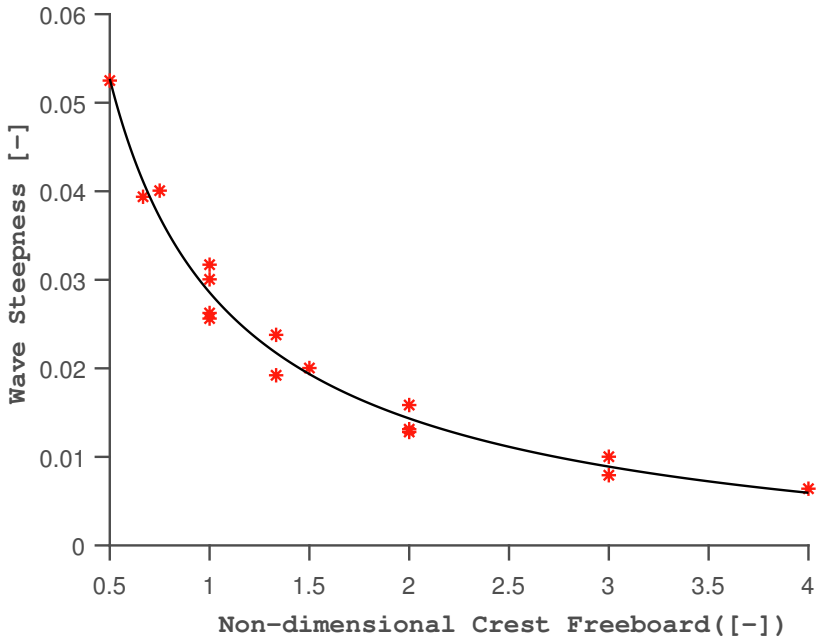

Figure 7.7 *Relationship between tested wave steepness and the R^* with swell percentages in a sea-state with equal energy*

Figure 7.8 shows that the highest presence of swell (at 75 %) gives the smallest wave steepness Figure 7.8b. It is the low wave steepness $S_{m-1,0}$ in the bimodal seas that accounts for the increase in the breaker parameter $\xi_{m-1,0}$ through the relationship of $\xi_{m-1,0} = tan\alpha/S_{m-1,0}$. It is larger values $\xi_{m-1,0}$ that corresponds to surging non-breaking waves that cause more overtopping in bimodal seas.

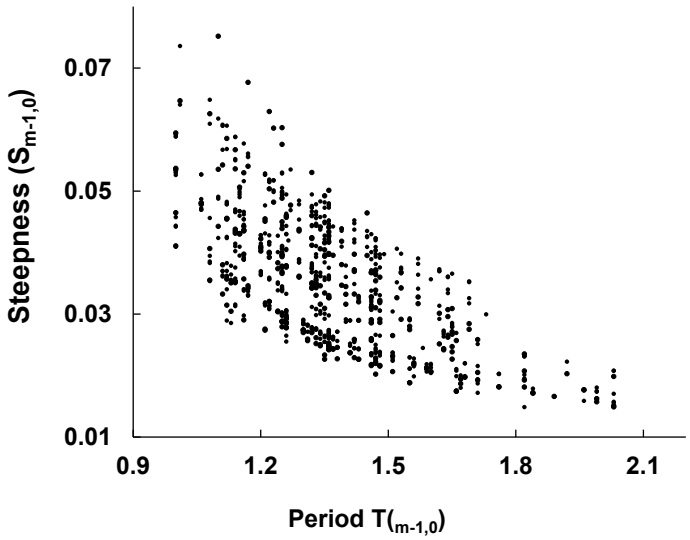

(a)

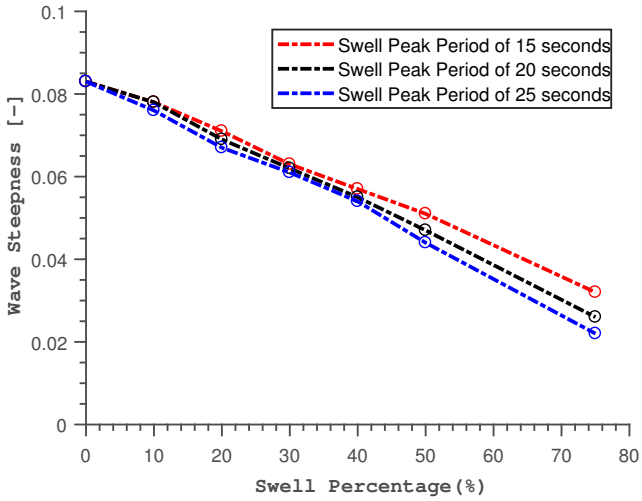

(b)

Figure 7.8 *Variations of wave steepness with (a) spectra peak periods $T_{m-1,0}$ and (b) swell percentages in a sea-state with equal energy*

7.3 Influence of Swell Percentage

In each of the sea states investigated, swell percentages were varied between 0 (unimodal), 25, 50, and 75 percents. Figure 7.8 shows the influence of swell percentage on wave overtopping estimates for all the cases investigated across the three slopes. Figure 7.8 represents the box plots created based on the dimensionless overtopping obtained from the experiments. Within the boxplots are the distributional characteristics as well as the level of the dimensionless overtopping obtained across different groups of swell percentages.

The boxplots describe the minimum (lower whisker) in each group, interquartile range (depicted by the boxes), and the upper whisker of the non-dimensional overtopping groups. To show the patterns of the effects of swell, the dimensionless overtopping are sorted according to the amount of the swell content in the sea state. There is obvious differences between the dimensionless overtopping presented in Figure 7.8. Shorter box plotes are obtained for unimodal cases and 25 percent swell.

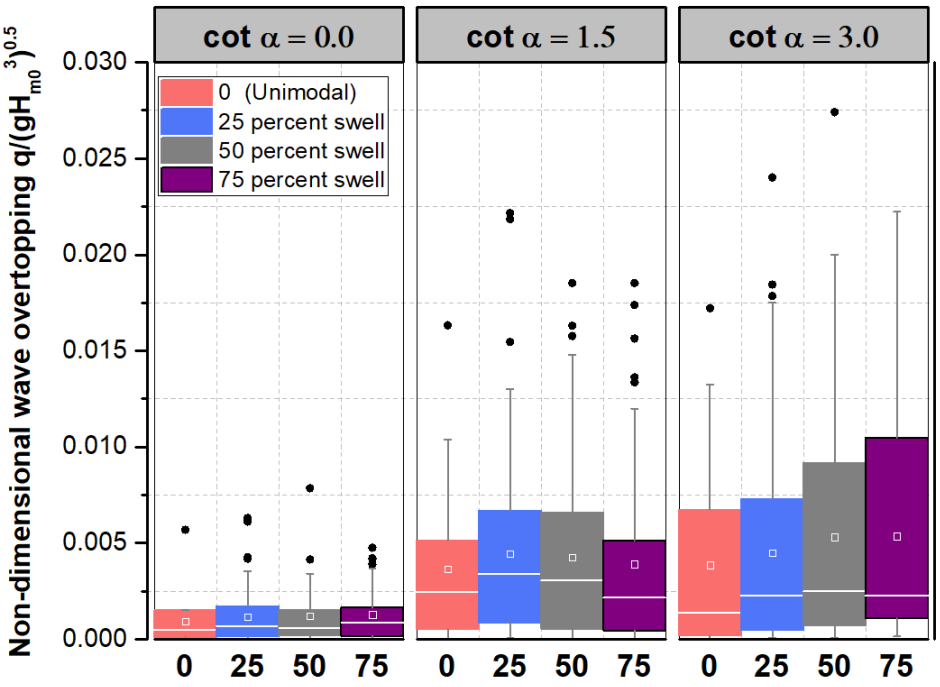

Figure 7.9 *The relationship between the non-dimensional overtopping rate* $\sqrt{H_{m0}^3}$ *with the swell percentages for cot* $\alpha = 0.0$ *and cot* $\alpha = 1.5$ *and cot* $\alpha = 3.0$

As described in Section 7.2, the overtopping is greater for the mildest slope. With further reference to Figure 7.8, as swell percentages increase in the bimodal sea cases, wave steepness reduces, overtopping increases, creating more non-breaking wave overtopping situations presented here in Figure 7.9.

The highest wave overtopping rates were observed for the sloping seawall with cot $\alpha = 3.0$ while compared to the unimodal cases in the absence of swell. There is slight difference in the trend across the slopes. Considering the steeper slope with cot $\alpha = 1.5$, this behaviour does not seem to follow directly as overtopping does not seem to increase monotonically as swell percentage reaches 50 percent. There seems to be a slight reduction in the wave overtopping for the extreme outliers seen in these results. In the case of the vertical seawall with cot $\alpha = 0.0$, the overtopping rate appears fairly insensitive to the swell percentage.

For the unimodal test cases, effects of $Tm-1,0$ on overtopping results are not as significant for non-breaking waves compared to the effects of crest freeboards and slope angles. The observation follows previous conclusions for example, Victor and Troch, (2012), Van Doorslaer et al., (2015) and EurOtop (2018). The influence of $Tm-1,0$ on overtopping are negligible for non-breaking waves. This can also be seen that Tm-1,0 are not included in the expressions for the non-breaking wave cases. However, for the non-breaking bimodal waves, effects of $Tm-1,0$ become more significant. These were not shown in present manuscript because relationship of $Tm-1,0$ with overtopping seem to be affected by combined interactions of swell percentages and the appearances of swell at different peak periods. Details of effect of swell period will be presented in section 7.5.

7.3.1 Modified Overtopping Formula for Swell Percentages

The trends in overtopping with respect to swell percentage suggest the existing formula for overtopping Equations (2.4) – (2.6) might be modified to reflect this influence. Four swell percentages that are considered are 0, 25, 50, and 75 percent, (with 0 percent representing the full wind-sea state). Figures 7.10–7.13 show results obtained by non-linear least squares regression analysis by percentage of swell applied to the observations.

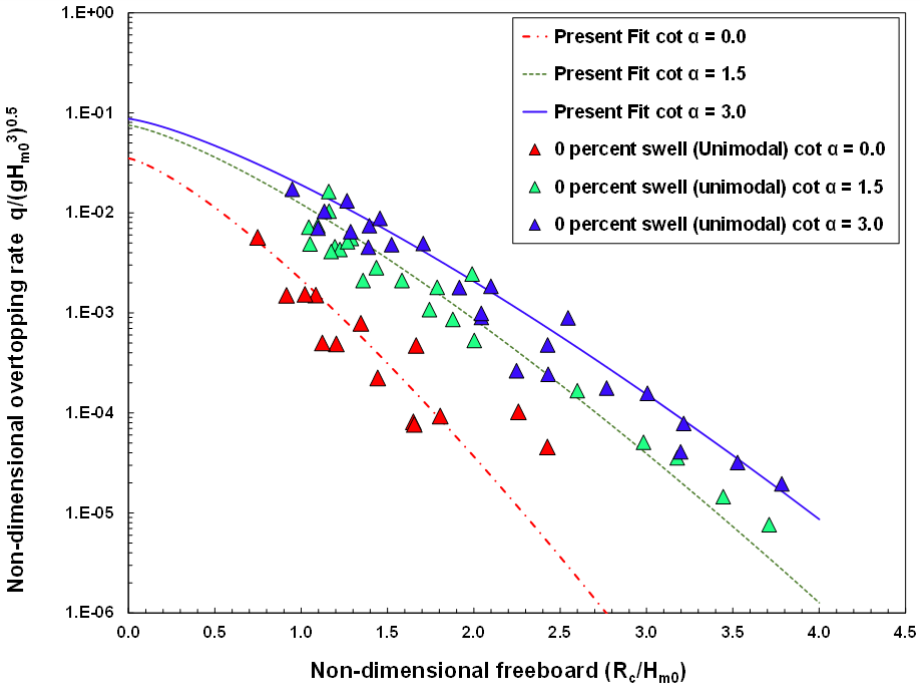

Figure 7.10 *Results of non-linear regression performed on different non-dimensional wave overtopping obtained across three slopes for cot* $\alpha = 0.0$*, cot* $\alpha = 1.5$ *and cot* $\alpha = 3.0$ *for unimodal seas with 0 percent swell*

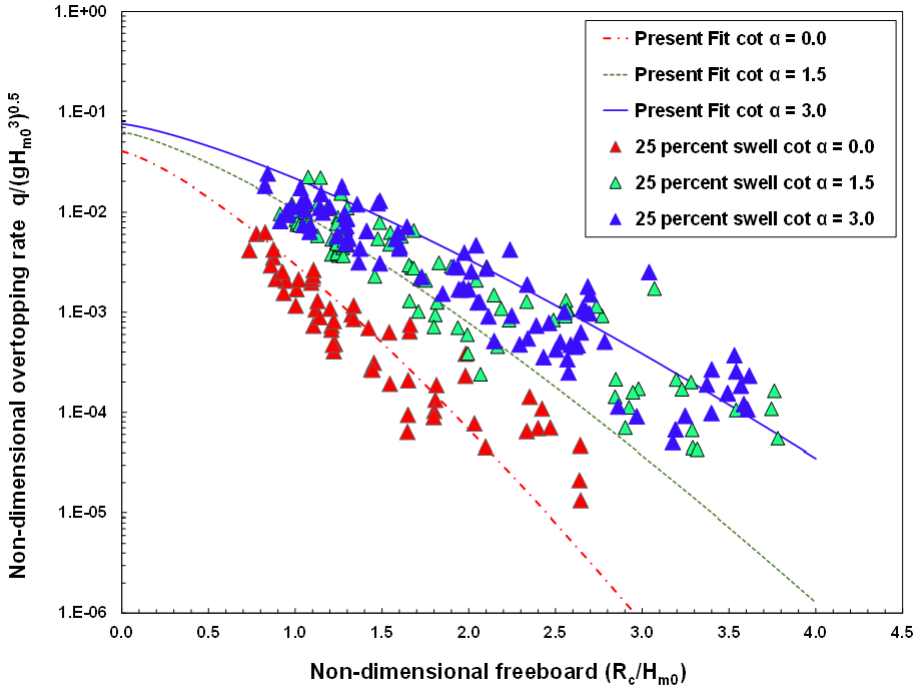

Figure 7.11 *Results of non-linear regression performed on different non-dimensional wave overtopping obtained across three slopes for cot* $\alpha = 0.0$*, cot* $\alpha = 1.5$ *and cot* $\alpha = 3.0$ *for bimodal seas with 25 percent swell*

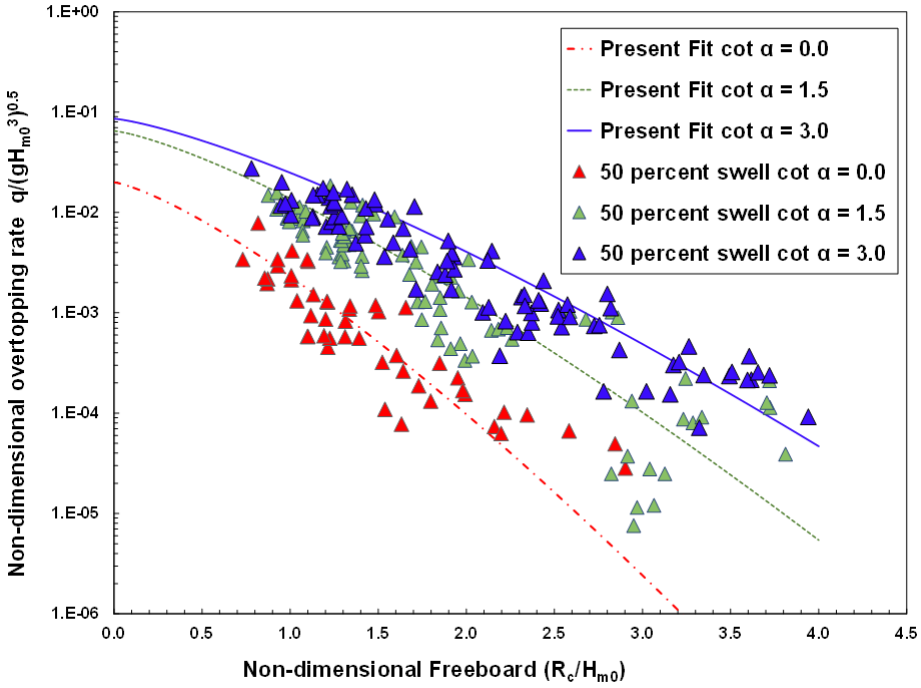

Figure 7.12 *Results of non-linear regression performed on different non-dimensional wave overtopping obtained across three slopes for cot* $\alpha = 0.0$*, cot* $\alpha = 1.5$ *and cot* $\alpha = 3.0$ *for bimodal seas with 50 percent swell*

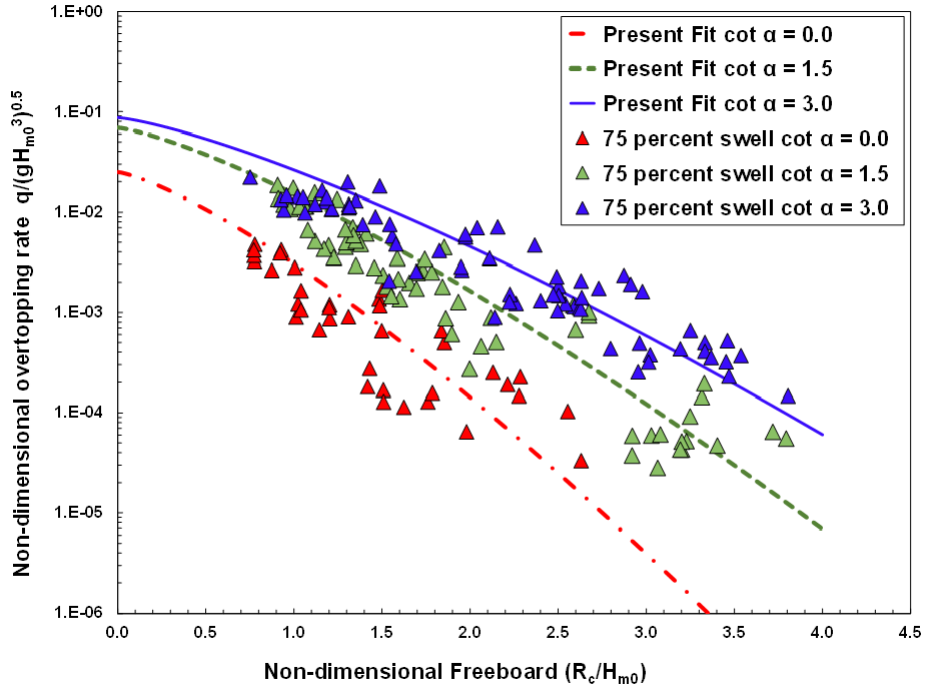

Figure 7.13 *Results of non-linear regression performed on different non-dimensional wave overtopping obtained across three slopes for cot* $\alpha = 0.0$*, cot* $\alpha = 1.5$ *and cot* $\alpha = 3.0$ *for bimodal seas with 75 percent swell*

Figure 7.14 represent plots of the coefficient values of A and B obtained as a result of the non-linear regression fitted on different percentages of swell obtained across different slopes. The fit for coefficient B has little scatter whereas the fits for coefficient A have wider scatter.

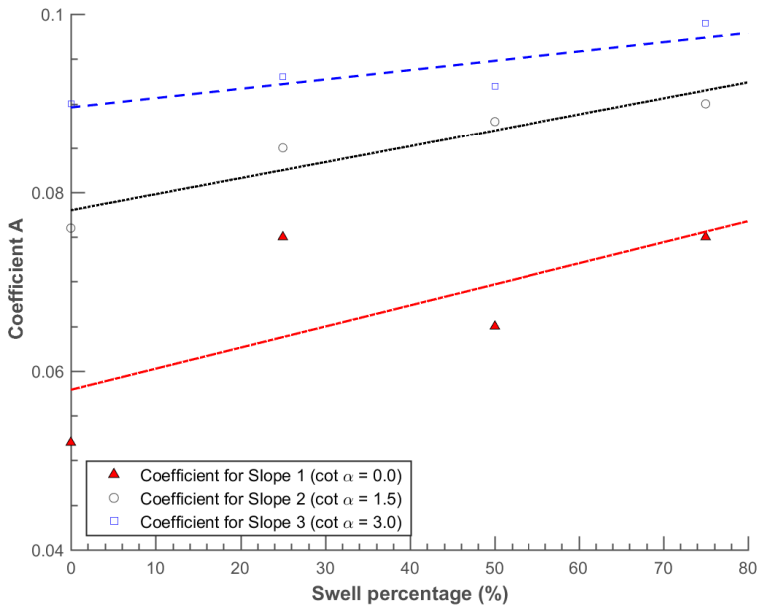

(a)

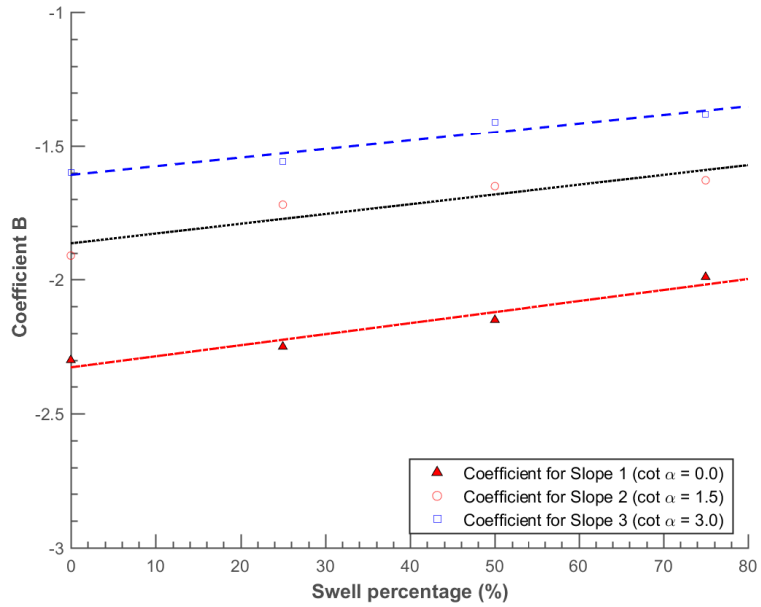

(b)

Figure 7.14 *(a) Coefficient A as a function of swell percentage, varying from 0 to 75 percent, (b) Coefficient B as a function of swell percentage, varying from 0 to 75 percent*

The linear variation of A and B with respect to swell percentage can be expressed as:

$$A_s = A + m_1 S_0 \tag{7.11}$$

$$B_s = B + m_2 S_0 \tag{7.12}$$

where values of A and B follow the same definition provided in EurOtop (2018) for different impermeable sloping seawalls whose values are dependent on structure slope $cot\alpha$. m_1 and m_2 are defined by the slope of the lines in Figure 7.14. A modified version of Equation (2.4) based on the regression against our new observations, which accounts for bimodal conditions may be written as:

$$\frac{q}{\sqrt{gH_{m0}^3}} = A_s * exp\left(-B_s \frac{R_c}{H_{m0}}\right)^{1.3} \tag{7.13}$$

where the values of A_s can be empirically redefined in terms of swell percentage S_0 as:

$$A_s = \begin{cases} A + 0.0002S_0 \; for \; cot\alpha \leq 1.5 \\ 0.09 + 0.0001S_0 \; for \; cot\alpha \geq 1.5 \end{cases} \tag{7.14}$$

and, for coefficient B_s:

$$B_s = \begin{cases} B + 0.0004S_0 \; for \; cot\alpha \leq 1.5 \\ -1.609 + 0.0003S_0 \; for \; cot\alpha \geq 1.5 \end{cases} \tag{7.15}$$

It must be noted that Equations (7.11) – (7.15) are defined to cater for the effect of swell percentage on the overtopping computed for bimodal cases only. The applicability is limited to slopes within the ranges shown ($0 \leq \cot\alpha \leq 3.0$). The usage also does not contradict the use of Equations (2.4) – (2.6) above. Coefficients for different slopes are calculated using the suggestions of Victor and Troch (2012) and van der Meer and Bruce (2013) in Equations (2.4) – (2.6), and then determine the equivalent effects due to swell percentage by applying Equations (7.11) – (7.15). It is because swell percentages follow a linear increasing relationship with the dimensionless overtopping. The trends of this slope are the same for both $\cot\alpha = 0$ and $\cot\alpha = 1.5$. However, there is a significant drift in this case for $\cot\alpha \leq 3.0$. In applying the new formulations proposed

in present study, various coefficients due to swell effects can be interpolated for other slope angles that are within with the limit discussed in this study.

7.4 Assessment of New Prediction Accuracy

Table 7.1 presents a follow up to the prediction of accuracy that was previously discussed in Section 6.5. The root mean square errors RMSE and the bias of the errors BE are both applied were determined using Equations (6.2) – (6.3) to assess the accuracy provided by the EurOtop (2018) and compared with the new swell formulations that was represented by Equations (7.13) – (7.15). The new formulation presented a better accuracy in predicting both the unimodal and bimodal dimensionless overtopping across the three slopes. Equation (7.13) – (7.15) shows an improvement in the prediction of bimodal overtopping values in terms of the RMSE and the bias values described by the new formulation.

Table 7.1 Values computed for *RMSE* in Equation (6.2) and bias Equation (6.3) by assessing the EurOtop for different ranges of relative crest freeboard $R_c = H_{m0}$ and slope angles

Formulation	**Equation (2.4)**		**Equation (7.13)**	
Item	**RMSE (-)**	**Bias (-)**	**RMSE (-)**	**Bias (-)**
cot α = 3.0				
All tests	0.00365	-7.46×10^{-6}	0.00271	6.10×10^{-6}
Unimodal	0.00284	8.82×10^{-4}	0.00221	6.34×10^{-4}
Bimodal	0.00463	-7.41×10^{-5}	0.00376	-4.95×10^{-5}
cot α = 1.5				
All tests	0.00336	-1.69×10^{-3}	0.00260	-1.36×10^{-3}
Unimodal	0.00191	1.36×10^{-4}	0.00135	1.06×10^{-4}
Bimodal	0.00304	-5.18×10^{-4}	0.00228	-3.78×10^{-4}
cot α = 0.0				
All tests	0.00972	-3.84×10^{-4}	0.00609	2.84×10^{-4}
Unimodal	0.00103	5.80×10^{-4}	0.000792	4.58×10^{-4}
Bimodal	0.00967	-3.65×10^{-4}	0.00628	3.22×10^{-4}

7.5 Sensitivity Analysis of the Fitted Coefficients

It was observed from Figure 7.14a that the coefficient A described for the vertical slope seems to pose certain uncertainties among other fitness parameters. To examine the effect of the uncertainty of that gradient on the overtopping predictions, sensitivity analysis were performed.

The Monte carlo sensitivity analysis are based on investigating various influences of the uncertainty of the input will pose on the output overtopping predictions. In this way the reliability and the robustness of the overtopping prediction can be improved. Different methods of performing sensitivity analysis have been fully described in Iooss and Lemaître (2015). In present study, the Monte Carlo analysis was adopted. This method allows the use of the uncertainty distributions obtained from different inputs into the model or determined from the model to establish effects of any of the uncertainties in the parameter. In this thesis both normal and exponential probability distributions are applied.

Figure 7.15(a–c) presents the graphical and statistical analysis obtained from the Monte Carlo sensitivity analysis. In all the three figures, the normal distributions are based on 3000 Monte Carlo simulations. Figure 7.15 shows the distribution of the sensitivities of all the parameters in the new formulation combined, while Figures 7.15(b & c) represent the normal distribution obtained using the parameters of coefficient A due to cot $\alpha = 0$ alone (the lowest gradient in Figure 7.14a). The process performance capability Ppk accounts shown in Figure 7.15a accounts for the overall variation in the simulation results. As shown here the overall variation of 1.322 was recorded using all the combined parameters. Only 0.1 percent are out of specification. According to Verbeeck et al. (2006), the Ppk shows the drifts and shifts between each of the parameters. Ppk depends largely on the values of the standard error obtained during the simulation. A smaller value is obtained in this case. This result is similar to the effects of cot $\alpha = 0$ (shown in Figures 7.15(b & c)). Smaller values of Ppk (1.343 and 1.35) are similarly obtained in both cases. These values are shown on the normal distributions.

The accurate reproduction of the normal distribution when effects due to cot $\alpha = 0$ are applied to Equations (7.13) – (7.15) also shows that the distributions are not strongly sensitive to the effects of the vertical seawall significantly. Moreover, a low percentages of the distribution are out of specification with only 0.121 % and 0.118 respectively. Due to the similarities of the normal statistical distribution, and little variations observed in the Ppk and the percentages that are out of specification, it can be concluded that effects of cot $\alpha = 0$ does not have significant effects on the fitness parameters applied in Equations (7.13) – (7.15).

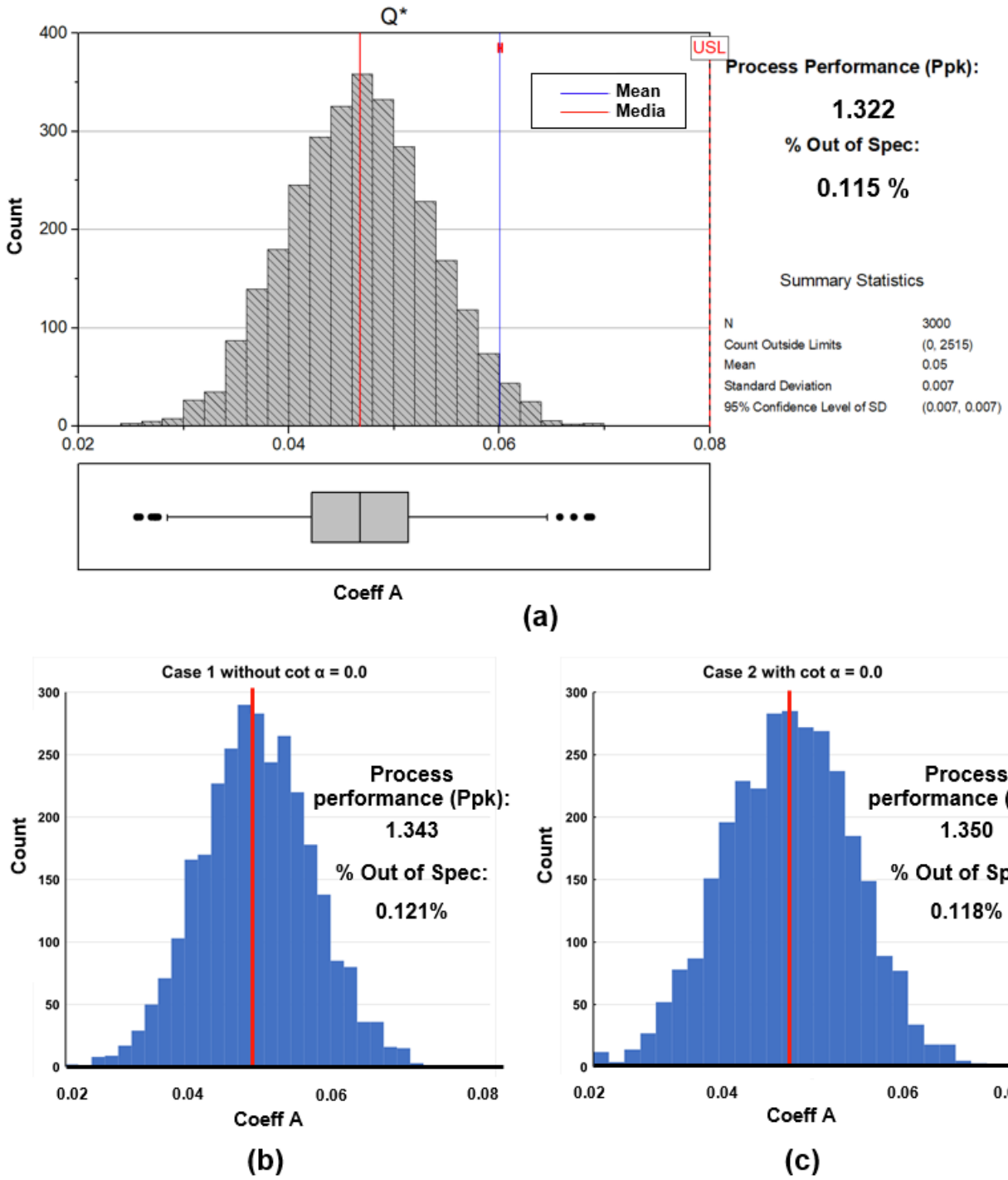

Figure 7.15 *Sensitivity analysis of the distribution obtained from Monte Carlo simulation performed on (a) all the coefficient parameters, (b) due to the effect of cot* $\alpha = 0$ *on both coefficients A and B and (c) due to the effect of cot* $\alpha = 0$ *on both coefficients A alone within the new overtopping formulations in Equations (7.13) – (7.15)*

7.6 Influence of Swell Spectral Peak Period

Figure 7.16 presents the influence of swell peak period that was investigated in this study. The box plots present present similar information as described in Section 7.3. In the present Section, at prototype scales, only swells with peak periods of 11, 15, 20 and 25 seconds are respectively considered. As visible in Figure 7.16, non-dimensional wave overtopping are strongly influenced by the peak periods (or frequencies) of swell in the energy spectrum for the same sea-state. These effects could be significant in coastal seawall designs and costs for certain locations. Non-dimensional wave overtopping seems to respond strongly to the separation of spectral peaks between the wind wave and swell wave frequencies in the bimodal energy spectrum. There seems to be clearer wave overtopping being triggered by swell periods at 11 seconds than the rest for both cot $\alpha = 0$ and 1.5. This effect does not seem to be very clear for cot $\alpha = 3.0$ except for few extreme non-dimensional wave overtopping estimates shown by the outliers.

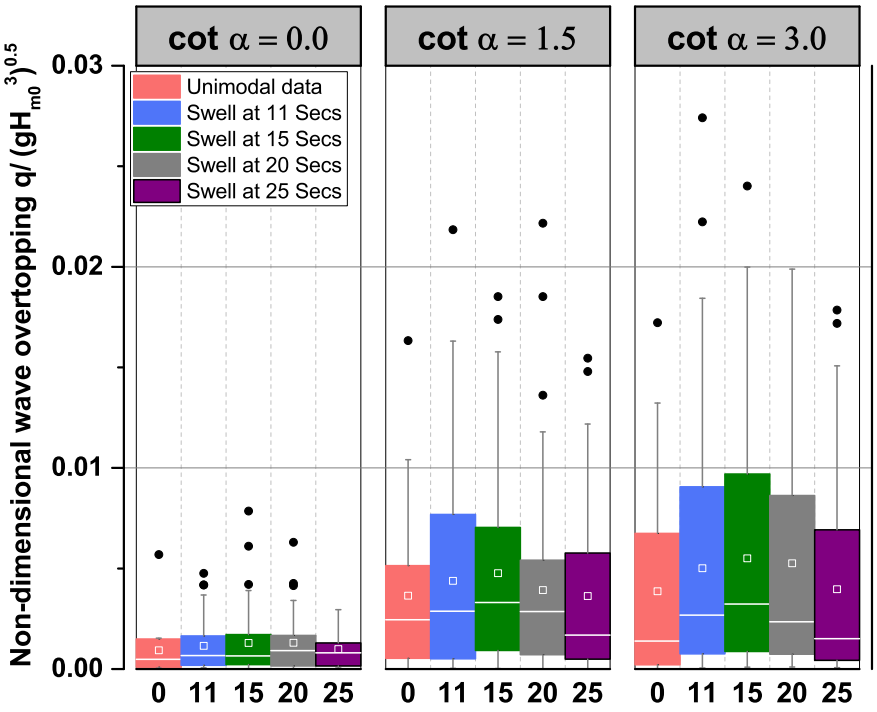

Figure 7.16 *The relationship between the non-dimensional overtopping rate* $q/\sqrt{H_{m0}^3}$ *with Swell peak periods of cot* $\alpha = 0.0$ *and cot* $\alpha = 1.5$ *and cot* $\alpha = 3.0$

In order to obtain a suitable empirical relationship between the non-dimensional wave overtopping and swell spectral peak periods, the non-linear regressions are applied to fit different dimensionless wave overtopping estimates for different swell periods.

Non-linear least squares regression analysis was obtained as a result of the fitting process on each sets of data. Plots of fitted results are presented in Figures 7.17–7.20.

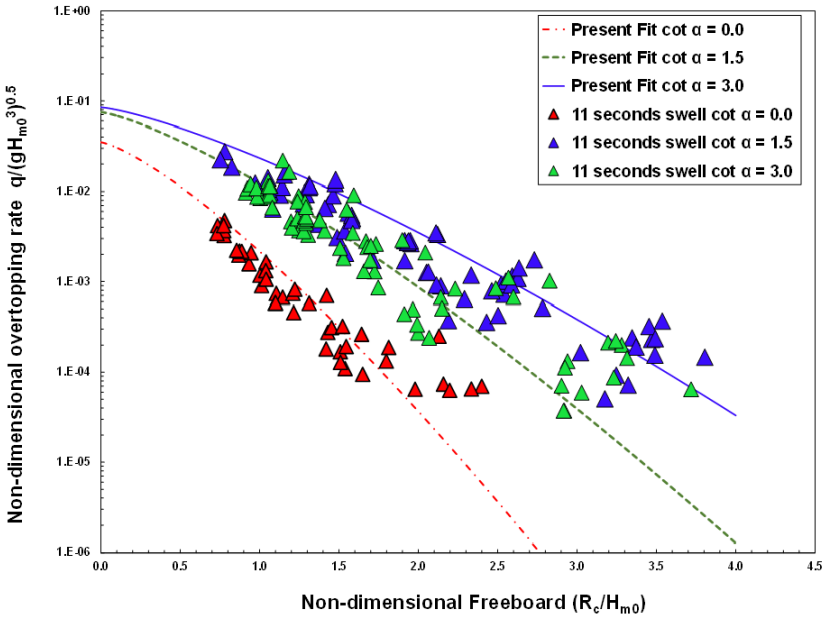

Figure 7.17 *Results of non-linear regression performed on different non-dimensional wave overtopping obtained across three slopes for cot* $\alpha = 0.0$*, cot* $\alpha = 1.5$ *and cot* $\alpha = 3.0$ *for swell with spectral peak periods at 11 secs*

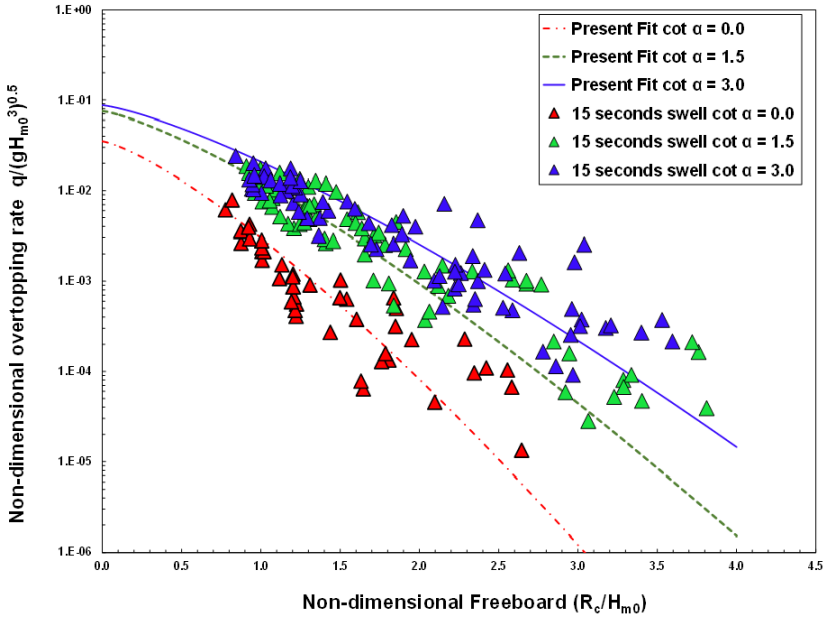

Figure 7.18 *Results of non-linear regression performed on different non-dimensional wave overtopping obtained across three slopes for cot* $\alpha = 0.0$*, cot* $\alpha = 1.5$ *and cot* $\alpha = 3.0$ *for swell with spectral peak periods at 15 secs*

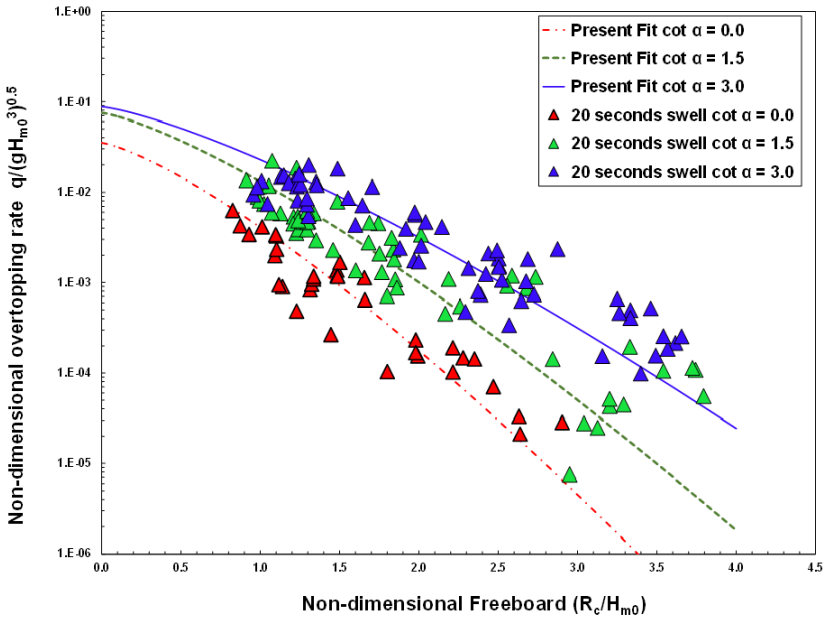

Figure 7.19 *Results of non-linear regression performed on different non-dimensional wave overtopping obtained across three slopes for cot* $\alpha = 0.0$*, cot* $\alpha = 1.5$ *and cot* $\alpha = 3.0$ *for swell with spectral peak periods at 20 secs*

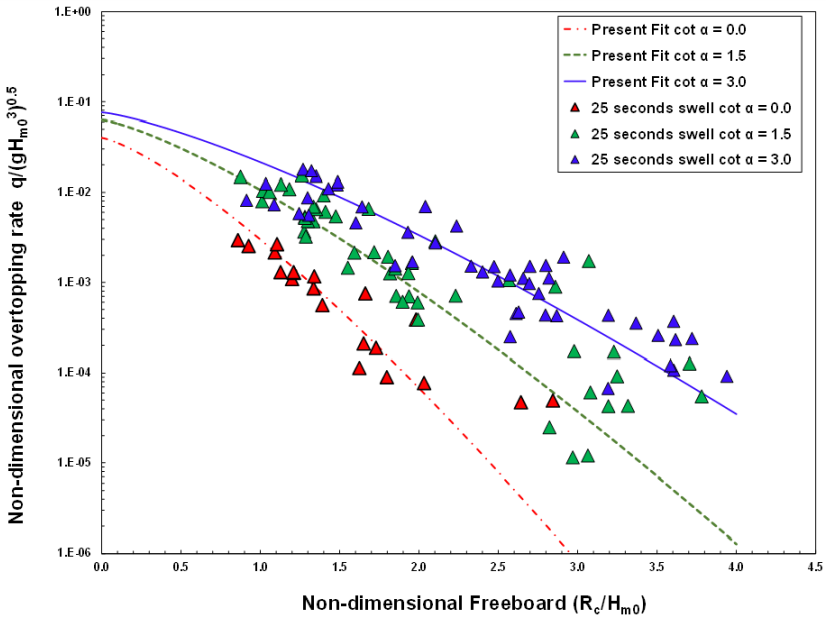

Figure 7.20 *Results of non-linear regression performed on different non-dimensional wave overtopping obtained across three slopes for cot* $\alpha = 0.0$*, cot* $\alpha = 1.5$ *and cot* $\alpha = 3.0$ *for swell with spectral peak periods at 25 secs*

Based on these fittings, individual coefficients A and B can be extracted as before. These are presented in Figure 7.21.

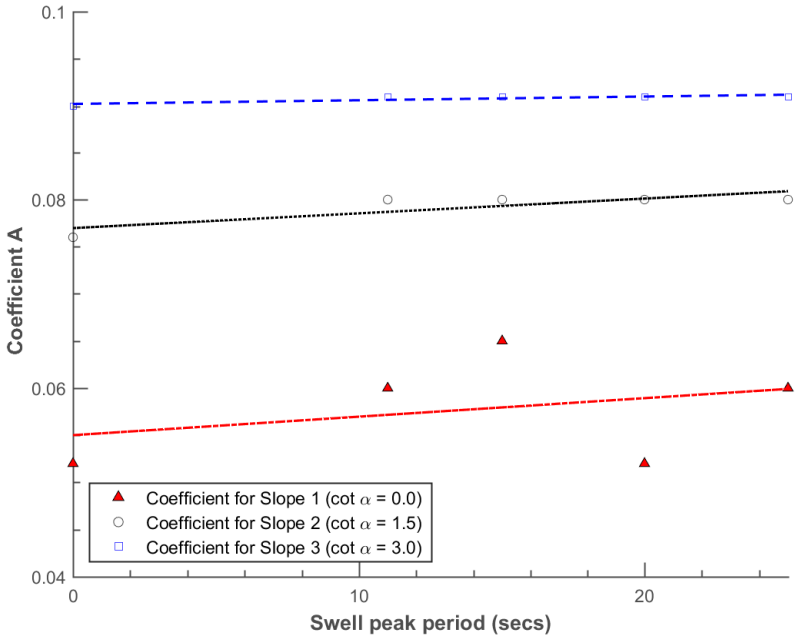

(a)

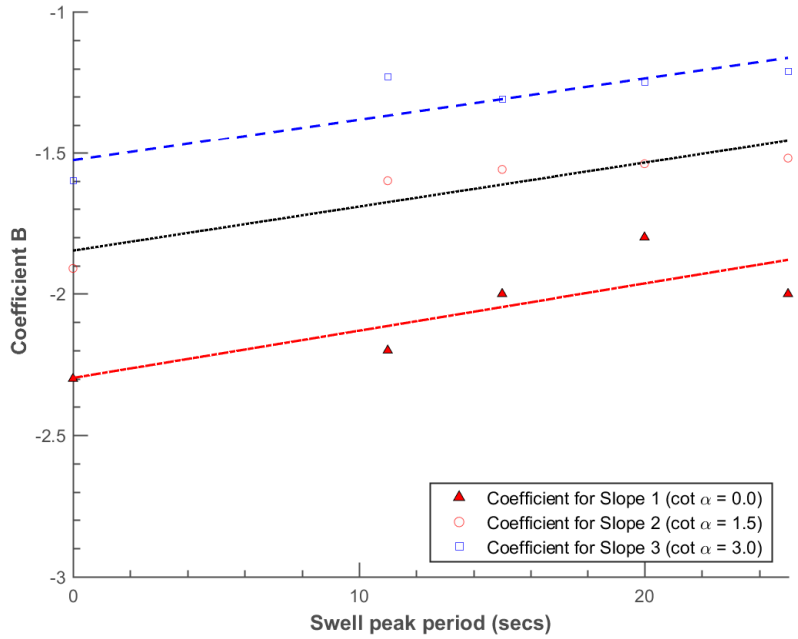

(b)

Figure 7.21 *(a) Coefficient A as a function of swell peak period, varying from unimode to 25 secs, (b) Coefficient B as a function of swell peak periods, varying from unimodal to 25 secs*

Concerning effects of swell peak period $T_{Sm-1,0}$, as the peak separation increases, the spectral width of the resulting bimodal spectrum also increases and in turn, creating larger overall spectra wave period $T_{m-1,0}$ and the resulting wave length $L_{m-1,0}$. Also as described earlier, the sensitivity of overtopping is greater for the mildest slope. As shown in Figure 7.21, the highest wave overtopping performances were demonstrated by this sloping seawall $cot\ \alpha = 3.0$. Unlike in the unimodal cases, lower frequency swells produce greater wave overtopping than swells at higher frequencies because the latter produces smaller overall spectra characteristics than the former.

7.7 Conclusions

In this chapter, different influences of the presence of swell in a sea-state have been described and analysed. Various parameters of spectra characteristics considered are the narrowness, the broadness, and peakedness parameters. Effects of swell percentages and swell peak periods on overtopping have also have been shown. Swell waves occuring at lower peak periods are producing the uppermost impact of wave overtopping on each slope investigated. However, it was hypothesise that the increased wave overtopping for longer waves/swell percentage is due to a change in wave behaviour, where more waves are surging than breaking on the structure. A simple modification to the existing formula for non-breaking waves is proposed that accounts for the presence of swell percentages in bimodal conditions. Further study is required on the non-linearities imposed by swell peak periods to have a more suitable formulation of this phenomena. Wave overtopping increases as the spectral values described by the narrowness, the broadness, and peakedness parameters reduces. Moreover, spectra values tend to be approaching asymptotic values for both the narrowness and the broadness parameters. Increasing trends of swell percentage in a bimodal sea could produce enormous wave overtopping with tendencies of more significant flooding. Broad-banded sea conditions yield less wave overtopping intensity than highly peaked bimodal seas.

Chapter 8

Reflection Analysis of Impermeable Slopes Under Bimodal Sea Conditions

Follow-up to the experimental test programme conducted in chapter 6, understanding of reflection characteristics of coastal seawalls is crucial for seawall designing and management. Wave reflection can cause difficulties to small vessel manoeuvring at the harbour entrance and cause damaging scouring at the toe of coastal structures. Previous studies have considered reflection characteristics of coastal seawalls, under wind-generated random waves, but have neglected to consider the effects of wave bimodality created by the presence of swell waves. Chapter 8 will focuse on the influence of random wave bimodality on reflective characteristics of coastal seawalls. Reflection coefficients were computed from each storms in the experimental test. Analysis of results suggests that both unimodal and bimodal waves give similar reflection characteristics. However, a higher reflection coefficient in bimodal sea states than in the unimodal sea states. It was found that the reflection coefficient of coastal seawalls is strongly influenced by the seawall slope, the wave steepness, relative water depth, and the surf similarity parameters. A new empirical reflection equation to describe the influence of wave bimodality on the reflection characteristics of coastal seawalls has been formulated based on this study.

8.1 Reflection Characteristics of Smooth Impermeable Slopes

Battjes (1974) identified the surf similarity parameter ξ as a critical parameter affecting the reflection characteristics of sloping impermeable slopes with slope angle α under

incident monochromatic waves. It can be expressed mathematically as:

$$\xi = \frac{tan\,\alpha}{\sqrt{2\pi H/gT^2}} \tag{8.1}$$

In this equation, H, and T represent the significant wave height and the wave period of the monochromatic wave, respectively. Values of $\xi \leq 2.3$ are correspond to breaking waves while for $\xi \geq 2.3$ non-breaking waves occur. The equation showing a simplified relationship between the reflection coefficient K_r and the breaker parameter ξ of breaking monochromatic waves has also been described in the same study (Battjes Battjes (1974)), and is:

$$K_r = 0.1\,\xi^2 \tag{8.2}$$

This expression is only valid for breaking monochromatic waves $\xi \leq 2.3$ as illustrated by Figure 8.1. In Seelig and Ahrens (1981), a modified version of Equation (8.2) has been presented. The modified relationship between the reflection coefficient K_r and the breaker parameter ξ is presented in Equation (8.3):

$$K_r = tanh\left(0.1\xi^2\right) \tag{8.3}$$

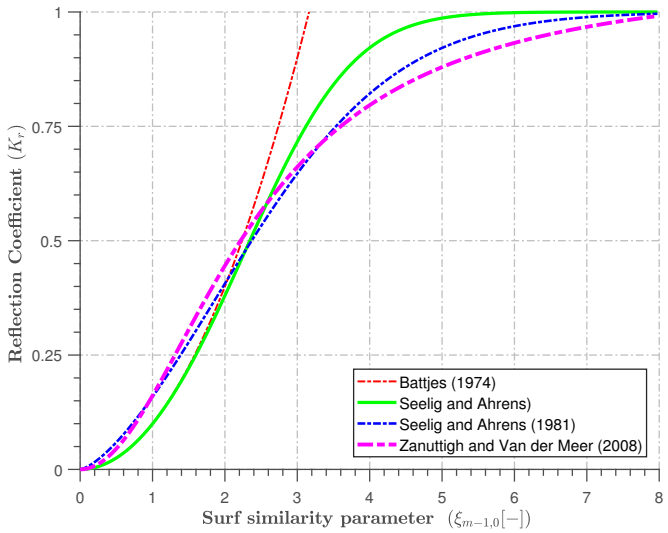

Figure 8.1 An illustration of the prediction of reflection characteristics of smooth impermeable slopes

It is worth noting that Equation (8.2) is a close approximation to Equation (8.3) for small values of the surf similarity parameter. For larger values of the parameter, Equation (8.3) tends asymptotically to 1. The mathematical expression from Seelig and Ahrens (1981) is valid for both breaking and non-breaking monochromatic waves. A more accurate expression was also proposed based on several experimental studies that were performed to describe the reflection behaviour of other sea defences, including revetments, beaches and breakwater. These expressions consider both the peak period of irregular waves and the spectrally determined breaker parameter $\xi_{m-1,0}$. These are described in Equation (8.4)a and (8.4)b below:

$$K_r = \frac{\xi_p^2}{\xi_p^2 + 5.5} \tag{8.4a}$$

$$K_r = \frac{\xi_{m-1,0}^2}{\xi_{m-1,0}^2 + 5.0} \tag{8.4b}$$

Equation (4b) is valid for $1.0 \leq \xi_{m-1,0} \leq 6.2$ and sloping seawalls with $1.5 \leq \cot \alpha \leq 2.5$ respectively.

Zanuttigh and Martinelli (2008) proposed a revised version of Equation (8.4)b from over 4000 reflection coefficient experimental test results. This can be generally expressed as:

$$K_r = tanh 0.16(\xi^{1.43}) \tag{8.5}$$

This equation extends the range of applicability to structure slopes with $1.5 \leq \cot \alpha \leq 4.0$ and $1.0 \leq \xi_{m-1,0} \leq 4.1$ with dimensionless crest freeboard of $0.58 \leq R_c/H_{m0} \leq 4.5$.

The reflection analyses by Mansard and Funke (1980); Zelt and Skjelbreia (1992) apply strictly to linear waves. For the breaking wave cases, the non-linearity of the reflection performances cannot be accurately estimated by the method. The accuracy of the Zelt & Skjelbreia method was determined using the flume without any structure. The free reflection characteristics of the open flume were used to calibrate the performance of the method of Zelt and Skjelbreia (1992). These adjustments are applied to all wave cases studied in this thesis.

8.1.1 Estimation of Reflection Parameters

Some reflection parameters required for this study were estimated. These include the linear wave length, wave steepness and the dimensionless Iribarren number. Relationships obtained from these parameters are of special relevance to this study. The linear wave length $L_{m-1,0}$ applied here is calculated using the Newton-Raphson iteration technique on the dispersion relationship, for example in Reeve et al. (2015).

$$L_{m-1,0} = \frac{gT_{m-1,0}}{2\pi} tanh\left(\frac{2\pi h}{L_{m-1,0}}\right) \tag{8.6}$$

In Equation (8.6), h is the offshore water depth, and $T_{m-1,0}$ represents the spectra wave period. Also, the wave steepness $S_{m-1,0}$ can be defined in terms of the dimensionless ratio of the spectral wave height H_{m0} and the wave length $L_{m-1,0}$ obtained from Equation (8.7).

$$S_{m-1,0} = \frac{H_{m0}}{L_{m-1,0}} \tag{8.7}$$

Similarly, the surf similarity parameter $\xi_{m-1,0}$ can be estimated from Equation (8.8):

$$\xi_{m-1,0} = \frac{tan\alpha}{\sqrt{S_{m-1,0}}} \tag{8.8}$$

Other relevant parameters are the non-dimensional wave height H_{m0}/h and non-dimensional water depth $d/L_{m-1,0}$. Full details of equations solved to determine the reflection coefficient K_r can be found in Zelt and Skjelbreia (1992) and Zelt and Skjelbreia (1992). Table 6.3 presents the wave conditions tested in this study. As shown in the table for each test numbers, there are four different swell peak periods across three different sloping seawalls.

8.2 Results and Discussions

To derive a functional improvement from the reflection coefficient K_r of impermeable walls under bimodal sea conditions, effects of various secondary factors influencing K_r will be considered in this section. Such factors includes the wall slope, water depth, wave steepness and the crest freeboard.

8.2.1 Influence of Wall Slope on Reflection Characteristics

Reflection characteristics of a coastal seawall can be determined by the steepness of the wall slope. Combined plots of the relationship between the reflection coefficient and the breaker index parameters are presented in Figures 8.2 and 8.3. Figure 8.2 presented results for unimodal sea-states while reflection results due to bimodal sea-states are represented in Figure 8.3. In general, for unimodal and bimodal sea conditions, K_r varies between 0.4 and 1.038. As expected, lower values of K_r are observed for the gentle slope of 1:3, while higher of K_r are clearly observed for the case of vertical seawall. These results are consistent with the findings of Seelig and Ahrens (1981) and Allsop and Hettiarachchi (1989).

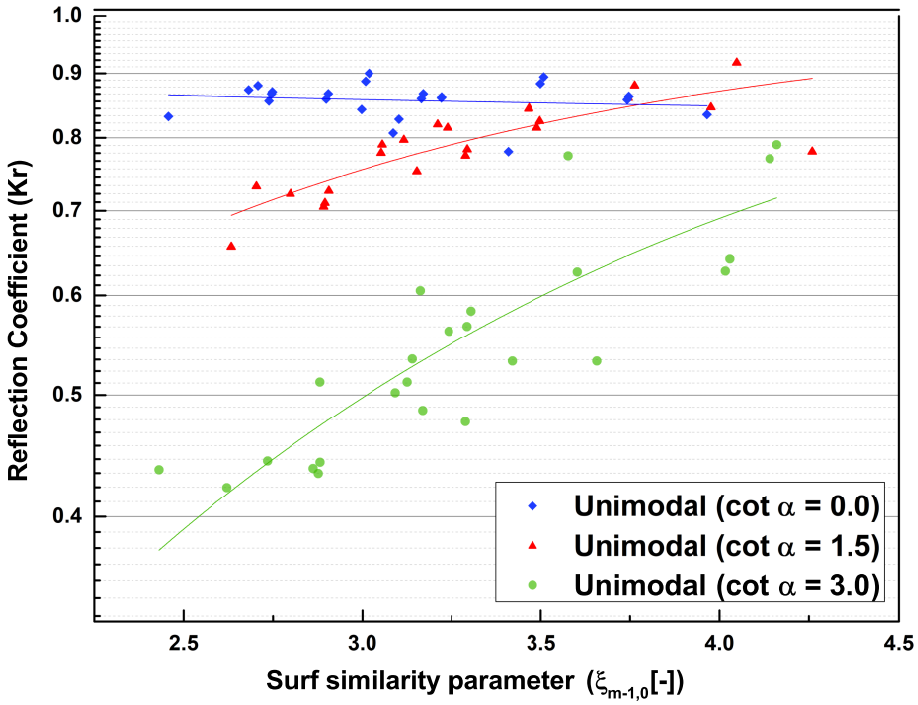

Figure 8.2 Comparison of the reflection coefficient K_r and breaker parameters $\xi_{m-1,0}$ across three slopes (cot α = 1.5, 3.0 and 0.0) as shown under unimodal sea states

The range in K_r for a vertical wall depends largely on the degree of wave overtopping, and it increases as the crest freeboard increases (Figures 6.14, 6.15 and 6.16). For sloped seawalls, the K_r is increases as the $\xi_{m-1,0}$ increases for the incident waves. This increments tends towards an asymptotic values for waves with longer periods. In bimodal seas, higher bound of K_r is created which corresponds to swell of long period exhibited by the bimodal seas. The case is different with a vertical seawall as K_r values are generally around 100 percent as expected.

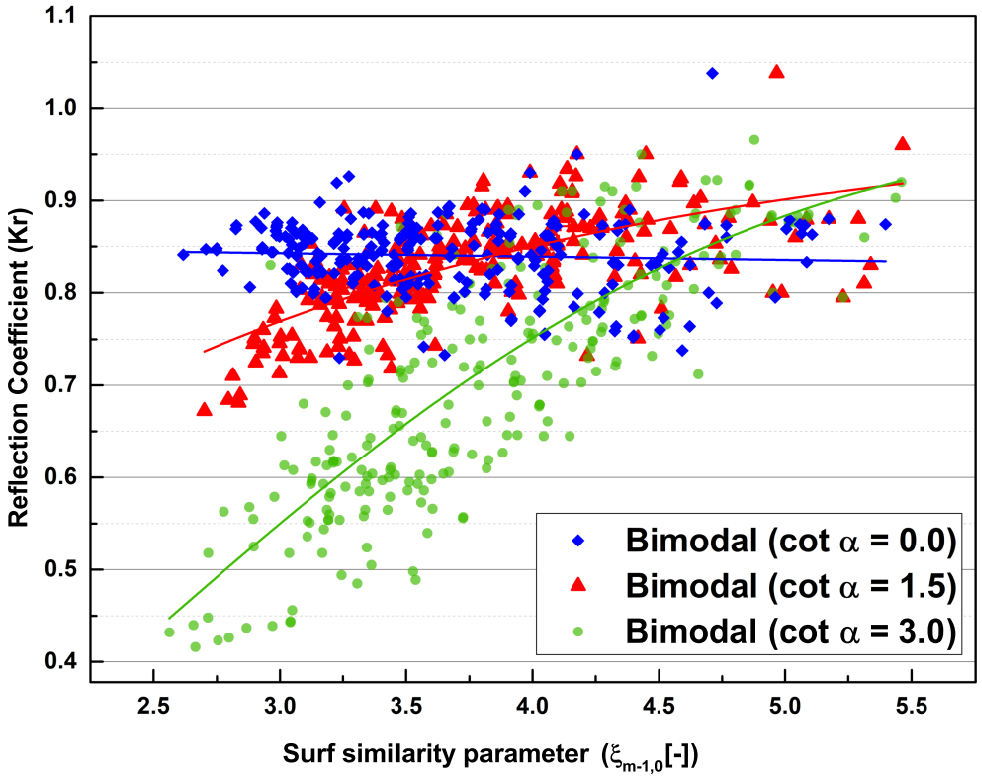

Figure 8.3 Comparison of the reflection coefficient K_r and breaker parameters $\xi_{m-1,0}$ across three slopes (cot α = 1.5, 3.0 and 0.0) as shown under bimodal sea conditions

Figure 8.4 shows a combined plot of the best-fit curves of K_r against $\xi_{m-1,0}$ for both unimodal (solid lines) and bimodal (in dotted lines) across different slopes. It is obtained by applying the non-linear fit algorithm to all the datasets under unimodal and bimodal seas. Unimodal sea states exhibited similar trends as the bimodal sea conditions under the same test conditions. However, the relationship between K_r and $\xi_{m-1,0}$ are more extended in the bimodal sea states than in the unimodal sea conditions. This is because of the longer periods in the bimodal seas (Figure 7.8a). As the wave period increases, there is a further reduction in wave steepness while values of $\xi_{m-1,0}$ increases. It follows that values of K_r are inversely proportional to the wave steepness as reported in previous studies, for example, Seelig and Ahrens (1981).

Least reflections are observed for the gentle slope (cot α = 3.0), which is in accordance with the observations of Neelamani and Sandhya (2003); Van Gent (1994), and is a result of the wave energy dissipation associated with energy losses due to wave overtopping.

Further examination of these results shows that the relationships between K_r and $\xi_{m-1,0}$ for unimodal state obtained in this study are within the bounds of previous

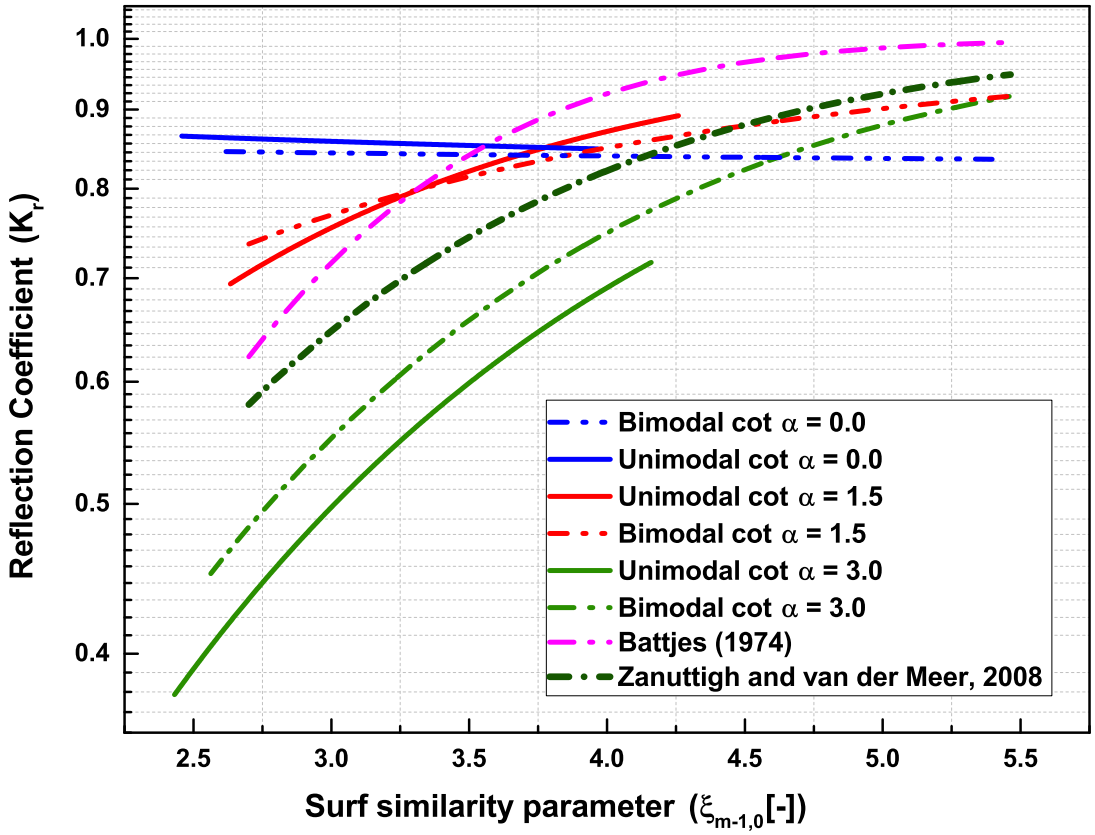

Figure 8.4 Variations of reflection coefficient K_r with breaker index $\xi_{m-1,0}$ across three different slopes

studies derived by Battjes Battjes (1974) and Zanuttigh and Martinelli (2008). However, a better fit is obtained from the modified K_r formulation derived by Zanuttigh and Martinelli (2008). The fitted coefficients of Zanuttigh and Martinelli (2008) does not accurately fit for the relationship between K_r and $\xi_{m-1,0}$ in bimodal seas.

8.2.2 Influence of Water Depth Variations

In this section the influence of water depth, h/L, on reflection coefficient, K_r, was investigated across three slopes (i.e., cot $\alpha = 0.0$, cot $\alpha = 1.5$ and cot $\alpha = 3.0$). Figure 8.5 presents these results for all the datasets acquired during this study. Generally, for the steep (cot $\alpha = 1.5$) and the mild sloping (cot $\alpha = 3.0$) seawalls, it is found that the value of K_r decreases with increasing relative depth h/L. This behaviour agrees with the findings of Neelamani and Sandhya (2003) and Nassar and Negm (2016). These observations are peculiar to plunging wave breaking phenomena as previously described in cited literatures. For the vertical seawall, the reflection coefficient K_r is almost independent of water depth. This is expected because of the reflection of waves by vertical walls irrespective of the depth limiting values. Standing waves are formed during these tests, and more energy is reflected than for sloping walls. These observations are similar for both the unimodal and bimodal sea states.

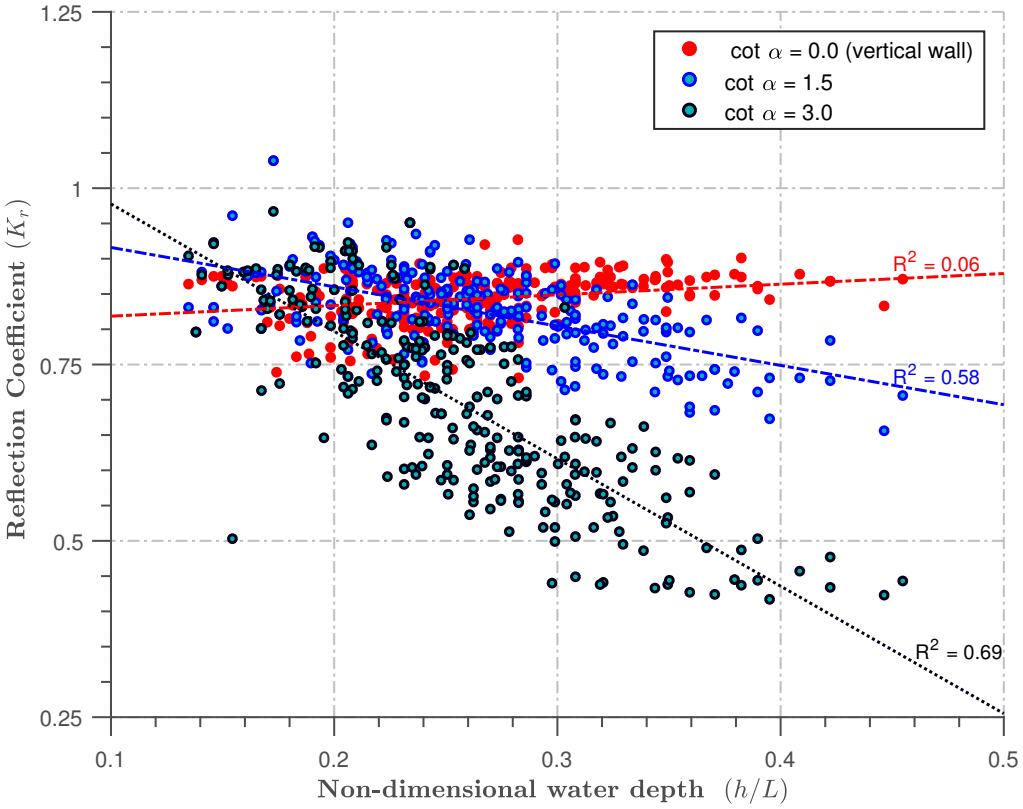

Figure 8.5 Variations of reflection coefficient K_r with non-dimensional water depth h/L across three different slopes investigated

8.2.3 Influence of Wave Steepness

Many sloping and vertical impermeable seawalls are built solely to dissipate wave energies that are directly incident on them. Reflected waves are produced whenever the waves are interacting with the plain seawalls. In sloping seawalls, it has been suggested in Goda (2010) that values of reflection coefficient K_r are inversely proportional to the incident wave steepness $S_{m-1,0}$. The suggestion is true for observations recorded in this study as shown in Figure 8.6. It forms completely similar correlation with the influence of water depth observed in previous section (8.3.2). However, the vertical seawall totally deviated from this theory in both cases. In the case of vertical seawalls, standing waves are mostly formed during propagation. This will eventually lead to cancelling out incident waves leading to destructive interference and higher K_r up to 100 percent in most cases (Figure 8.5).

The K_r performance of vertical seawall as shown in Figures 8.5 and 8.6 suggests that vertical seawalls would provide a more valuable protection to cities, harbours or ports as previously prescribed in previous studies. It is because of the high reflective characteristics that made them suitable for stopping waves from overtopping structures. However, this could in turn lead to more pronounced standing waves that can exacerbated scouring of sediments near the toe of the structure, and eventually to its failure and collapse (Zanuttigh and Martinelli, 2008).

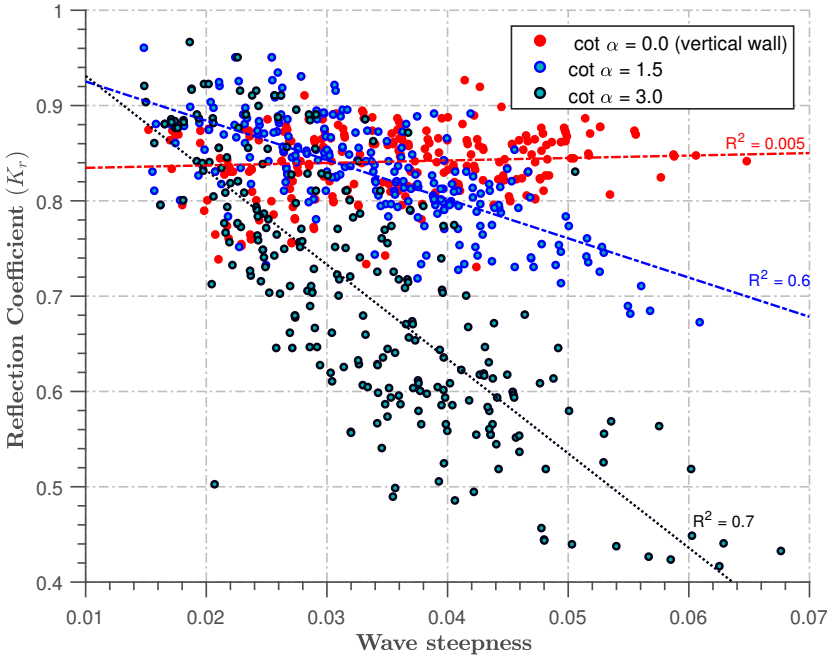

Figure 8.6 Relationships between wave steepness and the reflection coefficient K_r across three different slopes investigated

8.2.4 Effects of Crest Freeboard

Accurate selection of sizes of crest freeboard R_c/H_{m0} is an essential requirement for designing coastal seawalls against wave overtopping and to serve as flood barriers. Reliable prediction of reflection characteristics K_r of a coastal seawall suitable for selected R_c/H_{m0} is also key. In Figure 4.7, K_r is presented in terms of only R_c/H_{m0} across three seawall slopes. It can be seen that K_r is directly proportional to values of R_c/H_{m0}. As the crest freeboard increases, values of K_r also gradually increases. It implies that as crest freeboard reduces, there are more wave overtopping and tendencies for reflection reduces altogether.

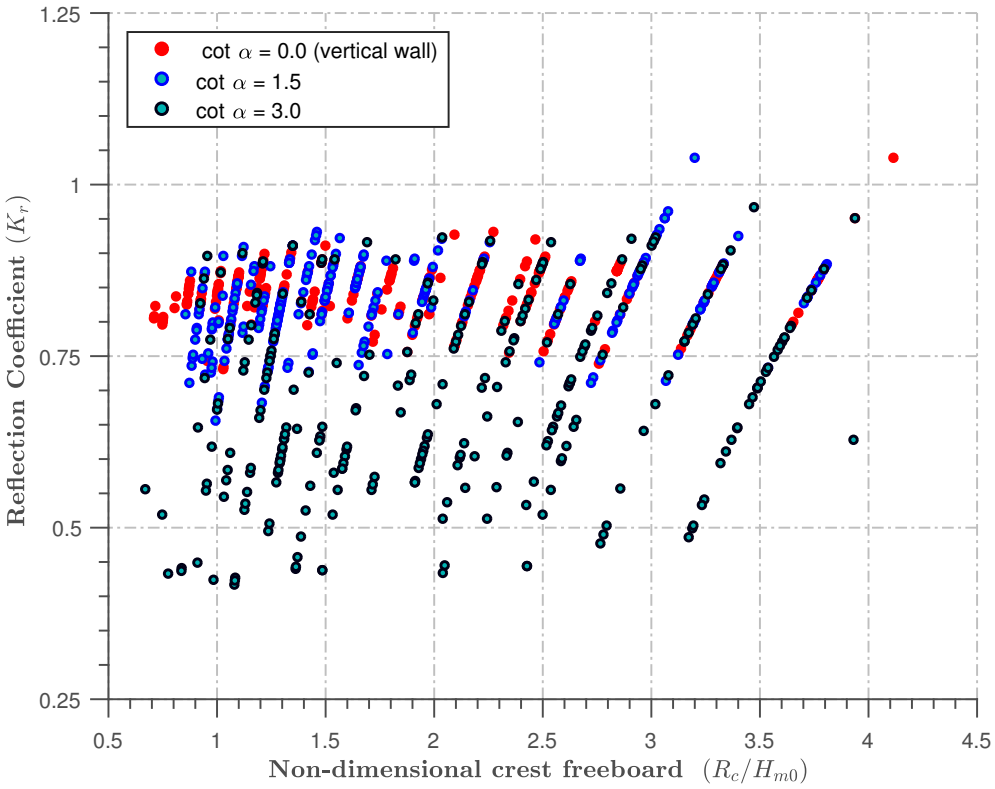

Figure 8.7 Influence of dimensionless crest freeboard R_c/H_{m0} with the reflection coefficient K_r across three different slopes investigated

8.3 Reflection Coefficients of Steep Slopes Under Bimodal Waves

In order to establish an improved formulation for the reflection coefficient K_r for bimodal sea conditions, a more detailed analysis of the results were performed. Figure 8.8 presents a more detailed relationship achieved between K_r and $\xi_{m-1,0}$ for each slope for the bimodal cases. The residuals obtained from the non-linear multi-regression fit algorithm are also presented in Figure 8.9. The residual plots show that the equation is suitable at predicting K_r under bimodal seas.

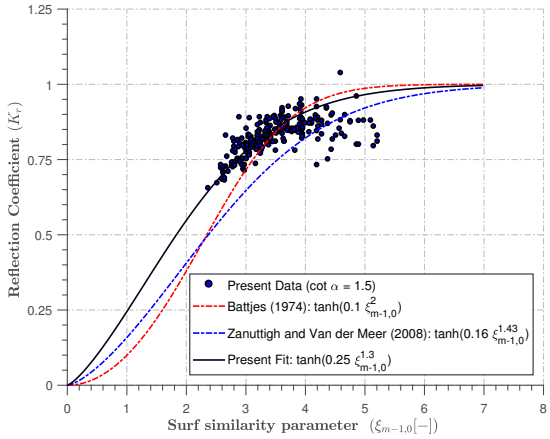

(a)

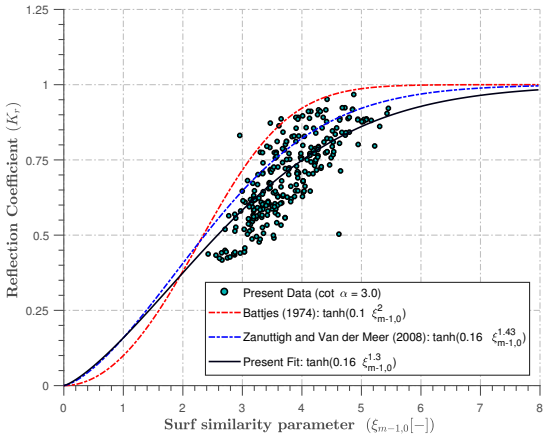

(b)

Figure 8.8 A representation of the non-linear multi-regression fit between K_r and $\xi_{m-1,0}$ for sloping seawalls

Figures 8.9(a-c) present the performance of the new formulation for the prediction of K_r of the impermeable slopes under the influence of bimodal seas. The residuals are plotted from the difference between the observed values and the predicted ones. A

positive residual values implies that the K_r predictions made by the new formulations are while on the other hand, negative values means that the new model is over predicting the K_r values. As visible from these Figure 8.9(a-c), the new equation performed very well under the bimodal sea conditions for across the three slopes. The residual plot for the mildest slope with cot α = 3.0 seems to give the best performance as shown in the residual plots. This may due to the possibility of obtaining the most extreme wave overtopping for this slope. The spread of the residual plots of the steeper slopes (cot α = 1.5) and vertical wall (cot α = 0.0) are symmetrically distributed showing more clustered properties around 3.5 as shown in the Figure 8.9(b-c).

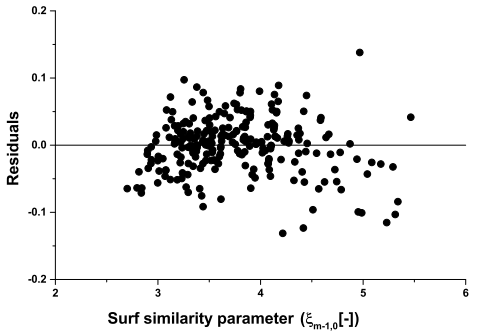

(a)

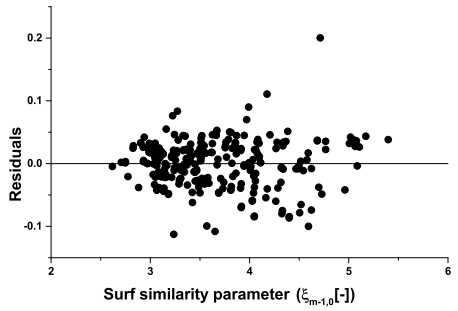

(b)

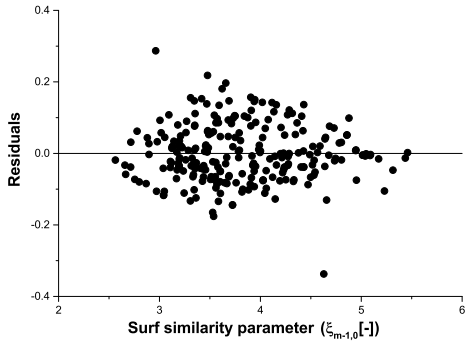

(c)

Figure 8.9 A residual plots between the residuals of K_r with respect to $\xi_{m-1,0}$ for sloping seawall with: (a) cot α = 0.0; (b) cot α = 1.5, (c) cot α = 3.0

Based on multiple regression analysis of the observed bimodal datasets, empirical relationship that considers effects of reflection due to bimodal waves is proposed. As suggested in Zanuttigh and Martinelli (2008), this equation contains two corresponding calibration coefficients applied in defining K_r of different impermeable slopes. It can only be applied for sloping seawalls under bimodal sea conditions. The coefficients are slightly modified from Zanuttigh and Martinelli (2008). For simplicity, a more general form of Equation (8.5) can be written in terms of coefficients a and b presented in Equation (8.9):

$$K_r(a,b) = tanh\, a(\xi_{m-1,0}^{b}) \tag{8.9}$$

As a general rule of conditions for bimodal seas, values of a and b can be simplified:

$$\left.\begin{array}{ll} & a = 0.25\,(for\ 1 \le cot\alpha \le 1.5) \\ K_r & = tanh\left(a\xi_{m-1,0}^{b}\right) \\ \xi_{m-1,0} & = (2.4 \le \xi_{m-1,0} \le 5.5) \\ & \vdots \\ \frac{R_c}{H_{m0}} & = \left(0.8 \le \frac{R_c}{H_{m0}} \le 4.0\right) \end{array}\right\} b = 1.3\,(Bimodal\ seas) \tag{8.10}$$

$$\left.\begin{array}{ll} & a = 0.16\,(for\ 1.5 \le cot\alpha \le 3.0) \\ K_r & = tanh\left(a\xi_{m-1,0}^{b}\right) \\ \xi_{m-1,0} & = (2.4 \le \xi_{m-1,0} \le 5.5) \\ & \vdots \\ \frac{R_c}{H_{m0}} & = \left(0.8 \le \frac{R_c}{H_{m0}} \le 4.0\right) \end{array}\right\} b = 1.3\,(Bimodal\ seas) \tag{8.11}$$

To assess the suitability and conformance of the new formulation, a correllation assessment of the new equation with Zanuttigh & van der Meer Zanuttigh and Martinelli (2008) is made. Figure 8.10 shows a comparison of the verification of Equation (8.5) from the Zanuttigh & van der Meer Zanuttigh and Martinelli (2008) and Equations (8.10) and (8.11) obtained in present study. The observed K_r and the predicted K_r are fully described in this figure for the two slopes ((**a**) with cot α = 1.5; and (**b**) with cot α = 3.0).

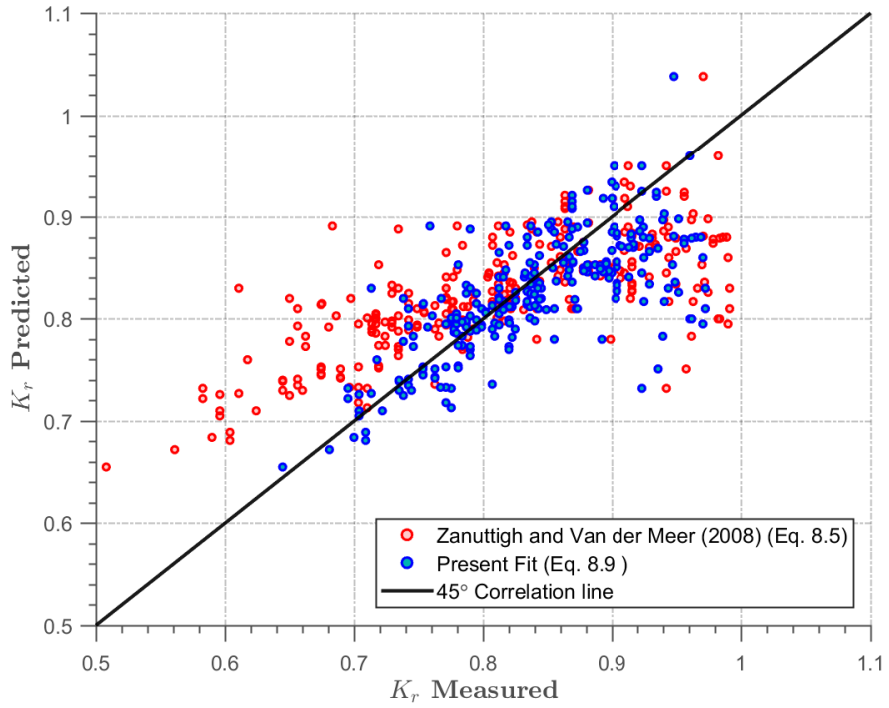

(a)

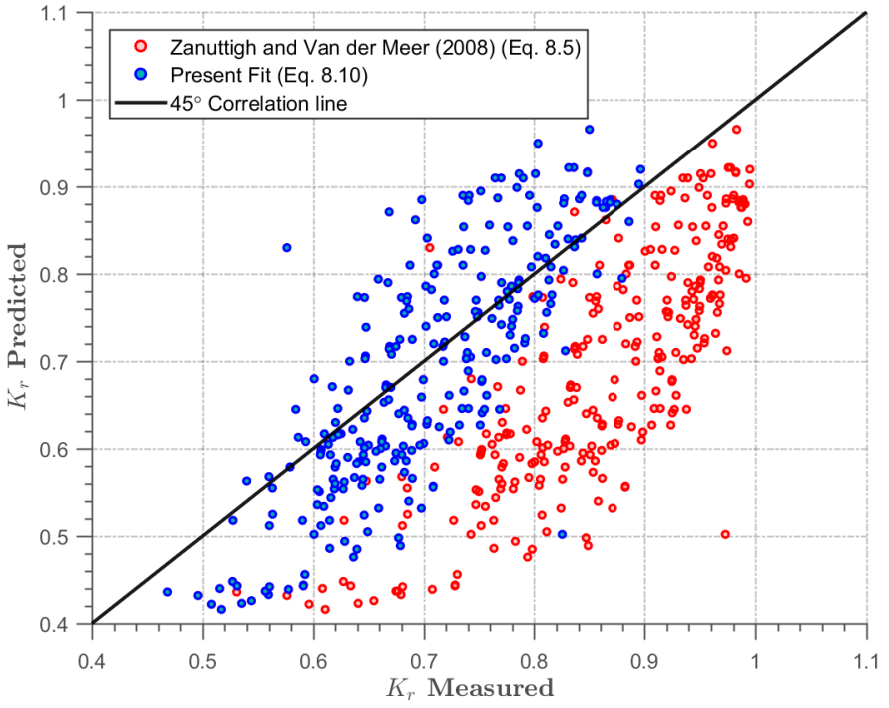

(b)

Figure 8.10 Comparison between the measured K_r and the predicted K_r of wave reflection coefficient (a) cot α = 1.5; and (b) cot α = 3.0

As shown in these figures, observed data points are well distributed either side within 45^o correlation line. It can be deduced from the slight convergence of the agreement between observed and predicted values that Equations (8.10) – (8.11) works better in defining reflection characteristics of sloping seawalls under the influence bimodal waves than Equation (8.5). The prediction of prolonged breaker index imposed longer periods in swell waves are more accurately predicted with Equations (8.10) – (8.11) than Equation (8.5). It is under-predicting K_r under the bimodal cases most especially with increasing gentle slopes. The present formulation (represented by Equations (8.10) – (8.11) will be applicable at locations exposed to local storm waves and open oceans under bimodal wave conditions.

The equations are valid within the following ranges of smooth impermeable slopes:

$0 \leq \cot \alpha \leq 1.5$ for Equation (8.9), and $0 \leq \cot \alpha \leq 1.5$

range of applicability of structure slopes to $1.5 \leq \cot \alpha \leq 4.0$ serving intervals of breaker indices within $1.0 \leq \xi_{m-1,0} \leq 4.1$ with dimensionless crest freeboard of $0.58 \leq R_c/H_{m0} \leq 4.5$.

8.4 Conclusions

This chapter has examined the reflection performance of smooth sloping impermeable aluminium seawall under bimodal sea states. Three different sloping seawalls were investigated at three different water levels to conduct 823 storm tests. An array of four wave gauges positioned around the centre (with constant water depth) were applied to effectively capture both incident and reflected wave elevations. The FFT were applied to decompose analysed wave signals from four number wave gauges into frequency components in the frequency domain. The analysed reflection response of the studied coastal seawall is highly dependent on the seawall slope and wave bimodality. The resultant reflection coefficient also increases with swell peak periods and swell percentages. From the results of the reflection tests are presented and analysed in this paper yielding an improved empirical formula to determining reflection under bimodal sea conditions. New expressions for the reflection coefficient to take into account swell driven seas with wave bimodality have been proposed.

Chapter 9

Analysis of Wave Overtopping in a Numerical Flume

The capability of the IH2VOF computational model to simulate wave overtopping of coastal seawalls is presented in Chapter. A method of managing the effect of bimodal wave overtopping is to test how more complex geometries will perform under these wave conditions in the numerical domain. Results are compared for calibration and validation of the numerical performance. Storm walls and parapets are then incorporated into the original structure geometry. Firstly I present the validated wave overtopping due to simple structures. This is followed by results of the simulated storm wall and parapet in order to reduce excess wave overtopping induced by bimodal waves. This chapter concludes by comparing the overtopping reduction capabilities of storm-walls and parapets under bimodal waves.

9.1 Tested Geometries and Cases

Figure 9.1 shows sets of possible seawall geometries that were selected for study within the numerical domain. Overall, different structure geometries are investigated to illustrate how best wave overtopping can be reduced by the incorporation of storm walls and parapets. Different geometries tested include a replication of the plain seawall

slopes already tested experimentally for validation and incorporations of both storm walls and parapets at the start of the crest with crest width B = 0.

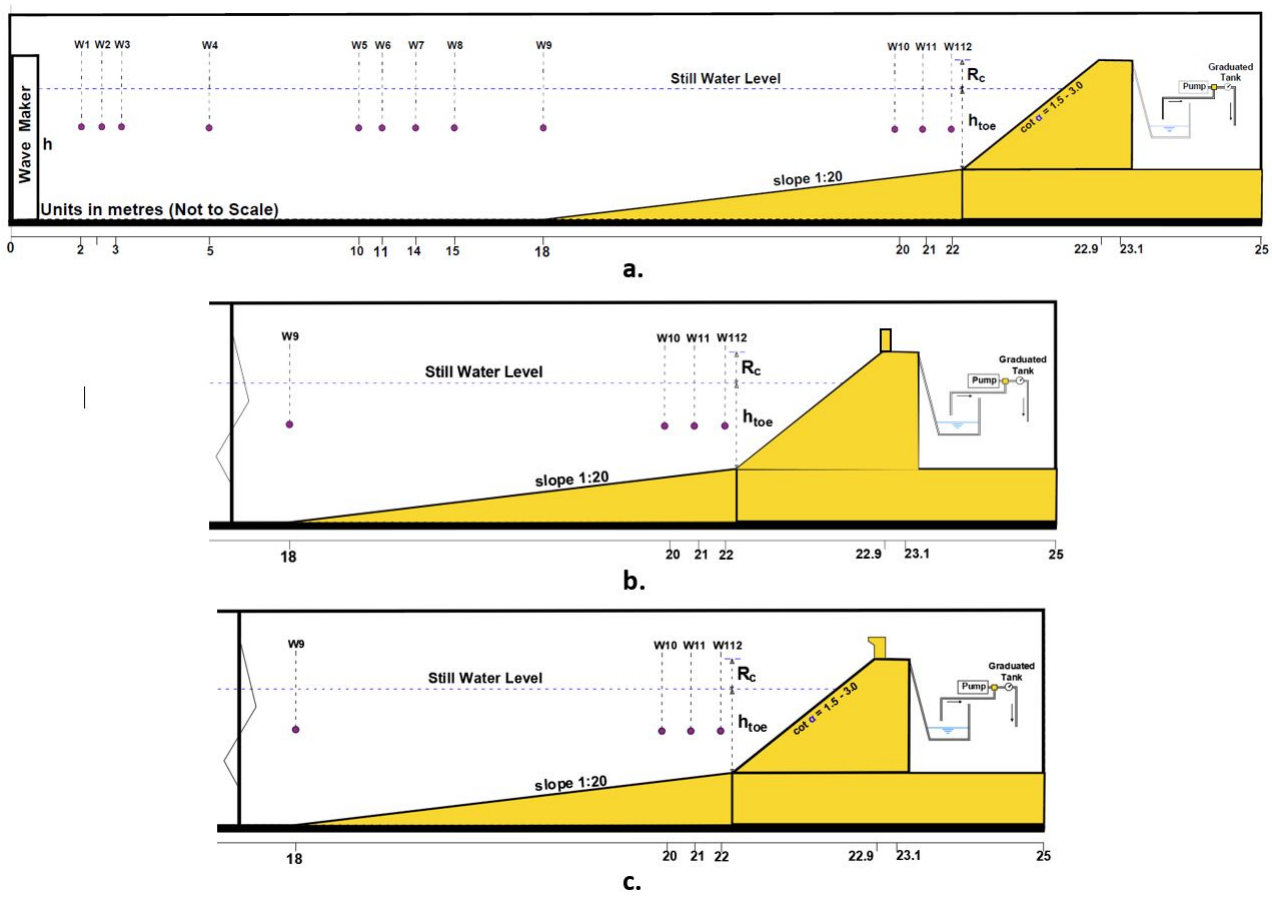

Figure 9.1 *Tested geometries for the wave overtopping simulation for plain sloping seawall with: (a) No storm wall and parapet; (b) Storm wall at B = 0 and (c) storm wall at B = 0*

The model set-up was similar to the descriptions we have in chapter 4. In the numerical tests conducted here, additional wave gauges are incorporated at the top of the crest to detect wave overtopping. Table 9.1 contains different wave conditions and water levels that are investigated. Cases with higher overtopping volumes were numerically simulated to reduce excess overtopping volumes using storm walls and parapets. Different numbers are selected for each seawall geometries: $cot\ \alpha = 1.5$ having 86 tests, $cot\ \alpha = 3.0$ having a total of 100 tests, while for the vertical seawall ($cot\ \alpha = 0.0$) has a total of 57 tests. Altogether for the numerical modelling, a total of number of 243 tests were conducted.

Table 9.1 Selected extreme wave conditions simulated in the numerical model

Test No	H_{m0} **(m)**	T_{pW} **(secs)**	T_{pS1} **(secs)**	T_{pS2} **(secs)**	T_{pS3} **(secs)**	T_{pS4} **(secs)**	$h(m)$	$cot\alpha =$ 0.0	$cot\alpha =$ 1.5	$cot\alpha =$ 3.0
T001	0.125	1.107	1.739	2.3712	3.162	3.953	0.7	0	1.5	3
T002	0.125	1.264	1.739	2.3712	3.162	3.953	0.7	0	1.5	3
T003	0.125	1.423	1.739	2.3712	3.162	3.953	0.7	0	1.5	3
T004	0.125	1.581	1.739	2.3712	3.162	3.953	0.7	0	1.5	3
T005	0.1	1.107	1.739	2.3712	3.162	3.953	0.65	0	1.5	3
T006	0.125	1.264	1.739	2.3712	3.162	3.953	0.65	0	1.5	3
T007	0.1	1.423	1.739	2.3712	3.162	3.953	0.65	0	1.5	3
T008	0.125	1.581	1.739	2.3712	3.162	3.953	0.65	0	1.5	3
T009	0.1	1.107	1.739	2.3712	3.162	3.953	0.6	0	1.5	3
T010	0.1	1.264	1.739	2.3712	3.162	3.953	0.6	0	1.5	3
T011	0.125	1.423	1.739	2.3712	3.162	3.953	0.6	0	1.5	3
T012	0.125	1.581	1.739	2.3712	3.162	3.953	0.6	0	1.5	3
T013	0.075	1.107	1.739	2.3712	3.162	3.953	0.65	0	1.5	3
T014	0.075	1.264	1.739	2.3712	3.162	3.953	0.65	0	1.5	3
T015	0.075	1.423	1.739	2.3712	3.162	3.953	0.65	0	1.5	3
T016	0.075	1.581	1.739	2.3712	3.162	3.953	0.65	0	1.5	3
T017	0.1	1.107	1.739	2.3712	3.162	3.953	0.7	0	1.5	3
T018	0.1	1.264	1.739	2.3712	3.162	3.953	0.7	0	1.5	3
T019	0.1	1.423	1.739	2.3712	3.162	3.953	0.7	0	1.5	3
T020	0.1	1.581	1.739	2.3712	3.162	3.953	0.7	0	1.5	3

9.2 Validation of Results

In order to rely on the numerical system to replicate other physical geometries or scenarios, model calibration and validation is necessary. This was achieved by applying how well the surface elevation time series and wave energy (spectra) were obtained from the numerical model, and how they conform to the expected theoretical and experimental values. The validated results are based on carefully selected vertical mesh resolution, horizontal mesh resolution, and domain sizes that are compatible with the experimental set-up. Moreover, the physical parameters have to be carefully chosen to

ensure suitable turbulence dissipation and avoid destructive interference of waves. This is because zero values are obtained for numerical wave gauges placed at those positions.

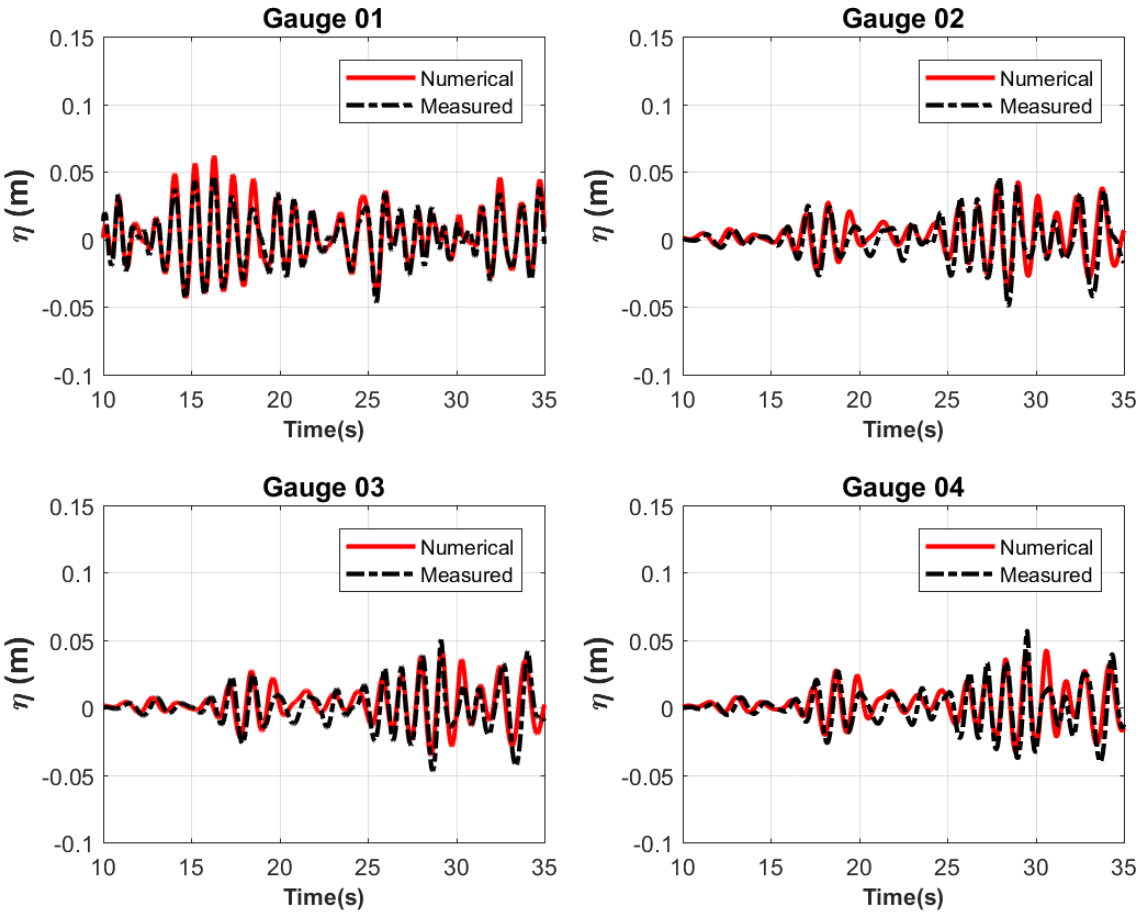

Figure 9.2 *An example of free surface validation between the numerical and experimental model obtained during this study for a wave with H_{m0} = 0.1 metres at a water depth 0.65 metres approaching a slope with* $\cot\alpha = 1.5$

Numerically reproduced wave conditions are compared with the experimental and theoretical values. At first, the output time series from the numerical domain are mostly out of phase in several cases due to incompatibility of generation sequences. It is because the numerical wave paddle start at different times with the physical model. This problem was resolved by reinforcing the boundary conditions with the same time series form the physical model. Wave gauge positions were severally calibrated until a compatible time series were obtained in the computational domain. Figures 9.2 and 9.3 show the validation of the reproduction of surface elevations and wave spectra respectively from the numerical domain.

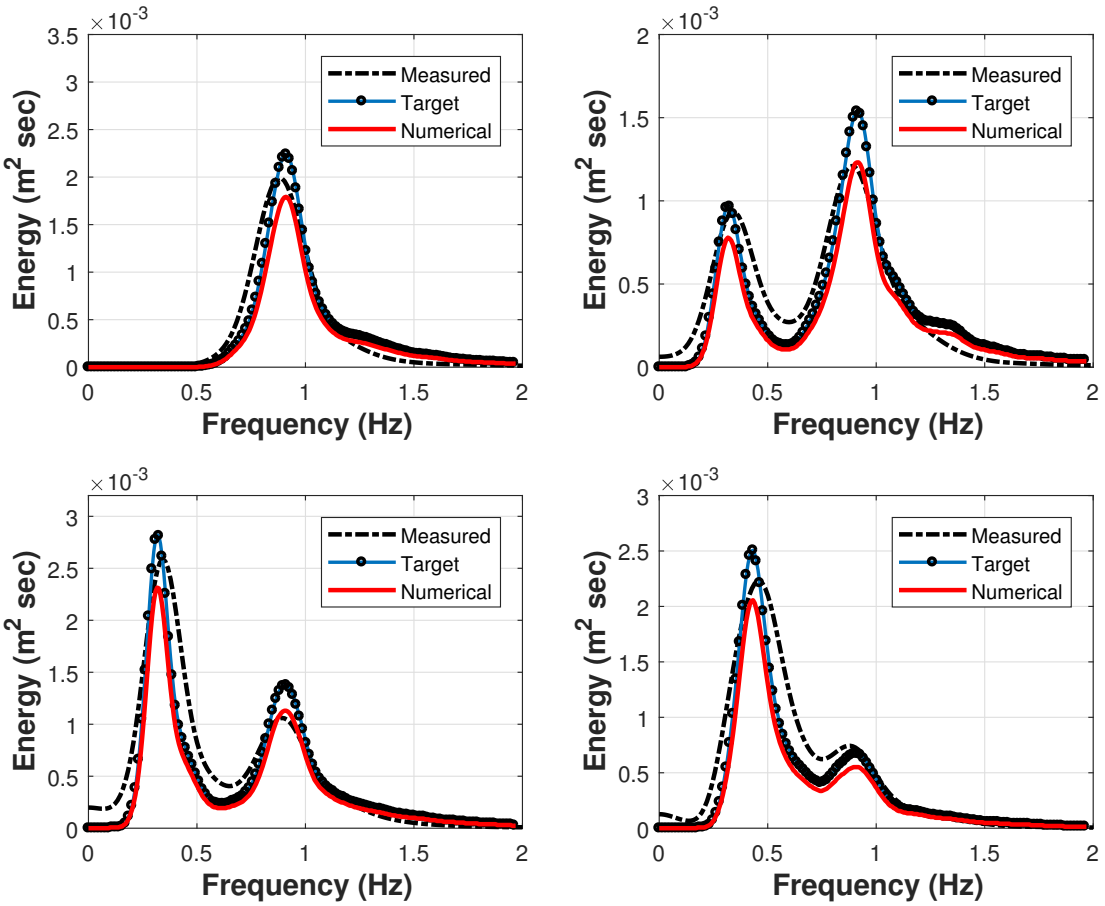

Figure 9.3 *An example of reproduction of different spectra types that are validated between the theoretical, numerical and experimental model for a wave with H_{m0} = 0.1 metres at a water depth 0.65 metres approaching a slope with* $\cot\alpha = 1.5$

As expected, good agreement was obtained in terms of the wave propagation pattern and the energy distribution within the spectra. The peak frequencies of the modal values obtained in the numerical model were well captured. The spectral values are under-predicted in this case due to extreme turbulence dissipation in the model. This may be due to the numerical inconsistencies that arise from numerical assumptions and scaling effects. However, the overall spectra energy were sufficient to describe both the theoretical and the physical wave-forcing across various frequencies for both spectra types.

9.2.1 Spectra Evolution Across Numerical Gauges

Generally across the numerical domain, the evolution of bimodal wave spectra were accurately described. Examples of the reproduction of a wave condition with a bimodal spectra of 75 % swell are presented in Figure 9.4 across the 6 wave gauges.

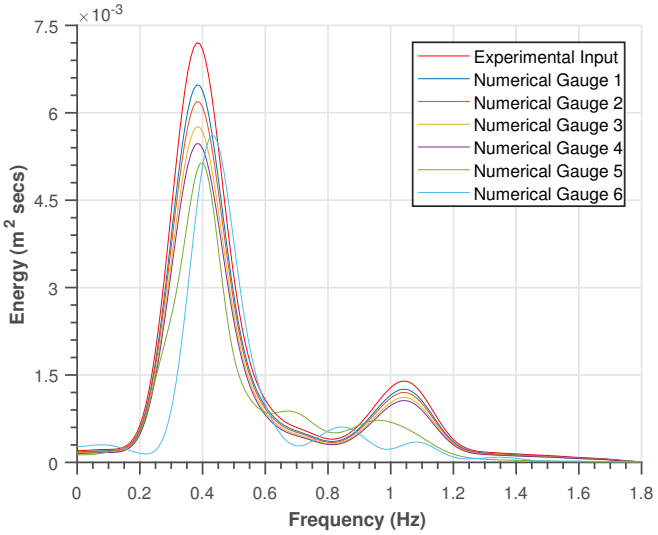

Figure 9.4 *Evolution of bimodal spectrum across different wave gauges in the numerical domain for cot* α *= 3.0 and test* $T001 - 10$ *and* 75% *swell*

As expected, similar energy patterns were maintained between the experiment and the numerical output at the peaks. Most deformations and transformations occurred with wave gauges 5 and 6 placed in sloping positions. More energy is shifted from lower to higher frequencies at these wave gauges than observed in other ones. Within the numerical domain as waves propagates, there's numerical dissipation going on in the tank as the energy spectra are decreasing with distance from the paddle from Gauge 1 near the wave paddle to Gauge 8 by the structure slope (Figure 9.4).

9.2.2 Flow Patterns in the Numerical System

Accurate modelling of the free surface and flow velocity is an essential component of a wave hydrodynamics processes. Within the IH2VOF model, the free surface and the velocity fields of wave can be accurately modelled and tracked. Figures 9.5 shows the free surface elevation of a propagating bimodal wave leading to overtopping. Figure 9.6 show examples of the flow magnitude obtained from the horizontal and vertical velocity vectors of a leading wave. The wave velocity pattern were very well described with the IH2VOF model. The velocity pattern within the crest portrays accurately the non-breaking surging wave overtopping as can be seen in the velocity magnitude as captured in the numerical model at the times shown.

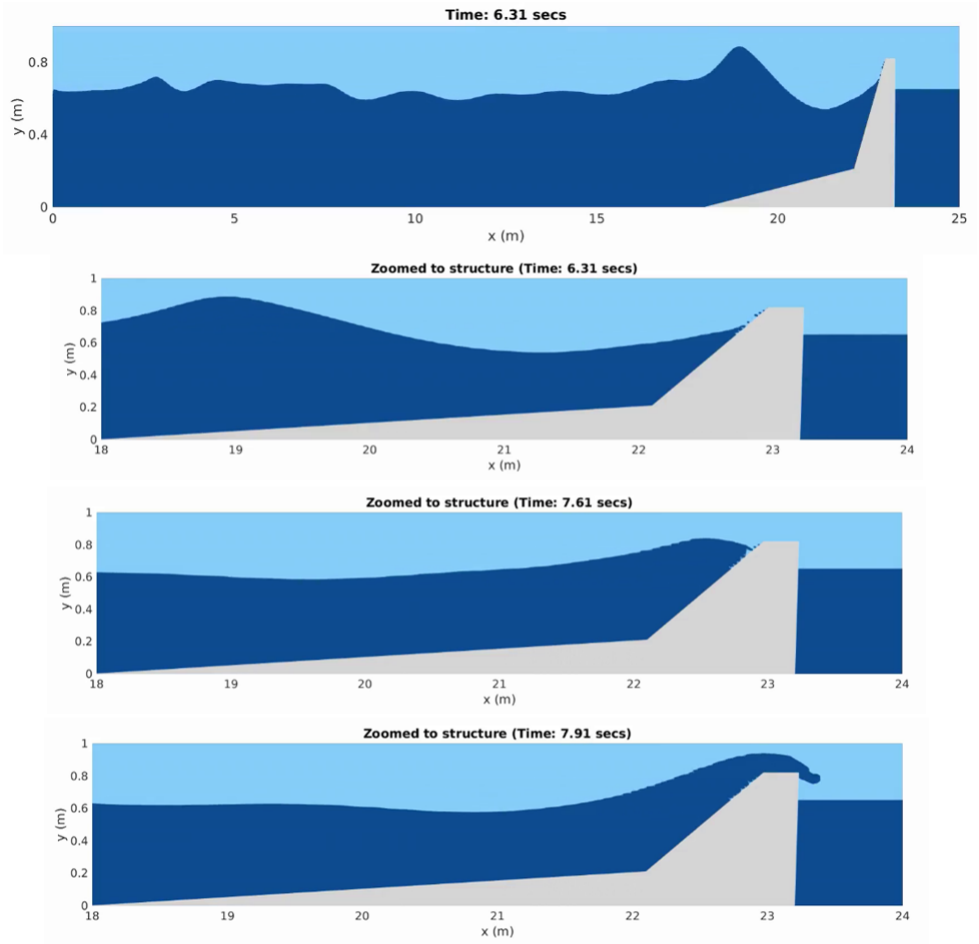

Figure 9.5 *An example of free surface by non-breaking (surging) overtopping waves with* H_{m0} *= 0.1 metres at a water depth 0.65 metres approaching a slope with* $\cot\alpha = 1.5$ *in a numerical domain IH2VOF*

Sufficient optimization of the meshes were performed to accurately visualise this behaviour. In the case shown in the following figures, the leading overtopping waves

are characterised by the highest velocity values (Figure 9.6). In some other cases these waves can be nullified by any returning reflected waves of equal or higher magnitude.

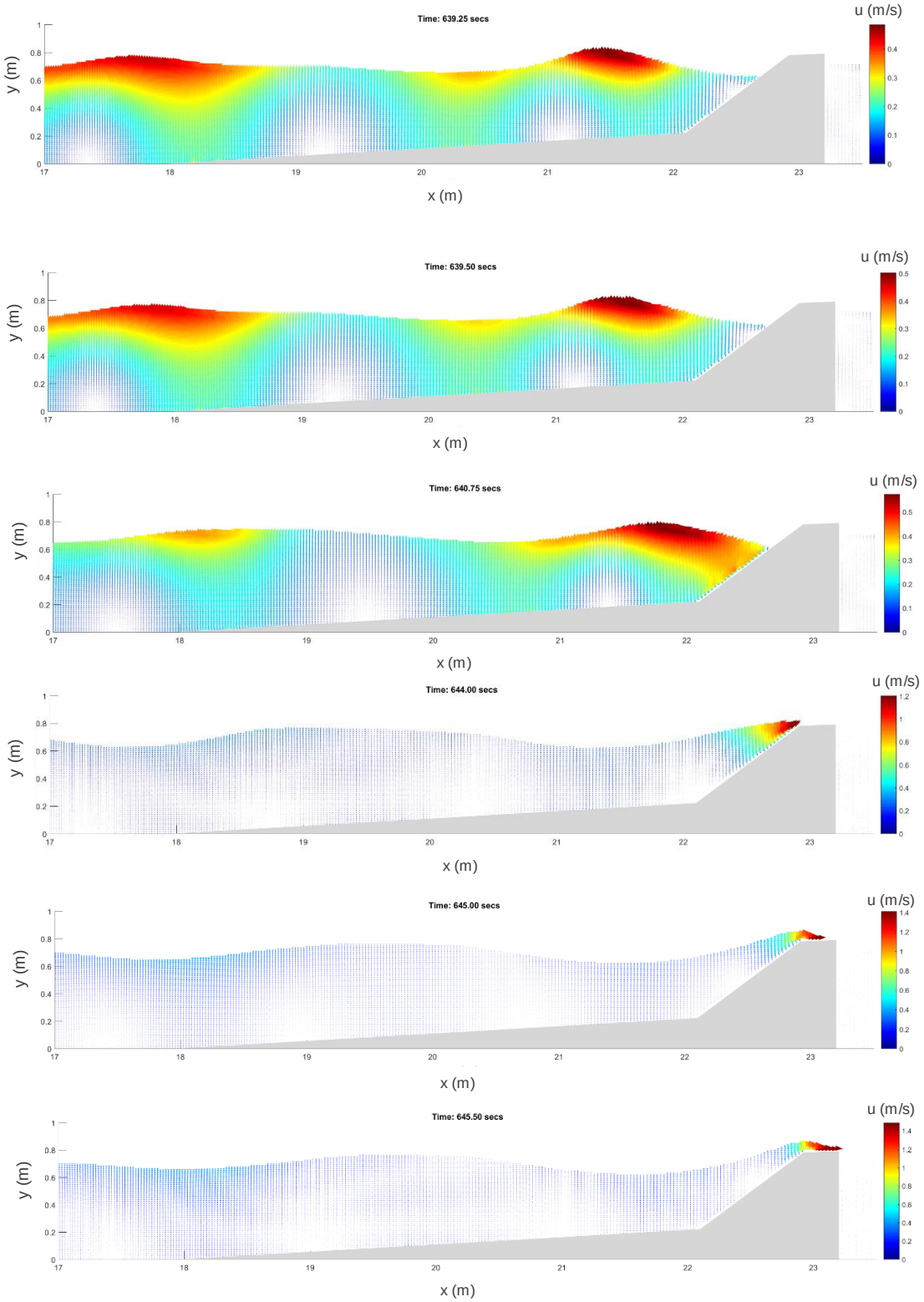

Figure 9.6 *An example of flow velocity showing non-breaking (surging) overtopping waves with H_{m0} = 0.1 metres at a water depth 0.65 metres approaching a slope with $\cot\alpha = 1.5$ in a numerical domain IH2VOF*

9.3 Determination of Wave Overtopping

It is important to derive wave overtopping estimate from the numerical results in order to compare with the experimental results. Recorded times series of the wave gauge placed on top of the crest has been applied to estimate wave overtopping. In this case, wave overtopping is computed using the method suggested in Schüttrumpf and Oumeraci (2005). Using this method, wave overtopping is computed using the product of the layer thickness $h(t)$ of the wave on top of the crest, and the depth-averaged velocity $V(t)$ at the same position. This can be expressed mathematically as shown in Equation (9.1):

$$q(t) = h(t) * v(t) \tag{9.1}$$

Figures 9.7 and 9.8 give a representation of wave overtopping thicknesses and velocities on top of the structure's crest for different percentages of the swell that are present in the sea-state.

As expected, the numerical domain accurately reproduced the times series of thicknesses and velocities of wave overtopping for different percentages of swell. The thicknesses and velocities of overtopping increases with increasing swell percentages. There is also a direct proportionality in the relationship between overtopping thicknesses and the velocity. It is the increment in the flow velocity on top of the crest that increases the thicknesses of the flow leading to more non-breaking/ flushing wave overtopping.

Moreover, this observation becomes more evident with results of the derived wave overtopping from the two figures by Equation (9.1). These are presented in Figure 9.9, which shows the mean overtopping discharge, and Figure 9.10, which shows the cumulative wave overtopping estimates.

The unimodal sea states without swell shows least overtopping thicknesses and velocities out of all cases. It is the presence of the swell in the sea-state that increases the flushing severities of the flow and causes more overtopping effects.

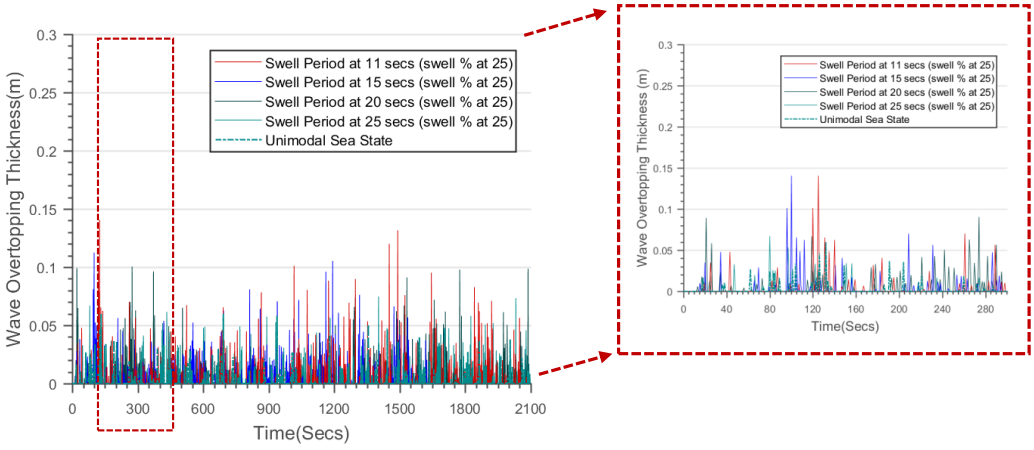

(a)

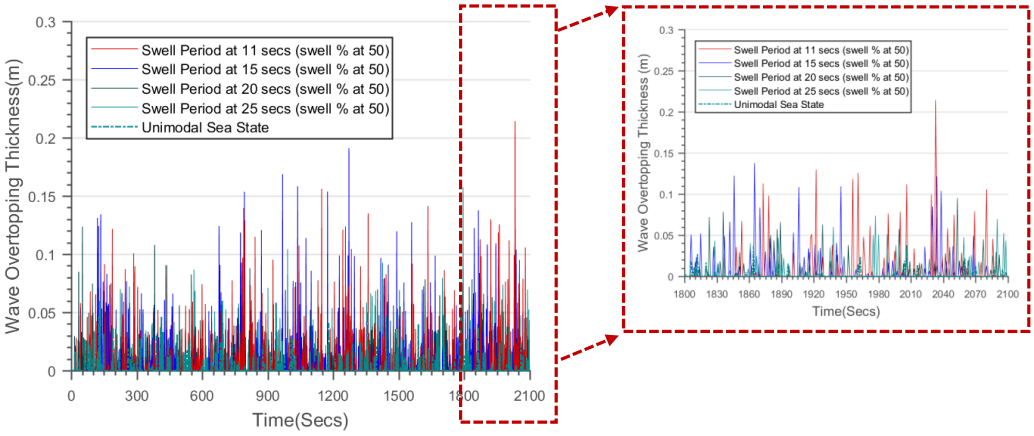

(b)

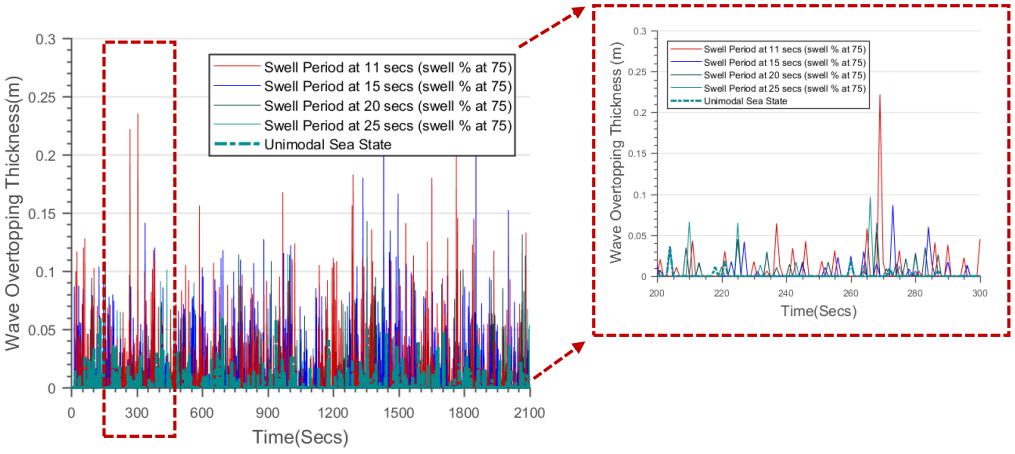

(c)

Figure 9.7 *An example of the wave overtopping thickness computed for (a) 25 % swell, (b) 50 % swell, and (c) 75 % swell*

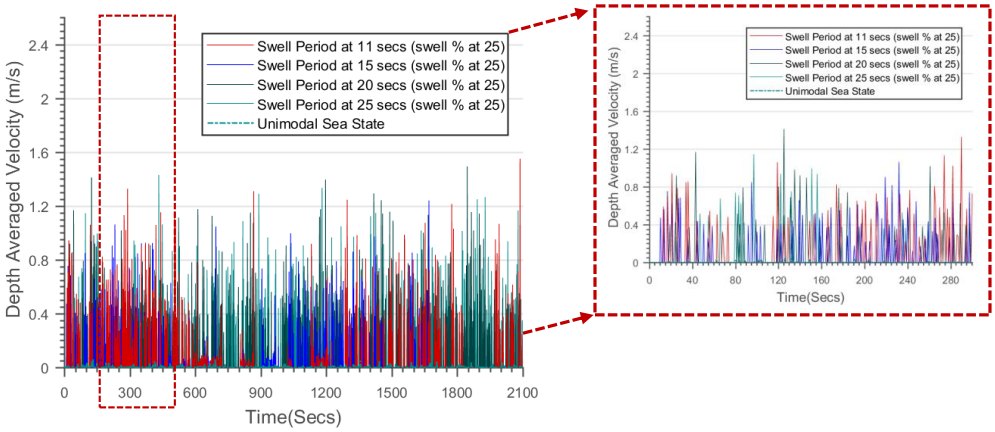

(a)

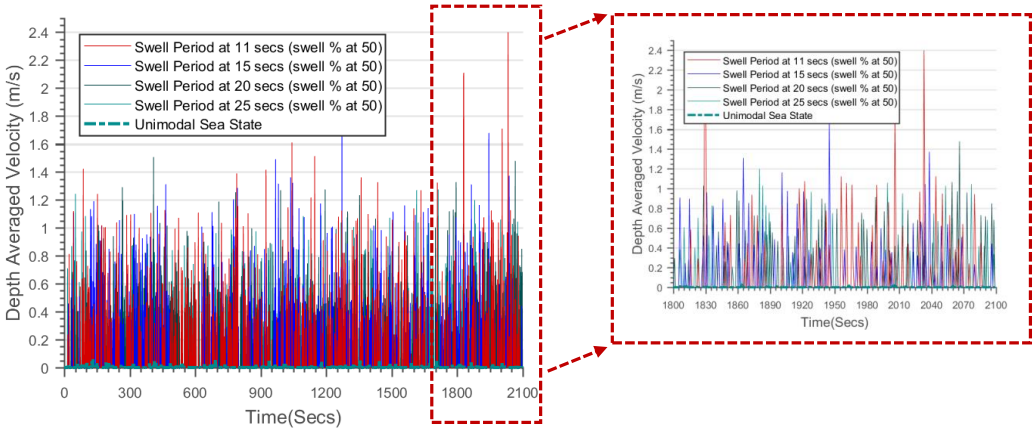

(b)

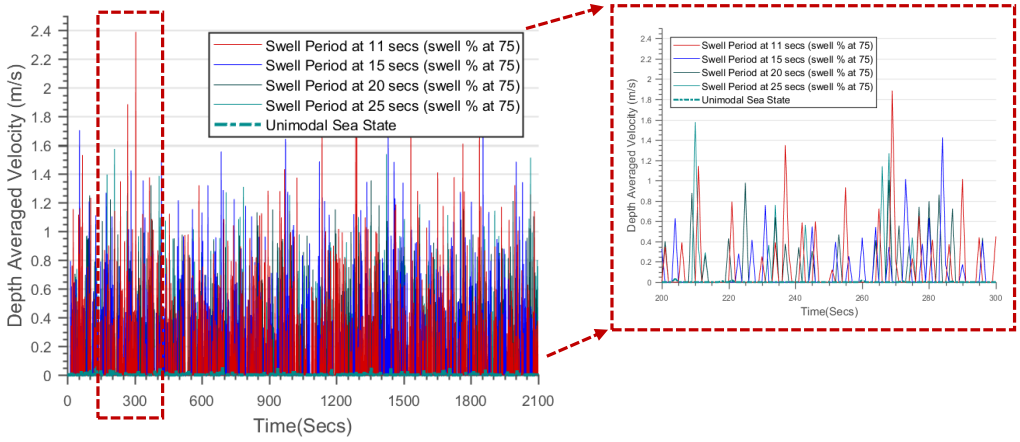

(c)

Figure 9.8 *An example of the depth-averaged velocity computed for (a) 25 % swell, (b) 50 % swell, and (c) 75 % swell*

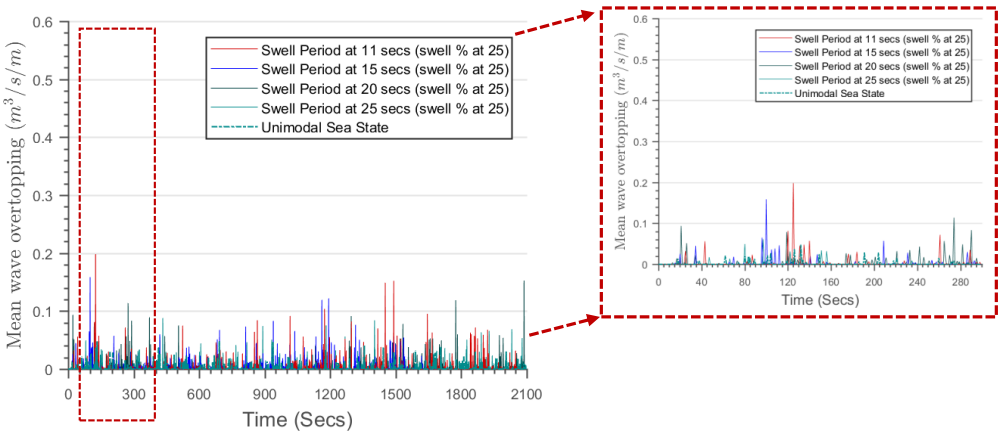

(a)

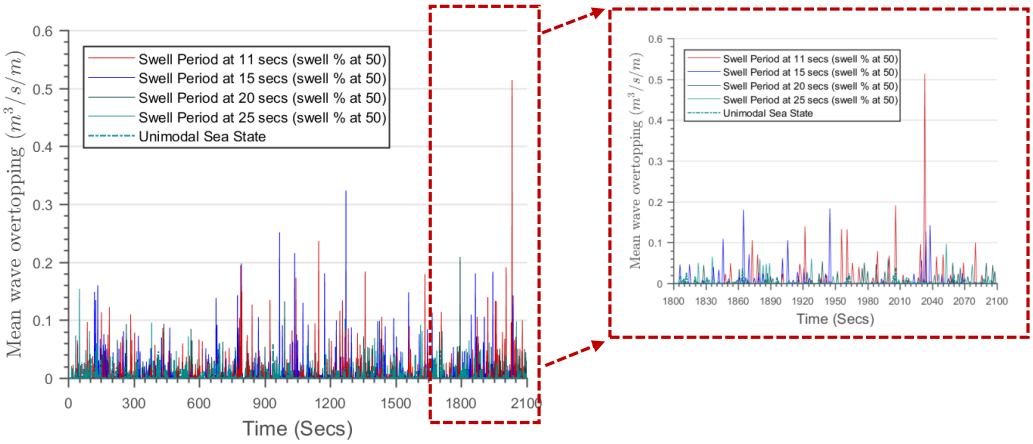

(b)

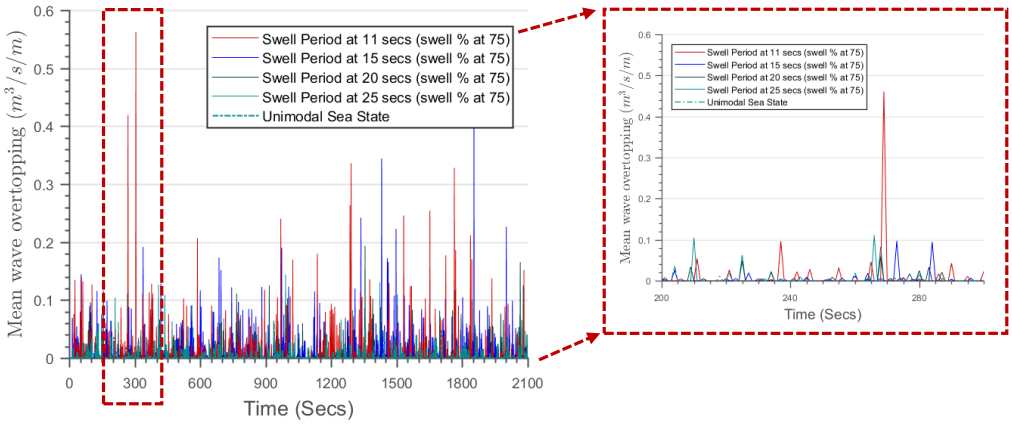

(c)

Figure 9.9 *Estimated mean wave overtopping volume from the numerical model for (a) 25 % swell, (b) 50 % swell, and (c) 75 % swell*

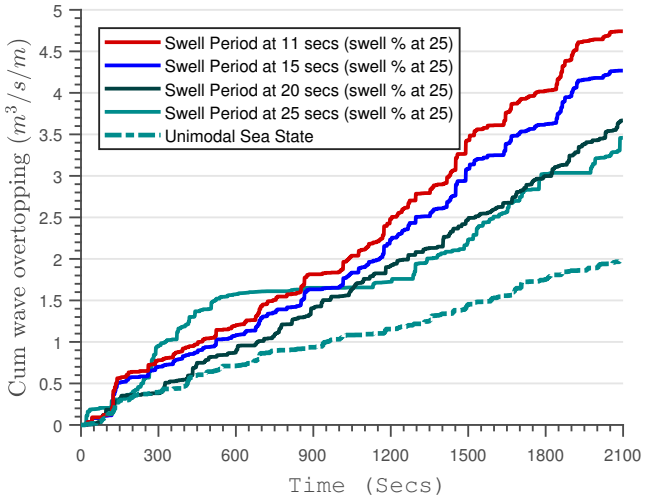

(a)

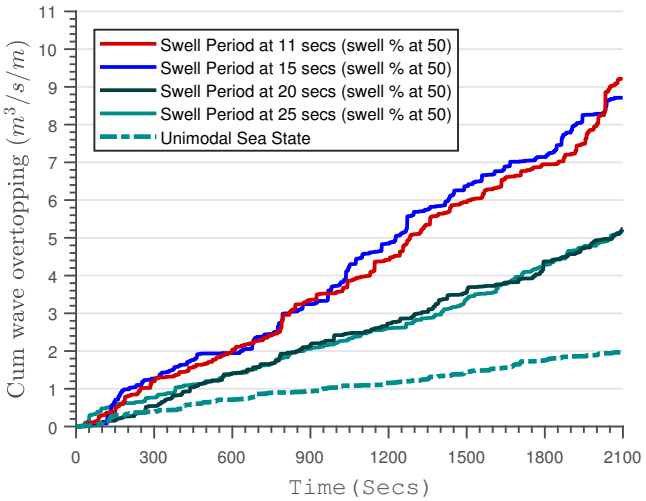

(b)

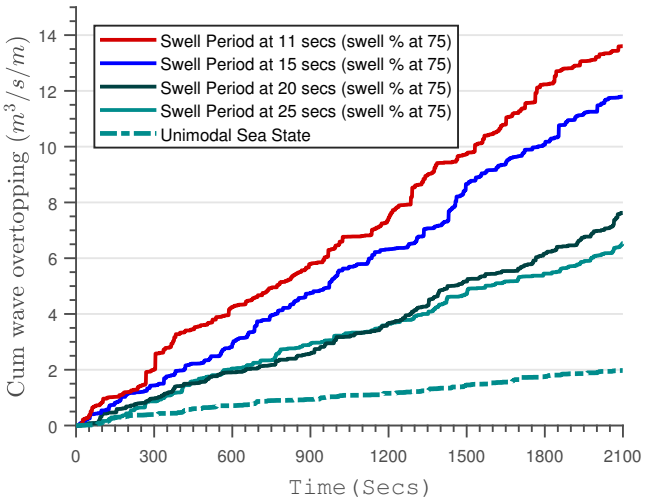

(c)

Figure 9.10 *Estimated cumulative wave overtopping volume from the numerical model for (a) 25 % swell, (b) 50 % swell, and (c) 75 % swell*

9.4 Validation of Wave overtopping Results

Figures 9.11 – 9.13 present a replot of the experimental overtopping results already reported in Chapter 6 across the three slopes investigated in this study. The validation are based on the impermeable geometry without parapet or storm wall. In this section, the dimensionless overtopping determined computationally are shown in Figures 9.11 – 9.13. Generally in the three figures, similar trends of wave overtopping are observed for both the numerical and the experimental outcomes each for different slopes. The combination of numerical and experimental overtopping for both sloping and vertical seawalls are represented by Figures 9.11 and 9.12. It can be observed that overtopping (determined from the numerical model) are lesser than values that are empirically determined. It is the loss in the energy of the computational domain that is responsible for this event. However, similar trends are observed in both numerical and experimental domains.

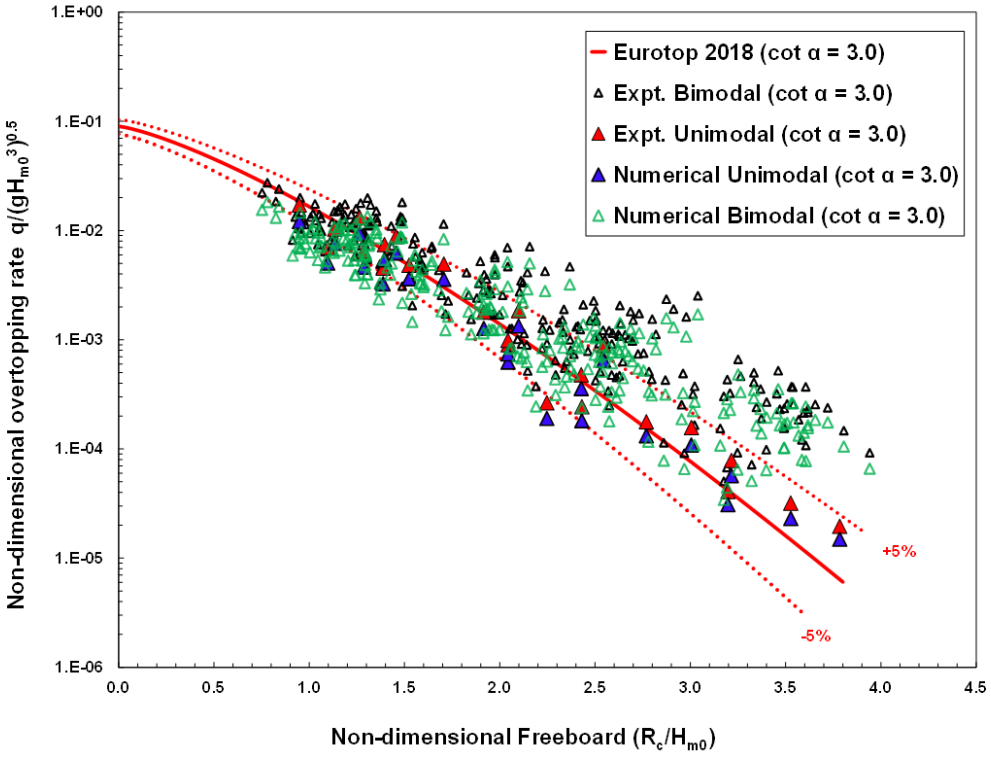

Figure 9.11 *Plots of computational and experimental non-dimensional overtopping rate* $\frac{q}{\sqrt{H_{m0}^3}}$ *against non-dimensional crest freeboard* $\frac{R_c}{H_{m0}}$ *plotted within the corresponding prediction band of EurOTop (2018) obtained for a sloping seawall with cot* $\alpha = 3.0$

Moreover, numerically determined overtopping values from unimodal sea states are accurately predicted by the corresponding 90 % confidence limits of EurOTop (2018).

However, bimodal seas were under-predicted across slopes with cot $\alpha = 1.5$ and cot $\alpha = 3.0$ and cot $\alpha = 0.0$.

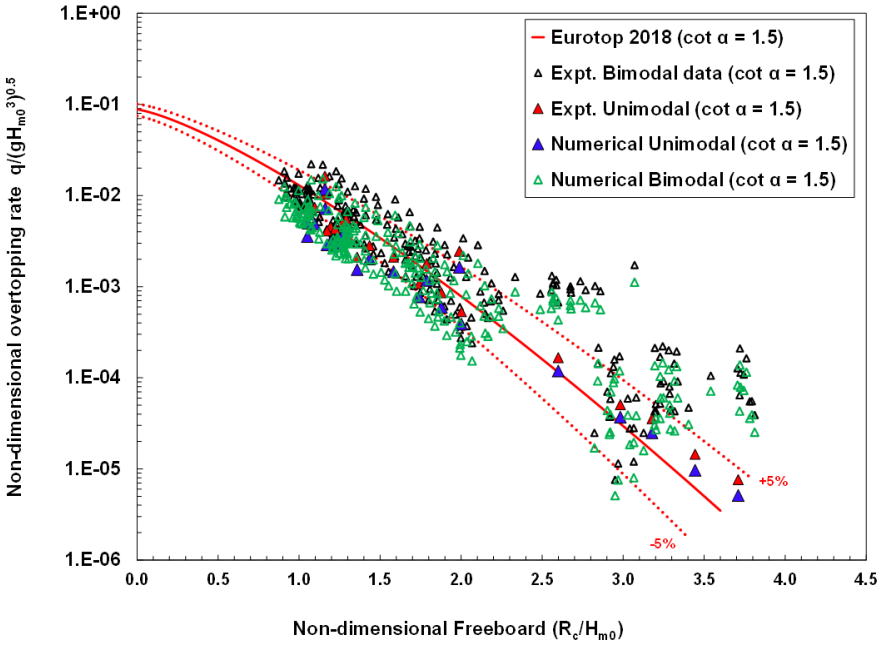

Figure 9.12 *Plots of computational and experimental non-dimensional overtopping rate* $\frac{q}{\sqrt{H_{m0}^3}}$ *against non-dimensional crest freeboard* $\frac{R_c}{H_{m0}}$ *plotted within the corresponding prediction band of EurOTop (2018) obtained for a sloping seawall with cot* $\alpha = 1.5$.

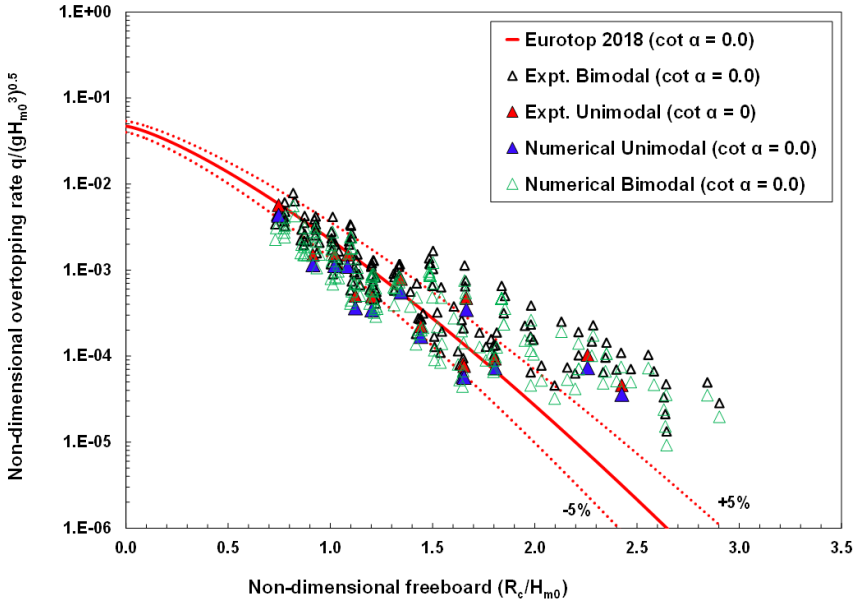

Figure 9.13 *Plots of computational and experimental non-dimensional overtopping rate* $\frac{q}{\sqrt{H_{m0}^3}}$ *against non-dimensional crest freeboard* $\frac{R_c}{H_{m0}}$ *plotted within the corresponding prediction band of EurOTop (2018) obtained for a sloping seawall with cot* $\alpha = 3.0$

9.5 Verification of Numerical and Experimental Results

It is necessary to verify the conformance of the numerical model with the experimental results. To achieve this purpose, two methods of coefficient of determination (R^2) and Nash–Sutcliffe efficiency (NSE) suggested by Krause et al. (2005) are applied. Basically R^2 can be computed using Equation (9.2).

$$R^2 = \left(\frac{\sum_{i=1}^{n}(E_i - \overline{E})(N_i - \overline{N})}{\sqrt{\sum_{i=1}^{n}(E_i - \overline{E})^2}\sqrt{\sum_{i=1}^{n}(N_i - \overline{N})^2}} \right)^2 \tag{9.2}$$

The equation describes the linear dependence between the numerical and the experimental variables expressed in the form of simple correlation coefficients existing between the datasets. In Equation (9.2), E_i represents the recorded dimensionless overtopping from the experimental results, N_i are numerical non-dimensional overtopping. Also, $\overline{E}$ and $\overline{N}$ are the mean values of n number wave overtopping datasets recorded in both experimental and numerical models. Values of R^2 lies between 0 and 1. It is the value of R^2 that describes the strength of linear association between E and N. The value of 1 shows the strongest positive correlation, while $R^2 = 0$ shows that no agreement exists between the two variables compared.

To validate the model using the efficiency, Equation (9.3) is applied. The equation was first proposed by Nash and Sutcliffe (1970). Values of NSE ranges from negative infinity ($-\infty$) to 1, a perfectly matched model between experimental and computational values using the NSE criteria should be greater than 80 %. In general, there is a strong agreement if the value of NSE is zero. Negative values of NSE shows that the experimental results presents a better predictor of the captured data.

$$NSE = 1 - \left(\frac{\sum_{i=1}^{n}(E_i - N_i)^2}{\sum_{i=1}^{n}(E_i - \overline{E})^2} \right) \tag{9.3}$$

Table 9.2 Values of R^2 and *NSE* computed between the numerical and experimental values for the smooth impermeable seawalls investigated during present study

Parameters	**Equations (9.1 & 9.2)**	
Item	R^2 **(-)**	**NSE (-)**
cot α = 3.0	0.93	0.701
cot α = 1.5	0.91	0.723
cot α = 0.0	0.89	0.699

Figure 9.14 presents the comparison to verify the relationship between E_i and the N_i across the three with cot $\alpha = 3.0$, cot $\alpha = 1.5$ and cot $\alpha = 0.0$ investigated. As visible in the figure, strong correlation (90 %) exists between numerical and experimental values for the three slopes. Table 9.2 presents summary of R^2 values across the three slopes.

In the present study, as shown in Table 9.2, for the three slopes, simulated results from the computational domain closely agree with the observed data with an efficiency of approximately 70 %. In this case, it is a high degree of closeness because of the numerical complexities of resolving bimodal wave patterns.

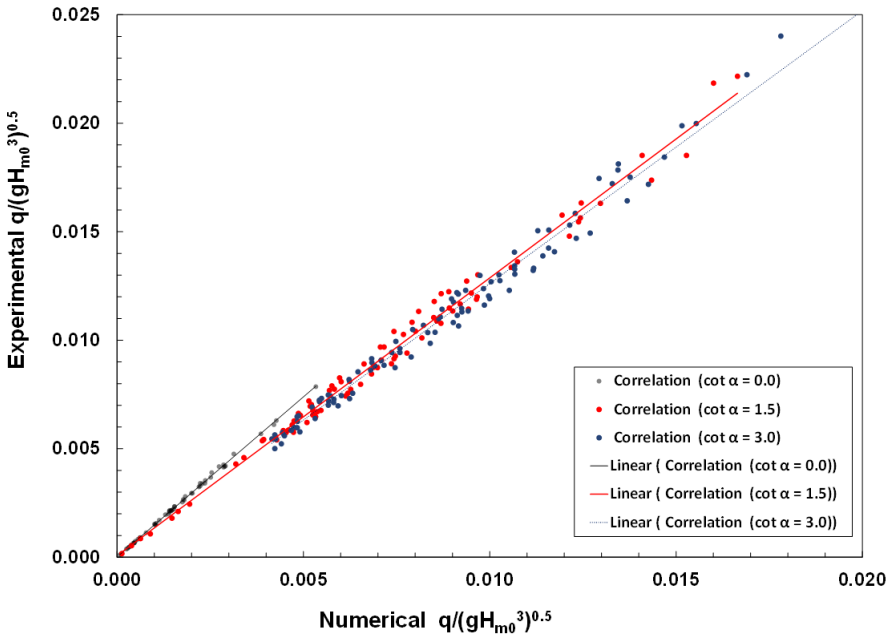

Figure 9.14 *Verification of computational and experimental non-dimensional overtopping rate* $\frac{q}{\sqrt{H_{m0}^3}}$ *across the three slopes with cot* $\alpha = 3.0$*, cot* $\alpha = 1.5$ *and cot* $\alpha = 0.0$

9.6 Bimodal Wave Overtopping Due to Storm Walls and Parapets

To reduce the excessive overtopping emerging from bimodal waves, the seawall geometry was modified using a storm wall and a parapet (Figure 9.15). The storm wall and the parapet were placed at a position with berm width B = 0 (in both cases), and selected test series (Table 9.1) were simulated using the validated model for the most vulnerable slope (cot $\alpha = 3.0$). Also these falls within the lower dimensionless freeboards ($0.5 \leq \frac{R_c}{H_{m0}} \leq 2.5$) with excessive overtopping.

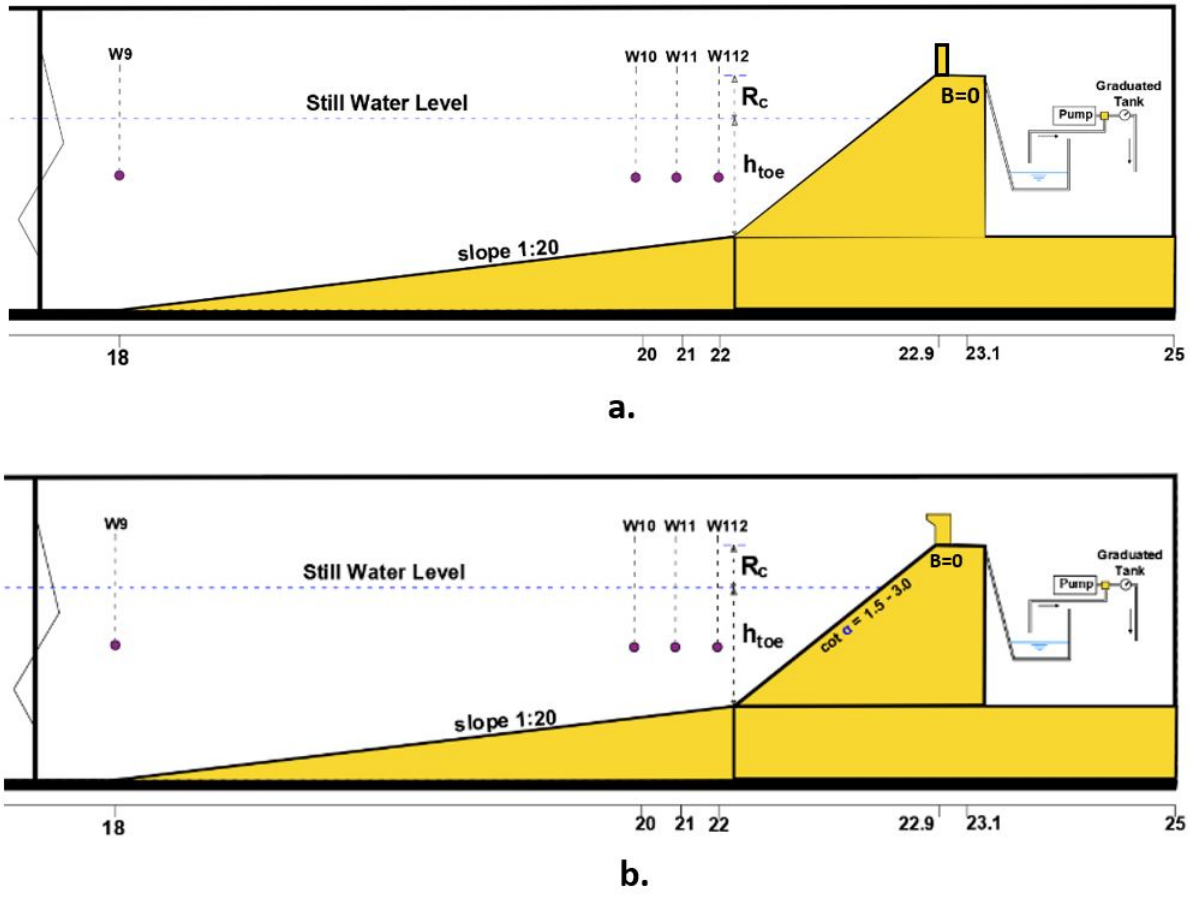

Figure 9.15 *Tested geometries for the wave overtopping simulation for plain sloping seawall with: (a) Storm wall at B = 0; (b) Parapet at B = 0*

Figure 9.16 shows the relationship between the non-breaking non-dimensional overtopping rate $\frac{q}{\sqrt{H_{m0}^3}}$ against the non-dimensional crest freeboard $\frac{R_c}{H_{m0}}$. It was plotted within the corresponding prediction band of EurOTop (2018) and present fit using Equation (7.13) obtained for a sloping seawall with cot $\alpha = 3.0$ numerically obtained between the storm walls and the parapet for cot $\alpha = 3.0$. Results obtained for the

original sea-wall geometry with cot $\alpha = 3.0$ were also presented for comparison. As clearly shown in Figure 9.16, bimodal overtopping rates were significantly reduced by the incorporation of both the storm wall and the parapets. However, with more scattering still experienced at the dimensionless crest freeboard above.

Generally as expected, the parapet clearly provides more overtopping reduction at B = 0 position. The parapet provides a more efficiency at reduction of overtopping volumes in up to 13.4 % at that portion of the crest (i.e., B = 0). Most overtopping estimates are far lower than the predicted overtopping and corresponding 90 % confidence limits of EurOTop (2018) for the bimodal cases are presented in each plot. The fitness obtained for present dataset with Equation (7.13) present a better prediction of bimodal overtopping than the For these cases, there is no means of checking any evidence of heteroscedasticity between data groups. This is because no bimodal dataset is available for to determine such analysis in this type of seawall.

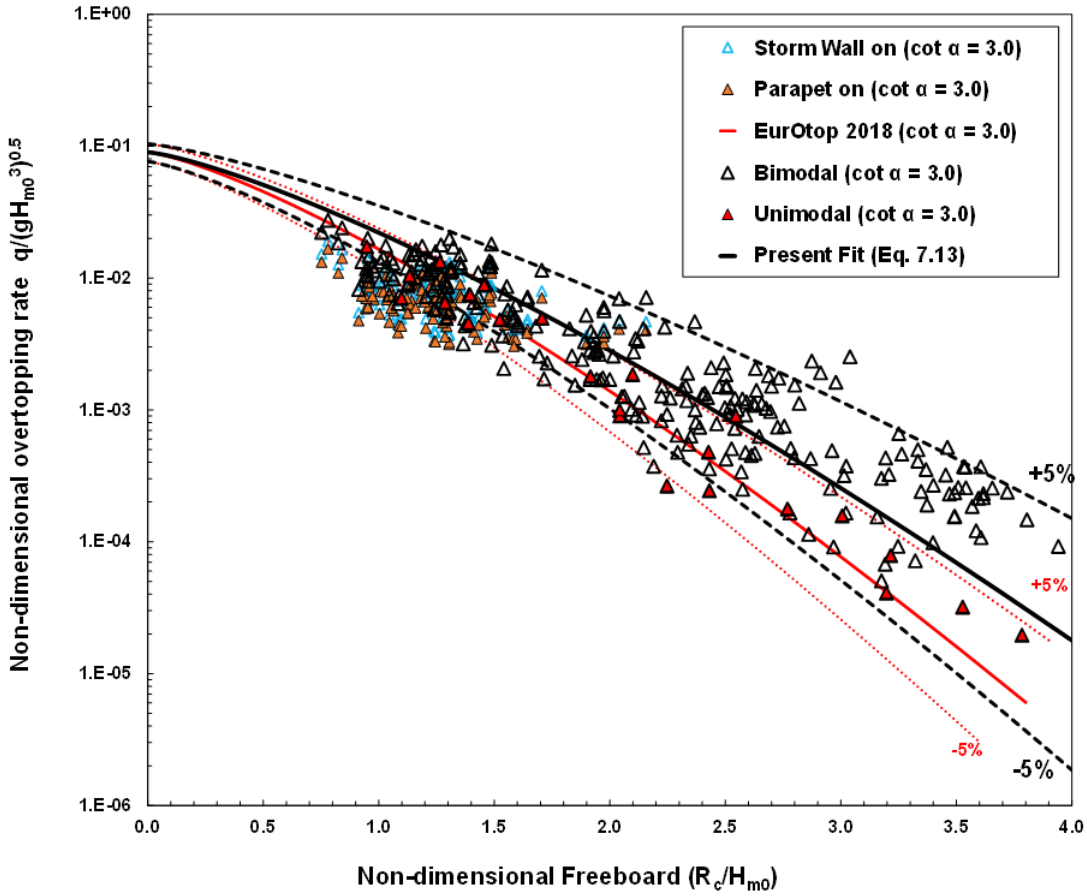

Figure 9.16 *Verification of computational and experimental non-dimensional overtopping rate* $\frac{q}{\sqrt{H_{m0}^3}}$ *for with cot* $\alpha = 3.0$*: (a) Storm wall at crest width B = 0; (b) Parapet at crest width B = 0*

9.7 Conclusion

A numerical approach to validate numerical wave overtopping has been presented in this chapter. It has also been complimented with the use of more complex geometries to reduce overtopping occurrences by bimodal waves. Significantly and similarly to the experiment, numerically determined overtopping values from unimodal sea states are more accurately predicted within the corresponding 90 % confidence limits of EurOTop (2018) than in bimodal seas. The computational model resolved the numerical complexities of propagating bimodal wave patterns. The agreement between simulated results from the computational domain and the observed empirical data is with a correlation R^2 of 90 % and efficiency greater than 70 %. Moreover, bimodal overtopping rates were drastically reduced by the incorporation of the storm wall and the parapets. However, as suggested in previous literatures, the parapets provided more reduction of up to 13 % than the implemented storm wall in this case.

Chapter 10

Conclusions and Future Research

In this chapter, the main conclusions that are drawn from each aspects investigated are presented. The overview of the objectives and methodology of the thesis was first presented. It was followed by summaries of results obtained to fulfil each objective.

10.1 Overview of the Thesis Contribution

The main problem studied in this thesis concerns the modelling of wave overtopping of coastal defences under storm-induced bimodal waves. This has been assessed by developing a specific form of energy-conserved bimodal spectrum that have varying proportions of swell, while at the same time containing a fixed amount of energy with the unimodal wind seas for easy comparison. Numerical and experimental methods have been applied to selected bimodal spectra and their corresponding unimodal sea states to compare the overtopping tendencies of smooth, sloping and vertical impermeable seawalls. The main conclusions are presented in each section below.

10.2 Effects of Swell in Energy-Conserved Bimodal Seas

Presence of swell in a bimodal sea state will significantly alter the non-linearity of the sea-state despite the fact that the energy content of the sea-state remain the same as the unimodal sea. This would in turn, effect the characteristics of waves derived from the unimodal and bimodal spectra, whether near a wave maker, or near a structure. There is an increasingly smooth and continuous exponential relationship between the skewness and kurtosis as the swell percentage or the peak period grows in an energy

conserved bimodal sea. The Weibull distributions produced the best fitness for wave patterns of high swell percentages in this study. As the swell frequency and percentages changes in a bimodal sea, the relationship between the skewness and the kurtosis are tending towards a unimodal sea. The distribution of the waveheight on the Rayleigh model shows that the non-linearity increases with the distance away from the wave maker. This could be caused by the development of other physical processes like reflection, wave breaking, and other shoaling processes arising from wave-structure interactions. In agreement with previous studies, the unimodal sea states showed the greatest non-linear behaviour however, non-linearity patterns vary as the swell grows. The Rayleigh distribution could not properly represent bimodal seas with wider spectral width and also overpredicts waveheight at low exceedances in these conditions.

10.3 Effects of Swell Percentage on Wave Overtopping

The wave overtopping performance of sloping impermeable seawalls under the influence of bimodal sea conditions have been investigated using 823 wave overtopping tests. Different percentages of swell components were derived for each sea state. Both unimodal and equivalent bimodal waves were tested in order to compare effects of bimodality. With wave overtopping derived from a minimum of 1000 waves, results show that relative wave overtopping increases with increasing swell percentages. It was hypothesised that the increased wave overtopping for longer waves/swell percentage is due to a change in wave behaviour, where more waves are surging than breaking on the structure. Also, for fixed wave conditions, more wave overtopping was observed with increasing slope mildness as established in previous studies. The unimodal tests agree closely with predictions using the EurOtop formulae. EurOtop formulae underpredict the observed wave overtopping rates for bimodal conditions, (even when using the $T_{m-1,0}$ period for such cases). A simple modification to the existing formula for non-breaking waves was proposed that accounts for the presence of swell percentages under bimodal conditions.

10.4 Effects of Swell Peak Periods on Wave Overtopping

Based on the same experiments, effects of swell appearance at different peak periods on wave overtopping were equally analysed. It was observed that swell occurrence at

lower peak periods produce the uppermost impact of wave overtopping on each slope investigated than those at higher peak periods. These observations are characterised by more non-linearities when compared to effects posed by swell percentages. Modification to the existing formula for non-breaking waves under the presence of swell peak periods under bimodal conditions have not been provided in this thesis. Further analysis would be necessary to establish better relationship between swell peak periods with overtopping estimates.

10.5 Effects of Spectral Characteristics on Wave Overtopping

Influences of different spectra characteristics such as the narrowness parameter, the broadness parameter, and the peakedness parameter on wave overtopping were analysed for different spectrum types in this thesis. It was observed that spectra characteristics of each parameter were strongly correlated with swell percentages in the sea for different spectra types. Overtopping increases as spectra values of each parameter reduces. However, spectra values tend to be approaching asymptotic values for both the narrowness and the broadness parameters. Increasing trends of swell percentage in a bimodal sea could produce enormous wave overtopping with tendencies of more significant flooding. Broad-banded sea conditions yield less wave overtopping intensity than highly peaked bimodal seas. Overtopping is highly sensitive to the succession of wave groups and wave patterns in the random wave sequence than overtopping caused by individual peaks. However, bimodal waves occurring from different percentages of wind waves while the swell content of the sea remain constant were not analysed in this study.

10.6 Reflection Analysis of Coastal Seawalls Under Bimodal seas

At locations exposed to local storm waves and open oceans, long period swell waves can be present leading to bimodal wave conditions. Existing literature provides little guidance on reflection characteristics in this situation. The experimental results from this thesis was applied to fill the gap in our understanding of seawall performance under bimodal wave conditions. As in previous literatures, the analysed reflection response of the studied coastal seawall is highly dependent on the seawall slope and wave bimodality. However, the resultant reflection coefficient increases with swell peak

periods and swell percentages. From these analyses, an improved formulation for the reflection coefficient to take into account swell driven seas with wave bimodality have been proposed.

10.7 Wave Overtopping in a Numerical Flume

The overtopping from the experiment was applied to validate the wave overtopping from the numerical model. More geometries involving a storm wall and a parapet were also simulated computationally to test their reductive capability on bimodal waves. Although simulating the storm walls and parapets in the computational domain is a very challenging task because of the complexity of numerically describing the structures' geometry. The challenges of multiple sampling of double-peak frequencies described by bimodal waves were resolved. There is a great agreement between simulated results from the computational domain and the observed empirical data. Moreover, bimodal overtopping rates were drastically reduced by the incorporation of the storm wall and the parapets as expected. However, a further reduction of up to 13 % was obtained in the overtopping of parapet simulation than storm walls.

10.8 Recommendations for Further Research

Having extensively studied bimodal waves in this present study, it would be essential in future to consider research in the following areas:

1. Large sets of experiments on the individual wave overtopping threats of bimodal waves. Emphasis of this study should be based on maximum wave overtopping occurrences.

2. Considering using rubble mounds (Figure 10.1) in model experiments and using extended experimental studies to examine structural responses to wave bimodality.

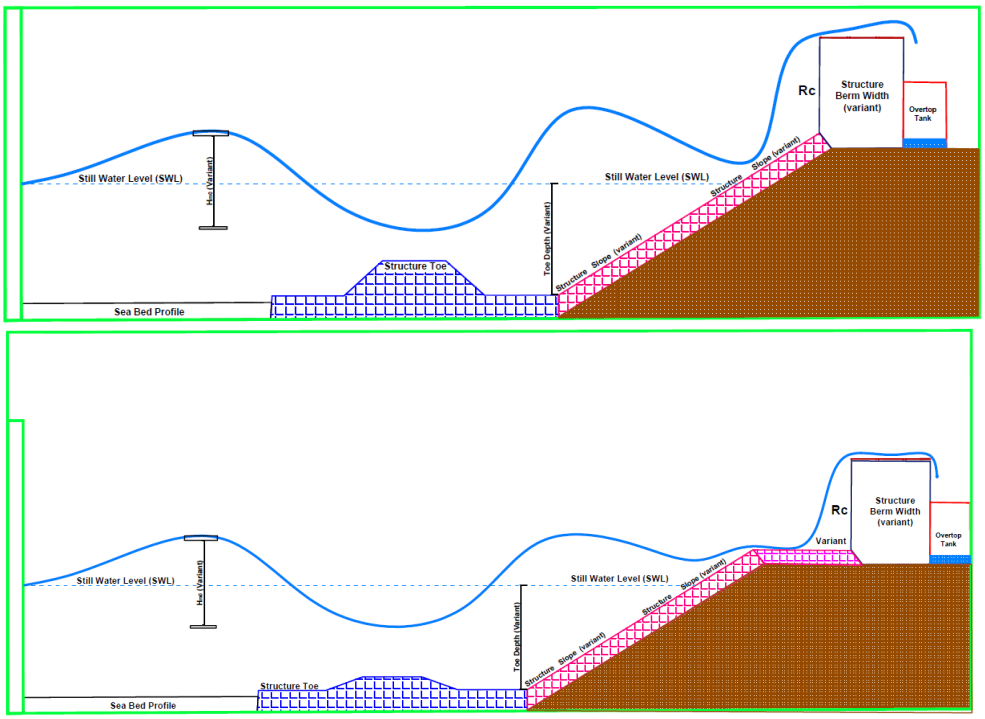

Figure 10.1 *Further modifications to coastal seawalls in future research.*

3. Examining the driven phenomena of force effects on different coastal structures under bimodal storms.

4. It is essential to replicate this entire study in a three-dimensional flume for a more realistic representation of the overtopping effects on coastal seawalls. Worst effects of wave overtopping usually occur in a normally incident wave-structure interaction, however, incorporating the directional component of the spectra into the energy-conserved bimodal spectra would be a useful aspect of research in a wave basin.

References

Ahrens, J. P. and Heimbaugh, M. S. (1988). Irregular wave runup on riprap revetments. *Journal of Waterway, Port, Coastal, and Ocean Engineering*, 114(4):524–530.

Allsop, N. and Hettiarachchi, S. (1989). Reflections from coastal structures. In *Coastal Engineering 1988*, pages 782–794.

Allsop, W., Bruce, T., Pearson, J., and Besley, P. (2005). Wave overtopping at vertical and steep seawalls. *Marine Engineering*, 158:103–114.

Altomare, C., Crespo, A. J., Domínguez, J. M., Gómez-Gesteira, M., Suzuki, T., and Verwaest, T. (2015). Applicability of smoothed particle hydrodynamics for estimation of sea wave impact on coastal structures. *Coastal Engineering*, 96:1–12.

Altomare, C., Suzuki, T., Chen, X., Verwaest, T., and Kortenhaus, A. (2016). Wave overtopping of sea dikes with very shallow foreshores. *Coastal Engineering*, 116:236–257.

Aminti, P. and Franco, L. (1988). Wave overtopping on rubble mound breakwaters. *Coastal Engineering*, pages 770–781.

Andersen, T. L. and Burcharth, H. F. (2009). Three dimensional investigations of wave overtopping on rubble mound structures. *Coastal Engineering*, 55:180–189.

Andersen, T. L., Frigaard, P., and Burcharth, H. F. (2014). Lecture notes for the course in water wave mechanics, 117 pages.

Aziztayfun, M. (2009). Statistics of nonlinear wave crests and groups. *Ocean Engineering*, 33.

Bakhtiary, A. Y., Hajivalie, F., and javan, A. H. (2010). Steady streaming and flow turbulence in front of vertical breakwater with wave overtopping. *Applied Ocean Engineering*, 55:484–498.

Batchelor, G. K. (1974). Introduction to fluid dynamics. *Cambridge university press, 226 pages*.

Battjes, J. A. (1974). Surf similarity. *Proc. 14th Conf. on Coastal Eng. ASCE*, pages 460–480.

Battjes, J. A. and Groenendijk, H. W. (2000). Wave height distributions on shallow foreshores. *Coastal Engineering*, 40(3):161–182.

Biesel F, S. F. (1951). Etude theorique d'un type d'appareil a la houle. *La Houille Blanche*, 2:156–65.

Boccotti, P. (2000). Wave Mechanics for Ocean Engineering, Amsterdam. *Elsevier Science B.V. 479 pages*.

Bradbury, A., Allsop, W., and Stephens, R. (1988). Hydraulics performance of breakwater crown walls. *Hydraulics Research Wallingford, 108 pages*.

Bradbury, A., Mason, T., and Poate, T. (2007). Implications of the spectral shape of wave conditions for engineering design and coastal hazard assessment–evidence from the english channel. In *10th International Workshop on Wave Hindcasting and Forecasting and Coastal Hazard Symposium North Shore, Oahu, Hawaii, November*, pages 11–16.

Briganti, R., Dodd, N., Pokrajac, D., and O'Donoghue, T. (2011). Nonlinear shallow water modelling of boredriven swash description of the bottom boundary layer. *Coastal Engineering*, 58:463–477.

Brocchini, M., Bernetti, R., Mancinelli, A., and Albertini, G. (2001). An efficient solver for nearshore flows based on the weighted average flux method. *Coastal Engineering*, 43(2):105–129.

Brodtkorb, P. A., Johannesson, P., Lindgren, G., Rychlik, I., Rydén, J., and Sjö, E. (2000). WAFO–a Matlab Toolbox for the Analysis of Random Waves and Loads. *Proc. 10'th Int. Offshore and Polar Eng. Conf., ISOPE, Seattle, USA*, 3:343–350.

Burcharth, H. (1978). The effect of wave grouping on on-shore structures. *Coastal Engineering*, 2:189–199.

Burcharth, H. and Hughes, S. (2002). Part vi, design of coastal project elements. *Coastal Engineering Manual; US Army Corps of Engineers:Washington, DC, USA, 720 pages*.

Burcharth, H. F. and Andersen, T. L. (2007). Overtopping of rubble mound breakwaters with front reservoir. *Coastal Engineering 2006:(In 5 Volumes)*, pages 4605–4615.

Canelas, R., Crespo, A., Domínguez, J., Ferreira, R., and Gómez-Gesteira, M. (2016). Users guide for dualsphysics code. *User Manual*, pages 1–140.

Casella, E., Rovere, A., Pedroncini, A., Mucerino, L., Casella, M., Cusati, L. A., Vacchi, M., Ferrari, M., and Firpo, M. (2014). Study of wave runup using numerical models and low altitude aerial photogrammetry a tool for coastal management. *Estaurine coastal and shelf science*, 26(149):160–167.

Cavannie, A., Arhan, M., and Ezraty, R. (1976). A statistical relationship between individual heights and periods of storm waves. In *In Proc. 1'st Int. Conf. on Behaviour of Offshore Structures, BOSS*, pages 354–360, Trondheim, Norway.

Chorin, A. J. (1968). Numerical solution of the navier-stokes equations. *Maths Computation*, 22:745–762.

Chorin, A. J. (1969). On the convergence of discrete approximations of the navier-stokes equations. *Maths Computation*, coe232:341–353.

Coelho, C., Cruz, T., and Roebeling, P. (2016). Longitudinal revetments to mitigate overtopping and flooding effectiveness costs and benefits. *Ocean and Coastal Management*, 134:93–102.

Coeveld, E., Van Gent, M., and Pozueta, B. (2005). Neural network manual for nn_overtopping program. *CLASH WP8, 38 pages*.

Cox, D. T. and Scott, C. P. (2001). Exceedance probability for wave overtopping on a fixed deck. *Ocean Engineering*, 28(6):707–721.

Crespo, A., Gómez-Gesteira, M., and Dalrymple, R. A. (2007). Boundary conditions generated by dynamic particles in sph methods. *Computer mater contin*, 5:173–184.

Davidson, M., Bird, P., Bullock, G., and Huntley, D. (1996). A new non-dimensional number for the analysis of wave reflection from rubble mound breakwaters. *Coastal Engineering*, 28(1—4):93–120.

De Rouck, J., Verhaeghe, H., and Geeraerts, J. (2009a). Crest level assessment of coastal structures — General overview. *Coastal Engineering*, 56(2):99–107.

De Rouck, J., Verhaeghe, H., and Geeraerts, J. (2009b). Crest level assessment of coastal structures — general overview. *Coastal Engineering*, 56(2):99–107.

De Waal, J. P. and van der Meer, J. W. (1993). Wave runup and overtopping on coastal structures. *Coastal Engineering*, pages 1758–1771.

del Jesus, M., Lara, J. L., and Losada, I. J. (2012). Three-dimensional interaction of waves and porous coastal structures:part i:numerical model formulation. *Coastal Engineering*, 64:57–72.

Didier, E., Neves, D., Martins, R., and Neves, M. (2014). Wave interaction with a vertical wall:{SPH} numerical and experimental modeling. *Ocean Engineering*, 88:330–341.

Dong, Z. and Zhan, J. M. (2009). Numerical modeling of wave evolution and runup in shallow water. *Hydrodynamics*, 21:731–738.

Du, Y., Pan, S., and Chen, Y. (2010). Modelling the effect of wave overtopping on nearshore hydrodynamics and morphodynamics around shore-parallel breakwaters. *Coastal Engineering*, 57(9):812–826.

Forristall, G. (1978). On the Statistical Distribution of Wave Heights in a Storm. *Geophysical Research*, 83(No. C5):2353–2358.

Franco, L., de Gerloni, M., and van der Meer, J. (1994). Wave overtopping on vertical and composite breakwaters. *Proceedings from 24th International Conference on Coastal Engineering Kobe, ASCE, New York, pages 1030–1045*.

Franco, L., Geeraerts, J., Briganti, R., Willems, M., Bellotti, G., and De Rouck, J. (2009). Prototype measurements and small-scale model tests of wave overtopping at shallow rubble-mound breakwaters:the Ostia-Rome yacht harbour case. *Coastal Engineering*, 56(2):154–165.

Gallach Sanchez, D., Illegems, M., Willems, Y., Troch, P., and Kortenhaus, A. (2016). Experimental study of average overtopping performance on steep low-crested structures for shallow water conditions. *Coastlab 2016*, pages 1–10.

Gao, R., Ren, B., Wang, G., and Wang, Y. (2012). Numerical modelling of regular wave slamming on subface of open-piled structures with the corrected sph method. *Applied ocean research*, 34:173–186.

Garrido, J. M. and Medina, J. R. (2012). New neural network-derived empirical formulas for estimating wave reflection on jarlan-type breakwaters. *Coastal Engineering*, 62:9–18.

Goda, Y. (2010). *Random Seas and Design of Maritime Structures*. World Scientific Publishing Co. Pte. Ltd., 708 pages.

Goda, Y., Kishira, Y., and Kamiyama, Y. (1975). Laboratory investigation on the overtopping rates of coastal structures. *Ports and harbour research institute*, 14:3–44.

Greenwood, B. and Osborne, P. D. (1990). Vertical and horizontal structure in cross-shore flows:an example of undertow and wave set-up on a barred beach. *Coastal Engineering*, 14(6):543–580.

Guanche, R., Losada, I. J., and Lara, J. L. (2009). Numerical analysis of wave loads for coastal structure stability. *Coastal Engineering*, 56(5—6):543–558.

Guedes Soares, C. (1984). Representation of Double-Peaked Sea Wave Spectra. *Ocean Engineering*, (11):185–207.

Gui, Q., Dong, P., Shao, S., and Chen, Y. (2015). Incompressible {SPH} simulation of wave interaction with porous structure. *Ocean Engineering*, 110, Part A:126–139.

Hasselmann, K., Barnett, T., Bouws, E., Carlson, H., Cartwright, D., Enke, K., Ewing, J., Gienapp, H., Hasselmann, D., Kruseman, P., Meerburg, A., Muller, P., Olbers, D., Ritcher, K., Sell, W., and Walden, H. (1973). Measurements of wind-wave growth and swell decay during the Joint North Sea Wave Project (JONSWAP). *Dtsch. Hydrogr*, A8(12).

Hedges, T. and Reis, M. (1998). Random wave overtopping of simple sea walls:a new regression model. *Proceedings of the Institution of Civil Engineers*, 130(1):0001–0010.

Hedges, T. and Shareef, M. (2003). Predicting seawall overtopping by bimodal seas. *Coastal Engineering 2002:Solving Coastal Conundrums*, pages 2153–2164.

Higuera, P., Lara, J. L., and Losada, I. J. (2013a). Realistic wave generation and active wave absorption for navier–stokes models:application to openfoam®. *Coastal Engineering*, 71:102–118.

Higuera, P., Lara, J. L., and Losada, I. J. (2013b). Simulating coastal engineering processes with openfoam®. *Coastal Engineering*, 71:119–134.

Higuera, P., Lara, J. L., and Losada, I. J. (2014). Three-dimensional interaction of waves and porous coastal structures using openfoam®. part i:formulation and validation. *Coastal Engineering*, 83:243–258.

Higuera, P., Losada, I. J., and Lara, J. L. (2015). Three-dimensional numerical wave generation with moving boundaries. *Coastal Engineering*, 101:35–47.

Hirt, C. W. and Nichols, B. D. (1981). Volume of fluid (vof) method for the dynamics of free boundaries. *Journal of computational physics*, 39(1):201–225.

Hsiao, S.-C. and Lin, T.-C. (2010). Tsunami-like solitary waves impinging and overtopping an impermeable seawall:experiment and {RANS} modeling. *Coastal Engineering*, 57(1):1–18.

Hu, K., Mingham, C., and Causon, D. (2000). Numerical simulation of wave overtopping of coastal structures using the non linear shallow water equations. *Coastal Engineering*, 41(4):433–465.

Hubbard, M. E. and Dodd, N. (2002). A 2d numerical model of wave run-up and overtopping. *Coastal Engineering*, 47(1):1–26.

Hunt, A. (2003). *Extreme waves, overtopping and flooding at sea defences*. PhD thesis, University of Oxford, 258 pages.

Iooss, B. and Lemaître, P. (2015). A review on global sensitivity analysis methods. In *Uncertainty management in simulation-optimization of complex systems*, pages 101–122. Springer.

Iribarren, C. and Nogales, C. (1949). Protection des ports. *XVIIth Int. Nav. Congress Section II*, Comm. 4(XVIIth):31–80.

Israeli, M. and Orszag, S. A. (1981). Approximation of radiation boundary conditions. *Journal of computational physics*, 41(1):115–135.

Kashima, H., Hirayama, K., and Hasegawa, I. (2010). Experimental study on wave overtopping rate of long period swell on seawall. *Journal of Japan Society of Civil Engineers, Ser B2*, 66(1):716–720.

Kimura, A. (1980). Statistical properties of random wave groups. In *Coastal Engineering 1980*, pages 2955–2973.

Kissling, K., Springer, J., Jasak, H., Schütz, S., Urban, K., and Piesche, M. (2010). A coupled pressure based solution algorithm based on the volume of fluid approach for two or more immiscible fluids. *V European Conference on Computational Fluid Dynamics ECCOMAS CFD, 14–17 pages*.

Kortenhaus, A., Oumeraci, H., Geeraerts, J., De Rouck, J., Medina, J., and González-Escrivá, J. (2005). Laboratory effects and further uncertainties associated with wave overtopping measurements. In *Coastal Engineering 2004:(In 4 Volumes)*, pages 4456–4468. World Scientific.

Krause, P., Boyle, D., and Bäse, F. (2005). Comparison of different efficiency criteria for hydrological model assessment. *Advances in geosciences*, 5:89–97.

Lara, J., Losada, I., and Guanche, R. (2008). Wave interaction with low-mound breakwaters using a {RANS} model. *Ocean Engineering*, 35(13):1388–1400.

Lara, J. L., Ruju, A., and Losada, I. . (2011). RANS modelling of long waves induced by a transient wave group on a beach. In *Proc. R. Soc. A 467*, pages 1212–1242.

Lin, P. and Liu, P. L. F. (1998). A User's Manual for a Breaking Wave Model. *User Manual School of Civil and Environmental Engineering Cornell University Ithaca NY 14853, 44 pages*.

Liu, Z. and Frigaard, P. (2001). Generation and analysis of random waves. *Laboratoriet for Hydraulik og Havnebygning, Instituttet for Vand Jord og Miljoeteknik Aalborg Universitet, 41 pages*.

Longuet-Higgins, M. S. (1952). On the statistical distribution of the heights of sea waves. *Journal of Marine Research*, 11:245-266.

Longuet-Higgins, M. S. (1983). On the joint distribution of wave periods and amplitudes in a random wave field. *Proceedings of the Royal Society of London. A. Mathematical and Physical Sciences*, 389(1797):241–258.

Lorenzo, A. M., Meer, J. v. d., and Hawkes, P. (2001). Effects of bi-modal waves on overtopping:application of UK and Dutch prediction methods. In *Coastal Engineering 2000*, pages 2114–2127.

Losada, M. A. and Gimenez-Curto, L. A. (1981). An approximation to the failure probability of maritime structures under a sea state. *Coastal Engineering*, 5:147–157.

Madsen, O. S. (1971). On the generation of long waves. *Geophysical research*, 76:8672–8783.

Mansard, E. P. and Funke, E. R. (1980). The measurement of incident and reflected spectra using a least squares method. *Proceedings 17th ICCE, Sydney*, pages 154–172.

Marthinsen, T. and Winterstein, S. (1992). On the skewness of random surface waves. In *Proc. 2'nd Int. O shore and Polar Eng. Conf., ISOPE,*, pages 472–478.

Maza, M., Lara, J. L., and Losada, I. J. (2015). Tsunami wave interaction with mangrove forests:a 3-d numerical approach. *Coastal Engineering*, 98:33–54.

Maza, M., Lara, J. L., and Losada, I. J. (2017). Training manuals for IH-2VOF numerical model. *Reports on the implementation of the IH2VOF Model, 280 pages*.

McCabe, M., Stansby, P., and Apsley, D. (2013). Random wave runup and overtopping a steep sea wall:shallow-water and boussinesq modelling with generalised breaking and wall impact algorithms validated against laboratory and field measurements. *Coastal Engineering*, 74:33–49.

Miche, M. (1951). Le pouvoir reflêchissant des ouvrages maritimes exposés à l'action de la houl. *Ann. Ponts Chausées*, (121):285–319.

Mizanur, R. S. M. and Hanif, C. M. (1995). Flood routing in channels with flood plains. *Journal of Hydrology*, (171):75–91.

Monaghan, J. J. (1992). Smoothed particle hydrodynamics. *Astrophysics*, 30:543–574.

Monaghan, J. J. and Kos, A. (1999). Solitary waves on a cretan beach. *Waterways ports and coasts*, 125:63–69.

Naess, A. (1985). On the distribution of crest-to-trough waveheights. *Ocean Engineering*, 12(3):221–234.

Nash, J. and Sutcliffe, J. (1970). River forcasting using conceptual models, 1. A discussion of principles. *Journal of Hydrology*, 10:280–290.

Nassar, K. and Negm, A. (2016). Determination of optimum wave reflection of seawalls via experimental modeling. In *Scour and Erosion:Proceedings of the 8th International Conference on Scour and Erosion (Oxford, UK, 12-15 September 2016)*, page 255.

Neelamani, S. and Sandhya, N. (2003). Wave reflection characteristics of plane, dentated and serrated seawalls. *Ocean Engineering*, 30(12):1507–1533.

Numata, A. (1976). Laboratory formulation for transmission and reflection at permeable breakwaters of artificial blocks. *Coastal Engineering in Japan*, 19(1):47–58.

Nørgaard, J. Q. H. and Andersen, T. L. (2016). Can the rayleigh distribution be used to determine extreme wave heights in non-breaking swell conditions? *Coastal Engineering*, 111:50–59.

Ochi, M. K. (2005). *Ocean waves:the stochastic approach*, volume 6. Cambridge University Press, 331 pages.

Ohyama, T., Kioka, W., and Tada, A. (1995). Applicability of numerical models to nonlinear dispersive waves. *Coastal Engineering*, 24(3—4):297–313.

Ohyama, T. and Nadaoka, K. (1994). Transformation of a nonlinear wave train passing over a submerged shelf without breaking. *Coastal Engineering*, 24(1—2):1–22.

Orimoloye, S., Horrillo-Caraballo, J., Karunarathna, H., and Reeve, D. (2019a). Modelling wave overtopping of steep impermeable structures under bimodal sea conditions. *Coastal Structures 2019*, pages 1211–1221.

Orimoloye, S., Karunarathna, H., and Reeve, D. E. (2019b). Effects of swell on wave height distribution of energy-conserved bimodal seas. *Journal of Marine Science and Engineering*, 7(3):79.

Owen, M. (1980). Design of seawalls allowing for wave overtopping. *Hydraulic Station Wallingford, Oxon OX10 8BA*, HR Report number Ex 924, 96 pages.

Owen, M. (1982). Overtopping of sea defences. *Proceedings from Conference Hydraulic Modelling of Civil Engineering Structures BHRA University of Warwick Coventry*, pages 469–480.

P. J. Hawkes and T. Coates and R. J. Jones (1998). Impacts of Bimodal Seas on Beaches, Hydraulic Research. *Hr Wallingford Report*, page 80.

Panizzo, A., Bellotti, G., and de Girolamo, P. (2002). Application of wavelet transform analysis to landslide generated waves. *Coastal Engineering*, 44:349–358.

Park, H. and Cox, D. T. (2016). Empirical wave run-up formula for wave, storm surge and berm width. *Coastal Engineering*, 115:67–78.

Pedersen, J. and Burcharth, H. F. (1993). Wave forces on crown walls. *Coastal Engineering*, pages 1489–1502.

Peng, Z. and Zou, Q.-P. (2011). Spatial distribution of wave overtopping water behind coastal structures. *Coastal Engineering*, 58(6):489–498.

Petrova, P. G. and Guedes Soares, C. (2011). Wave height distributions in bimodal sea states from offshore basin. *Ocean Engineering*, 38:658–672.

Petrova, P. G. and Guedes Soares, C. (2014). Distributions of nonlinear wave amplitudes and heights from laboratory generated following and crossing bimodal seas. *Natural Hazards and Earth System Sciences*, 14:1207–1222.

Polidoro, A., Pullen, T., and Eade, J. (2018). Gravel beach profile response allowing for bimodal sea states. *Proceedings of the Institution of Civil Engineers – Maritime Engineering*, 171(4):145–146.

Postma, G. (1989). Wave reflection from rock slopes under random wave attack. *MS thesis, Delft University of Technology, Department of Civil Engingineering*.

Pullen, T., Allsop, N., Bruce, T., Kortenhaus, A., Schüttrumpf, H., and van der Meer, J. (2007). Eurotop. *Wave overtopping of sea defences and related structures:assessment manual*, page 178.

Reeve, D., Chadwick, A., and Fleming, C. (2015). Coastal Engineering:Processes, Theory and Design Practice. *Spon, London, 518 pages*.

Rodriguez, G., Guedes Soares, C., Pacheco, M., and Perez-Martell, E. (2002). Wave Height Distribution in Mixed Sea States. *Offshore Mechanics and Arctic Engineering*, 124(1):34–40.

Ruju, A., Lara, J. L., and Losada, I. J. (2014). Numerical analysis of run-up oscillations under dissipative conditions. *Coastal Engineering*, 86:45–56.

Rusche, H. (2002). Computational fluid dynamics of dispersed two-phase flows at high phase fractions. *Thesis Department of Mechanical Engineering Imperial College London, 343 pages*.

Rychlik, I., Johannesson, P., and Leadbutter, M. (1997a). Modelling and Statistical Analysis of Ocean-wave Data Using Transformed Gaussian Processes. *Marine Structures*, 10:13–47.

Rychlik, I., Johannesson, P., and Leadbutter, M. R. (1997b). Modelling and Statistical Analysis of Ocean-wave Data Using Transformed Gaussian Processes. *Marine Structures*, 10:13–47.

Schaeffer, H. A. (1996). Second-order wavemaker theory for irregular waves. *Ocean Engineering*, 23(1):47–88.

Schüttrumpf, H. and Oumeraci, H. (2005). Layer thicknesses and velocities of wave overtopping flow at seadikes. *Coastal Engineering*, 52(6):473–495.

Schäffer, H. A. and Klopman, G. (2000). Review of multidirectional active wave absorption methods. *Journal of Waterway Port Coastal and Ocean Engineering*, pages 88–97.

Scitools (2019). A python programming website:Using cartopy with matplotlib — cartopy 0.15.0 documentation, [online] Available at:https://scitools.org.uk/cartopy/docs/v0.15/matplotlib/intro.html, [Accessed 7 Nov. 2019].

Seelig, W. N. and Ahrens, J. P. (1981). Estimation of wave reflection and energy dissipation coefficients for beaches, revetments, and breakwaters. *Technical Paper No. 81-1, US Army Corps of Engineers*, pages 1–41.

Shi-Igai, H. and Rong-Chung, H. (1977). An analytical and computer study on wave overtopping. *Coastal Engineering*, 1:221–241.

Smith, G. M., Seijffert, J. W. W., and van der Meer, J. W. (1995). Erosion and overtopping of a grass dike large scale model tests. *Coastal Engineering*, pages 2639–2652.

Sun, Z., Liu, S., and Li, J. (2012). Numerical study of multidirectional focusing wave run up on a vertical surface piercing cylinder. *Hydrodynamics Ser B*, 24:86–96.

Tayfun, M. A. (1981). Distribution of crest-to-trough waveheights. *Journal of waterways ports and coastal*, 116(6):149–158.

Thompson, D. A., H, K., and E, R. D. (2017). Modelling extreme wave overtopping at Aberystwyth Promenade. *Water*, 9(9).

Toffoli, A., M., O., and Monbaliu, J. (2006). Wave statistics in unimodal and bimodal seas from a second-order model. *European Journal of Mechanics B/Fluids*, 25:649–661.

Torres-Freyermuth, A., Lara, J. L., Losada, I. J., and ... (2014). Modeling of surf zone processes on a natural beach using Reynolds-Averaged Navier–Stokes equations. *J. Geophysi. Res. Oceans AGU. (Am. Geophys. Union)*, 112(C09014).

Torres-Freyermuth, A., Lara, J. L., and Losada, I. J. (2010). Numerical modelling of short-and long-wave transformation on a barred beach. *Coastal Engineering*, 57(3):317–330.

Troch, P., Geeraerts, J., van de Walle, B., De Rouck, J., Van Damme, L., Allsop, W., and Franco, L. (2004). Full-scale wave-overtopping measurements on the zeebrugge rubble mound breakwater. *Coastal Engineering*, 51(7):609–628.

Tsung, W.-S., Hsiao, S.-C., and Lin, T.-C. (2012). Numerical simulation of solitary wave run-up and overtopping using boussinesq-type model. *Journal of Hydrodynamics, Ser. B*, 24(6):899–913.

Tuan, T. Q. and Oumeraci, H. (2010). A numerical model of wave overtopping on seadikes. *Coastal Engineering*, 57(8):757–772.

Ursell, J., Dean, R. G., and Yu, Y. (1960). Forced small amplitude water waves:a comparison of theory and experiment. *Journal of Fluid Mech.*, 7(1):33–52.

van der Meer, J., Allsop, N., Bruce, T., De Rouck, J., Kortenhaus, A., Pullen, T., Schüttrumpf, H., Troch, P., and Zanuttigh, B. (2016). Manual on wave overtopping of sea defences and related structures. An overtopping manual largely based on European research, but for worldwide application. *Eurotop Manual, 264 pages*.

van der Meer, J., Allsop, N., Bruce, T., De Rouck, J., Kortenhaus, A., Pullen, T., Schüttrumpf, H., Troch, P., and Zanuttigh, B. (2018). Manual on wave overtopping of sea defences and related structures. An overtopping manual largely based on European research, but for worldwide application. *Eurotop Manual, 320 pages*.

van der Meer, J. and Bruce, T. (2013). New physical insights and design formulas on wave overtopping at sloping and vertical structures. *Journal of Waterway, Port, Coastal, and Ocean Engineering*, 140(6):04014025.

van der Meer, J., Verhaeghe, H., and Steendam, G. (2005). Database on wave overtopping at coastal structures. *CLASH WP2 database, Inframm, Marknesse, NL, Workpackage 2*.

van der Meer, J. W. (1993). Conceptual design of rubble mound breakwaters. *Delft Hydraulics, 48 pages*.

van der Meer, J. W. (1995a). Conceptual design of rubble mound breakwaters. In *Advances In Coastal And Ocean Engineering:(Volume 1)*, pages 221–315. World Scientific.

van der Meer, J. W. (1995b). Wave run-up and wave overtopping at dikes. *Journal of Waterway, Port, Coastal, and Ocean Engineering, 6:635–646*.

van der Meer, J. W. (2002). Wave run up and wave overtopping at dikes technical advisory committee on flood defence. *Coastal Engineering*, 1(1—3):101–131.

van der Meer, J. W. and Veldman, J. J. (1992). Singular points at berm breakwaters:scale effects, rear, round head and longshore transport. *Coastal Engineering*, 17(3—4):153–171.

van der Meer, J. W., Verhaeghe, H., and Steendam, G. J. (2009). The new wave overtopping database for coastal structures. *Coastal Engineering*, 56(2):108–120.

van der Werf, I. and van Gent, M. (2018). Wave overtopping over coastal structures with oblique wind and swell waves. *Journal of Marine Science and Engineering*, 6(4):149.

Van Gent, M. and Smith, G. (1999). Physical model investigations on coastal structures with shallow foreshores:2d model tests with single and double-peaked wave energy spectra. *Hydraulic Lab. report, Number, V257(235182), 70 pages*.

Van Gent, M. R. (1994). The modelling of wave action on and in coastal structures. *Coastal Engineering*, 22(3–4):311–339.

van Gent, M. R., van den Boogaard, H. F., Pozueta, B., and Medina, J. R. (2007). Neural network modelling of wave overtopping at coastal structures. *Coastal Engineering*, 54(8):586–593.

Verbeeck, H., Samson, R., Verdonck, F., and Lemeur, R. (2006). Parameter sensitivity and uncertainty of the forest carbon flux model forug:a monte carlo analysis. *Tree physiology*, 26(6):807–817.

Verhaeghe, H., De Rouck, J., and van der Meer, J. (2008). Combined classifier–quantifier model:a 2-phases neural model for prediction of wave overtopping at coastal structures. *Coastal Engineering*, 55(5):357–374.

Verlet, L. (1967). Computer experiments on classical fluids. *Thermodynamics*, 159:98–103.

Victor, L. and Troch, P. (2012). Wave overtopping at smooth impermeable steep slopes with low crest freeboards. *Journal of Waterway, Port, Coastal, and Ocean Engineering*, 138(5):372–385.

Vinje, T. (1989). The statistical distribution of waveheights in a random seaway. *Applied Ocean Research*, 11(3):143–152.

Wendland, H. (1995). Piecewise polynomial positive definite and compactly supported radial functions of minimal degree. *Advanced computational Mathematics*, 4:389–396.

Weston, B., Borthwick, A., Taylor, P., Hunt, A., and Stansby, P. (2005). The performance of a hybrid boussinesq model on wave runup and overtopping predictions for coastal structures. *International Conference on Coastlines, structures and breakwaters 2005*, pages 279–289.

Zanuttigh, B. and Martinelli, L. (2008). Transmission of wave energy at permeable low crested structures. *Coastal Engineering*, 55(12):1135–1147.

Zanuttigh, B., Martinelli, L., Lamberti, A., Moschella, P., Hawkins, S., Marzetti, S., and Ceccherelli, V. U. (2005). Environmental design of coastal defence in lido di dante, italy. *Coastal Engineering*, 52(10—11):1089–1125.

Zanuttigh, B., Simcic, D., Bagli, S., Bozzeda, F., Pietrantoni, L., Zagonari, F., Hoggart, S., and Nicholls, R. J. (2014). {THESEUS} decision support system for coastal risk management. *Coastal Engineering*, 87:218–239.

Zelt, J. A. and Skjelbreia, J. E. (1992). Estimating incident and reflected wave fields using an arbitrary number of wave gauges. *Proccedings, 23rd ICCE, Venice*, pages 777–788.

Zheng, K., chen Sun, Z., wen Sun, J., ming Zhang, Z., ping Yang, G., and Zhou, F. (2009). Numerical simulations of water wave dynamics based on {SPH} methods. *Journal of Hydrodynamics, Ser. B*, 21(6):843–850.

Appendix A

Outcome of Current Research

Orimoloye, S., Karunarathna, H., and Reeve, D. E. (2019). "Effects of swell on wave height distribution of energy-conserved bimodal seas". Journal of Marine Science and Engineering, 7(3):79.

Orimoloye, S., Horrillo-Caraballo, J., Karunarathna, H., and Reeve, D. E. (2019). "Modelling wave overtopping of steep impermeable structures under bimodal sea conditions", In Proceedings of the 8^{th} International Conference of Coastal Structures, Hannover, Germany, 30 September – 2 October, 2019, https://doi.org/10.18451/978-3-939230-64-9_121.

Orimoloye, S., Karunarathna, H., and Reeve, D. E. (2020). "Reflection analysis of impermeable slopes under bimodal sea conditions". Journal of Marine Science and Engineering, 8(2), 133; https://doi.org/10.3390/jmse8020133 .

Orimoloye, S., Horrillo-Caraballo, J., Karunarathna, H., and Reeve, D. E., 2019. Wave overtopping under bimodal sea conditions. Coastal Engineering (Under review).

Orimoloye, S., Horrillo-Caraballo, J., Karunarathna, H., and Reeve, D. E., 2019. "A novel method for wave overtopping study under bimodal sea conditions". Coastal Engineering (Under review).

Orimoloye, S., Horrillo-Caraballo, J., Karunarathna, H., and Reeve, D. E., 2019. "Experimental investigation of the sensitivity of bimodal overtopping on spectral shape". Journal of Water, (Under Review).

Orimoloye, S., Horrillo-Caraballo, J., Lara,J. L, Karunarathna, H., and Reeve, D. E. (2019). "Numerical and experimental study of reduction of bimodal wave overtopping using crest modifications". Coastal Engineering (In preparation).

Appendix B

Bimodal Wave Overtopping Test Conditions and Results

Table B.1 Dimensionless Wave Overtopping Results for cot $\alpha = 3.0$

ID	Test No	Mode Uni = 1 Bi = 2	Swell (%)	T_{pW} (secs)	T_{pS} (secs)	h (m)	R_c (m)	H_{m0} (m)	R^* (-)	Q^* (-)
1	$T001-1$	2	25	7	11	0.70	0.10	0.125	1.08	0.006396
2	$T001-2$	2	25	7	15	0.70	0.10	0.125	1.03	0.017520
3	$T001-3$	2	25	7	20	0.70	0.10	0.125	1.05	0.007447
4	$T001-4$	2	25	7	25	0.70	0.10	0.125	1.09	0.007323
5	$T001-5$	2	50	7	11	0.70	0.10	0.125	1.13	0.009150
6	$T001-6$	2	50	7	15	0.70	0.10	0.125	1.00	0.009440
7	$T001-7$	2	50	7	20	0.70	0.10	0.125	1.22	0.014079
8	$T001-9$	2	75	7	11	0.70	0.10	0.125	1.06	0.009861
9	$T001-10$	2	75	7	15	0.70	0.10	0.125	0.94	0.010494
10	$T001-13$	1	0	7	-	0.70	0.10	0.125	1.10	0.007010
11	$T002-1$	2	25	8	11	0.70	0.10	0.125	0.83	0.018440
12	$T002-2$	2	25	8	15	0.70	0.10	0.125	0.84	0.024020
13	$T002-3$	2	25	8	20	0.70	0.10	0.125	0.96	0.009442
14	$T002-4$	2	25	8	25	0.70	0.10	0.125	0.91	0.008193
15	$T002-5$	2	50	8	11	0.70	0.10	0.125	0.78	0.027410
16	$T002-6$	2	50	8	15	0.70	0.10	0.125	0.95	0.019990
17	$T002-7$	2	50	8	20	0.70	0.10	0.125	1.01	0.013278

(cot $\alpha = 3.0$) Continue on the next page

Table B.1 Dimensionless Wave Overtopping Results for cot $\alpha = 3.0$ (cont.)

ID	Test No	Mode Uni = 1 Bi = 2	Swell (%)	T_{pW} (secs)	T_{pS} (secs)	h (m)	R_c (m)	H_{m0} (m)	R^* (-)	Q^* (-)
18	$T002-9$	2	75	8	11	0.70	0.10	0.125	0.75	0.022240
19	$T002-10$	2	75	8	15	0.70	0.10	0.125	1.02	0.014251
20	$T002-13$	1	0	8	-	0.70	0.10	0.125	0.95	0.017220
21	$T003-1$	2	25	9	11	0.70	0.10	0.125	1.14	0.011150
22	$T003-2$	2	25	9	15	0.70	0.10	0.125	0.95	0.010370
23	$T003-3$	2	25	9	20	0.70	0.10	0.125	0.98	0.011350
24	$T003-4$	2	25	9	25	0.70	0.10	0.125	1.04	0.012380
25	$T003-5$	2	50	9	11	0.70	0.10	0.125	1.16	0.015050
26	$T003-6$	2	50	9	15	0.70	0.10	0.125	0.95	0.011760
27	$T003-7$	2	50	9	20	0.70	0.10	0.125	1.13	0.014940
28	$T003-9$	2	75	9	11	0.70	0.10	0.125	1.05	0.014060
29	$T003-10$	2	75	9	15	0.70	0.10	0.125	0.93	0.013320
30	$T003-13$	1	0	9	-	0.70	0.10	0.125	1.13	0.010359
31	$T004-1$	2	25	10	11	0.70	0.10	0.125	1.05	0.010660
32	$T004-2$	2	25	10	15	0.70	0.10	0.125	1.06	0.012990
33	$T004-3$	2	25	10	20	0.70	0.10	0.125	1.15	0.015310
34	$T004-4$	2	25	10	25	0.70	0.10	0.125	1.27	0.017850
35	$T004-5$	2	50	10	11	0.70	0.10	0.125	0.97	0.012300
36	$T004-6$	2	50	10	15	0.70	0.10	0.125	1.19	0.017460
37	$T004-9$	2	75	10	11	0.70	0.10	0.125	1.16	0.016430
38	$T004-10$	2	75	10	15	0.70	0.10	0.125	0.96	0.014700
39	$T004-13$	1	0	10	-	0.70	0.10	0.125	1.27	0.013223
40	$T005-1$	2	25	7	11	0.65	0.15	0.100	2.05	0.001260
41	$T005-2$	2	25	7	15	0.65	0.15	0.100	1.94	0.001700
42	$T005-3$	2	25	7	20	0.65	0.15	0.100	1.97	0.001750
43	$T005-4$	2	25	7	25	0.65	0.15	0.100	1.96	0.001690
44	$T005-5$	2	50	7	11	0.65	0.15	0.100	1.72	0.001720
45	$T005-6$	2	50	7	15	0.65	0.15	0.100	1.84	0.002570
46	$T005-7$	2	50	7	20	0.65	0.15	0.100	1.88	0.002410
47	$T005-8$	2	50	7	25	0.65	0.15	0.100	1.93	0.003610
48	$T005-9$	2	75	7	11	0.65	0.15	0.100	1.95	0.002640
49	$T005-10$	2	75	7	15	0.65	0.15	0.100	1.83	0.004120

(cot $\alpha = 3.0$) Continue on the next page

Table B.1 Dimensionless Wave Overtopping Results for cot $\alpha = 3.0$ (cont.)

ID	Test No	Mode Uni = 1 Bi = 2	Swell (%)	T_{pW} (secs)	T_{pS} (secs)	h (m)	R_c (m)	H_{m0} (m)	R^* (-)	Q^* (-)
50	$T005-11$	2	75	7	20	0.65	0.15	0.100	1.98	0.005640
51	$T005-13$	1	0	7	-	0.65	0.15	0.100	2.04	0.000899
52	$T006-1$	2	25	8	11	0.65	0.15	0.125	1.49	0.003090
53	$T006-2$	2	25	8	15	0.65	0.15	0.125	1.37	0.003170
54	$T006-3$	2	25	8	20	0.65	0.15	0.125	1.60	0.004350
55	$T006-4$	2	25	8	25	0.65	0.15	0.125	1.60	0.004590
56	$T006-5$	2	50	8	11	0.65	0.15	0.125	1.54	0.003640
57	$T006-6$	2	50	8	15	0.65	0.15	0.125	1.37	0.004940
58	$T006-7$	2	50	8	20	0.65	0.15	0.125	1.55	0.008630
59	$T006-9$	2	75	8	11	0.65	0.15	0.125	1.56	0.005750
60	$T006-10$	2	75	8	15	0.65	0.15	0.125	1.55	0.007560
61	$T006-13$	1	0	8	-	0.65	0.15	0.125	1.52	0.004820
62	$T007-1$	2	25	9	11	0.65	0.15	0.100	1.91	0.002850
63	$T007-2$	2	25	9	15	0.65	0.15	0.100	1.73	0.002270
64	$T007-3$	2	25	9	20	0.65	0.15	0.100	2.02	0.002560
65	$T007-4$	2	25	9	25	0.65	0.15	0.100	2.10	0.002750
66	$T007-5$	2	50	9	11	0.65	0.15	0.100	1.93	0.002720
67	$T007-6$	2	50	9	15	0.65	0.15	0.100	1.68	0.004320
68	$T007-7$	2	50	9	20	0.65	0.15	0.100	1.92	0.003940
69	$T007-9$	2	75	9	11	0.65	0.15	0.100	1.95	0.002840
70	$T007-10$	2	75	9	15	0.65	0.15	0.100	1.69	0.002550
71	$T007-11$	2	75	9	20	0.65	0.15	0.100	1.97	0.005990
72	$T007-12$	2	75	9	25	0.65	0.15	0.100	2.04	0.006980
73	$T007-13$	1	0	9	-	0.65	0.15	0.100	1.92	0.001790
74	$T008-1$	2	25	10	11	0.65	0.15	0.125	1.58	0.005450
75	$T008-2$	2	25	10	15	0.65	0.15	0.125	1.59	0.006270
76	$T008-3$	2	25	10	20	0.65	0.15	0.125	1.64	0.007170
77	$T008-4$	2	50	10	25	0.65	0.15	0.125	1.64	0.006920
78	$T008-5$	2	50	10	11	0.65	0.15	0.125	1.59	0.005010
79	$T008-6$	2	50	10	15	0.65	0.15	0.125	1.43	0.005970
80	$T008-7$	2	50	10	20	0.65	0.15	0.125	1.71	0.011470
81	$T008-9$	2	75	10	11	0.65	0.15	0.125	1.58	0.004790

(cot $\alpha = 3.0$) Continue on the next page

Table B.1 Dimensionless Wave Overtopping Results for cot $\alpha = 3.0$ (cont.)

ID	Test No	Mode Uni = 1 Bi = 2	Swell (%)	T_{pW} (secs)	T_{pS} (secs)	h (m)	R_c (m)	H_{m0} (m)	R^* (-)	Q^* (-)
82	$T008-10$	2	75	10	15	0.65	0.15	0.125	1.39	0.007480
83	$T008-13$	1	0	10	-	0.65	0.15	0.125	1.71	0.004940
84	$T009-1$	2	25	7	11	0.60	0.20	0.100	2.43	0.000357
85	$T009-2$	2	25	7	15	0.60	0.20	0.100	2.59	0.000475
86	$T009-3$	2	25	7	20	0.60	0.20	0.100	2.65	0.000630
87	$T009-4$	2	25	7	25	0.60	0.20	0.100	2.61	0.000452
88	$T009-5$	2	50	7	11	0.60	0.20	0.100	2.54	0.000723
89	$T009-6$	2	50	7	15	0.60	0.20	0.100	2.22	0.000828
90	$T009-7$	2	50	7	20	0.60	0.20	0.100	2.52	0.001070
91	$T009-8$	2	50	7	25	0.60	0.20	0.100	2.57	0.001210
92	$T009-9$	2	75	7	11	0.60	0.20	0.100	2.59	0.001150
93	$T009-10$	2	75	7	15	0.60	0.20	0.100	2.98	0.001620
94	$T009-11$	2	75	7	20	0.60	0.20	0.100	2.87	0.002350
95	$T009-13$	1	0	7	-	0.60	0.20	0.100	2.43	0.000244
96	$T010-1$	2	25	8	11	0.60	0.20	0.100	2.50	0.000424
97	$T010-2$	2	25	8	15	0.60	0.20	0.100	2.34	0.000550
98	$T010-3$	2	25	8	20	0.60	0.20	0.100	2.39	0.000738
99	$T010-4$	2	25	8	25	0.60	0.20	0.100	2.66	0.001110
100	$T010-5$	2	50	8	11	0.60	0.20	0.100	2.29	0.000643
101	$T010-6$	2	50	8	15	0.60	0.20	0.100	2.09	0.001010
102	$T010-7$	2	50	8	20	0.60	0.20	0.100	2.31	0.001440
103	$T010-8$	2	50	8	25	0.60	0.20	0.100	2.33	0.001520
104	$T010-9$	2	75	8	11	0.60	0.20	0.100	2.14	0.000895
105	$T010-10$	2	75	8	15	0.60	0.20	0.100	2.63	0.002060
106	$T010-13$	1	0	8	-	0.60	0.20	0.100	2.25	0.000265
107	$T011-1$	2	25	9	11	0.60	0.20	0.125	2.06	0.001270
108	$T011-2$	2	25	9	15	0.60	0.20	0.125	2.34	0.001900
109	$T011-3$	2	25	9	20	0.60	0.20	0.125	2.00	0.001700
110	$T011-4$	2	25	9	25	0.60	0.20	0.125	1.85	0.001540
111	$T011-5$	2	50	9	11	0.60	0.20	0.125	1.91	0.001700
112	$T011-6$	2	50	9	15	0.60	0.20	0.125	1.89	0.003290
113	$T011-7$	2	50	9	20	0.60	0.20	0.125	2.15	0.004130

(cot $\alpha = 3.0$) Continue on the next page

Table B.1 Dimensionless Wave Overtopping Results for cot $\alpha = 3.0$ (cont.)

ID	Test No	Mode Uni = 1 Bi = 2	Swell (%)	T_{pW} (secs)	T_{pS} (secs)	h (m)	R_c (m)	H_{m0} (m)	R^* (-)	Q^* (-)
114	$T011-9$	2	75	9	11	0.60	0.20	0.125	1.54	0.002060
115	$T011-10$	2	75	9	15	0.60	0.20	0.125	2.37	0.004670
116	$T011-13$	1	0	9	-	0.60	0.20	0.125	2.04	0.000990
117	$T0012-1$	2	25	10	11	0.60	0.20	0.125	1.94	0.002820
118	$T0012-2$	2	25	10	15	0.60	0.20	0.125	1.97	0.003950
119	$T0012-3$	2	25	10	20	0.60	0.20	0.125	2.04	0.004680
120	$T0012-4$	2	25	10	25	0.60	0.20	0.125	2.24	0.004240
121	$T0012-5$	2	50	10	11	0.60	0.20	0.125	2.12	0.003330
122	$T0012-6$	2	50	10	15	0.60	0.20	0.125	1.90	0.005230
123	$T0012-9$	2	75	10	11	0.60	0.20	0.125	2.11	0.003470
124	$T0012-10$	2	75	10	15	0.60	0.20	0.125	2.16	0.007130
125	$T0012-13$	1	0	10	-	0.60	0.20	0.125	2.10	0.001850
126	$T013-1$	2	25	7	11	0.65	0.15	0.075	2.78	0.000510
127	$T013-2$	2	25	7	15	0.65	0.15	0.075	2.53	0.000508
128	$T013-3$	2	25	7	20	0.65	0.15	0.075	2.57	0.000339
129	$T013-4$	2	25	7	25	0.65	0.15	0.075	2.58	0.000250
130	$T013-5$	2	50	7	11	0.65	0.15	0.075	2.19	0.000374
131	$T013-6$	2	50	7	15	0.65	0.15	0.075	2.35	0.000634
132	$T013-7$	2	50	7	20	0.65	0.15	0.075	2.73	0.000742
133	$T013-8$	2	50	7	25	0.65	0.15	0.075	2.87	0.000427
134	$T013-9$	2	75	7	11	0.65	0.15	0.075	2.62	0.001120
135	$T013-10$	2	75	7	15	0.65	0.15	0.075	2.54	0.001220
136	$T013-11$	2	75	7	20	0.65	0.15	0.075	2.51	0.001530
137	$T013-12$	2	75	7	25	0.65	0.15	0.075	2.40	0.001310
138	$T013-13$	1	0	7	-	0.65	0.15	0.075	2.77	0.000177
139	$T014-1$	2	25	8	11	0.65	0.15	0.075	2.46	0.000786
140	$T014-2$	2	25	8	15	0.65	0.15	0.075	2.15	0.000518
141	$T014-3$	2	25	8	20	0.65	0.15	0.075	2.29	0.000477
142	$T014-4$	2	25	8	25	0.65	0.15	0.075	2.63	0.000468
143	$T014-5$	2	50	8	11	0.65	0.15	0.075	2.52	0.000924
144	$T014-6$	2	50	8	15	0.65	0.15	0.075	2.13	0.001140
145	$T014-7$	2	50	8	20	0.65	0.15	0.075	2.37	0.000803

(cot $\alpha = 3.0$) Continue on the next page

Table B.1 Dimensionless Wave Overtopping Results for cot $\alpha = 3.0$ (cont.)

ID	Test No	Mode Uni = 1 Bi = 2	Swell (%)	T_{pW} (secs)	T_{pS} (secs)	h (m)	R_c (m)	H_{m0} (m)	R^* (-)	Q^* (-)
146	$T014-8$	2	50	8	25	0.65	0.15	0.075	2.76	0.000754
147	$T014-9$	2	75	8	11	0.65	0.15	0.075	2.63	0.001080
148	$T014-10$	2	75	8	15	0.65	0.15	0.075	2.26	0.001230
149	$T014-11$	2	75	8	20	0.65	0.15	0.075	2.50	0.001850
150	$T014-12$	2	75	8	25	0.65	0.15	0.075	2.50	0.001040
151	$T014-13$	1	0	8	-	0.65	0.15	0.075	2.43	0.000478
152	$T015-1$	2	25	9	11	0.65	0.15	0.075	2.55	0.001010
153	$T015-2$	2	25	9	15	0.65	0.15	0.075	2.25	0.000926
154	$T015-3$	2	25	9	20	0.65	0.15	0.075	2.68	0.001030
155	$T015-4$	2	25	9	25	0.65	0.15	0.075	2.70	0.000973
156	$T015-5$	2	50	9	11	0.65	0.15	0.075	2.59	0.000915
157	$T015-6$	2	50	9	15	0.65	0.15	0.075	2.37	0.001000
158	$T015-7$	2	50	9	20	0.65	0.15	0.075	2.42	0.001240
159	$T015-8$	2	50	9	25	0.65	0.15	0.075	2.82	0.001120
160	$T015-9$	2	75	9	11	0.65	0.15	0.075	2.73	0.001740
161	$T015-10$	2	75	9	15	0.65	0.15	0.075	2.23	0.001520
162	$T015-11$	2	75	9	20	0.65	0.15	0.075	2.50	0.001480
163	$T015-12$	2	75	9	25	0.65	0.15	0.075	2.47	0.001500
164	$T015-13$	1	0	9	-	0.65	0.15	0.075	2.55	0.000893
165	$T016-1$	2	25	10	11	0.65	0.15	0.075	2.11	0.000912
166	$T016-2$	2	25	10	15	0.65	0.15	0.075	3.04	0.002528
167	$T016-3$	2	25	10	20	0.65	0.15	0.075	2.69	0.001815
168	$T016-4$	2	25	10	25	0.65	0.15	0.075	2.70	0.001511
169	$T016-5$	2	50	10	11	0.65	0.15	0.075	2.33	0.001175
170	$T016-6$	2	50	10	15	0.65	0.15	0.075	2.41	0.001337
171	$T016-7$	2	50	10	20	0.65	0.15	0.075	2.44	0.002092
172	$T016-8$	2	50	10	25	0.65	0.15	0.075	2.80	0.001545
173	$T016-9$	2	75	10	11	0.65	0.15	0.075	2.63	0.001410
174	$T016-10$	2	75	10	15	0.65	0.15	0.075	2.22	0.001275
175	$T016-11$	2	75	10	20	0.65	0.15	0.075	2.49	0.002271
176	$T016-12$	2	75	10	25	0.65	0.15	0.075	2.91	0.001911
177	$T016-13$	1	0	10	-	0.65	0.15	0.075	3.01	0.000157

(cot $\alpha = 3.0$) Continue on the next page

Table B.1 Dimensionless Wave Overtopping Results for cot $\alpha = 3.0$ (cont.)

ID	Test No	Mode Uni = 1 Bi = 2	Swell (%)	T_{pW} (secs)	T_{pS} (secs)	h (m)	R_c (m)	H_{m0} (m)	R^* (-)	Q^* (-)
178	$T017-1$	2	25	7	11	0.70	0.10	0.100	1.37	0.004340
179	$T017-2$	2	25	7	15	0.70	0.10	0.100	1.29	0.004920
180	$T017-3$	2	25	7	20	0.70	0.10	0.100	1.30	0.005440
181	$T017-4$	2	25	7	25	0.70	0.10	0.100	1.31	0.005600
182	$T017-5$	2	50	7	11	0.70	0.10	0.100	1.43	0.007200
183	$T017-6$	2	50	7	15	0.70	0.10	0.100	1.20	0.007240
184	$T017-7$	2	50	7	20	0.70	0.10	0.100	1.24	0.008110
185	$T017-8$	2	50	7	25	0.70	0.10	0.100	1.48	0.012130
186	$T017-9$	2	75	7	11	0.70	0.10	0.100	1.46	0.008970
187	$T017-10$	2	75	7	15	0.70	0.10	0.100	1.21	0.010690
188	$T017-11$	2	75	7	20	0.70	0.10	0.100	1.18	0.012700
189	$T017-13$	1	0	7	-	0.70	0.10	0.100	1.39	0.004540
190	$T018-1$	2	25	8	11	0.70	0.10	0.100	1.41	0.006520
191	$T018-2$	2	25	8	15	0.70	0.10	0.100	1.24	0.005780
192	$T018-3$	2	25	8	20	0.70	0.10	0.100	1.29	0.007310
193	$T018-4$	2	25	8	25	0.70	0.10	0.100	1.25	0.005850
194	$T018-5$	2	50	8	11	0.70	0.10	0.100	1.28	0.007280
195	$T018-6$	2	50	8	15	0.70	0.10	0.100	1.25	0.009070
196	$T018-7$	2	50	8	20	0.70	0.10	0.100	1.23	0.011620
197	$T018-8$	2	50	8	25	0.70	0.10	0.100	1.43	0.011000
198	$T018-9$	2	75	8	11	0.70	0.10	0.100	1.31	0.011910
199	$T018-10$	2	75	8	15	0.70	0.10	0.100	1.22	0.010820
200	$T018-11$	2	75	8	20	0.70	0.10	0.100	1.35	0.013020
201	$T018-13$	1	0	8	-	0.70	0.10	0.100	1.40	0.007440
202	$T019-1$	2	25	9	11	0.70	0.10	0.100	1.28	0.009620
203	$T019-2$	2	25	9	15	0.70	0.10	0.100	1.16	0.009950
204	$T019-3$	2	25	9	20	0.70	0.10	0.100	1.30	0.008550
205	$T019-4$	2	25	9	25	0.70	0.10	0.100	1.30	0.008740
206	$T019-5$	2	50	9	11	0.70	0.10	0.100	1.29	0.009230
207	$T019-6$	2	50	9	15	0.70	0.10	0.100	1.12	0.008850
208	$T019-7$	2	50	9	20	0.70	0.10	0.100	1.25	0.012200
209	$T019-8$	2	50	9	25	0.70	0.10	0.100	1.35	0.015080

(cot $\alpha = 3.0$) Continue on the next page

Table B.1 Dimensionless Wave Overtopping Results for cot $\alpha = 3.0$ (cont.)

ID	Test No	Mode Uni = 1 Bi = 2	Swell (%)	T_{pW} (secs)	T_{pS} (secs)	h (m)	R_c (m)	H_{m0} (m)	R^* (-)	Q^* (-)
210	$T019-9$	2	75	9	11	0.70	0.10	0.100	1.31	0.011080
211	$T019-10$	2	75	9	15	0.70	0.10	0.100	1.12	0.011920
212	$T019-11$	2	75	9	20	0.70	0.10	0.100	1.49	0.018130
213	$T019-13$	1	0	9	-	0.70	0.10	0.100	1.29	0.006480
214	$T020-1$	2	25	10	11	0.70	0.10	0.100	1.48	0.012300
215	$T020-2$	2	25	10	15	0.70	0.10	0.100	1.20	0.011310
216	$T020-3$	2	25	10	20	0.70	0.10	0.100	1.36	0.012040
217	$T020-4$	2	25	10	25	0.70	0.10	0.100	1.49	0.013050
218	$T020-5$	2	50	10	11	0.70	0.10	0.100	1.48	0.013430
219	$T020-6$	2	50	10	15	0.70	0.10	0.100	1.25	0.012750
220	$T020-7$	2	50	10	20	0.70	0.10	0.100	1.25	0.015850
221	$T020-8$	2	50	10	25	0.70	0.10	0.100	1.32	0.017190
222	$T020-9$	2	75	10	11	0.70	0.10	0.100	1.32	0.011430
223	$T020-10$	2	75	10	15	0.70	0.10	0.100	1.19	0.013890
224	$T020-11$	2	75	10	20	0.70	0.10	0.100	1.31	0.019890
225	$T020-13$	1	0	10	-	0.70	0.10	0.100	1.46	0.008820
226	$T021-1$	2	25	7	11	0.60	0.20	0.075	3.18	0.000051
227	$T021-2$	2	25	7	15	0.60	0.20	0.075	2.97	0.000091
228	$T021-3$	2	25	7	20	0.60	0.20	0.075	3.40	0.000098
229	$T021-4$	2	25	7	25	0.60	0.20	0.075	3.19	0.000068
230	$T021-5$	2	50	7	11	0.60	0.20	0.075	3.32	0.000072
231	$T021-6$	2	50	7	15	0.60	0.20	0.075	2.78	0.000165
232	$T021-7$	2	50	7	20	0.60	0.20	0.075	3.16	0.000154
233	$T021-8$	2	50	7	25	0.60	0.20	0.075	3.94	0.000092
234	$T021-9$	2	75	7	11	0.60	0.20	0.075	3.47	0.000231
235	$T021-10$	2	75	7	15	0.60	0.20	0.075	3.02	0.000375
236	$T021-11$	2	75	7	20	0.60	0.20	0.075	3.46	0.000521
237	$T021-12$	2	75	7	25	0.60	0.20	0.075	2.80	0.000434
238	$T021-13$	1	0	7	-	0.60	0.20	0.075	3.20	0.000041
239	$T022-1$	2	25	8	11	0.60	0.20	0.075	3.25	0.000092
240	$T022-2$	2	25	8	15	0.60	0.20	0.075	2.86	0.000114
241	$T022-3$	2	25	8	20	0.60	0.20	0.075	3.49	0.000156

(cot $\alpha = 3.0$) Continue on the next page

Table B.1 Dimensionless Wave Overtopping Results for cot $\alpha = 3.0$ (cont.)

ID	Test No	Mode Uni = 1 Bi = 2	Swell (%)	T_{pW} (secs)	T_{pS} (secs)	h (m)	R_c (m)	H_{m0} (m)	R^* (-)	Q^* (-)
242	$T022-4$	2	25	8	25	0.60	0.20	0.075	3.61	0.000108
243	$T022-5$	2	50	8	11	0.60	0.20	0.075	3.35	0.000240
244	$T022-6$	2	50	8	15	0.60	0.20	0.075	3.18	0.000303
245	$T022-7$	2	50	8	20	0.60	0.20	0.075	3.62	0.000216
246	$T022-8$	2	50	8	25	0.60	0.20	0.075	3.61	0.000370
247	$T022-9$	2	75	8	11	0.60	0.20	0.075	3.45	0.000321
248	$T022-10$	2	75	8	15	0.60	0.20	0.075	3.01	0.000318
249	$T022-11$	2	75	8	20	0.60	0.20	0.075	3.33	0.000500
250	$T022-13$	1	0	8	-	0.60	0.20	0.075	3.22	0.000079
251	$T023-1$	2	25	9	11	0.60	0.20	0.075	3.37	0.000190
252	$T023-2$	2	25	9	15	0.60	0.20	0.075	3.40	0.000269
253	$T023-3$	2	25	9	20	0.60	0.20	0.075	3.57	0.000185
254	$T023-4$	2	25	9	25	0.60	0.20	0.075	3.59	0.000121
255	$T023-5$	2	50	9	11	0.60	0.20	0.075	3.02	0.000165
256	$T023-6$	2	50	9	15	0.60	0.20	0.075	3.60	0.000214
257	$T023-7$	2	50	9	20	0.60	0.20	0.075	3.66	0.000256
258	$T023-8$	2	50	9	25	0.60	0.20	0.075	3.72	0.000238
259	$T023-9$	2	75	9	11	0.60	0.20	0.075	3.54	0.000368
260	$T023-10$	2	75	9	15	0.60	0.20	0.075	2.96	0.000491
261	$T023-11$	2	75	9	20	0.60	0.20	0.075	3.33	0.000408
262	$T023-12$	2	75	9	25	0.60	0.20	0.075	3.19	0.000432
263	$T023-13$	1	0	9	-	0.60	0.20	0.075	3.78	0.000020
264	$T024-1$	2	25	10	11	0.60	0.20	0.075	3.49	0.000154
265	$T024-2$	2	25	10	15	0.60	0.20	0.075	3.53	0.000372
266	$T024-3$	2	25	10	20	0.60	0.20	0.075	3.54	0.000257
267	$T024-4$	2	25	10	25	0.60	0.20	0.075	3.62	0.000232
268	$T024-5$	2	50	10	11	0.60	0.20	0.075	3.49	0.000235
269	$T024-6$	2	50	10	15	0.60	0.20	0.075	3.21	0.000324
270	$T024-7$	2	50	10	20	0.60	0.20	0.075	3.26	0.000463
271	$T024-8$	2	50	10	25	0.60	0.20	0.075	3.51	0.000258
272	$T024-9$	2	75	10	11	0.60	0.20	0.075	3.81	0.000147
273	$T024-10$	2	75	10	15	0.60	0.20	0.075	2.95	0.000254

(cot $\alpha = 3.0$) Continue on the next page

Table B.1 Dimensionless Wave Overtopping Results for cot $\alpha = 3.0$ (cont.)

ID	Test No	Mode Uni = 1 Bi = 2	Swell (%)	T_{pW} (secs)	T_{pS} (secs)	h (m)	R_c (m)	H_{m0} (m)	R^* (-)	Q^* (-)
274	$T024-11$	2	75	10	20	0.60	0.20	0.075	3.25	0.000661
275	$T024-12$	2	75	10	25	0.60	0.20	0.075	3.37	0.000353
276	$T024-13$	1	0	10	-	0.60	0.20	0.075	3.53	0.000032

Table B.2 Dimensionless Wave Overtopping Results for cot $\alpha = 1.5$

ID	Test No	Mode Uni = 1 Bi = 2	Swell (%)	T_{pW} (secs)	T_{pS} (secs)	h (m)	R_c (m)	H_{m0} (m)	R^* (-)	Q^* (-)
1	$T001-1$	2	25	7	11	0.70	0.10	0.125	1.00	0.008450
2	$T001-2$	2	25	7	15	0.70	0.10	0.125	1.01	0.007560
3	$T001-3$	2	25	7	20	0.70	0.10	0.125	1.21	0.005370
4	$T001-4$	2	25	7	25	0.70	0.10	0.125	1.01	0.007970
5	$T001-5$	2	50	7	11	0.70	0.10	0.125	1.05	0.008760
6	$T001-6$	2	50	7	15	0.70	0.10	0.125	1.08	0.008270
7	$T001-7$	2	50	7	20	0.70	0.10	0.125	0.98	0.008910
8	$T001-9$	2	75	7	11	0.70	0.10	0.125	1.07	0.011490
9	$T001-10$	2	75	7	15	0.70	0.10	0.125	0.91	0.018520
10	$T001-13$	1	0	7	-	0.70	0.10	0.125	1.10	0.007429
11	$T002-1$	2	25	8	11	0.70	0.10	0.125	0.91	0.009690
12	$T002-2$	2	25	8	15	0.70	0.10	0.125	0.96	0.009410
13	$T002-3$	2	25	8	20	0.70	0.10	0.125	1.02	0.007450
14	$T002-4$	2	25	8	25	0.70	0.10	0.125	1.02	0.010420
15	$T002-5$	2	50	8	11	0.70	0.10	0.125	0.92	0.010780
16	$T002-6$	2	50	8	15	0.70	0.10	0.125	0.97	0.012240
17	$T002-7$	2	50	8	20	0.70	0.10	0.125	1.23	0.018520
18	$T002-8$	2	50	8	25	0.70	0.10	0.125	0.88	0.014800
19	$T002-9$	2	75	8	11	0.70	0.10	0.125	0.94	0.012000
20	$T002-10$	2	75	8	15	0.70	0.10	0.125	1.00	0.017380
21	$T002-11$	2	75	8	20	0.70	0.10	0.125	0.91	0.013620
22	$T002-13$	1	0	8	-	0.70	0.10	0.125	1.04	0.007203

(cot $\alpha = 1.5$) Continue on the next page

Table B.2 Dimensionless Wave Overtopping Results for cot $\alpha = 1.5$ (cont.)

ID	Test No	Mode Uni = 1 Bi = 2	Swell (%)	T_{pW} (secs)	T_{pS} (secs)	h (m)	R_c (m)	H_{m0} (m)	R^* (-)	Q^* (-)
23	$T003-1$	2	25	9	11	0.70	0.10	0.125	1.06	0.009150
24	$T003-2$	2	25	9	15	0.70	0.10	0.125	1.28	0.006480
25	$T003-3$	2	25	9	20	0.70	0.10	0.125	1.24	0.005410
26	$T003-4$	2	25	9	25	0.70	0.10	0.125	1.26	0.015460
27	$T003-5$	2	50	9	11	0.70	0.10	0.125	0.98	0.008740
28	$T003-6$	2	50	9	15	0.70	0.10	0.125	0.93	0.015770
29	$T003-7$	2	50	9	20	0.70	0.10	0.125	1.00	0.011670
30	$T003-9$	2	75	9	11	0.70	0.10	0.125	0.98	0.010830
31	$T003-10$	2	75	9	15	0.70	0.10	0.125	1.12	0.015640
32	$T003-13$	1	0	9	-	0.70	0.10	0.125	1.16	0.010406
33	$T004-1$	2	25	10	11	0.70	0.10	0.125	1.05	0.013020
34	$T004-2$	2	25	10	15	0.70	0.10	0.125	0.98	0.012150
35	$T004-3$	2	25	10	20	0.70	0.10	0.125	1.05	0.011790
36	$T004-4$	2	25	10	25	0.70	0.10	0.125	1.06	0.010110
37	$T004-5$	2	50	10	11	0.70	0.10	0.125	1.05	0.011350
38	$T004-6$	2	50	10	15	0.70	0.10	0.125	1.09	0.010270
39	$T004-9$	2	75	10	11	0.70	0.10	0.125	1.06	0.011440
40	$T004-10$	2	75	10	15	0.70	0.10	0.125	1.03	0.011330
41	$T004-13$	1	0	10	-	0.70	0.10	0.125	1.16	0.016328
42	$T005-1$	2	25	7	11	0.65	0.15	0.100	1.55	0.006280
43	$T005-2$	2	25	7	15	0.65	0.15	0.100	1.54	0.004800
44	$T005-3$	2	25	7	20	0.65	0.15	0.100	1.46	0.002290
45	$T005-4$	2	25	7	25	0.65	0.15	0.100	1.68	0.006590
46	$T005-5$	2	50	7	11	0.65	0.15	0.100	1.31	0.003290
47	$T005-6$	2	50	7	15	0.65	0.15	0.100	1.41	0.002630
48	$T005-7$	2	50	7	20	0.65	0.15	0.100	1.74	0.004550
49	$T005-8$	2	50	7	25	0.65	0.15	0.100	1.40	0.009270
50	$T005-9$	2	75	7	11	0.65	0.15	0.100	1.53	0.001820
51	$T005-10$	2	75	7	15	0.65	0.15	0.100	1.85	0.004470
52	$T005-11$	2	75	7	20	0.65	0.15	0.100	1.35	0.002940
53	$T005-13$	1	0	7	-	0.65	0.15	0.100	1.44	0.002830
54	$T006-1$	2	25	8	11	0.65	0.15	0.125	1.15	0.021850

(cot $\alpha = 1.5$) Continue on the next page

Table B.2 Dimensionless Wave Overtopping Results for cot $\alpha = 1.5$ (cont.)

ID	Test No	Mode Uni = 1 Bi = 2	Swell (%)	T_{pW} (secs)	T_{pS} (secs)	h (m)	R_c (m)	H_{m0} (m)	R^* (-)	Q^* (-)
55	$T006-2$	2	25	8	15	0.65	0.15	0.125	1.30	0.011050
56	$T006-3$	2	25	8	20	0.65	0.15	0.125	1.13	0.005840
57	$T006-4$	2	25	8	25	0.65	0.15	0.125	1.18	0.010890
58	$T006-5$	2	50	8	11	0.65	0.15	0.125	1.19	0.016310
59	$T006-6$	2	50	8	15	0.65	0.15	0.125	1.07	0.006560
60	$T006-7$	2	50	8	20	0.65	0.15	0.125	1.00	0.008090
61	$T006-9$	2	75	8	11	0.65	0.15	0.125	1.20	0.004660
62	$T006-10$	2	75	8	15	0.65	0.15	0.125	1.25	0.013360
63	$T006-13$	1	0	8	-	0.65	0.15	0.125	1.05	0.004880
64	$T007-1$	2	25	9	11	0.65	0.15	0.100	1.25	0.003690
65	$T007-2$	2	25	9	15	0.65	0.15	0.100	1.61	0.005750
66	$T007-3$	2	25	9	20	0.65	0.15	0.100	1.49	0.007900
67	$T007-4$	2	25	9	25	0.65	0.15	0.100	1.48	0.005430
68	$T007-5$	2	50	9	11	0.65	0.15	0.100	1.41	0.003660
69	$T007-6$	2	50	9	15	0.65	0.15	0.100	1.40	0.002920
70	$T007-7$	2	50	9	20	0.65	0.15	0.100	1.21	0.004510
71	$T007-9$	2	75	9	11	0.65	0.15	0.100	1.51	0.002350
72	$T007-10$	2	75	9	15	0.65	0.15	0.100	1.46	0.002780
73	$T007-11$	2	75	9	20	0.65	0.15	0.100	1.23	0.003530
74	$T007-12$	2	75	9	25	0.65	0.15	0.100	1.41	0.006100
75	$T007-13$	1	0	9	-	0.65	0.15	0.100	1.36	0.002110
76	$T008-1$	2	25	10	11	0.65	0.15	0.125	1.25	0.008920
77	$T008-2$	2	25	10	15	0.65	0.15	0.125	1.21	0.003810
78	$T008-3$	2	25	10	20	0.65	0.15	0.125	1.07	0.022170
79	$T008-4$	2	25	10	25	0.65	0.15	0.125	1.13	0.012180
80	$T008-5$	2	50	10	11	0.65	0.15	0.125	1.20	0.003950
81	$T008-6$	2	50	10	15	0.65	0.15	0.125	1.35	0.012730
82	$T008-7$	2	50	10	20	0.65	0.15	0.125	1.07	0.005950
83	$T008-9$	2	75	10	11	0.65	0.15	0.125	1.38	0.004800
84	$T008-10$	2	75	10	15	0.65	0.15	0.125	1.17	0.004280
85	$T008-13$	1	0	10	-	0.65	0.15	0.125	1.20	0.004593
86	$T009-1$	2	25	7	11	0.60	0.20	0.100	2.49	0.000841

(cot $\alpha = 1.5$) Continue on the next page

Table B.2 Dimensionless Wave Overtopping Results for cot $\alpha = 1.5$ (cont.)

ID	Test No	Mode Uni = 1 Bi = 2	Swell (%)	T_{pW} (secs)	T_{pS} (secs)	h (m)	R_c (m)	H_{m0} (m)	R^* (-)	Q^* (-)
87	$T009-2$	2	25	7	15	0.60	0.20	0.100	2.77	0.000921
88	$T009-3$	2	25	7	20	0.60	0.20	0.100	2.74	0.001150
89	$T009-4$	2	25	7	25	0.60	0.20	0.100	3.07	0.001730
90	$T009-5$	2	50	7	11	0.60	0.20	0.100	2.83	0.001020
91	$T009-6$	2	50	7	15	0.60	0.20	0.100	2.59	0.001040
92	$T009-7$	2	50	7	20	0.60	0.20	0.100	2.68	0.000861
93	$T009-8$	2	50	7	25	0.60	0.20	0.100	2.86	0.000898
94	$T009-9$	2	75	7	11	0.60	0.20	0.100	2.60	0.000673
95	$T009-10$	2	75	7	15	0.60	0.20	0.100	2.68	0.000937
96	$T009-11$	2	75	7	20	0.60	0.20	0.100	2.59	0.001190
97	$T009-13$	1	0	7	-	0.60	0.20	0.100	2.60	0.000167
98	$T010-1$	2	25	8	11	0.60	0.20	0.100	2.57	0.001100
99	$T010-2$	2	25	8	15	0.60	0.20	0.100	2.56	0.001320
100	$T010-3$	2	25	8	20	0.60	0.20	0.100	2.56	0.000919
101	$T010-4$	2	25	8	25	0.60	0.20	0.100	2.57	0.001060
102	$T010-5$	2	50	8	11	0.60	0.20	0.100	2.14	0.000671
103	$T010-6$	2	50	8	15	0.60	0.20	0.100	2.18	0.000690
104	$T010-7$	2	50	8	20	0.60	0.20	0.100	2.26	0.000545
105	$T010-8$	2	50	8	25	0.60	0.20	0.100	2.23	0.000714
106	$T010-9$	2	75	8	11	0.60	0.20	0.100	2.15	0.000506
107	$T010-10$	2	75	8	15	0.60	0.20	0.100	2.68	0.001010
108	$T011-1$	2	25	9	11	0.60	0.20	0.125	2.23	0.000833
109	$T011-2$	2	25	9	15	0.60	0.20	0.125	2.15	0.001490
110	$T011-3$	2	25	9	20	0.60	0.20	0.125	2.17	0.000455
111	$T011-4$	2	25	9	25	0.60	0.20	0.125	1.94	0.000702
112	$T011-5$	2	50	9	11	0.60	0.20	0.125	1.72	0.001290
113	$T011-6$	2	50	9	15	0.60	0.20	0.125	1.91	0.002270
114	$T011-7$	2	50	9	20	0.60	0.20	0.125	1.84	0.002310
115	$T011-9$	2	75	9	11	0.60	0.20	0.125	1.73	0.002610
116	$T011-10$	2	75	9	15	0.60	0.20	0.125	1.78	0.002520
117	$T011-13$	1	0	9	-	0.60	0.20	0.125	1.99	0.002450
118	$T0012-1$	2	25	10	11	0.60	0.20	0.125	1.67	0.002810

(cot $\alpha = 1.5$) Continue on the next page

Table B.2 Dimensionless Wave Overtopping Results for cot $\alpha = 1.5$ (cont.)

ID	Test No	Mode Uni = 1 Bi = 2	Swell (%)	T_{pW} (secs)	T_{pS} (secs)	h (m)	R_c (m)	H_{m0} (m)	R^* (-)	Q^* (-)
119	$T0012-2$	2	25	10	15	0.60	0.20	0.125	1.66	0.002970
120	$T0012-3$	2	25	10	20	0.60	0.20	0.125	1.68	0.002770
121	$T0012-4$	2	25	10	25	0.60	0.20	0.125	1.72	0.002170
122	$T0012-5$	2	50	10	11	0.60	0.20	0.125	1.68	0.002410
123	$T0012-6$	2	50	10	15	0.60	0.20	0.125	1.72	0.003210
124	$T0012-9$	2	75	10	11	0.60	0.20	0.125	1.70	0.002490
125	$T0012-10$	2	75	10	15	0.60	0.20	0.125	1.74	0.003410
126	$T0012-13$	1	0	10	-	0.60	0.20	0.125	1.79	0.001800
127	$T013-1$	2	25	7	11	0.65	0.15	0.075	1.90	0.002880
128	$T013-2$	2	25	7	15	0.65	0.15	0.075	1.71	0.001020
129	$T013-3$	2	25	7	20	0.65	0.15	0.075	1.83	0.003130
130	$T013-4$	2	25	7	25	0.65	0.15	0.075	1.99	0.000597
131	$T013-5$	2	50	7	11	0.65	0.15	0.075	1.97	0.000494
132	$T013-6$	2	50	7	15	0.65	0.15	0.075	1.84	0.000537
133	$T013-7$	2	50	7	20	0.65	0.15	0.075	1.85	0.001080
134	$T013-8$	2	50	7	25	0.65	0.15	0.075	1.96	0.001650
135	$T013-9$	2	75	7	11	0.65	0.15	0.075	1.59	0.003470
136	$T013-10$	2	75	7	15	0.65	0.15	0.075	1.66	0.001980
137	$T013-11$	2	75	7	20	0.65	0.15	0.075	1.86	0.000874
138	$T013-12$	2	75	7	25	0.65	0.15	0.075	1.93	0.001270
139	$T013-13$	1	0	7	-	0.65	0.15	0.075	1.74	0.001080
140	$T014-1$	2	25	8	11	0.65	0.15	0.075	1.66	0.001300
141	$T014-2$	2	25	8	15	0.65	0.15	0.075	1.60	0.004340
142	$T014-3$	2	25	8	20	0.65	0.15	0.075	1.75	0.002090
143	$T014-4$	2	25	8	25	0.65	0.15	0.075	2.10	0.002870
144	$T014-5$	2	50	8	11	0.65	0.15	0.075	1.75	0.000857
145	$T014-6$	2	50	8	15	0.65	0.15	0.075	1.64	0.003780
146	$T014-7$	2	50	8	20	0.65	0.15	0.075	2.01	0.003400
147	$T014-8$	2	50	8	25	0.65	0.15	0.075	1.86	0.000709
148	$T014-9$	2	75	8	11	0.65	0.15	0.075	2.00	0.000273
149	$T014-10$	2	75	8	15	0.65	0.15	0.075	2.12	0.000886
150	$T014-11$	2	75	8	20	0.65	0.15	0.075	1.60	0.001360

(cot $\alpha = 1.5$) Continue on the next page

Table B.2 Dimensionless Wave Overtopping Results for cot $\alpha = 1.5$ (cont.)

ID	Test No	Mode Uni = 1 Bi = 2	Swell (%)	T_{pW} (secs)	T_{pS} (secs)	h (m)	R_c (m)	H_{m0} (m)	R^* (-)	Q^* (-)
151	$T014-12$	2	75	8	25	0.65	0.15	0.075	1.55	0.001460
152	$T014-13$	1	0	8	-	0.65	0.15	0.075	1.58	0.002110
153	$T015-1$	2	25	9	11	0.65	0.15	0.075	2.04	0.002090
154	$T015-2$	2	25	9	15	0.65	0.15	0.075	1.81	0.000944
155	$T015-3$	2	25	9	20	0.65	0.15	0.075	1.80	0.000715
156	$T015-4$	2	25	9	25	0.65	0.15	0.075	1.82	0.001260
157	$T015-5$	2	50	9	11	0.65	0.15	0.075	1.99	0.000336
158	$T015-6$	2	50	9	15	0.65	0.15	0.075	2.04	0.000371
159	$T015-7$	2	50	9	20	0.65	0.15	0.075	1.69	0.004600
160	$T015-8$	2	50	9	25	0.65	0.15	0.075	1.81	0.001930
161	$T015-9$	2	75	9	11	0.65	0.15	0.075	1.70	0.001730
162	$T015-10$	2	75	9	15	0.65	0.15	0.075	2.06	0.000459
163	$T015-11$	2	75	9	20	0.65	0.15	0.075	1.84	0.001800
164	$T015-12$	2	75	9	25	0.65	0.15	0.075	1.90	0.000609
165	$T015-13$	1	0	9	-	0.65	0.15	0.075	1.88	0.000861
166	$T016-1$	2	25	10	11	0.65	0.15	0.075	2.07	0.000240
167	$T016-2$	2	25	10	15	0.65	0.15	0.075	2.33	0.001280
168	$T016-3$	2	25	10	20	0.65	0.15	0.075	2.19	0.001090
169	$T016-4$	2	25	10	25	0.65	0.15	0.075	1.99	0.000387
170	$T016-5$	2	50	10	11	0.65	0.15	0.075	1.91	0.000440
171	$T016-6$	2	50	10	15	0.65	0.15	0.075	2.03	0.001280
172	$T016-7$	2	50	10	20	0.65	0.15	0.075	1.77	0.001300
173	$T016-8$	2	50	10	25	0.65	0.15	0.075	1.85	0.001420
174	$T016-12$	2	75	10	25	0.65	0.15	0.075	1.59	0.002150
175	$T016-13$	1	0	10	-	0.65	0.15	0.075	2.00	0.000532
176	$T017-1$	2	25	7	11	0.70	0.10	0.100	1.24	0.005010
177	$T017-2$	2	25	7	15	0.70	0.10	0.100	1.25	0.004210
178	$T017-3$	2	25	7	20	0.70	0.10	0.100	1.24	0.003900
179	$T017-4$	2	25	7	25	0.70	0.10	0.100	1.28	0.005370
180	$T017-5$	2	50	7	11	0.70	0.10	0.100	1.28	0.003620
181	$T017-6$	2	50	7	15	0.70	0.10	0.100	1.31	0.004800
182	$T017-7$	2	50	7	20	0.70	0.10	0.100	1.30	0.003870

(cot $\alpha = 1.5$) Continue on the next page

Table B.2 Dimensionless Wave Overtopping Results for cot $\alpha = 1.5$ (cont.)

ID	Test No	Mode Uni = 1 Bi = 2	Swell (%)	T_{pW} (secs)	T_{pS} (secs)	h (m)	R_c (m)	H_{m0} (m)	R^* (-)	Q^* (-)
183	$T017-8$	2	50	7	25	0.70	0.10	0.100	1.34	0.004780
184	$T017-9$	2	75	7	11	0.70	0.10	0.100	1.29	0.004480
185	$T017-10$	2	75	7	15	0.70	0.10	0.100	1.12	0.005140
186	$T017-13$	1	0	7	-	0.70	0.10	0.100	1.22	0.004300
187	$T018-1$	2	25	8	11	0.70	0.10	0.100	1.28	0.004780
188	$T018-2$	2	25	8	15	0.70	0.10	0.100	1.27	0.004410
189	$T018-3$	2	25	8	20	0.70	0.10	0.100	1.27	0.004680
190	$T018-4$	2	25	8	25	0.70	0.10	0.100	1.28	0.003670
191	$T018-5$	2	50	8	11	0.70	0.10	0.100	1.28	0.005290
192	$T018-6$	2	50	8	15	0.70	0.10	0.100	1.41	0.011890
193	$T018-7$	2	50	8	20	0.70	0.10	0.100	1.30	0.004760
194	$T018-8$	2	50	8	25	0.70	0.10	0.100	1.29	0.003240
195	$T018-9$	2	75	8	11	0.70	0.10	0.100	1.30	0.004980
196	$T018-10$	2	75	8	15	0.70	0.10	0.100	1.35	0.005160
197	$T018-13$	1	0	8	-	0.70	0.10	0.100	1.17	0.004100
198	$T019-1$	2	25	9	11	0.70	0.10	0.100	1.29	0.007690
199	$T019-2$	2	25	9	15	0.70	0.10	0.100	1.29	0.006770
200	$T019-3$	2	25	9	20	0.70	0.10	0.100	1.30	0.004690
201	$T019-4$	2	25	9	25	0.70	0.10	0.100	1.30	0.004820
202	$T019-5$	2	50	9	11	0.70	0.10	0.100	1.29	0.005250
203	$T019-6$	2	50	9	15	0.70	0.10	0.100	1.48	0.009690
204	$T019-7$	2	50	9	20	0.70	0.10	0.100	1.31	0.005760
205	$T019-8$	2	50	9	25	0.70	0.10	0.100	1.35	0.006540
206	$T019-9$	2	75	9	11	0.70	0.10	0.100	1.08	0.006630
207	$T019-10$	2	75	9	15	0.70	0.10	0.100	1.34	0.007040
208	$T019-11$	2	75	9	20	0.70	0.10	0.100	1.34	0.005860
209	$T019-13$	1	0	9	-	0.70	0.10	0.100	1.29	0.005550
210	$T020-1$	2	25	10	11	0.70	0.10	0.100	1.24	0.007750
211	$T020-2$	2	25	10	15	0.70	0.10	0.100	1.06	0.007740
212	$T020-3$	2	25	10	20	0.70	0.10	0.100	1.24	0.004880
213	$T020-4$	2	25	10	25	0.70	0.10	0.100	1.28	0.005230
214	$T020-5$	2	50	10	11	0.70	0.10	0.100	1.59	0.009090

(cot $\alpha = 1.5$) Continue on the next page

Table B.2 Dimensionless Wave Overtopping Results for cot $\alpha = 1.5$ (cont.)

ID	Test No	Mode Uni = 1 Bi = 2	Swell (%)	T_{pW} (secs)	T_{pS} (secs)	h (m)	R_c (m)	H_{m0} (m)	R^* (-)	Q^* (-)
215	$T020-6$	2	50	10	15	0.70	0.10	0.100	1.31	0.006770
216	$T020-7$	2	50	10	20	0.70	0.10	0.100	1.30	0.006210
217	$T020-8$	2	50	10	25	0.70	0.10	0.100	1.34	0.006960
218	$T020-9$	2	75	10	11	0.70	0.10	0.100	1.29	0.006710
219	$T020-13$	1	0	10	-	0.70	0.10	0.100	1.27	0.005140
220	$T021-1$	2	25	7	11	0.60	0.20	0.075	3.20	0.000213
221	$T021-2$	2	25	7	15	0.60	0.20	0.075	2.85	0.000214
222	$T021-3$	2	25	7	20	0.60	0.20	0.075	2.84	0.000143
223	$T021-4$	2	25	7	25	0.60	0.20	0.075	2.98	0.000172
224	$T021-5$	2	50	7	11	0.60	0.20	0.075	3.23	0.000087
225	$T021-6$	2	50	7	15	0.60	0.20	0.075	3.29	0.000080
226	$T021-7$	2	50	7	20	0.60	0.20	0.075	3.04	0.000028
227	$T021-8$	2	50	7	25	0.60	0.20	0.075	3.07	0.000012
228	$T021-9$	2	75	7	11	0.60	0.20	0.075	3.03	0.000059
229	$T021-10$	2	75	7	15	0.60	0.20	0.075	3.07	0.000028
230	$T021-11$	2	75	7	20	0.60	0.20	0.075	3.20	0.000043
231	$T021-12$	2	75	7	25	0.60	0.20	0.075	3.08	0.000061
232	$T021-13$	1	0	7	-	0.60	0.20	0.075	3.18	0.000036
233	$T022-1$	2	25	8	11	0.60	0.20	0.075	3.28	0.000200
234	$T022-2$	2	25	8	15	0.60	0.20	0.075	3.76	0.000164
235	$T022-3$	2	25	8	20	0.60	0.20	0.075	3.74	0.000109
236	$T022-4$	2	25	8	25	0.60	0.20	0.075	3.78	0.000055
237	$T022-5$	2	50	8	11	0.60	0.20	0.075	2.94	0.000132
238	$T022-6$	2	50	8	15	0.60	0.20	0.075	3.34	0.000091
239	$T022-7$	2	50	8	20	0.60	0.20	0.075	2.95	0.000008
240	$T022-8$	2	50	8	25	0.60	0.20	0.075	2.97	0.000012
241	$T022-9$	2	75	8	11	0.60	0.20	0.075	2.92	0.000037
242	$T022-10$	2	75	8	15	0.60	0.20	0.075	3.40	0.000047
243	$T022-11$	2	75	8	20	0.60	0.20	0.075	3.80	0.000055
244	$T022-13$	1	0	8	-	0.60	0.20	0.075	3.44	0.000015
245	$T023-1$	2	25	9	11	0.60	0.20	0.075	2.92	0.000112
246	$T023-2$	2	25	9	15	0.60	0.20	0.075	3.29	0.000067

(cot $\alpha = 1.5$) Continue on the next page

Table B.2 Dimensionless Wave Overtopping Results for cot $\alpha = 1.5$ (cont.)

ID	Test No	Mode Uni = 1 Bi = 2	Swell (%)	T_{pW} (secs)	T_{pS} (secs)	h (m)	R_c (m)	H_{m0} (m)	R^* (-)	Q^* (-)
247	$T023-3$	2	25	9	20	0.60	0.20	0.075	3.29	0.000045
248	$T023-4$	2	25	9	25	0.60	0.20	0.075	3.32	0.000043
249	$T023-5$	2	50	9	11	0.60	0.20	0.075	2.92	0.000037
250	$T023-6$	2	50	9	15	0.60	0.20	0.075	3.81	0.000039
251	$T023-7$	2	50	9	20	0.60	0.20	0.075	3.13	0.000025
252	$T023-8$	2	50	9	25	0.60	0.20	0.075	2.82	0.000025
253	$T023-9$	2	75	9	11	0.60	0.20	0.075	3.72	0.000065
254	$T023-10$	2	75	9	15	0.60	0.20	0.075	3.23	0.000052
255	$T023-11$	2	75	9	20	0.60	0.20	0.075	3.20	0.000052
256	$T023-12$	2	75	9	25	0.60	0.20	0.075	3.19	0.000043
257	$T023-13$	1	0	9	-	0.60	0.20	0.075	3.71	0.000008
258	$T024-1$	2	25	10	11	0.60	0.20	0.075	2.90	0.000071
259	$T024-2$	2	25	10	15	0.60	0.20	0.075	2.95	0.000159
260	$T024-3$	2	25	10	20	0.60	0.20	0.075	3.54	0.000106
261	$T024-4$	2	25	10	25	0.60	0.20	0.075	3.23	0.000170
262	$T024-5$	2	50	10	11	0.60	0.20	0.075	3.24	0.000222
263	$T024-6$	2	50	10	15	0.60	0.20	0.075	3.72	0.000210
264	$T024-7$	2	50	10	20	0.60	0.20	0.075	3.72	0.000114
265	$T024-8$	2	50	10	25	0.60	0.20	0.075	3.71	0.000127
266	$T024-9$	2	75	10	11	0.60	0.20	0.075	3.32	0.000144
267	$T024-10$	2	75	10	15	0.60	0.20	0.075	2.92	0.000059
268	$T024-11$	2	75	10	20	0.60	0.20	0.075	3.33	0.000195
269	$T024-12$	2	75	10	25	0.60	0.20	0.075	3.25	0.000092
270	$T024-13$	1	0	10	-	0.60	0.20	0.075	2.98	0.000051

Table B.3 Dimensionless Wave Overtopping Results for cot $\alpha = 0.0$

ID	Test No	Mode Uni = 1 Bi = 2	Swell (%)	T_{pW} (secs)	T_{pS} (secs)	h (m)	R_c (m)	H_{m0} (m)	R^* (-)	Q^* (-)
1	$T001-1$	2	25	7	11	0.10	0.70	0.125	0.93	0.001570

(cot $\alpha = 0.0$) Continue on the next page

Table B.3 Dimensionless Wave Overtopping Results for cot $\alpha = 0.0$ (cont.)

ID	Test No	Mode Uni = 1 Bi = 2	Swell (%)	T_{pW} (secs)	T_{pS} (secs)	h (m)	R_c (m)	H_{m0} (m)	R^* (-)	Q^* (-)
2	$T001-2$	2	25	7	15	0.10	0.70	0.125	1.01	0.001710
3	$T001-3$	2	25	7	20	0.10	0.70	0.125	1.09	0.001980
4	$T001-4$	2	25	7	25	0.10	0.70	0.125	1.09	0.002160
5	$T001-5$	2	50	7	11	0.10	0.70	0.125	0.87	0.001960
6	$T001-6$	2	50	7	15	0.10	0.70	0.125	1.01	0.002140
7	$T001-7$	2	50	7	20	0.10	0.70	0.125	1.10	0.003280
8	$T001-9$	2	75	7	11	0.10	0.70	0.125	0.78	0.003240
9	$T001-10$	2	75	7	15	0.10	0.70	0.125	0.88	0.002630
10	$T001-13$	1	0	7	-	0.10	0.70	0.125	1.08	0.001504
11	$T002-1$	2	25	8	11	0.10	0.70	0.125	0.95	0.002080
12	$T002-2$	2	25	8	15	0.10	0.70	0.125	1.02	0.002130
13	$T002-3$	2	25	8	20	0.10	0.70	0.125	1.10	0.002330
14	$T002-4$	2	25	8	25	0.10	0.70	0.125	1.11	0.002660
15	$T002-5$	2	50	8	11	0.10	0.70	0.125	0.87	0.002180
16	$T002-6$	2	50	8	15	0.10	0.70	0.125	1.01	0.002340
17	$T002-7$	2	50	8	20	0.10	0.70	0.125	1.10	0.003390
18	$T002-9$	2	75	8	11	0.10	0.70	0.125	0.77	0.003680
19	$T002-10$	2	75	8	15	0.10	0.70	0.125	1.01	0.002800
20	$T002-13$	1	0	8	-	0.10	0.70	0.125	1.02	0.001531
21	$T003-1$	2	25	9	11	0.10	0.70	0.125	0.89	0.002160
22	$T003-2$	2	25	9	15	0.10	0.70	0.125	0.87	0.003540
23	$T003-3$	2	25	9	20	0.10	0.70	0.125	0.87	0.004260
24	$T003-4$	2	25	9	25	0.10	0.70	0.125	0.93	0.002540
25	$T003-5$	2	50	9	11	0.10	0.70	0.125	0.86	0.002220
26	$T003-6$	2	50	9	15	0.10	0.70	0.125	0.93	0.002950
27	$T003-7$	2	50	9	20	0.10	0.70	0.125	1.01	0.004150
28	$T003-9$	2	75	9	11	0.10	0.70	0.125	0.78	0.004760
29	$T003-10$	2	75	9	15	0.10	0.70	0.125	0.93	0.004210
30	$T003-13$	1	0	9	-	0.10	0.70	0.125	0.92	0.001497
31	$T004-1$	2	25	10	11	0.10	0.70	0.125	0.74	0.004180
32	$T004-2$	2	25	10	15	0.10	0.70	0.125	0.78	0.006110
33	$T004-3$	2	25	10	20	0.10	0.70	0.125	0.83	0.006300

(cot $\alpha = 0.0$) Continue on the next page

Table B.3 Dimensionless Wave Overtopping Results for cot $\alpha = 0.0$ (cont.)

ID	Test No	Mode Uni = 1 Bi = 2	Swell (%)	T_{pW} (secs)	T_{pS} (secs)	h (m)	R_c (m)	H_{m0} (m)	R^* (-)	Q^* (-)
34	$T004-4$	2	25	10	25	0.10	0.70	0.125	0.86	0.002950
35	$T004-5$	2	50	10	11	0.10	0.70	0.125	0.73	0.003410
36	$T004-6$	2	50	10	15	0.10	0.70	0.125	0.82	0.007860
37	$T004-7$	2	50	10	20	0.10	0.70	0.125	0.93	0.003410
38	$T004-9$	2	75	10	11	0.10	0.70	0.125	0.77	0.004180
39	$T004-10$	2	75	10	15	0.10	0.70	0.125	0.92	0.003900
40	$T004-13$	1	0	10	-	0.10	0.70	0.125	0.75	0.005690
41	$T005-1$	2	25	7	11	0.15	0.65	0.100	1.81	0.000188
42	$T005-2$	2	25	7	15	0.15	0.65	0.100	1.81	0.000134
43	$T005-3$	2	25	7	20	0.15	0.65	0.100	1.98	0.000233
44	$T005-4$	2	25	7	25	0.15	0.65	0.100	1.65	0.000210
45	$T005-5$	2	50	7	11	0.15	0.65	0.100	1.80	0.000132
46	$T005-6$	2	50	7	15	0.15	0.65	0.100	1.95	0.000225
47	$T005-7$	2	50	7	20	0.15	0.65	0.100	1.99	0.000155
48	$T005-8$	2	50	7	25	0.15	0.65	0.100	1.73	0.000187
49	$T005-9$	2	75	7	11	0.15	0.65	0.100	1.51	0.000168
50	$T005-10$	2	75	7	15	0.15	0.65	0.100	1.76	0.000128
51	$T005-11$	2	75	7	20	0.15	0.65	0.100	2.28	0.000147
52	$T005-13$	1	0	7	-	0.15	0.65	0.100	1.81	0.000093
53	$T006-1$	2	25	8	11	0.15	0.65	0.125	1.42	0.000699
54	$T006-2$	2	25	8	15	0.15	0.65	0.125	1.54	0.000631
55	$T006-3$	2	25	8	20	0.15	0.65	0.125	1.66	0.000646
56	$T006-4$	2	25	8	25	0.15	0.65	0.125	1.66	0.000753
57	$T006-5$	2	50	8	11	0.15	0.65	0.125	1.31	0.000578
58	$T006-6$	2	50	8	15	0.15	0.65	0.125	1.50	0.001030
59	$T006-7$	2	50	8	20	0.15	0.65	0.125	1.66	0.001130
60	$T006-9$	2	75	8	11	0.15	0.65	0.125	1.01	0.000898
61	$T006-10$	2	75	8	15	0.15	0.65	0.125	1.50	0.000655
62	$T006-13$	1	0	8	-	0.15	0.65	0.125	1.67	0.000472
63	$T007-1$	2	25	9	11	0.15	0.65	0.100	1.55	0.000193
64	$T007-2$	2	25	9	15	0.15	0.65	0.100	1.65	0.000064
65	$T007-3$	2	25	9	20	0.15	0.65	0.100	1.80	0.000104

(cot $\alpha = 0.0$) Continue on the next page

Table B.3 Dimensionless Wave Overtopping Results for cot $\alpha = 0.0$ (cont.)

ID	Test No	Mode Uni = 1 Bi = 2	Swell (%)	T_{pW} (secs)	T_{pS} (secs)	h (m)	R_c (m)	H_{m0} (m)	R^* (-)	Q^* (-)
66	$T007-4$	2	25	9	25	0.15	0.65	0.100	1.80	0.000090
67	$T007-5$	2	50	9	11	0.15	0.65	0.100	1.54	0.000109
68	$T007-6$	2	50	9	15	0.15	0.65	0.100	1.63	0.000078
69	$T007-7$	2	50	9	20	0.15	0.65	0.100	1.98	0.000168
70	$T007-9$	2	75	9	11	0.15	0.65	0.100	1.51	0.000128
71	$T007-10$	2	75	9	15	0.15	0.65	0.100	1.79	0.000157
72	$T007-11$	2	75	9	20	0.15	0.65	0.100	2.21	0.000190
73	$T007-12$	2	75	9	25	0.15	0.65	0.100	1.62	0.000114
74	$T007-13$	1	0	9	-	0.15	0.65	0.100	1.65	0.000081
75	$T008-1$	2	25	10	11	0.15	0.65	0.125	1.11	0.000738
76	$T008-2$	2	25	10	15	0.15	0.65	0.125	1.22	0.000408
77	$T008-3$	2	25	10	20	0.15	0.65	0.125	1.23	0.000487
78	$T008-4$	2	50	10	25	0.15	0.65	0.125	1.39	0.000559
79	$T008-5$	2	50	10	11	0.15	0.65	0.125	1.21	0.000456
80	$T008-6$	2	50	10	15	0.15	0.65	0.125	1.23	0.000559
81	$T008-7$	2	50	10	20	0.15	0.65	0.125	1.31	0.000828
82	$T008-9$	2	75	10	11	0.15	0.65	0.125	1.15	0.000670
83	$T008-10$	2	75	10	15	0.15	0.65	0.125	1.31	0.000906
84	$T008-13$	1	0	10	-	0.15	0.65	0.125	1.20	0.000491
85	$T009-1$	2	25	7	11	0.20	0.60	0.100	2.40	0.000070
86	$T009-2$	2	25	7	15	0.20	0.60	0.100	2.65	0.000013
87	$T009-3$	2	25	7	20	0.20	0.60	0.100	2.64	0.000021
88	$T009-4$	2	25	7	25	0.20	0.60	0.100	2.64	0.000047
89	$T009-5$	2	50	7	11	0.20	0.60	0.100	2.16	0.000074
90	$T009-6$	2	50	7	15	0.20	0.60	0.100	2.58	0.000067
91	$T009-7$	2	50	7	20	0.20	0.60	0.100	2.90	0.000028
92	$T009-8$	2	50	7	25	0.20	0.60	0.100	2.84	0.000050
93	$T009-9$	2	75	7	11	0.20	0.60	0.100	1.98	0.000065
94	$T009-10$	2	75	7	15	0.20	0.60	0.100	2.56	0.000104
95	$T009-11$	2	75	7	20	0.20	0.60	0.100	2.63	0.000033
96	$T009-13$	1	0	7	-	0.20	0.60	0.100	2.43	0.000046
97	$T010-1$	2	25	8	11	0.20	0.60	0.100	2.33	0.000065

(cot $\alpha = 0.0$) Continue on the next page

Table B.3 Dimensionless Wave Overtopping Results for cot $\alpha = 0.0$ (cont.)

ID	Test No	Mode Uni = 1 Bi = 2	Swell (%)	T_{pW} (secs)	T_{pS} (secs)	h (m)	R_c (m)	H_{m0} (m)	R^* (-)	Q^* (-)
98	$T010-2$	2	25	8	15	0.20	0.60	0.100	2.10	0.000046
99	$T010-3$	2	25	8	20	0.20	0.60	0.100	2.47	0.000071
100	$T010-4$	2	25	8	25	0.20	0.60	0.100	2.03	0.000078
101	$T010-5$	2	50	8	11	0.20	0.60	0.100	2.20	0.000063
102	$T010-6$	2	50	8	15	0.20	0.60	0.100	2.35	0.000096
103	$T010-7$	2	50	8	20	0.20	0.60	0.100	2.22	0.000102
104	$T010-8$	2	50	8	25	0.20	0.60	0.100	2.23	0.000000
105	$T010-9$	2	75	8	11	0.20	0.60	0.100	2.13	0.000251
106	$T010-10$	2	75	8	15	0.20	0.60	0.100	2.29	0.000228
107	$T010-13$	1	0	8	-	0.20	0.60	0.100	2.26	0.000103
108	$T011-1$	2	25	9	11	0.20	0.60	0.125	1.65	0.000095
109	$T011-2$	2	25	9	15	0.20	0.60	0.125	2.42	0.000109
110	$T011-3$	2	25	9	20	0.20	0.60	0.125	2.35	0.000143
111	$T011-4$	2	25	9	25	0.20	0.60	0.125	1.74	0.000000
112	$T011-5$	2	50	9	11	0.20	0.60	0.125	1.64	0.000263
113	$T011-6$	2	50	9	15	0.20	0.60	0.125	1.85	0.000316
114	$T011-7$	2	50	9	20	0.20	0.60	0.125	1.71	0.000000
115	$T011-9$	2	75	9	11	0.20	0.60	0.125	1.43	0.000276
116	$T011-10$	2	75	9	15	0.20	0.60	0.125	1.85	0.000499
117	$T011-13$	1	0	9	-	0.20	0.60	0.125	1.65	0.000077
118	$T0012-1$	2	25	10	11	0.20	0.60	0.125	1.45	0.000313
119	$T0012-2$	2	25	10	15	0.20	0.60	0.125	1.44	0.000271
120	$T0012-3$	2	25	10	20	0.20	0.60	0.125	1.45	0.000267
121	$T0012-4$	2	25	10	25	0.20	0.60	0.125	1.98	0.000386
122	$T0012-5$	2	50	10	11	0.20	0.60	0.125	1.52	0.000322
123	$T0012-6$	2	50	10	15	0.20	0.60	0.125	1.60	0.000377
124	$T0012-9$	2	75	10	11	0.20	0.60	0.125	1.42	0.000181
125	$T0012-10$	2	75	10	15	0.20	0.60	0.125	1.84	0.000654
126	$T0012-13$	1	0	10	-	0.20	0.60	0.125	1.44	0.000224
127	$T013-1$	2	25	7	11	0.15	0.65	0.075	2.21	0.000000
128	$T013-2$	2	25	7	15	0.15	0.65	0.075	2.49	0.000000
129	$T013-3$	2	25	7	20	0.15	0.65	0.075	2.49	0.000000

(cot $\alpha = 0.0$) Continue on the next page

Table B.3 Dimensionless Wave Overtopping Results for cot $\alpha = 0.0$ (cont.)

ID	Test No	Mode Uni = 1 Bi = 2	Swell (%)	T_{pW} (secs)	T_{pS} (secs)	h (m)	R_c (m)	H_{m0} (m)	R^* (-)	Q^* (-)
130	$T013-4$	2	25	7	25	0.15	0.65	0.075	2.49	0.000000
131	$T013-5$	2	50	7	11	0.15	0.65	0.075	2.20	0.000000
132	$T013-6$	2	50	7	15	0.15	0.65	0.075	2.43	0.000000
133	$T013-7$	2	50	7	20	0.15	0.65	0.075	2.85	0.000000
134	$T013-8$	2	50	7	25	0.15	0.65	0.075	2.49	0.000000
135	$T013-9$	2	75	7	11	0.15	0.65	0.075	1.93	0.000000
136	$T013-10$	2	75	7	15	0.15	0.65	0.075	2.40	0.000000
137	$T013-11$	2	75	7	20	0.15	0.65	0.075	2.85	0.000000
138	$T013-12$	2	75	7	25	0.15	0.65	0.075	2.74	0.000000
139	$T013-13$	1	0	7	-	0.15	0.65	0.075	2.21	0.000000
140	$T014-1$	2	25	8	11	0.15	0.65	0.075	2.24	0.000000
141	$T014-2$	2	25	8	15	0.15	0.65	0.075	2.51	0.000000
142	$T014-3$	2	25	8	20	0.15	0.65	0.075	2.86	0.000000
143	$T014-4$	2	25	8	25	0.15	0.65	0.075	2.85	0.000000
144	$T014-5$	2	50	8	11	0.15	0.65	0.075	2.20	0.000000
145	$T014-6$	2	50	8	15	0.15	0.65	0.075	2.43	0.000000
146	$T014-7$	2	50	8	20	0.15	0.65	0.075	2.85	0.000000
147	$T014-8$	2	50	8	25	0.15	0.65	0.075	2.85	0.000000
148	$T014-9$	2	75	8	11	0.15	0.65	0.075	1.93	0.000000
149	$T014-10$	2	75	8	15	0.15	0.65	0.075	2.35	0.000000
150	$T014-11$	2	75	8	20	0.15	0.65	0.075	2.85	0.000000
151	$T014-12$	2	75	8	25	0.15	0.65	0.075	2.85	0.000000
152	$T014-13$	1	0	8	-	0.15	0.65	0.075	2.52	0.000000
153	$T015-1$	2	25	9	11	0.15	0.65	0.075	1.98	0.000000
154	$T015-2$	2	25	9	15	0.15	0.65	0.075	2.18	0.000000
155	$T015-3$	2	25	9	20	0.15	0.65	0.075	2.19	0.000000
156	$T015-4$	2	25	9	25	0.15	0.65	0.075	2.45	0.000000
157	$T015-5$	2	50	9	11	0.15	0.65	0.075	1.96	0.000000
158	$T015-6$	2	50	9	15	0.15	0.65	0.075	2.13	0.000000
159	$T015-7$	2	50	9	20	0.15	0.65	0.075	2.45	0.000000
160	$T015-8$	2	50	9	25	0.15	0.65	0.075	2.47	0.000000
161	$T015-9$	2	75	9	11	0.15	0.65	0.075	1.90	0.000000

(cot $\alpha = 0.0$) Continue on the next page

Table B.3 Dimensionless Wave Overtopping Results for cot $\alpha = 0.0$ (cont.)

ID	Test No	Mode Uni = 1 Bi = 2	Swell (%)	T_{pW} (secs)	T_{pS} (secs)	h (m)	R_c (m)	H_{m0} (m)	R^* (-)	Q^* (-)
162	$T015-10$	2	75	9	15	0.15	0.65	0.075	2.11	0.000000
163	$T015-11$	2	75	9	20	0.15	0.65	0.075	2.85	0.000000
164	$T015-12$	2	75	9	25	0.15	0.65	0.075	2.85	0.000000
165	$T015-13$	1	0	9	-	0.15	0.65	0.075	2.20	0.000000
166	$T016-1$	2	25	10	11	0.15	0.65	0.075	1.95	0.000000
167	$T016-2$	2	25	10	15	0.15	0.65	0.075	1.72	0.000000
168	$T016-3$	2	25	10	20	0.15	0.65	0.075	1.95	0.000000
169	$T016-4$	2	25	10	25	0.15	0.65	0.075	1.95	0.000000
170	$T016-5$	2	50	10	11	0.15	0.65	0.075	1.91	0.000000
171	$T016-6$	2	50	10	15	0.15	0.65	0.075	2.10	0.000000
172	$T016-7$	2	50	10	20	0.15	0.65	0.075	2.17	0.000000
173	$T016-8$	2	50	10	25	0.15	0.65	0.075	2.44	0.000000
174	$T016-9$	2	75	10	11	0.15	0.65	0.075	1.88	0.000000
175	$T016-10$	2	75	10	15	0.15	0.65	0.075	2.10	0.000000
176	$T016-11$	2	75	10	20	0.15	0.65	0.075	2.50	0.000000
177	$T016-12$	2	75	10	25	0.15	0.65	0.075	2.49	0.000000
178	$T016-13$	1	0	10	-	0.15	0.65	0.075	1.95	0.000000
179	$T017-1$	2	25	7	11	0.10	0.70	0.100	1.21	0.000738
180	$T017-2$	2	25	7	15	0.10	0.70	0.100	1.21	0.000671
181	$T017-3$	2	25	7	20	0.10	0.70	0.100	1.32	0.000954
182	$T017-4$	2	25	7	25	0.10	0.70	0.100	1.20	0.001090
183	$T017-5$	2	50	7	11	0.10	0.70	0.100	1.10	0.000581
184	$T017-6$	2	50	7	15	0.10	0.70	0.100	1.20	0.000864
185	$T017-7$	2	50	7	20	0.10	0.70	0.100	1.34	0.001090
186	$T017-8$	2	50	7	25	0.10	0.70	0.100	1.21	0.001280
187	$T017-9$	2	75	7	11	0.10	0.70	0.100	1.02	0.001220
188	$T017-10$	2	75	7	15	0.10	0.70	0.100	1.20	0.001200
189	$T017-11$	2	75	7	20	0.10	0.70	0.100	1.48	0.001370
190	$T017-13$	1	0	7	-	0.10	0.70	0.100	1.21	0.000000
191	$T018-1$	2	25	8	11	0.10	0.70	0.100	1.22	0.000818
192	$T018-2$	2	25	8	15	0.10	0.70	0.100	1.22	0.000474
193	$T018-3$	2	25	8	20	0.10	0.70	0.100	1.34	0.001170

(cot $\alpha = 0.0$) Continue on the next page

Table B.3 Dimensionless Wave Overtopping Results for cot $\alpha = 0.0$ (cont.)

ID	Test No	Mode Uni = 1 Bi = 2	Swell (%)	T_{pW} (secs)	T_{pS} (secs)	h (m)	R_c (m)	H_{m0} (m)	R^* (-)	Q^* (-)
194	$T018-4$	2	25	8	25	0.10	0.70	0.100	1.34	0.000858
195	$T018-5$	2	50	8	11	0.10	0.70	0.100	1.10	0.000583
196	$T018-6$	2	50	8	15	0.10	0.70	0.100	1.19	0.000591
197	$T018-7$	2	50	8	20	0.10	0.70	0.100	1.49	0.001190
198	$T018-8$	2	50	8	25	0.10	0.70	0.100	1.34	0.001170
199	$T018-9$	2	75	8	11	0.10	0.70	0.100	1.04	0.001650
200	$T018-10$	2	75	8	15	0.10	0.70	0.100	1.20	0.000867
201	$T018-11$	2	75	8	20	0.10	0.70	0.100	1.50	0.001670
202	$T018-13$	1	0	8	-	0.10	0.70	0.100	1.35	0.000788
203	$T019-1$	2	25	9	11	0.10	0.70	0.100	1.00	0.001170
204	$T019-2$	2	25	9	15	0.10	0.70	0.100	1.12	0.001070
205	$T019-3$	2	25	9	20	0.10	0.70	0.100	1.14	0.000898
206	$T019-4$	2	25	9	25	0.10	0.70	0.100	1.13	0.001300
207	$T019-5$	2	50	9	11	0.10	0.70	0.100	1.04	0.001320
208	$T019-6$	2	50	9	15	0.10	0.70	0.100	1.13	0.001520
209	$T019-7$	2	50	9	20	0.10	0.70	0.100	1.12	0.000942
210	$T019-8$	2	50	9	25	0.10	0.70	0.100	1.21	0.001300
211	$T019-9$	2	75	9	11	0.10	0.70	0.100	1.04	0.001060
212	$T019-10$	2	75	9	15	0.10	0.70	0.100	1.20	0.001120
213	$T019-11$	2	75	9	20	0.10	0.70	0.100	1.49	0.001170
214	$T019-13$	1	0	9	-	0.10	0.70	0.100	1.12	0.000501
215	$T020-1$	2	25	10	11	0.10	0.70	0.100	1.03	0.000000
216	$T020-2$	2	25	10	15	0.10	0.70	0.100	0.96	0.000000
217	$T020-3$	2	25	10	20	0.10	0.70	0.100	1.03	0.000000
218	$T020-4$	2	25	10	25	0.10	0.70	0.100	1.07	0.000000
219	$T020-5$	2	50	10	11	0.10	0.70	0.100	1.16	0.000000
220	$T020-6$	2	50	10	15	0.10	0.70	0.100	1.01	0.000000
221	$T020-7$	2	50	10	20	0.10	0.70	0.100	1.18	0.000000
222	$T020-8$	2	50	10	25	0.10	0.70	0.100	1.48	0.000000
223	$T020-9$	2	75	10	11	0.10	0.70	0.100	1.08	0.000000
224	$T020-10$	2	75	10	15	0.10	0.70	0.100	1.18	0.000000
225	$T020-11$	2	75	10	20	0.10	0.70	0.100	1.44	0.000000

(cot $\alpha = 0.0$) Continue on the next page

Table B.3 Dimensionless Wave Overtopping Results for cot $\alpha = 0.0$ (cont.)

ID	Test No	Mode Uni = 1 Bi = 2	Swell (%)	T_{pW} (secs)	T_{pS} (secs)	h (m)	R_c (m)	H_{m0} (m)	R^* (-)	Q^* (-)
226	$T020-13$	1	0	10	-	0.10	0.70	0.100	1.06	0.000000
227	$T021-1$	2	25	7	11	0.20	0.60	0.075	3.30	0.000000
228	$T021-2$	2	25	7	15	0.20	0.60	0.075	3.78	0.000000
229	$T021-3$	2	25	7	20	0.20	0.60	0.075	3.77	0.000000
230	$T021-4$	2	25	7	25	0.20	0.60	0.075	3.77	0.000000
231	$T021-5$	2	50	7	11	0.20	0.60	0.075	3.28	0.000000
232	$T021-6$	2	50	7	15	0.20	0.60	0.075	3.66	0.000000
233	$T021-7$	2	50	7	20	0.20	0.60	0.075	3.77	0.000000
234	$T021-8$	2	50	7	25	0.20	0.60	0.075	3.94	0.000000
235	$T021-9$	2	75	7	11	0.20	0.60	0.075	2.56	0.000000
236	$T021-10$	2	75	7	15	0.20	0.60	0.075	3.17	0.000000
237	$T021-11$	2	75	7	20	0.20	0.60	0.075	4.12	0.000000
238	$T021-12$	2	75	7	25	0.20	0.60	0.075	3.77	0.000000
239	$T021-13$	1	0	7	-	0.20	0.60	0.075	3.77	0.000000
240	$T022-1$	2	25	8	11	0.20	0.60	0.075	2.97	0.000000
241	$T022-2$	2	25	8	15	0.20	0.60	0.075	3.33	0.000000
242	$T022-3$	2	25	8	20	0.20	0.60	0.075	3.32	0.000000
243	$T022-4$	2	25	8	25	0.20	0.60	0.075	3.31	0.000000
244	$T022-5$	2	50	8	11	0.20	0.60	0.075	3.30	0.000000
245	$T022-6$	2	50	8	15	0.20	0.60	0.075	3.68	0.000000
246	$T022-7$	2	50	8	20	0.20	0.60	0.075	3.77	0.000000
247	$T022-8$	2	50	8	25	0.20	0.60	0.075	3.31	0.000000
248	$T022-9$	2	75	8	11	0.20	0.60	0.075	2.56	0.000000
249	$T022-10$	2	75	8	15	0.20	0.60	0.075	3.13	0.000000
250	$T022-11$	2	75	8	20	0.20	0.60	0.075	3.80	0.000000
251	$T022-13$	1	0	8	-	0.20	0.60	0.075	3.34	0.000000
252	$T023-1$	2	25	9	11	0.20	0.60	0.075	2.93	0.000000
253	$T023-2$	2	25	9	15	0.20	0.60	0.075	2.90	0.000000
254	$T023-3$	2	25	9	20	0.20	0.60	0.075	3.28	0.000000
255	$T023-4$	2	25	9	25	0.20	0.60	0.075	3.27	0.000000
256	$T023-5$	2	50	9	11	0.20	0.60	0.075	2.90	0.000000
257	$T023-6$	2	50	9	15	0.20	0.60	0.075	3.18	0.000000

(cot $\alpha = 0.0$) Continue on the next page

Table B.3 Dimensionless Wave Overtopping Results for cot $\alpha = 0.0$ (cont.)

ID	Test No	Mode Uni = 1 Bi = 2	Swell (%)	T_{pW} (secs)	T_{pS} (secs)	h (m)	R_c (m)	H_{m0} (m)	R^* (-)	Q^* (-)
258	$T023-7$	2	50	9	20	0.20	0.60	0.075	3.18	0.000000
259	$T023-8$	2	50	9	25	0.20	0.60	0.075	3.74	0.000000
260	$T023-9$	2	75	9	11	0.20	0.60	0.075	2.54	0.000000
261	$T023-10$	2	75	9	15	0.20	0.60	0.075	3.14	0.000000
262	$T023-11$	2	75	9	20	0.20	0.60	0.075	3.78	0.000000
263	$T023-12$	2	75	9	25	0.20	0.60	0.075	3.65	0.000000
264	$T023-13$	1	0	9	-	0.20	0.60	0.075	3.29	0.000000
265	$T024-1$	2	25	10	11	0.20	0.60	0.075	2.61	0.000000
266	$T024-2$	2	25	10	15	0.20	0.60	0.075	2.53	0.000000
267	$T024-3$	2	25	10	20	0.20	0.60	0.075	2.89	0.000000
268	$T024-4$	2	25	10	25	0.20	0.60	0.075	2.86	0.000000
269	$T024-5$	2	50	10	11	0.20	0.60	0.075	2.56	0.000000
270	$T024-6$	2	50	10	15	0.20	0.60	0.075	2.79	0.000000
271	$T024-7$	2	50	10	20	0.20	0.60	0.075	3.25	0.000000
272	$T024-8$	2	50	10	25	0.20	0.60	0.075	3.24	0.000000
273	$T024-9$	2	75	10	11	0.20	0.60	0.075	2.51	0.000000
274	$T024-10$	2	75	10	15	0.20	0.60	0.075	2.76	0.000000
275	$T024-11$	2	75	10	20	0.20	0.60	0.075	3.31	0.000000
276	$T024-12$	2	75	10	25	0.20	0.60	0.075	3.30	0.000000
277	$T024-13$	1	0	10	-	0.20	0.60	0.075	2.61	0.000000

Appendix C

Reflection Characteristics Under Bimodal Seas

Table C.1 Reflection Characteristics Under Bimodal Seas for cot $\alpha = 3.0$

ID	Test No	Swell (%)	Reff Coeff K_r (-)	Surf Similarity Parameter $\xi_{m-1,0}$ (-)
1	$T001-1$	25	0.416	2.665
2	$T001-2$	25	0.423	2.755
3	$T001-3$	25	0.568	2.879
4	$T001-4$	25	0.426	2.799
5	$T001-5$	50	0.525	2.896
6	$T001-6$	50	0.671	3.182
7	$T001-7$	50	0.700	3.269
8	$T001-9$	75	0.608	3.052
9	$T001-10$	75	0.862	3.621
10	$T001-13$	1	0.422	2.621
11	$T002-1$	25	0.432	2.563
12	$T002-2$	25	0.440	2.658
13	$T002-3$	25	0.563	2.778
14	$T002-4$	25	0.448	2.715
15	$T002-5$	50	0.518	2.716
16	$T002-6$	50	0.645	3.005
17	$T002-7$	50	0.680	3.093
18	$T002-9$	75	0.555	2.895

(cot $\alpha = 3.0$) Continue on the next page

Table C.1 Reflection Characteristics Under Bimodal Seas for cot $\alpha = 3.0$ (cont.).

ID	Test No	Swell (%)	Ref. Coeff K_r (-)	Surf Similarity Parameter $\xi_{m-1,0}$ (-)
19	$T002-10$	75	0.871	3.476
20	$T002-13$	1	0.436	2.431
21	$T003-1$	25	0.551	3.118
22	$T003-2$	25	0.553	3.109
23	$T003-3$	25	0.617	3.225
24	$T003-4$	25	0.544	3.175
25	$T003-5$	50	0.579	3.196
26	$T003-6$	50	0.717	3.479
27	$T003-7$	50	0.740	3.682
28	$T003-9$	75	0.583	3.201
29	$T003-10$	75	0.826	3.841
30	$T003-13$	1	0.534	3.140
31	$T004-1$	25	0.774	3.308
32	$T004-2$	25	0.790	3.469
33	$T004-3$	25	0.773	3.543
34	$T004-4$	25	0.782	3.714
35	$T004-5$	50	0.773	3.345
36	$T004-6$	50	0.841	3.689
37	$T004-9$	75	0.794	3.418
38	$T004-10$	75	0.895	4.020
39	$T004-13$	1	0.774	3.576
40	$T005-1$	25	0.444	3.041
41	$T005-2$	25	0.599	3.127
42	$T005-3$	25	0.630	3.198
43	$T005-4$	25	0.618	3.213
44	$T005-5$	50	0.554	3.192
45	$T005-6$	50	0.706	3.350
46	$T005-7$	50	0.755	3.560
47	$T005-8$	50	0.810	3.591
48	$T005-9$	75	0.611	3.438
49	$T005-10$	75	0.890	3.945
50	$T005-11$	75	0.856	4.078
51	$T005-13$	1	0.433	2.877

(cot $\alpha = 3.0$) Continue on the next page

Table C.1 Reflection Characteristics Under Bimodal Seas for cot $\alpha = 3.0$ (cont.).

ID	Test No	Swell (%)	Ref. Coeff K_r (-)	Surf Similarity Parameter $\xi_{m-1,0}$ (-)
52	$T006-1$	25	0.437	2.868
53	$T006-2$	25	0.439	2.971
54	$T006-3$	25	0.613	3.017
55	$T006-4$	25	0.617	3.143
56	$T006-5$	50	0.518	3.037
57	$T006-6$	50	0.643	3.358
58	$T006-7$	50	0.739	3.353
59	$T006-9$	75	0.554	3.236
60	$T006-10$	75	0.890	3.905
61	$T006-13$	1	0.437	2.862
62	$T007-1$	25	0.565	3.426
63	$T007-2$	25	0.573	3.560
64	$T007-3$	25	0.679	3.667
65	$T007-4$	25	0.770	3.790
66	$T007-5$	50	0.586	3.506
67	$T007-6$	50	0.720	3.728
68	$T007-7$	50	0.797	4.022
69	$T007-9$	75	0.606	3.669
70	$T007-10$	75	0.915	4.287
71	$T007-11$	75	0.855	4.347
72	$T007-12$	75	0.922	4.730
73	$T007-13$	1	0.567	3.293
74	$T008-1$	25	0.585	3.315
75	$T008-2$	25	0.603	3.457
76	$T008-3$	25	0.673	3.460
77	$T008-4$	50	0.670	3.458
78	$T008-5$	50	0.593	3.339
79	$T008-6$	50	0.725	3.604
80	$T008-7$	50	0.751	3.803
81	$T008-9$	75	0.585	3.352
82	$T008-10$	75	0.828	3.875
83	$T008-13$	1	0.562	3.242
84	$T009-1$	25	0.443	3.041

(cot $\alpha = 3.0$) Continue on the next page

Table C.1 Reflection Characteristics Under Bimodal Seas for cot $\alpha = 3.0$ (cont.).

ID	Test No	Swell (%)	Ref. Coeff K_r (-)	Surf Similarity Parameter $\xi_{m-1,0}$ (-)
85	$T009-2$	25	0.596	3.125
86	$T009-3$	25	0.646	3.209
87	$T009-4$	25	0.618	3.213
88	$T009-5$	50	0.554	3.192
89	$T009-6$	50	0.703	3.348
90	$T009-7$	50	0.769	3.572
91	$T009-8$	50	0.810	3.750
92	$T009-9$	75	0.600	3.430
93	$T009-10$	75	0.910	4.158
94	$T009-11$	75	0.820	4.428
95	$T009-13$	1	0.443	2.735
96	$T010-1$	25	0.518	3.168
97	$T010-2$	25	0.608	3.323
98	$T010-3$	25	0.653	3.448
99	$T010-4$	25	0.656	3.473
100	$T010-5$	50	0.558	3.332
101	$T010-6$	50	0.760	3.585
102	$T010-7$	50	0.786	3.681
103	$T010-8$	50	0.800	3.730
104	$T010-9$	75	0.622	3.285
105	$T010-10$	75	0.854	3.910
106	$T010-13$	1	0.512	2.881
107	$T011-1$	25	0.536	3.108
108	$T011-2$	25	0.604	3.366
109	$T011-3$	25	0.830	2.963
110	$T011-4$	25	0.667	3.262
111	$T011-5$	50	0.565	3.186
112	$T011-6$	50	0.714	3.476
113	$T011-7$	50	0.810	3.745
114	$T011-9$	75	0.579	2.978
115	$T011-10$	75	0.854	4.205
116	$T011-13$	1	0.512	3.126
117	$T0012-1$	25	0.593	3.172

(cot $\alpha = 3.0$) Continue on the next page

Table C.1 Reflection Characteristics Under Bimodal Seas for cot $\alpha = 3.0$ (cont.).

ID	Test No	Swell (%)	Ref. Coeff K_r (-)	Surf Similarity Parameter $\xi_{m-1,0}$ (-)
118	$T0012-2$	25	0.635	3.345
119	$T0012-3$	25	0.708	3.489
120	$T0012-4$	25	0.717	3.513
121	$T0012-5$	50	0.601	3.345
122	$T0012-6$	50	0.722	3.792
123	$T0012-9$	75	0.590	3.259
124	$T0012-10$	75	0.828	3.953
125	$T0012-13$	1	0.605	3.162
126	$T013-1$	25	0.489	3.537
127	$T013-2$	25	0.625	3.759
128	$T013-3$	25	0.661	3.820
129	$T013-4$	25	0.666	3.911
130	$T013-5$	50	0.603	3.554
131	$T013-6$	50	0.756	4.001
132	$T013-7$	50	0.786	4.230
133	$T013-8$	50	0.890	4.364
134	$T013-9$	75	0.705	3.953
135	$T013-10$	75	0.915	4.410
136	$T013-11$	75	0.886	4.782
137	$T013-12$	75	0.800	4.952
138	$T013-13$	1	0.476	3.289
139	$T014-1$	25	0.566	3.604
140	$T014-2$	25	0.557	3.725
141	$T014-3$	25	0.704	3.927
142	$T014-4$	25	0.710	3.932
143	$T014-5$	50	0.619	3.826
144	$T014-6$	50	0.793	4.285
145	$T014-7$	50	0.775	4.429
146	$T014-8$	50	0.808	4.533
147	$T014-9$	75	0.710	4.057
148	$T014-10$	75	0.917	4.858
149	$T014-11$	75	0.884	4.947
150	$T014-12$	75	0.880	5.172

(cot $\alpha = 3.0$) Continue on the next page

Table C.1 Reflection Characteristics Under Bimodal Seas for cot $\alpha = 3.0$ (cont.).

ID	Test No	Swell (%)	Ref. Coeff K_r (-)	Surf Similarity Parameter $\xi_{m-1,0}$ (-)
151	$T014-13$	1	0.532	3.656
152	$T015-1$	25	0.646	3.899
153	$T015-2$	25	0.661	4.059
154	$T015-3$	25	0.748	4.239
155	$T015-4$	25	0.763	4.278
156	$T015-5$	50	0.677	4.026
157	$T015-6$	50	0.772	4.403
158	$T015-7$	50	0.818	4.490
159	$T015-8$	50	0.855	4.591
160	$T015-9$	75	0.790	4.282
161	$T015-10$	75	0.886	4.646
162	$T015-11$	75	0.885	5.092
163	$T015-12$	75	0.860	5.314
164	$T015-13$	1	0.641	4.029
165	$T016-1$	25	0.780	4.199
166	$T016-2$	25	0.721	4.327
167	$T016-3$	25	0.756	4.498
168	$T016-4$	25	0.766	4.531
169	$T016-5$	50	0.740	4.231
170	$T016-6$	50	0.808	4.378
171	$T016-7$	50	0.831	4.736
172	$T016-8$	50	0.841	4.804
173	$T016-9$	75	0.715	4.252
174	$T016-10$	75	0.883	5.048
175	$T016-11$	75	0.876	5.014
176	$T016-12$	75	0.920	5.460
177	$T016-13$	1	0.770	4.140
178	$T017-1$	25	0.456	3.048
179	$T017-2$	25	0.593	3.123
180	$T017-3$	25	0.613	3.185
181	$T017-4$	25	0.616	3.212
182	$T017-5$	50	0.560	3.196
183	$T017-6$	50	0.670	3.485

(cot $\alpha = 3.0$) Continue on the next page

Table C.1 Reflection Characteristics Under Bimodal Seas for cot $\alpha = 3.0$ (cont.).

ID	Test No	Swell (%)	Ref. Coeff K_r (-)	Surf Similarity Parameter $\xi_{m-1,0}$ (-)
184	$T017-7$	50	0.725	3.534
185	$T017-8$	50	0.885	3.658
186	$T017-9$	75	0.608	3.436
187	$T017-10$	75	0.884	3.939
188	$T017-11$	75	0.827	4.049
189	$T017-13$	1	0.442	2.882
190	$T018-1$	25	0.524	3.344
191	$T018-2$	25	0.494	3.244
192	$T018-3$	25	0.597	3.405
193	$T018-4$	25	0.505	3.362
194	$T018-5$	50	0.565	3.337
195	$T018-6$	50	0.750	3.751
196	$T018-7$	50	0.717	3.782
197	$T018-8$	50	0.810	3.906
198	$T018-9$	75	0.628	3.603
199	$T018-10$	75	0.887	4.134
200	$T018-11$	75	0.910	4.317
201	$T018-13$	1	0.486	3.169
202	$T019-1$	25	0.579	3.436
203	$T019-2$	25	0.586	3.570
204	$T019-3$	25	0.598	3.600
205	$T019-4$	25	0.604	3.646
206	$T019-5$	50	0.595	3.513
207	$T019-6$	50	0.728	3.917
208	$T019-7$	50	0.757	3.984
209	$T019-8$	50	0.910	4.116
210	$T019-9$	75	0.628	3.687
211	$T019-10$	75	0.899	4.270
212	$T019-11$	75	0.890	4.803
213	$T019-13$	1	0.583	3.305
214	$T020-1$	25	0.627	3.602
215	$T020-2$	25	0.659	3.656
216	$T020-3$	25	0.700	3.785

(cot $\alpha = 3.0$) Continue on the next page

Table C.1 Reflection Characteristics Under Bimodal Seas for cot $\alpha = 3.0$ (cont.).

ID	Test No	Swell (%)	Ref. Coeff K_r (-)	Surf Similarity Parameter $\xi_{m-1,0}$ (-)
217	$T020-4$	25	0.646	3.940
218	$T020-5$	50	0.632	3.690
219	$T020-6$	50	0.749	4.094
220	$T020-7$	50	0.742	4.159
221	$T020-8$	50	0.645	4.147
222	$T020-9$	75	0.635	3.579
223	$T020-10$	75	0.838	4.240
224	$T020-11$	75	0.840	4.678
225	$T020-13$	1	0.626	3.602
226	$T021-1$	25	0.485	3.306
227	$T021-2$	25	0.640	3.529
228	$T021-3$	25	0.644	3.559
229	$T021-4$	25	0.498	3.528
230	$T021-5$	50	0.593	3.546
231	$T021-6$	50	0.751	3.997
232	$T021-7$	50	0.771	4.214
233	$T021-8$	50	0.950	4.430
234	$T021-9$	75	0.689	3.938
235	$T021-10$	75	0.922	4.685
236	$T021-11$	75	0.966	4.878
237	$T021-12$	75	0.502	4.629
238	$T021-13$	1	0.502	3.092
239	$T022-1$	25	0.540	3.584
240	$T022-2$	25	0.556	3.724
241	$T022-3$	25	0.703	3.926
242	$T022-4$	25	0.770	3.989
243	$T022-5$	50	0.610	3.818
244	$T022-6$	50	0.783	4.275
245	$T022-7$	50	0.776	4.430
246	$T022-8$	50	0.793	4.516
247	$T022-9$	75	0.679	4.028
248	$T022-10$	75	0.916	4.857
249	$T022-11$	75	0.882	4.945

(cot $\alpha = 3.0$) Continue on the next page

Table C.1 Reflection Characteristics Under Bimodal Seas for cot $\alpha = 3.0$ (cont.).

ID	Test No	Swell (%)	Ref. Coeff K_r (-)	Surf Similarity Parameter $\xi_{m-1,0}$ (-)
250	$T022-13$	1	0.532	3.420
251	$T023-1$	25	0.627	3.883
252	$T023-2$	25	0.645	4.044
253	$T023-3$	25	0.748	4.239
254	$T023-4$	25	0.758	4.273
255	$T023-5$	50	0.679	4.028
256	$T023-6$	50	0.764	4.143
257	$T023-7$	50	0.845	4.520
258	$T023-8$	50	0.834	4.567
259	$T023-9$	75	0.730	4.221
260	$T023-10$	75	0.881	4.640
261	$T023-11$	75	0.882	5.088
262	$T023-12$	75	0.795	5.230
263	$T023-13$	1	0.627	4.016
264	$T024-1$	25	0.702	4.122
265	$T024-2$	25	0.726	4.332
266	$T024-3$	25	0.732	4.472
267	$T024-4$	25	0.776	4.542
268	$T024-5$	50	0.703	4.194
269	$T024-6$	50	0.804	4.639
270	$T024-7$	50	0.839	4.746
271	$T024-8$	50	0.712	4.656
272	$T024-9$	75	0.876	4.422
273	$T024-10$	75	0.876	5.039
274	$T024-11$	75	0.876	5.014
275	$T024-12$	75	0.903	5.437
276	$T024-13$	1	0.790	4.160

Table C.2 Reflection Characteristics Under Bimodal Seas for cot $\alpha = 1.5$

ID	Test No	Swell (%)	Reff Coeff K_r (-)	Surf Similarity Parameter $\xi_{m-1,0}$ (-)
1	$T001-1$	25	0.672	2.811
2	$T001-2$	25	0.684	2.910
3	$T001-3$	25	0.681	3.235
4	$T001-4$	25	0.689	2.959
5	$T001-5$	50	0.760	3.054
6	$T001-6$	50	0.814	3.292
7	$T001-7$	50	0.796	3.345
8	$T001-9$	75	0.803	3.325
9	$T001-10$	75	0.872	3.380
10	$T001-13$	0	0.655	2.634
11	$T002-1$	25	0.710	2.815
12	$T002-2$	25	0.735	2.932
13	$T002-3$	25	0.746	2.998
14	$T002-4$	25	0.753	3.117
15	$T002-5$	50	0.773	2.979
16	$T002-6$	50	0.825	3.246
17	$T002-7$	50	0.810	3.296
18	$T002-8$	50	0.790	3.462
19	$T002-9$	75	0.787	3.161
20	$T002-10$	75	0.872	3.599
21	$T002-11$	75	0.810	3.852
22	$T002-13$	0	0.722	2.799
23	$T003-1$	25	0.792	3.296
24	$T003-2$	25	0.793	3.518
25	$T003-3$	25	0.727	3.295
26	$T003-4$	25	0.770	3.811
27	$T003-5$	50	0.798	3.347
28	$T003-6$	50	0.848	3.460
29	$T003-7$	50	0.820	3.754
30	$T003-9$	75	0.788	3.357
31	$T003-10$	75	0.895	4.067
32	$T003-13$	0	0.778	3.178

(cot $\alpha = 1.5$) Continue on the next page

Table C.2 Reflection Characteristics Under Bimodal Seas for cot $\alpha = 1.5$ (cont.).

ID	Test No	Swell (%)	Ref. Coeff K_r (-)	Surf Similarity Parameter $\xi_{m-1,0}$ (-)
33	$T004-1$	25	0.774	3.444
34	$T004-2$	25	0.790	3.469
35	$T004-3$	25	0.773	3.688
36	$T004-4$	25	0.782	3.714
37	$T004-5$	50	0.773	3.482
38	$T004-6$	50	0.841	3.840
39	$T004-9$	75	0.794	3.558
40	$T004-10$	75	0.895	4.020
41	$T004-13$	0	0.774	3.424
42	$T005-1$	25	0.739	2.600
43	$T005-2$	25	0.751	2.841
44	$T005-3$	25	0.753	2.886
45	$T005-4$	25	0.732	2.788
46	$T005-5$	50	0.804	2.761
47	$T005-6$	50	0.865	3.087
48	$T005-7$	50	0.842	3.223
49	$T005-8$	50	0.780	3.188
50	$T005-9$	75	0.830	3.176
51	$T005-10$	75	0.921	3.657
52	$T005-11$	75	0.930	3.845
53	$T005-13$	0	0.726	2.549
54	$T006-1$	25	0.725	2.494
55	$T006-2$	25	0.741	2.520
56	$T006-3$	25	0.745	2.508
57	$T006-4$	25	0.751	2.451
58	$T006-5$	50	0.783	2.710
59	$T006-6$	50	0.833	2.869
60	$T006-7$	50	0.817	2.790
61	$T006-9$	75	0.795	2.963
62	$T006-10$	75	0.880	3.273
63	$T006-13$	0	0.732	2.321
64	$T007-1$	25	0.817	2.872
65	$T007-2$	25	0.827	3.084

(cot $\alpha = 1.5$) Continue on the next page

Table C.2 Reflection Characteristics Under Bimodal Seas for cot $\alpha = 1.5$ (cont.).

ID	Test No	Swell (%)	Ref. Coeff K_r (-)	Surf Similarity Parameter $\xi_{m-1,0}$ (-)
66	$T007-3$	25	0.834	3.108
67	$T007-4$	25	0.836	3.045
68	$T007-5$	50	0.826	3.135
69	$T007-6$	50	0.871	3.428
70	$T007-7$	50	0.853	3.188
71	$T007-9$	75	0.830	3.392
72	$T007-10$	75	0.918	3.802
73	$T007-11$	75	0.880	3.788
74	$T007-12$	75	0.830	4.004
75	$T007-13$	0	0.825	2.856
76	$T008-1$	25	0.792	2.922
77	$T008-2$	25	0.813	3.145
78	$T008-3$	25	0.797	2.948
79	$T008-4$	25	0.799	2.949
80	$T008-5$	50	0.803	3.037
81	$T008-6$	50	0.853	2.933
82	$T008-7$	50	0.837	3.212
83	$T008-9$	75	0.810	3.307
84	$T008-10$	75	0.873	3.426
85	$T008-13$	0	0.790	2.959
86	$T009-1$	25	0.740	3.077
87	$T009-2$	25	0.743	3.408
88	$T009-3$	25	0.718	3.440
89	$T009-4$	25	0.713	3.672
90	$T009-5$	50	0.786	3.549
91	$T009-6$	50	0.821	3.613
92	$T009-7$	50	0.891	3.860
93	$T009-8$	50	0.810	4.146
94	$T009-9$	75	0.830	3.621
95	$T009-10$	75	0.888	4.135
96	$T009-11$	75	0.820	4.428
97	$T009-13$	0	0.710	3.052
98	$T010-1$	25	0.805	3.383

(cot $\alpha = 1.5$) Continue on the next page

Table C.2 Reflection Characteristics Under Bimodal Seas for cot $\alpha = 1.5$ (cont.).

ID	Test No	Swell (%)	Ref. Coeff K_r (-)	Surf Similarity Parameter $\xi_{m-1,0}$ (-)
99	$T010-2$	25	0.799	3.475
100	$T010-3$	25	0.796	3.567
101	$T010-4$	25	0.805	3.599
102	$T010-5$	50	0.807	3.222
103	$T010-6$	50	0.845	3.504
104	$T010-7$	50	0.915	3.800
105	$T010-8$	50	0.890	3.814
106	$T010-9$	75	0.814	3.437
107	$T010-10$	75	0.888	4.135
108	$T011-1$	25	0.891	3.388
109	$T011-2$	25	0.810	3.225
110	$T011-3$	25	0.830	3.084
111	$T011-4$	25	0.888	3.316
112	$T011-5$	50	0.820	3.024
113	$T011-6$	50	0.891	3.497
114	$T011-7$	50	0.810	3.609
115	$T011-9$	75	0.830	3.158
116	$T011-10$	75	0.888	3.631
117	$T011-13$	0	0.820	3.085
118	$T0012-1$	25	0.754	3.048
119	$T0012-2$	25	0.736	3.188
120	$T0012-3$	25	0.770	3.296
121	$T0012-4$	25	0.812	3.346
122	$T0012-5$	50	0.764	3.108
123	$T0012-6$	50	0.809	3.531
124	$T0012-9$	75	0.792	3.181
125	$T0012-10$	75	0.842	3.693
126	$T0012-13$	0	0.752	3.153
127	$T013-1$	25	0.812	2.906
128	$T013-2$	25	0.812	3.001
129	$T013-3$	25	0.813	2.906
130	$T013-4$	25	0.862	3.380
131	$T013-5$	50	0.835	3.357

(cot $\alpha = 1.5$) Continue on the next page

Table C.2 Reflection Characteristics Under Bimodal Seas for cot $\alpha = 1.5$ (cont.).

ID	Test No	Swell (%)	Ref. Coeff K_r (-)	Surf Similarity Parameter $\xi_{m-1,0}$ (-)
132	$T013-6$	50	0.894	3.379
133	$T013-7$	50	0.867	3.385
134	$T013-8$	50	0.890	3.424
135	$T013-9$	75	0.846	3.209
136	$T013-10$	75	0.925	3.545
137	$T013-11$	75	0.881	3.974
138	$T013-12$	75	0.800	4.120
139	$T013-13$	0	0.783	2.947
140	$T014-1$	25	0.848	3.233
141	$T014-2$	25	0.855	3.133
142	$T014-3$	25	0.850	3.191
143	$T014-4$	25	0.875	3.342
144	$T014-5$	50	0.851	3.549
145	$T014-6$	50	0.881	3.435
146	$T014-7$	50	0.870	3.427
147	$T014-8$	50	0.897	3.503
148	$T014-9$	75	0.849	3.753
149	$T014-10$	75	0.920	4.349
150	$T014-11$	75	0.878	4.110
151	$T014-12$	75	0.880	4.147
152	$T014-13$	0	0.844	2.883
153	$T015-1$	25	0.850	3.343
154	$T015-2$	25	0.856	3.473
155	$T015-3$	25	0.856	3.553
156	$T015-4$	25	0.872	3.587
157	$T015-5$	50	0.845	3.838
158	$T015-6$	50	0.879	4.043
159	$T015-7$	50	0.869	3.937
160	$T015-8$	50	0.897	4.017
161	$T015-9$	75	0.835	3.396
162	$T015-10$	75	0.903	4.426
163	$T015-11$	75	0.879	4.403
164	$T015-12$	75	0.860	4.261

(cot $\alpha = 1.5$) Continue on the next page

Table C.2 Reflection Characteristics Under Bimodal Seas for cot $\alpha = 1.5$ (cont.).

ID	Test No	Swell (%)	Ref. Coeff K_r (-)	Surf Similarity Parameter $\xi_{m-1,0}$ (-)
165	$T015-13$	0	0.861	3.243
166	$T016-1$	25	0.847	3.818
167	$T016-2$	25	0.841	3.984
168	$T016-3$	25	0.845	4.112
169	$T016-4$	25	0.860	4.147
170	$T016-5$	50	0.828	3.866
171	$T016-6$	50	0.879	3.858
172	$T016-7$	50	0.866	3.695
173	$T016-8$	50	0.898	4.054
174	$T016-12$	75	0.810	4.421
175	$T016-13$	0	0.846	3.773
176	$T017-1$	25	0.730	3.069
177	$T017-2$	25	0.742	3.232
178	$T017-3$	25	0.733	3.275
179	$T017-4$	25	0.801	3.354
180	$T017-5$	50	0.795	3.374
181	$T017-6$	50	0.841	3.630
182	$T017-7$	50	0.824	3.797
183	$T017-8$	50	0.885	4.007
184	$T017-9$	75	0.819	3.611
185	$T017-10$	75	0.908	3.794
186	$T017-13$	0	0.705	2.892
187	$T018-1$	25	0.800	3.378
188	$T018-2$	25	0.789	3.467
189	$T018-3$	25	0.783	3.556
190	$T018-4$	25	0.794	3.589
191	$T018-5$	50	0.806	3.529
192	$T018-6$	50	0.853	3.511
193	$T018-7$	50	0.836	4.082
194	$T018-8$	50	0.810	4.096
195	$T018-9$	75	0.827	3.777
196	$T018-10$	75	0.910	4.158
197	$T018-13$	0	0.815	3.238

(cot $\alpha = 1.5$) Continue on the next page

Table C.2 Reflection Characteristics Under Bimodal Seas for cot $\alpha = 1.5$ (cont.).

ID	Test No	Swell (%)	Ref. Coeff K_r (-)	Surf Similarity Parameter $\xi_{m-1,0}$ (-)
198	$T019-1$	25	0.809	3.625
199	$T019-2$	25	0.817	3.768
200	$T019-3$	25	0.825	3.798
201	$T019-4$	25	0.830	3.846
202	$T019-5$	50	0.818	3.702
203	$T019-6$	50	0.855	3.688
204	$T019-7$	50	0.842	4.265
205	$T019-8$	50	0.910	4.509
206	$T019-9$	75	0.820	3.522
207	$T019-10$	75	0.885	4.462
208	$T019-11$	75	0.890	4.803
209	$T019-13$	0	0.815	3.489
210	$T020-1$	25	0.730	3.121
211	$T020-2$	25	0.742	2.951
212	$T020-3$	25	0.733	3.250
213	$T020-4$	25	0.801	3.379
214	$T020-5$	50	0.795	3.035
215	$T020-6$	50	0.841	3.654
216	$T020-7$	50	0.824	3.819
217	$T020-8$	50	0.885	3.899
218	$T020-9$	75	0.819	4.085
219	$T020-13$	0	0.780	4.259
220	$T021-1$	25	0.796	3.546
221	$T021-2$	25	0.801	3.456
222	$T021-3$	25	0.798	3.480
223	$T021-4$	25	0.892	3.643
224	$T021-5$	50	0.819	3.739
225	$T021-6$	50	0.853	4.097
226	$T021-7$	50	0.934	4.136
227	$T021-8$	50	0.950	4.177
228	$T021-9$	75	0.926	3.934
229	$T021-10$	75	0.950	4.448
230	$T021-11$	75	1.038	4.967

(cot $\alpha = 1.5$) Continue on the next page

Table C.2 Reflection Characteristics Under Bimodal Seas for cot $\alpha = 1.5$ (cont.).

ID	Test No	Swell (%)	Ref. Coeff K_r (-)	Surf Similarity Parameter $\xi_{m-1,0}$ (-)
231	$T021-12$	75	0.960	5.152
232	$T021-13$	0	0.797	3.306
233	$T022-1$	25	0.850	3.852
234	$T022-2$	25	0.856	4.270
235	$T022-3$	25	0.847	4.346
236	$T022-4$	25	0.867	4.367
237	$T022-5$	50	0.866	3.826
238	$T022-6$	50	0.884	4.382
239	$T022-7$	50	0.873	4.277
240	$T022-8$	50	0.886	4.357
241	$T022-9$	75	0.852	3.959
242	$T022-10$	75	0.924	4.867
243	$T022-11$	75	0.874	5.596
244	$T022-13$	0	0.845	3.930
245	$T023-1$	25	0.855	3.502
246	$T023-2$	25	0.854	4.251
247	$T023-3$	25	0.856	4.352
248	$T023-4$	25	0.872	4.393
249	$T023-5$	50	0.849	3.956
250	$T023-6$	50	0.883	4.837
251	$T023-7$	50	0.751	4.685
252	$T023-8$	50	0.783	4.510
253	$T023-9$	75	0.833	4.626
254	$T023-10$	75	0.817	4.845
255	$T023-11$	75	0.800	5.289
256	$T023-12$	75	0.795	5.547
257	$T023-13$	0	0.880	4.267
258	$T024-1$	25	0.840	4.018
259	$T024-2$	25	0.870	4.230
260	$T024-3$	25	0.732	4.781
261	$T024-4$	25	0.817	4.588
262	$T024-5$	50	0.827	4.321
263	$T024-6$	50	0.834	4.996

(cot $\alpha = 1.5$) Continue on the next page

Table C.2 Reflection Characteristics Under Bimodal Seas for cot $\alpha = 1.5$ (cont.).

ID	Test No	Swell (%)	Ref. Coeff K_r (-)	Surf Similarity Parameter $\xi_{m-1,0}$ (-)
264	$T024-7$	50	0.836	5.377
265	$T024-8$	50	0.826	5.427
266	$T024-9$	75	0.871	4.417
267	$T024-10$	75	0.853	4.724
268	$T024-11$	75	0.880	5.611
269	$T024-12$	75	0.830	5.663
270	$T024-13$	0	0.918	4.048

Table C.3 Reflection Characteristics Under Bimodal Seas for cot $\alpha = 0.0$

ID	Test No	Swell (%)	Reff Coeff K_r (-)	Surf Similarity Parameter $\xi_{m-1,0}$ (-)
1	$T001-1$	25	0.841	2.618
2	$T001-2$	25	0.847	2.707
3	$T001-3$	25	0.848	2.750
4	$T001-4$	25	0.846	2.749
5	$T001-5$	50	0.824	2.775
6	$T001-6$	50	0.844	2.966
7	$T001-7$	50	0.864	3.066
8	$T001-9$	75	0.806	2.882
9	$T001-10$	75	0.850	3.361
10	$T001-13$	1	0.832	2.458
11	$T002-1$	25	0.869	2.826
12	$T002-2$	25	0.870	2.927
13	$T002-3$	25	0.867	2.983
14	$T002-4$	25	0.871	2.986
15	$T002-5$	50	0.847	2.930
16	$T002-6$	50	0.843	3.150
17	$T002-7$	50	0.857	3.228
18	$T002-9$	75	0.802	3.065
19	$T002-10$	75	0.841	3.450
20	$T002-13$	1	0.873	2.682

(cot $\alpha = 0.0$) Continue on the next page

Table C.3 Reflection Characteristics Under Bimodal Seas for cot $\alpha = 0.0$ (cont.).

ID	Test No	Swell (%)	Ref. Coeff K_r (-)	Surf Similarity Parameter $\xi_{m-1,0}$ (-)
21	$T003-1$	25	0.853	3.097
22	$T003-2$	25	0.829	3.086
23	$T003-3$	25	0.840	3.166
24	$T003-4$	25	0.826	3.155
25	$T003-5$	50	0.826	3.028
26	$T003-6$	50	0.832	3.330
27	$T003-7$	50	0.854	3.412
28	$T003-9$	75	0.800	3.135
29	$T003-10$	75	0.830	3.466
30	$T003-13$	1	0.859	2.899
31	$T004-1$	25	0.822	3.116
32	$T004-2$	25	0.799	3.134
33	$T004-3$	25	0.836	3.243
34	$T004-4$	25	0.840	3.369
35	$T004-5$	50	0.804	3.138
36	$T004-6$	50	0.819	3.308
37	$T004-7$	50	0.832	3.467
38	$T004-9$	75	0.795	3.183
39	$T004-10$	75	0.817	3.554
40	$T004-13$	1	0.807	3.087
41	$T005-1$	25	0.877	2.904
42	$T005-2$	25	0.870	3.044
43	$T005-3$	25	0.862	3.085
44	$T005-4$	25	0.863	3.109
45	$T005-5$	50	0.859	3.129
46	$T005-6$	50	0.832	3.307
47	$T005-7$	50	0.875	3.510
48	$T005-8$	50	0.780	3.425
49	$T005-9$	75	0.815	3.293
50	$T005-10$	75	0.817	3.709
51	$T005-11$	75	0.930	3.990
52	$T005-13$	1	0.867	2.746
53	$T006-1$	25	0.873	2.829

(cot $\alpha = 0.0$) Continue on the next page

Table C.3 Reflection Characteristics Under Bimodal Seas for cot $\alpha = 0.0$ (cont.).

ID	Test No	Swell (%)	Ref. Coeff K_r (-)	Surf Similarity Parameter $\xi_{m-1,0}$ (-)
54	$T006-2$	25	0.886	2.939
55	$T006-3$	25	0.873	2.988
56	$T006-4$	25	0.876	2.990
57	$T006-5$	50	0.849	2.932
58	$T006-6$	50	0.834	3.143
59	$T006-7$	50	0.864	3.234
60	$T006-9$	75	0.801	3.065
61	$T006-10$	75	0.829	3.440
62	$T006-13$	1	0.880	2.708
63	$T007-1$	25	0.855	3.216
64	$T007-2$	25	0.857	3.474
65	$T007-3$	25	0.863	3.499
66	$T007-4$	25	0.859	3.536
67	$T007-5$	50	0.845	3.402
68	$T007-6$	50	0.839	3.673
69	$T007-7$	50	0.861	3.912
70	$T007-9$	75	0.810	3.513
71	$T007-10$	75	0.846	4.034
72	$T007-11$	75	0.874	4.367
73	$T007-12$	75	0.830	4.624
74	$T007-13$	1	0.861	3.221
75	$T008-1$	25	0.826	3.038
76	$T008-2$	25	0.836	3.266
77	$T008-3$	25	0.848	3.253
78	$T008-4$	50	0.829	3.344
79	$T008-5$	50	0.823	3.052
80	$T008-6$	50	0.841	3.341
81	$T008-7$	50	0.852	3.514
82	$T008-9$	75	0.822	3.169
83	$T008-10$	75	0.846	3.508
84	$T008-13$	1	0.843	2.998
85	$T009-1$	25	0.861	3.021
86	$T009-2$	25	0.858	3.035

(cot $\alpha = 0.0$) Continue on the next page

Table C.3 Reflection Characteristics Under Bimodal Seas for cot $\alpha = 0.0$ (cont.).

ID	Test No	Swell (%)	Ref. Coeff K_r (-)	Surf Similarity Parameter $\xi_{m-1,0}$ (-)
87	$T009-3$	25	0.848	3.074
88	$T009-4$	25	0.844	2.973
89	$T009-5$	50	0.823	3.101
90	$T009-6$	50	0.817	3.295
91	$T009-7$	50	0.866	3.502
92	$T009-8$	50	0.810	3.591
93	$T009-9$	75	0.810	3.289
94	$T009-10$	75	0.795	3.689
95	$T009-11$	75	0.856	4.078
96	$T009-13$	1	0.856	2.739
97	$T010-1$	25	0.805	3.088
98	$T010-2$	25	0.926	3.274
99	$T010-3$	25	0.919	3.225
100	$T010-4$	25	0.863	3.332
101	$T010-5$	50	0.859	3.264
102	$T010-6$	50	0.815	3.478
103	$T010-7$	50	0.875	3.763
104	$T010-8$	50	0.890	3.814
105	$T010-9$	75	0.796	3.422
106	$T010-10$	75	0.794	3.688
107	$T010-13$	1	0.887	3.009
108	$T011-1$	25	0.861	2.998
109	$T011-2$	25	0.880	3.281
110	$T011-3$	25	0.830	3.084
111	$T011-4$	25	0.840	3.065
112	$T011-5$	50	0.852	3.048
113	$T011-6$	50	0.821	3.215
114	$T011-7$	50	0.808	3.374
115	$T011-9$	75	0.810	3.043
116	$T011-10$	75	0.814	3.452
117	$T011-13$	1	0.867	2.905
118	$T0012-1$	25	0.843	3.033
119	$T0012-2$	25	0.821	3.151

(cot $\alpha = 0.0$) Continue on the next page

Table C.3 Reflection Characteristics Under Bimodal Seas for cot $\alpha = 0.0$ (cont.).

ID	Test No	Swell (%)	Ref. Coeff K_r (-)	Surf Similarity Parameter $\xi_{m-1,0}$ (-)
120	$T0012-3$	25	0.832	3.240
121	$T0012-4$	25	0.811	3.740
122	$T0012-5$	50	0.822	3.052
123	$T0012-6$	50	0.804	3.487
124	$T0012-9$	75	0.794	3.182
125	$T0012-10$	75	0.809	3.547
126	$T0012-13$	1	0.828	3.103
127	$T013-1$	25	0.873	3.407
128	$T013-2$	25	0.874	3.519
129	$T013-3$	25	0.870	3.542
130	$T013-4$	25	0.873	3.626
131	$T013-5$	50	0.858	3.559
132	$T013-6$	50	0.820	3.832
133	$T013-7$	50	0.874	4.075
134	$T013-8$	50	0.872	4.096
135	$T013-9$	75	0.804	3.817
136	$T013-10$	75	0.800	4.286
137	$T013-11$	75	0.873	4.767
138	$T013-12$	75	0.800	4.698
139	$T013-13$	1	0.867	3.171
140	$T014-1$	25	0.894	3.671
141	$T014-2$	25	0.891	3.799
142	$T014-3$	25	0.885	3.869
143	$T014-4$	25	0.873	3.857
144	$T014-5$	50	0.865	3.825
145	$T014-6$	50	0.825	3.863
146	$T014-7$	50	0.873	4.277
147	$T014-8$	50	0.873	4.343
148	$T014-9$	75	0.808	3.916
149	$T014-10$	75	0.754	4.401
150	$T014-11$	75	0.875	4.683
151	$T014-12$	75	0.880	5.172
152	$T014-13$	1	0.894	3.508

(cot $\alpha = 0.0$) Continue on the next page

Table C.3 Reflection Characteristics Under Bimodal Seas for cot $\alpha = 0.0$ (cont.).

ID	Test No	Swell (%)	Ref. Coeff K_r (-)	Surf Similarity Parameter $\xi_{m-1,0}$ (-)
153	$T015-1$	25	0.864	3.873
154	$T015-2$	25	0.841	3.995
155	$T015-3$	25	0.851	4.098
156	$T015-4$	25	0.841	4.111
157	$T015-5$	50	0.836	3.943
158	$T015-6$	50	0.799	4.179
159	$T015-7$	50	0.842	4.516
160	$T015-8$	50	0.855	4.591
161	$T015-9$	75	0.780	4.027
162	$T015-10$	75	0.773	4.519
163	$T015-11$	75	0.873	5.077
164	$T015-12$	75	0.874	5.059
165	$T015-13$	1	0.863	3.747
166	$T016-1$	25	0.829	4.007
167	$T016-2$	25	0.770	3.916
168	$T016-3$	25	0.833	4.321
169	$T016-4$	25	0.830	4.339
170	$T016-5$	50	0.793	4.040
171	$T016-6$	50	0.764	4.331
172	$T016-7$	50	0.835	4.498
173	$T016-8$	50	0.833	5.085
174	$T016-9$	75	0.755	4.047
175	$T016-10$	75	0.764	4.623
176	$T016-11$	75	0.879	5.018
177	$T016-12$	75	0.874	5.398
178	$T016-13$	1	0.835	3.966
179	$T017-1$	25	0.877	2.904
180	$T017-2$	25	0.876	3.049
181	$T017-3$	25	0.868	3.090
182	$T017-4$	25	0.862	2.986
183	$T017-5$	50	0.858	3.128
184	$T017-6$	50	0.864	3.333
185	$T017-7$	50	0.886	3.519

(cot $\alpha = 0.0$) Continue on the next page

Table C.3 Reflection Characteristics Under Bimodal Seas for cot $\alpha = 0.0$ (cont.).

ID	Test No	Swell (%)	Ref. Coeff K_r (-)	Surf Similarity Parameter $\xi_{m-1,0}$ (-)
186	$T017-8$	50	0.882	3.512
187	$T017-9$	75	0.837	3.311
188	$T017-10$	75	0.866	3.754
189	$T017-11$	75	0.885	3.946
190	$T017-13$	1	0.870	2.748
191	$T018-1$	25	0.898	3.159
192	$T018-2$	25	0.889	3.244
193	$T018-3$	25	0.887	3.330
194	$T018-4$	25	0.886	3.351
195	$T018-5$	50	0.863	3.267
196	$T018-6$	50	0.848	3.506
197	$T018-7$	50	0.887	3.626
198	$T018-8$	50	0.892	3.666
199	$T018-9$	75	0.828	3.449
200	$T018-10$	75	0.869	3.757
201	$T018-11$	75	0.910	3.971
202	$T018-13$	1	0.900	3.019
203	$T019-1$	25	0.853	3.214
204	$T019-2$	25	0.859	3.475
205	$T019-3$	25	0.865	3.364
206	$T019-4$	25	0.864	3.402
207	$T019-5$	50	0.846	3.403
208	$T019-6$	50	0.848	3.682
209	$T019-7$	50	0.864	3.915
210	$T019-8$	50	0.878	4.083
211	$T019-9$	75	0.818	3.520
212	$T019-10$	75	0.862	4.050
213	$T019-11$	75	0.890	4.385
214	$T019-13$	1	0.862	3.222
215	$T020-1$	25	0.730	3.236
216	$T020-2$	25	0.742	3.569
217	$T020-3$	25	0.733	3.653
218	$T020-4$	25	0.801	3.731

(cot $\alpha = 0.0$) Continue on the next page

Table C.3 Reflection Characteristics Under Bimodal Seas for cot $\alpha = 0.0$ (cont.).

ID	Test No	Swell (%)	Ref. Coeff K_r (-)	Surf Similarity Parameter $\xi_{m-1,0}$ (-)
219	$T020-5$	50	0.795	3.501
220	$T020-6$	50	0.841	3.822
221	$T020-7$	50	0.824	4.062
222	$T020-8$	50	0.885	4.206
223	$T020-9$	75	0.819	3.579
224	$T020-10$	75	0.820	4.042
225	$T020-11$	75	0.830	4.468
226	$T020-13$	1	0.780	3.409
227	$T021-1$	25	0.860	3.396
228	$T021-2$	25	0.865	3.511
229	$T021-3$	25	0.861	3.534
230	$T021-4$	25	0.859	3.613
231	$T021-5$	50	0.851	3.768
232	$T021-6$	50	0.799	3.812
233	$T021-7$	50	0.862	4.063
234	$T021-8$	50	0.950	4.177
235	$T021-9$	75	0.798	3.811
236	$T021-10$	75	0.779	4.265
237	$T021-11$	75	1.038	4.712
238	$T021-12$	75	0.860	4.767
239	$T021-13$	1	0.860	3.165
240	$T022-1$	25	0.886	3.664
241	$T022-2$	25	0.879	3.787
242	$T022-3$	25	0.874	3.858
243	$T022-4$	25	0.869	3.853
244	$T022-5$	50	0.859	3.623
245	$T022-6$	50	0.812	4.059
246	$T022-7$	50	0.863	4.267
247	$T022-8$	50	0.867	4.336
248	$T022-9$	75	0.801	3.910
249	$T022-10$	75	0.752	4.399
250	$T022-11$	75	0.874	4.682
251	$T022-13$	1	0.883	3.499

(cot $\alpha = 0.0$) Continue on the next page

Table C.3 Reflection Characteristics Under Bimodal Seas for cot $\alpha = 0.0$ (cont.).

ID	Test No	Swell (%)	Ref. Coeff K_r (-)	Surf Similarity Parameter $\xi_{m-1,0}$ (-)
252	$T023-1$	25	0.856	3.866
253	$T023-2$	25	0.841	3.995
254	$T023-3$	25	0.850	4.097
255	$T023-4$	25	0.841	4.111
256	$T023-5$	50	0.838	3.945
257	$T023-6$	50	0.785	4.165
258	$T023-7$	50	0.789	4.729
259	$T023-8$	50	0.844	4.578
260	$T023-9$	75	0.781	4.028
261	$T023-10$	75	0.760	4.505
262	$T023-11$	75	0.864	5.065
263	$T023-12$	75	0.795	4.961
264	$T023-13$	1	0.858	3.742
265	$T024-1$	25	0.835	4.013
266	$T024-2$	25	0.772	3.918
267	$T024-3$	25	0.832	4.320
268	$T024-4$	25	0.809	4.317
269	$T024-5$	50	0.802	4.049
270	$T024-6$	50	0.759	4.326
271	$T024-7$	50	0.830	4.492
272	$T024-8$	50	0.827	4.542
273	$T024-9$	75	0.756	4.048
274	$T024-10$	75	0.738	4.594
275	$T024-11$	75	0.869	5.005
276	$T024-12$	75	0.863	5.107
277	$T024-13$	1	0.835	3.966

Appendix D

Examples of Wave Gauge Calibration

Accuracy of recorded surface elevation is an essential component of this research. As earlier mentioned, the wave gauges are regularly calibrated to ascertain better reliability of the outcome. Using the calibration routine of the HR Daq system, the linear relationship between raw voltages at zero water level and the voltages during wave motion are established. Recorded voltages are linearly converted into water surface elevation using Equation D.1.

$$Mod_{value} = \left(mod_{fac} * Dat_{volts}\right) - Zero_{volts} \tag{D.1}$$

where Mod_{value} is the recorded surface elevation at the model scale, mod_{fac} is the model factor of calibration, and $Zero_{volts}$ is the voltage values recorded at still water level. Appendix D present results of wave gauge calibration obtained for the first five tests conducted during this study. Respective channel numbers represent each wave gauge. Channel 1 is closest to the wavemaker while Channel 8 is positioned at the crest of the structure. Acceptability of calibration results depends on the value of the correlation R^2 factor at 95 per cent CI. Calibration values that are less than 0.999 are repeated to obtain a better result. Appendix D contains examples of outputs of selected wave gauge calibration results.

Table D.1 Test 1. wave gauge calibration

Name	Cal (m/V)	Zero (V)	R^2	95% CI
Channel 1	0.0335	0.029	1.00000	0.0000
Channel 2	0.0388	-0.115	0.99999	0.0002
Channel 3	0.0394	-0.084	0.99999	0.0002
Channel 5	0.0365	-0.024	1.00000	0.0001
Channel 6	0.0353	-0.109	0.99998	0.0003
Channel 7	0.0323	-0.092	0.99995	0.0004
Channel 8	0.0288	0.017	1.00000	0.0000

Table D.2 Test 2. wave gauge calibration

Name	Cal (m/V)	Zero (V)	R^2	95% CI
Channel 1	0.0281	0.093	0.99986	0.0005
Channel 2	0.0323	0.004	0.99994	0.0004
Channel 3	0.0331	-0.022	0.99985	0.0006
Channel 5	0.0316	-0.133	0.99995	0.0003
Channel 6	0.0299	-0.015	0.99984	0.0005
Channel 7	0.0298	-0.141	0.99996	0.0003
Channel 8	0.0216	-0.037	0.99979	0.0004

Table D.3 Test 3. wave gauge calibration

Name	Cal (m/V)	Zero (V)	R^2	95% CI
Channel 1	0.0274	-0.006	1.00000	0.0001
Channel 2	0.0314	-0.127	1.00000	0.0000
Channel 3	0.0319	-0.119	1.00000	0.0001
Channel 4	0.0292	-0.009	1.00000	0.0000
Channel 5	0.0302	0.003	1.00000	0.0000
Channel 6	0.0282	-0.093	0.99998	0.0002
Channel 7	0.0183	-0.367	1.00000	0.0000
Channel 8	0.0195	0.048	1.00000	0.0000

Table D.4 Test 4. wave gauge calibration

Name	Cal (m/V)	Zero (V)	R^2	95% CI
Channel 1	0.0259	0.014	0.99990	0.0004
Channel 2	0.0298	-0.105	0.99995	0.0003
Channel 3	0.0303	-0.123	1.00000	0.0000
Channel 4	0.0279	0.005	0.99999	0.0001
Channel 5	0.0291	-0.041	1.00000	0.0001
Channel 6	0.0273	-0.123	0.99999	0.0001
Channel 7	0.0234	-0.065	0.99994	0.0003
Channel 8	0.026	0.043	0.99996	0.0003

Table D.5 Test 5. wave gauge calibration

Name	Cal (m/V)	Zero (V)	R^2	95% CI
Channel 1	0.0256	0.034	1.00000	0.0001
Channel 2	0.0294	-0.066	1.00000	0.0000
Channel 3	0.0299	-0.106	1.00000	0.0001
Channel 4	0.0273	0.029	0.99999	0.0001
Channel 5	0.0285	-0.039	1.00000	0.0001
Channel 6	0.0267	-0.09	1.00000	0.0001
Channel 7	0.0229	-0.064	1.00000	0.0001
Channel 8	0.0261	-0.025	1.00000	0.0000